University of Bath

PHD

Improvement of the In-Cycle Speed Fluctuation and System Efficiency of an Auxiliary Power Unit

Liu, Dian

Award date:
2016

Awarding institution:
University of Bath

Link to publication

Alternative formats
If you require this document in an alternative format, please contact:
openaccess@bath.ac.uk

Copyright of this thesis rests with the author. Access is subject to the above licence, if given. If no licence is specified above, original content in this thesis is licensed under the terms of the Creative Commons Attribution-NonCommercial 4.0 International (CC BY-NC-ND 4.0) Licence (https://creativecommons.org/licenses/by-nc-nd/4.0/). Any third-party copyright material present remains the property of its respective owner(s) and is licensed under its existing terms.

Take down policy
If you consider content within Bath's Research Portal to be in breach of UK law, please contact: openaccess@bath.ac.uk with the details. Your claim will be investigated and, where appropriate, the item will be removed from public view as soon as possible.

Download date: 06. May. 2023

Improvement of the In-Cycle Speed Fluctuation and System Efficiency of an Auxiliary Power Unit

Dian Liu

A thesis submitted for the degree of Doctor of Philosophy

University of Bath

Department of Mechanical Engineering

September 2016

COPYRIGHT

Attention is drawn to the fact that copyright of this thesis rests with the author. A copy of this thesis has been supplied on condition that anyone who consults it is understood to recognise that its copyright rests with the author and that they must not copy it or use material from it except as permitted by law or with the consent of the author.

This thesis may be made available for consultation within the University Library and may be photocopied or lent to other libraries for the purposes of consultation with effect from 09/2016

Signed on behalf of the Faculty/School of Engineering & Design

Abstract

Well reported problems around air quality and climate change, together with the energy crisis resulting from finite fossil fuel resources is motivating all the automotive manufacturers to develop new propulsion systems through electrification and hybridisation. The range extended electric vehicle (REEV) is one of these solutions that seeks a practical compromise between the on-board battery size and the one-charge driving range. The auxiliary power unit (APU) is the key component in a REEV and is designed to maintain the battery charge for long distance trips. Since the APU does not propel the vehicle, it only requires a small capacity engine with low-cylinder-count. This type of engine exhibits severe speed fluctuations due to its low firing frequency. As the engine and the M/G are isolated from the vehicle driving wheels, it is possible to use the electric machine to deliver a counteracting torque to the engine reducing the resultant torque spikes and thus the system speed oscillation but likely to increase the electric losses. This research work aims to minimise the speed fluctuation balanced against the extra losses introduced. A Dynamic Torque Control (DTC) strategy was designed and tested on an APU using a novel approach to achieve this target.

The system components were modelled individually regarding to the prototype system specifications, which is developed within a collaborative R&D project. The empirical engine model was calibrated with extensive bench testing data to recreate the in-cycle torque waveforms. The motor/generator was modelled as a novel hybrid between an analytical model and an FEA model which allowed the winding inductance variation due to the current rise to be included in the model. This approach was designed to replicate the electric machine performance with high fidelity whilst keeping the computational time and cost low. With the help from the system model, the DTC torque demand patterns were designed based on detailed analysis of the contribution factors of the speed fluctuation and the electric machine losses. A unique Pareto Curve of the speed fluctuation reduction and the electrical loss was identified

during the analysis and allowed the optimal demand pattern to be developed for a given torque capability electric machine. The simulation results showed that the system in-cycle speed fluctuations could be reduced by 16.4% and 19.11% at 2000rpm full load and 4500rpm full load condition respectively while the electric specific fuel consumption (ESFC) rose by 2.26% and 1.35% at the same operation points. The DTC strategy was implemented in the prototype APU and successfully tested on the rig at 2000rpm and 4500rpm. A reduction in the speed oscillation and the ESFC increase consistent with the simulation results were observed. The simulation estimates on ESFC was proved within an error of 2.19%.

This research improves the insight into the mechanisms that are responsible for increased losses when dynamic torque control is used and develops an optimisation approach which takes account of these factors. When an electric machine, which does not have the same instantaneous peak torque capability as the engine, is used in an APU, a better compromise between speed fluctuation smoothing and system efficiency can be achieved.

Acknowledgement

First, I would like to express my most sincere gratitude to my lead supervisor Prof. Chris Brace for his continuous support and guidance. His patience, enthusiasm and broad perspective on the automotive technology have been motivating me throughout my PhD study, especially during the most difficult first and half years. I also would like to express my appreciation to my second supervisor Dr Sam Akehurst. Your immense practical knowledge on the test facilities helped me a lot. You both have been tremendous mentors to me.

I would like to thank the project partners, Ashwoods and Tata European Technical Centre for allowing me to involve in this exciting project. My thanks especially goes to Lloyds Ash, Calum Roke from Ashwoods, Gary Kirkpatrick, Johnathan Breddy, Marco Cecotti and Yash Gandhi from TMETC. Thanks for your help, advice and insight comments.

My sincere thanks also goes to our technicians, Bob Gusthart, Jim Cansell, Martin Fullick and Vijay Rajput. I benefited so much from your experiences and skills. Without you, the test bench setup and operation could never happen such smoothly.

I would like to thank Dr Richard Burke for providing me the opportunity to work with the research groups from Technische Universität Berlin. Thank you, Artur Giedymin, Jürgen Funck and Andreas Bock. It was my fortune meeting you. Your research broadened my experience and I really enjoyed working with you all.

I would like to thank my colleagues from the PVRC, Deepak Hari, Ashwini Agarwal, Leon Rodrigues, Calo Avola, Karl Giles, Andy Lewis and the Chinese colleagues, Huayin Tang, Nic Zhang, Bo Hu, Pengfei Lu, Zhihang Chen, Qiyou Deng, Pin Lu, Dai Liu. I'm really pleased working with you for the last four years and thanks for offering me your valuable help.

I would like to thank China Scholarship Council (CSC) and Graduate School Scholarship from University of Bath for funding my study. You picked the right one!

Finally, special thanks to my parents. I really appreciate the opportunity and the support that you offered allowing me to study abroad. I did not disappoint you and hope you are proud of me as well. Also, thank you, my fiancée. Your company, either from China or right next to me, encouraged me to keep going. Yes, we will get married soon!

（最后，我要特别地感谢我的父母。非常非常感谢你们能够给我提供出国学习的机会，以及各方面的支持。我没有让你们失望，也希望你们能因为我而骄傲。另外还要感谢我的未婚妻。不管距离远近，有你的陪伴就有我坚持下去的动力。我们很快就要结婚啦！）

Contents

List of figures

List of tables

List of abbreviations

AFPM	Axial flux permanent magnet machine
APU	Auxiliary power unit
ASC	APU supervisor control
BLDC	Brushless DC motor
BMEP	Brake mean effective pressure
BSFC	Brake specific fuel consumption
CA	Crank angle
CAD	Computer aided design
CAS	Combustion analysis system
CSI	Current source inverter
DOD	Depth of discharge
DTC	Dynamic torque control; direct torque control
EMF	Electromagnetic motive force
EMS	Engine management system
ESFC	Electrical specific fuel consumption
EV	Electric vehicle
FE	Finite element
FEA	Finite element analysis
FFT	Fast Fourier transform
FMEP	friction mean effective pressure
FOC	Field oriented control
GCU	Generator control unit
HEV	Hybrid electric vehicle
ICE	Internal combustion engine
IGBT	Isolated gate bipolar transistor
IM	Induction motor
IMEP	Indicated mean effective pressure
IPM	Interior permanent magnet motor
LPG	Liquefied petroleum gas
M/G	Motor/generator
MMF	Magnetic motive force
MPSF	mean piston speed factor
MPSSF	mean piston speed squared factor
NEDC	New European drive cycle
NVH	Noise, vibration and harshness
PCPF	peak cylinder pressure factor
PF	Power factor
PM	Permanent magnet
PMSM	Permanent magnet synchronous machines
PWM	Pulse width modulation
REEV	Range extended electric vehicle
RFPM	Radial flux permanent magnet machine
RMS	Root mean square
SOC	State of Charge
SPP	Number of slots per pole per phase
SPP	Slot per pole per phase
SV	Space vector
TDC	Top dead centre
TDCF	Top dead centre fire
THI	Third harmonic injection
TPA	Three pressure analysis
VSI	Voltage source inverter
WOT	Wide open throttle

List of symbols

A	Piston surface area
B	Flux density
C	Battery capacity
e	Back-EMF
f	Frequency
F_f	Friction torque
H	Field intensity
i_d, i_q	d, q axes current
I	Moment of inertia
I_s	Current phasor
J	Current density
k_e	Back-EMF constant
k_d	Winding distribution factor
k_p	Winding pitch factor
k_w	Winding factor
KE	Kinetic energy
L_d, L_q	d,q axes inductance
m	number of phases
m_c	Connecting rod mass
m_{mod}	Modulation index
m_p	Piston assembly mass
mp	Machine periodicity
n	Speed; synchronous speed
p	number of pole pairs; pressure
P	Power; Electrical loss
q	number of slots per pole per phase (SPP)
R, r	Resistance
s	Total number of slots
t	Time
T	Torque
T_{gas}	Gas torque
T_i	Inertia torque
U	Voltage
u_d, u_q	d, q axes voltage
V	Translational speed; Voltage
V_d	Engine displacement
γ	Current angle
δ	Conductor skin depth
λ	Flux
μ	Permeability
σ	Conductivity
ϕ	Load angle
ψ	Flux linkage
ψ_r	Rotor flux linkage
ψ_s	Stator flux linkage
ω_{elec}	electrical angular speed
ω_c	Rotational speed of the connecting rod
ω_{mech}	Mechanical angular speed

CHAPTER - 1
Introduction

This chapter presents the background information of the electrification on modern automotive powertrain and the features of the range extended electric vehicle. The second part introduces the aims and objectives of this research work. The thesis' structure is given at the end of this chapter.

1.1 The modern electric hybridised vehicle powertrain

Recent years as the global environment change and the unstable international oil market price became the big concern for the government and the public. All car manufacturers are seeking solutions to make their product meet the rigorous emission regulations and more fuel economy at the same time. Substantial efforts have been expended on the conventional powertrain system i.e. the internal combustion (IC) engine to achieve the targets, such as engine downsizing with turbocharger boost. At the same time, propelling the vehicle with a different energy format is another trend that every company is trying to follow.

The electric drive, which uses relatively low-cost electricity as the energy source and zero emission at the product end, is regarded as one of the potential substitutes, although the initial idea is as old as the IC engine. Intensive research and development on full electric (EV) and hybrid electric (HEV) vehicle have been carried out in the past decades. Now the concept is gradually accepted by the public. However, the market expansion is still at a slow pace. The share of HEV of overall new vehicle sales is predicted to increase to 6.1% in 2020 while the plug-in EV will expand from 0.4% to 1.5% from 2012 to the same year [1]. The vehicle retail price, travel range and refuelling (charging) time are the most important factors that the customers consider when deciding whether to go for the 'greener' way. However, EV and HEV do not always have an advantage over petrol cars in this comparison. The fact forms a barrier for these low emission and fuel consumption vehicles to become the mainstream. Furthermore, the lithium-ion battery packs, which is a key component in an electric drive system, in HEV/plug-in HEV could be as much as half of the vehicle cost [1, 2]. Consequently, manufacturers are reluctant to put more battery capacity into the car to exchange for more travel range due to the high cost and the extra weight. Therefore, minimising the battery size by improving the system efficiency or attempting different powertrain architectures turn out to be crucial for EV and HEV promotion.

There are three types of hybrid powertrain architectures (parallel, series and power-split) on the market at present. The parallel hybrid system has two sets of power unit, the IC engine, which is the main drive, and the electric motor. Regarding the electric drive output proportion, the system can be classified as micro hybrid (the start-stop system), mild hybrid (the electric motor only assists the engine at high power demand) or full hybrid (the electric motor is capable of driving the vehicle itself). According to the electric motor installation location, the parallel system is also categorised into five configurations (Figure 1-1). The series hybrid vehicle fully depends on the electric motor for drive but with an auxiliary power unit (APU). The APU normally consists a small IC engine or micro turbine and a generator to charge the battery when the vehicle travelled beyond the full electric range. The power-split hybrid system, also known as series-parallel, is the combination of the both the parallel and the series system as the name indicated. It offers the most flexible operation mode but comes with complex system structure and control strategy as the cost.

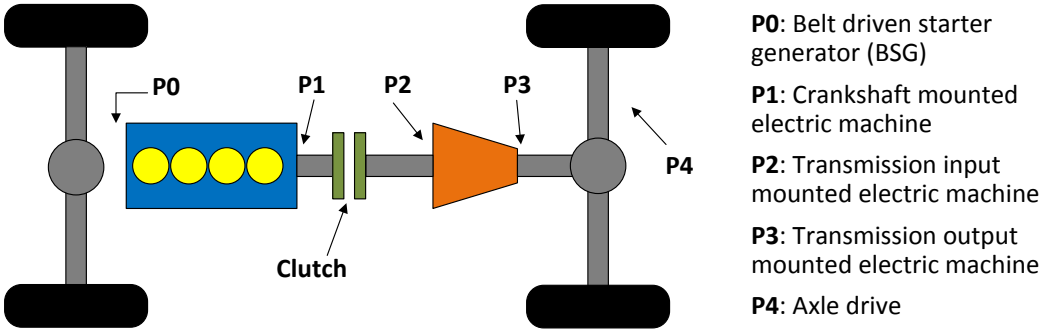

Figure 1-1 P0 to P4 hybrid configurations

1.2 Characteristics of the range extended electric vehicle

The series hybrid vehicle that can be charged from the mains and run in full electric mode can be named as range extended electric vehicle (REEV). Research suggest that the vehicle daily mileage which is less than 50 km counts for 50% in the US and the UK [3, 4] and 70-80% in Germany [5]. The use of an APU to extend the vehicle range is a potential solution that compromises the battery size and the total

driving range. It offers the full electric drive with zero tailpipe emission to fulfil most of the daily commute. When the battery charge is depleted during longer trips, the APU switches on to maintain the battery at a safe state of charge (SOC). Even if the fuel tank ran out, the owner could refill the tank as in a conventional car and the continuation of the journey would not be disturbed.

Since the APU does not directly drive the wheels, it brings two significant benefits over the other hybrid powertrain architectures. First, only a small engine is needed for the APU. When it turns on, the APU only has to provide the average power the vehicle requires at current speed and the reserved battery charge will help for the transient high power demand. Second, the engine could simply run at one or a few operating points to meet different electric power requirements. This brings much easier engine optimisation for the most efficient steady state conditions only. The transient and part load circumstances are not as critical in this case. However, since the energy conversion occurs on board, the process efficiency is not as good as in a fixed power plant. Additionally, the extra weight of the APU has to be carried all the times regardless whether it will be used. Therefore, the more APU operation, the less efficient of the system from the perspective of energy saving. Furthermore, if a low-cylinder-count IC engine were used in the APU, the system noise, vibration and harshness (NVH) might be an issue during the intermittent operation because this type of engine experiences more severe torque pulsation and consequent speed oscillation inherently due to low firing frequency. The speed and torque fluctuation can be noticeable to the passengers, which has negative impacts on the driving comfort.

1.3 Aims and objectives

The aims of this research are (1) to understand and optimise the factor affecting efficiency, performance and in-cycle speed fluctuation of an APU for REEV and (2) minimising the in-cycle shaft speed fluctuation of a low-cylinder-count engine in the APU. This is achieved by actively controlling the motor/generator (M/G) to counteract

the engine torque ripple. The motor/generator used is the permanent magnet synchronous type. Its fast and accurate response due to vector control theory makes the in-cycle torque variation possible.

The following objectives are required to achieve the aims:

- Understanding the causes of engine in-cycle torque variation and model this engine behaviour in MATLAB/Simulink based on the bench testing data;
- Model the M/G with finite element analysis (FEA) package. Understand the motor behaviour and correlate the model to the motor testing data;
- With the model results from the FEA model, model the electric machine analytically in MATLAB/Simulink for the aim of fast simulation response;
- Model the APU system in MATLAB/Simulink;
- Study the effect of various counteracting torque patterns on the engine-in-cycle speed fluctuation and the motor/generator losses;
- Evaluate the factors that affect the system efficiency;
- Design the final dynamic torque control (DTC) torque pattern based on the knowledge of objective 5 and evaluate the simulation results;
- Test the dynamic torque control strategy on the test bench and assess the effect.

1.4 Thesis structure

As per the objectives of this research work, the detailed contents are presented in the following seven chapters of this thesis.

Chapter 2 is the review on the previous works in the related areas of the REEV. It covers the APU operating strategies comparison, APU noise, vibration and harshness (NVH) reduction approaches and the thermal management. The review on permanent magnet electric motors and its control algorithms fundamentals are also included.

Chapter 3 details the modelling work on the engine which was selected for this particular project. It is mainly focusing on the engine in-cycle torque waveform identification and its influence on the in-cycle crankshaft speed fluctuation. Bench testing data

Chapter 4 is the electric machine modelling section. The prototype M/G are first modelled in the FEA software. Its characteristics are extracted from the simulation results and used for the analytical model building. The M/G drive control logic algorithm is built along with the inverter power electronics. The transistors' losses are calculated real time during the simulation. The M/G electric losses is assessed in the FEA model.

Chapter 5 firstly describes the modelling work of the complete APU system which couples the engine and M/G individual models. Then, the rest demonstrate the development process of the APU dynamic torque control strategy. The system model is simulated with a series of simple torque patterns. The speed fluctuation and electric losses trends are assessed. Based on the findings, more torque pattern detail refinements are done on the torque patterns across the system operating range to meet the design criterions.

Chapter 6 presents the bench test results of the APU with and without the dynamic torque control strategy. The speed fluctuation reduction and the system loss (efficiency) variation with DTC enabled are evaluated.

Chapter 7 summarises the results and key findings from this research work. The opportunities and future work that could further improve the low-cylinder-count engine NVH in an APU were discussed.

CHAPTER - 2
Literature Review

This chapter presents a review of previous work and literature focusing on APU operation strategies, NVH reduction and the system thermal management. The fundamentals of permanent magnet synchronous machines and their control algorithms are introduced.

2.1 Introduction

In this chapter, a series of review work is presented which mainly on the auxiliary power unit (APU) in a range extended electric vehicle (REEV) and the fundamentals of permanent magnet synchronous machines (PMSM). In the first part, the pros and cons of different high-level APU operation control strategies are investigated first based on the results from previous researches. Then, a number of techniques from various perspectives to reduce the powertrain vibration and shaft speed fluctuation are introduced. Finally, several cooling system arrangements specifically for hybrid powertrains are presented. The second part of the reviews focuses on all on electric machines. The two most common types of PMSM, radial and axial flux, are compared. It is followed by an introduction to the winding styles in the stator. Lastly, the basic principles of two electric machine vector control techniques are explained. Other types of electric motors (such as DC, asynchronous, switch reluctance, etc.) and sensorless control techniques are not specifically studied here in this report.

2.2 Reviews on Auxiliary Power Unit (APU)

2.2.1 Operating strategy of the APU in a range extended vehicle

For a range extended electric vehicle (REEV), the operation normally has two phases, the charge depleting phase and the charge sustaining phase. The charge depleting phase gives vehicle zero tailpipe emission with full electric drive when the battery state of charge (SOC) is high. When the battery charge drops below a predefined threshold, the APU switches on to maintain a certain level of SOC. The battery pack should never go below this SOC level that determined by the manufacturers since deep discharge will affect the battery lifespan [6, 7].

The system's fuel economy and efficiency are primarily determined by the engine operation, hence the timing to activate it and the speed and load set points are crucial to the APU performance. Due to the extra phase between chemical energy (fuel) to vehicle kinetic energy process, the energy conversion in a REEV is relatively inefficient. Consequently, the APU usually does not intend to charge the battery over that pre-defined SOC. When a transient behaviour is demanded, such as accelerating, the residual battery charge is still be able to supplement the power surge. For the steady state scenario or the case of battery failure, the APU alone should provide a 'minimum' power to the vehicle propulsion unit. It allows the vehicle capable to overtake a heavy truck on the motorway [8]. The minimum wheel power requirement for various road gradients is plotted in Figure 2-1. These curves are based on Fiat 500 test fleet [8].

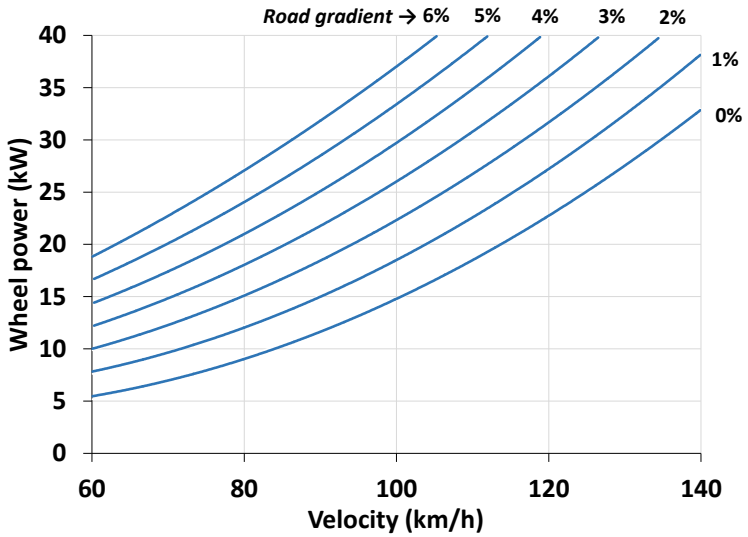

Figure 2-1 Wheel power requirements for different road gradients [8]

Rogge et al performed a comparison of three APU strategies in simulation, which were single operating point, three operating points, and a characteristic curve [7]. A vehicle with similar specifications to the Mitsubishi i-MiEV was modelled and the APU unit was developed by Lotus. The system featured a 1.2L three-cylinder engine and a permanent magnet (PM) synchronous generator. The one-point strategy allows the engine to run only at its maximum efficiency (36kW) condition. When the battery SOC is low, the range extender (RE) unit supplies power directly to the traction motor.

If the power demand is lower than 36kW, the surplus energy produced will be stored in the battery. The Three-point strategy allows the engine to adopt the most appropriate power rating with regard to the vehicle power demand to protect the battery by reducing charge/discharge cycles. The characteristic curve strategy was developed from the engine's minimum fuel consumption curve. With this strategy, the engine output can match the exact power requirement as long as it is higher than 4.7 kW. It was not recommended to run in the area below this point, as the engine offers very poor efficiency. These three strategies were simulated over the Hybrid Technology Approaching Efficient Zero Emission Mobility (HYZEM) drive cycle and the New European Driving Cycle (NEDC). The vehicle started with the same amount of fuel and fully charged battery for each run. The results showed that the single operating point strategy gives the best range and thus has the least fuel consumption of the three strategies in all drive cycles. However, when only the highway driving was considered, very little difference were observed between these strategies due to the long period high power demand. A similar result was also stated in the research from *Tulpule et al* [9]. A series hybrid system is usually equipped with a relatively small sized battery to handle the daily commute range. Long distance motorway driving has to rely on the APU. In this case, the single operating point strategy is the worst among the three regarding to the battery aging effect. This is because the battery acts as an energy buffer to absorb the exceeded engine power, which leads to a larger number of charging cycles. However, the authors claim it should not be an issue when it compares to the vehicle lifespan and concluded that the characteristic curve strategy is the best compromise in terms of overall efficiency and the battery life.

Capaldi presented a range extender for compact city car [10]. As per their power demand calculation, a 10kWe RE unit is enough for the vehicles in this class. A 210cc single cylinder engine from a scooter was used in this prototype. Since it was designated to be a low power unit, the operating strategy is a simple one-point approach. To meet the required performance and optimise the fuel consumption, a series of modifications were made on the engine to achieve the peak torque (18.3Nm)

at 5700rpm. When the engine was tested individually, it gave the brake specific fuel consumption (BSFC) of 275 g/kWh. Afterward coupled to the generator, the unit had to run at a lower speed of 5400rpm to be stable. This is due to the current fluctuation caused by the torque variation from the single cylinder engine. However, the lower speed could not generate high enough output voltage to charge the battery, so further modifications were conducted on the engine to achieve the same torque at requested speed (5700rpm). Although the target output voltage and electric power output were met after the modifications, the current fluctuation issue was not resolved from the root which leads to adverse effect on the system efficiency. The final electrical specific fuel consumption (ESFC) of the system was left at 321 g/kWh.

Liang et al developed a range extender with a 125cc liquefied petroleum gas (LPG) engine to achieve even lower running costs and exhaust emissions [11]. The engine was controlled by a torque-based engine management system (EMS). Two operating points strategy were chosen. The first one is at 4000rpm with a wide-open throttle (WOT). The engine has the best BSFC and the least CO_2 emissions at this point. For better NVH performance, a lower engine speed of 2500rpm WOT was chosen and a torque of 6.1Nm was achieved. This point provided the least HC emission. These engine performance and emission parameters were collected from test bench. However, the authors did not provide any testing or simulation results on the overall unit performance over a driving cycle.

Pischinger et al from KSPG and FEV investigated a few operating strategies on its vertically mounted V-2 engine range extender unit under the NEDC and a real world drive cycle [8]. The single operating point strategy gave the best emission results in NEDC but under real driving condition, this was not favourable since the energy loss during energy conversion (battery charge/discharge) is unavoidable. The authors also claimed that both the single point and the multi-point strategies had negative effects on the drivability especially at low speed due to the disturbance to the driver from

engine switching on/off events. Therefore, the operating curve strategy was adopted and the RE unit was activated only when the vehicle speed exceeds 50kph.

Bassett from Mahle Powertrain used a characteristic curve strategy for an RE unit [12]. According to their analysis of a fleet in the UK, a 30kW unit was recommended for the target C-segment vehicle [13]. The range extender unit was evaluated under Artemis drive cycle since this cycle best represents real driving conditions according to the analysed data collected from the fleet. When defining the operating curve, running the engine in the minimum cyclic system speed fluctuation region was preferred, but other factors, such as the fuel economy and NVH, mean that a compromise had to be found. The speed fluctuation was a cause of concern because of the unconventional engine firing order adopted. The unit was activated when the SOC was lower than 20% and provided a power output which was 1kW higher than the road load demand of the vehicle. The weighted CO_2 emissions on NEDC drive cycle was 42g/km in charge sustaining mode, where the SOC of the battery was retained at about 20% to the end of the drive cycle.

Bhiwapurkar and Ganti compared two charging strategies of a range extender in the charge sustaining mode [6]. One was called the Additional Power method. When a power was demanded by the vehicle driving motor, an extra power was requested from the engine to maintain battery SOC. The additional power demand was proportional to the difference between reference SOC and actual SOC. If the deviation was more than 5%, the linear coefficient increases to make the battery recovery faster. The other method had similar principle but replaced the predefined linear control logic to a PI controller. The simulation results showed a negligible difference in total fuel consumption and battery depth of discharge (DOD) between these two control methods. However, the PI control method allowed the engine able to perform with slow transient response, which helped increase the engine life span. It was believed that high fuel consumption and emissions would occur during engine transient

operation [14], but due to lack of engine transient fuel map data available to the authors it was unable to be shown in simulation results.

2.2.2 NVH reduction for APU in REEVs

The APU only switches on when the vehicle has travelled beyond the full electric range. The engine operation may introduce distinct noise from the electric drivetrain. Therefore the NVH control of a RE unit is one of the key factors to the driving comfort. Some previous work on NVH and torque ripple reduction are reviewed in this section.

For *Mahle*'s range extender that featured an in-line two-cylinder engine, an active torque cancellation control strategy was used for the generator to reduce the engine speed fluctuation and oscillating acceleration [12, 15]. The generator is directly bolted to the crankshaft replacing the flywheel. The overall length is then reduced by 40mm and thus the bearing on the generator rotor side is not required. Since the rotor has low inertia, a flywheel still has to be implemented and located between the two crankpin journals. In order to eliminate the balance shaft, the engine operates with an odd firing interval, i.e. the engine is fired at 360° and 540° in crank angle (CA). Consequently, there is no primary unbalanced force since the two crank pins are on the opposite side of the crank axis. However, the engine experiences nearly zero torque in one engine revolution (small negative torque present in the second half due to compression stroke) and two combustion torque ripples occur in the next revolution. This caused up to 740rpm peak-to-peak speed fluctuation which was undesired. Instead of applying a constant brake torque from the generator, Mahle's dynamic control strategy turns the generator off for the first revolution and then applies a constant torque that is twice the mean cycle torque to the engine crankshaft. The strategy reduces the engine speed variation by nearly half at 2000rpm with 80% throttle and one-third acceleration oscillation decrease is observed at 2500rpm with 50% throttle. Further testing also proved that the active torque cancellation control benefits the system across the whole operating speed range. However, the authors did

not give any details of the influence on the system efficiency by using this control strategy.

Rust and Graf from AVL used a passive method to improve the NVH performance of a rotary engine range extender [16]. Since the rotary engine has inherently low vibration feature, the main issues are the intake and exhaust airborne noise and the system vibration transmitted to the chassis. The target RE unit was fully enclosed in a box with air inlet and outlet designed to be acoustic labyrinths. The main components of the range extender were supported by a frame. The frame was suspended underneath the chassis at the back of the vehicle via elastic mounts. This design allowed the noise level to be less than 65dbA at one meter away from the unit and 58dbA in the cabin. In order to provide better fuel economy and emissions, *Hubmann et al* replaced the rotary engine with a single cylinder engine packaged in the same enclosure [17]. As the goal was to achieve similar NVH performance as the rotary engine, a few optimized designs of the engine were proposed. Two balance shafts setup were introduced equidistant to the cylinder axis. Compared to the one balance shaft design, the first order force on the engine top torque support mount was reduced by 58%. For the torsional vibration, a 1:1 gear stage was added between the generator and the engine to make the rotor rotate in the opposite direction to the crankshaft. Since this rotor had a bigger inertia than the engine, the crank counterweights were increased to match the inertia, which reduced the force on the top mount by nearly twelve times. Since all the analysis was done in virtual environment, the actual system cost and efficiency compared to the rotary engine RE were not provided.

Pischinger et al and Govindswamy et al from FEV developed a concept called *FEVcom (Full Engine Vibration compensator)* to remove engine vibration caused by torque pulsation on a V-2 range extender from KSPG [8, 18]. The authors stated that by making the generator torque dynamically follow the engine torque pattern to minimize the roll moment, the motor would be greatly oversized and the generator

power variation would also lead to a voltage fluctuation, which in turn produced more electrical losses. Therefore, instead of coupling the generator directly to the crankshaft, it is driven by the flywheel via gear in the FEVcom, which allows the electric machine to spin in the opposite direction to the engine. As long as the effective rotational inertias of the engine and the motor were identical with the help of the selected gear ratio, the system roll moment could be balanced out. This concept was tested on a single cylinder engine and showed significant improvement. Half order vertical vibration in engine mounts in were reduced by 90%.

Nakajima et al from Nissan proposed an active engine vibration reduction method in [19]. The electric machine is directly located between the engine and the gearbox. In order to counteract the engine torque ripple, the e-machine alternates between motoring and generating modes to create positive and negative torque. They examined three types of counteracting torque waveform patterns in previous studies - sine wave, the square wave and opposite phase wave (which follows the engine torque profile in the opposite phase). They found that the rectangular wave allowed the use of a smaller sized motor as it could achieve a large effective vibration reduction at a comparatively lower torque level. A multi-rectangular waveform, which was equivalent to a lower resolution version of the opposite phase wave was then proposed as the control methodology. The torque pattern is defined by the mean engine torque for every 90° crank angle starting from the top dead centre (TDC) as shown in Figure 2-2. However, it was found that higher peak torques from the electric machine was not necessarily beneficial to engine speed variation. Another factor which needs to be considered was the cyclic mean torque of the electric machine. Since this work was done on a hybrid powertrain application, the mean torque of the electric machine did not have to equal the engine as in an APU. The more energy generated, the harder the engine worked thus more the fuel consumption. Therefore, the goal of this work was to find out a compromise between four elements - vibration reduction, peak torque ratio, motor mean torque and fuel consumption. The authors claimed that this strategy could provide similar vibration performance as a conventional engine and generate

electric power at the same time without reducing fuel economy. However, over optimisation of vibration and peak electric power would lead to worse fuel economy. However, it was not discussed in the paper whether the frequent motor/generator mode switching will cause any effect on the inverter, the motor or any other components in the electric system in the long term.

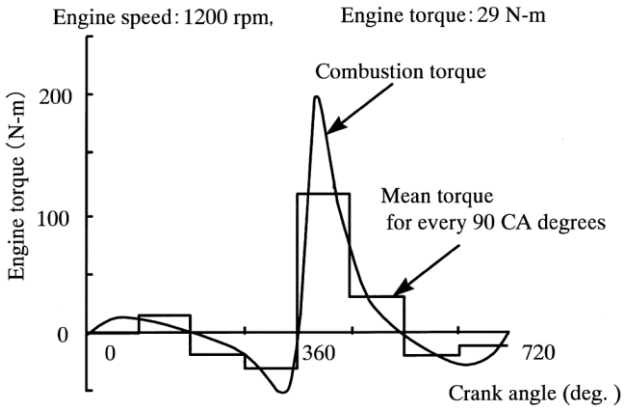

Figure 2-2 The multi-rectangular torque waveform in [19]

Ayana et al from Cummins used a similar approach but with a sinusoidal torque waveform to reduce the engine roll motion in an APU application [20, 21], which was named as the Active Torque Cancellation (ATC). The target system contained a two-cylinder 482cc engine and a 7.5 kW permanent magnet synchronous machine (PMSM). As it is an odd firing order, the authors stated that focus should be on the half order vibration since the low order components (1-2.5) were less noticeable and the higher order ones could be filtered out by flexible engine mounts. The sinusoidal wave was determined by the amplitude and phase of the standard deviations of the excitation. Since the cancellation torque switches between positive and negative values periodically, the dc bus voltage fluctuation is unavoidable. Consequently, capacitors have to be used to smooth out the oscillation. The capacitor size used in the system was 6.38mF. The ATC strategy showed a significant reduction in low frequency transmitted vibration which has more effect on cabin comfort. With ATC, the engine can run at lower speed to achieve the same vibration reduction purpose instead of running at a higher speed, which also brought the benefits of less windage and friction losses. The fuel consumption was reduced by 33% and also a 10dB(A) noise drop was

seen due to speed falling to 1300rpm from 3000rpm. At 1700rpm and 1 kW load, the fuel consumption increased 4% if ATC enabled. The authors realised there was extra loss introduced due to the ATC. However, no detailed analysis or exact number provided in the paper on the system efficiency or power loss.

Instead of using full sinusoidal wave, *Capaldi et al* proposed injecting two half-sine waves to balance out the engine torque pulsations [22]. Since the application was for a 20kW micro-generation plant, the engine used was a modified 1.3L four-cylinder Fiat diesel engine running on methane fuel to meet the emission regulations. The torque pattern of the engine repeats every 360° CA with two ripples in each period (blue dashed line in Figure 2-3). Two half-sine waves generating torque are introduced 'in phase' with the engine ripples. The amplitudes of generator torque were fine tuned to make the mean torque of both the engine and the generator equal for minimum resultant torque variation. However, this was achieved by sacrificing electrical efficiency and oversizing the electric machine. If maximizing the shaft torque damping effect was required, a 3% efficiency drop and 11% extra power requirement was seen compared to a constant generator torque control strategy. In this particular application, there was no negative torque demanded by the torque ripple pattern, i.e. the generator never worked in the motoring mode. Therefore, no battery power was consumed. With this control strategy and the optimal sized generator, the peak resultant torque exerting on the shaft drop to 0.66pu. However, there was no shaft speed fluctuation improvement presented in the paper.

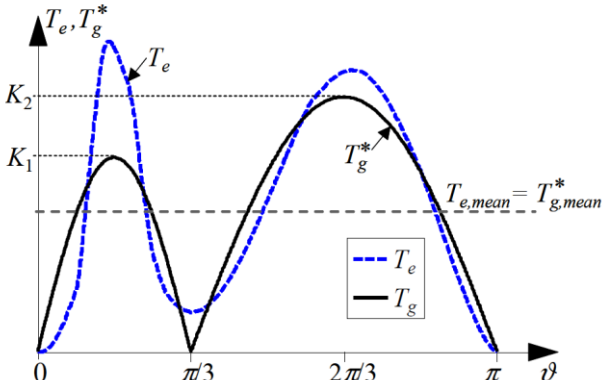

Figure 2-3 The engine and the generator torque pulsations in [22]

The research conducted by *Teichmann et al* was to minimize the drivetrain torsional vibration in a parallel hybrid system [23]. The test system contained an 850cc in-line twin cylinder engine coupled to a 34kW PMSM via an elastic disc clutch. The idea was to reduce engine peak torque amplitude and increase torque pulsation frequency by inducing an electric motor torque pulse between combustion events. This piece of work focused on at the engine speed of 1200rpm. The motor torque was set to 150Nm for 20ms with a 30ms interval in between pulses. This gives the same average torque value as that when a constant motor torque of 60Nm was applied. However, this method was based on off-line calculation for one speed. Further work for online analysis with real time vibration measurement (angle deviation) was underway.

Ito et al from Toyota developed two controllers designed to minimize the torsional vibration of the drive shaft and the transmission of vibration ripple from the engine to the wheels respectively for a parallel hybrid system [24]. The system used a planetary gear to connect three main components which were an IC engine (planetary gear carrier), a generator (sun gear) and a traction motor (ring gear). When the engine needs to be turned on, during the cranking phase the engine expresses torque pulses due to the compression stroke and the pumping work. In order to minimise the torque fluctuations transmitted to the drive shaft, i.e. the ring gear, the generator was demanded to inject torque pulses on top of the mean cranking torque. For the former controller, the engine torque ripple control was the target. The instant ripple was determined by the measured crank angle position based on the pre-measured engine torque pattern. This method showed that only 20% of the peak floor acceleration observed with a conventional control method.

Davis and Lorenz used a starter alternator which was directly mounted to the engine crankshaft as an external torque source to cancel out the engine torque ripple [25]. An analytical engine model was developed and an observer based on it was used to accurately estimate the engine instantaneous torque waveform. The starter alternator

was commanded to apply the inverse torque to the crankshaft. This torque demand from the observer was open loop and the outer loop was closed with the engine speed feedback signal from a physical sensor. Therefore, there was no need to implement extra sensor. The transfer function between engine indicated torque and observer demand torque was tuned to give output equal to input at 1 to 100Hz but attenuated elsewhere. The rig test was conducted on a 1.8L diesel engine with an induction motor as the starter alternator at the speed range from 850 to 2000rpm. The observer showed a very good correlation to the measured engine torque and the speed oscillation especially at low mean speed was improved significantly. However, the authors did not give the specifications of the induction motor. To follow the exact in-cycle torque, an electric motor having high peak torque as required. This may lead to the starter alternator oversizing thus higher cost.

In [26], a range extender unit with a single cylinder diesel engine and a surface-mounted PM machine was adopted with three control approaches to achieve active torque ripple damping. The first approach was the conventional speed PI control. The controller responded to the instantaneous speed rather than the mean engine speed with 120Hz bandwidth. The second one was the PI controller with feedforward regarding to the shaft position. The third one was resonant harmonic compensation. Only the first four speed harmonics were considered due to their domination in the frequency domain. The harmonics compensation technique showed the best results comparing to the other two, especially at low order harmonics. A slight amplitude increase at high order harmonics was observed, but the authors believed that it was less of a concern since these harmonics could be damped by the physical system. The bench testing showed the same results, however, the effectiveness was limited by the electric machine torque range.

2.2.3 Thermal management in an APU

Thermal management is a critical part in vehicle systems. It is more challenging in a hybrid system as extra components are cooperating compared to the conventional IC engine powertrain. The IC engine prefers to run at a high temperature for the benefit of thermal efficiency. However, when the oil is too hot, the oil viscosity drops and leads to more friction and wear. Consequently, the engine coolant temperature normally maintains at 90~100 °C. On the contrary, the electrical devices (generator, power electronics, battery, etc.) prefer operating at lower temperature which mainly required by the insulation. As for the motor windings which is mainly in copper, the resistance will rise as the temperature. This will result in more copper loss. Due to the different requirements from both systems, additional considerations are required in terms of cooling loop arrangement, packaging, complexity etc.

Comprehensive thermal management analysis on a heavy duty serial hybrid electric military use vehicle was done by *Park* [27]. The impacts on the thermal load from both vehicle cooling system (VCS) and climate control system (CCS) were taken into consideration in this study. The battery pack was designed to be cooled by the CCS. The first system configuration (architecture A) kept the original engine cooling circuit unchanged and added a dedicated circuit for all electrical components with an electric pump. This design had the advantage of simplicity, but the target coolant temperature was restricted by the power bus that needed to be the coolest among them. Therefore, as an improvement, in architecture B, the power bus was cooled by another separated circuit. In architecture C, further improvement was made by grouping components that had similar working conditions. Two divided cooling modules with individual fans were introduced as shown in Figure 2-4. The simulation results under different drive cycle showed that configuration C could reduce the VCS power consumption by 26% ~ 47%, but when including the CCS, the total power saved dropped to 13% ~ 24% since the re-design of the cooling circuit did not have much influence on the working load of the air conditioning system. The vehicle fuel

consumption was also improved by 6.1% comparing to architecture A. An interesting finding was that architecture A and B did not show expected difference in power consumption. Although in architecture B the cooling loop for electrical components was separated, the fan was still shared between the two circuits. It indicated that for this particular case the power consumed by the fan contributes a much larger proportion than the electric pump did. The advantage of an electric pump was proven in an earlier study [28]. The author suggested that by replacing the mechanical pump with an electric one, the cooling system power consumption could be reduced and a smaller radiator was required. The electric pump could be actively controlled to meet the required coolant flow rate regardless of the engine speed. This is important for range extender powertrain as the engine is not running all the time. The advantage of an electric pump in engine cooling strategy was also explored in [29]. Another benefit from the improved cooling system design was that less temperature variation of each working component was observed.

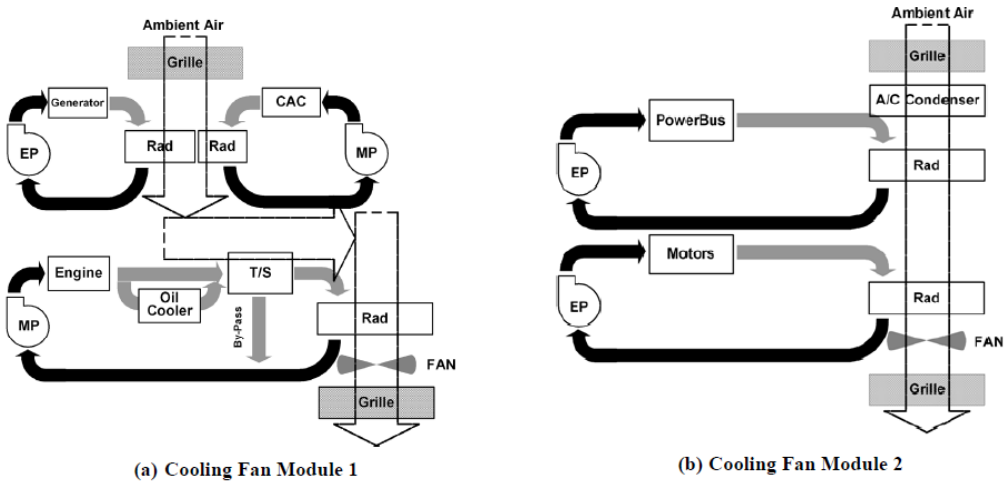

Figure 2-4 Architecture C in [27]

(EP: electric pump, MP: mechanical pump, CAC: charge air cooler, T/S: thermostat)

The *Chevrolet Volt* uses four independent cooling loops to achieve the thermal requirements of each sub-systems [30]. The power electronics and on-board charger share the same cooling circuit, which uses the upper section of the front radiator. The lower section is for the battery. Since the battery (normally lithium-ion) has a narrow

operating temperature window (20~40°C) that is close to the cabin temperature, the common practice is to use the cabin air conditioner (A/C) and engine waste heat or electric heater to maintain the battery health [31]. In the *Chevrolet Volt*, a three-way valve for the battery cooling circuit is used. Apart from the extreme conditions when the cabin A/C or a dedicated heater is connected into the loop, the battery coolant is air cooled by the car front radiator. The engine and the two motor/generators have their own cooling circuit with radiator for different temperature levels as shown in Figure 2-5.

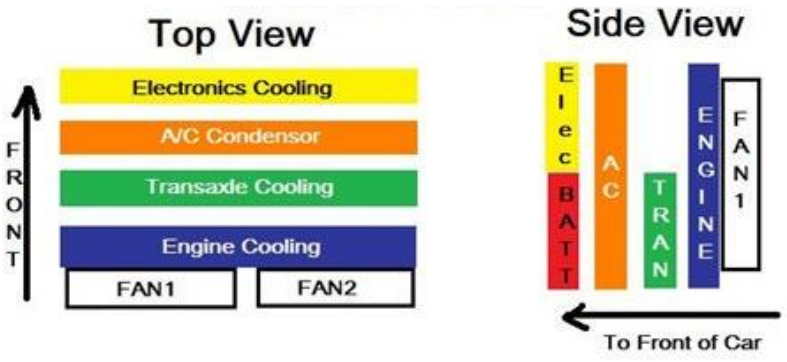

Figure 2-5 Chevrolet Volt radiators layout [30]

Cao et al presented a thermal modelling work for a 2013 Chevrolet Malibu which was converted to a parallel hybrid powertrain [32]. The cooling system was developed from Chevrolet Volt, but consisted of a combined cooling loop for the electric motor and inverter. It was made possible due to their similar operating temperature (90°C for the motor and 70°C for the inverter) to save cost and space at the same time. However, the simulation results showed that the peak temperature of the motor under high load condition was beyond the target while the motor control unit's temperature was 16°C lower than the target, which indicated that the inverter was unnecessarily over cooled. It suggested that this design provided the cost benefit over the original setup but sacrificed the energy efficiency.

Multiple cooling circuit design is effective, but the system complexity, installation requirements and associated costs are significant. Combining cooling

loops of some sub-systems in a proper way can bring cost benefits, which is desired by the OEMs. For example, Toyota Prius consists of a dedicated cooling loop for the Power Electronics and Electric Machine with 65°C peak at the radiator outlet. *Staunton et al* estimated if Prius' electrical system could share the same coolant with ICE which is in around 105°C, approximate $188 saving in cost could be seen [33].

Bennion and Thornton evaluated the impact of thermal load when integrating the electrical system within different temperature coolant circuits for a parallel HEV [34]. The first one was the high temperature integration, which integrated power electronics, electric machine and IC engine cooling loop. Simulation results showed the potential for mass adoption and cost reduction [33]. High temperature will increase the cost and size of the inverter electronics and DC link capacitors. It can also reduce performance of the permanent magnet machine and cause extra copper loss which means more current is required to compensate the torque reduction in the case of a drive motor, or sacrifice the efficiency in the case of a generator. Another cooling configuration is the low temperature loop integration which used the same coolant to cool all fluids in a vehicle [35]. A single radiator in front was only for the common coolant and dual temperature level in the cooling circuit was achievable. It not only helped to save package space but also fuel consumption (up to 6% with cold start with A/C on under NEDC). For HEV, due to the similar working temperatures, the electric drive system could share the coolant with other low temperature sub systems i.e. A/C condenser, charge air cooler and fuel cooler. As the condenser did not have to be in the front of the vehicle, the refrigerant line was reduced and the location of installation was more flexible. Shorter refrigerant line also reduced pressure drop and the risk of leak which helped improve A/C efficiency.

Due to the intermittent operation of the engine in a range extender system, more cold starts could occur. A quick warm-up is very helpful to reduce the emissions and friction loss during this phase. *Revereault et al* studied the effect of different thermal management solutions for rapid warm-up on the fuel economy [36]. The 'coolant heat

battery' solution gave the best improvement in fuel economy (over 4%) over the NEDC. A heat battery is a device used to store heat energy from the engine coolant when it is at operating temperature and release the heat back when it is cold. The heat battery is insulated in vacuum, so the energy loss is limited. This concept was very similar to the one used in *Toyota Prius* which stores hot coolant in a flask and use it to warm the cold engine up. Another solution studied in this paper was the split oil sump which is depicted in Figure 2-6. It showed similar fuel consumption improvement. A compartment is 'isolated' to the rest sump by perforated basket, so only a small proportion of the oil needs to be heated up at the beginning which is faster than heating the total volume. When the oil is hot, its viscosity drops, so sufficient quantity of oil is still available for normal operation.

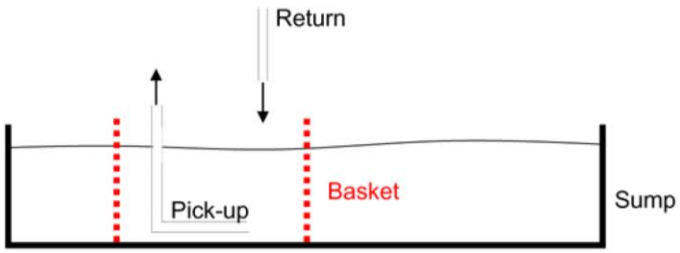

Figure 2-6 Split oil sump solution [36]

2.3 Reviews on Permanent Magnet Synchronous Machines (PMSM)

Induction machine (IM) and permanent magnet synchronous machine (PMSM) are the two main types of electric motor used in automotive drive applications. The former and its drive have been studied and well understood for a few decades while the latter one draws more attentions in recent years due to its better efficiency. *Bucherl et al* simulated both PMSM and IM motors in a parallel hybrid system. The result shows the overall system fuel consumption was reduced up to 4% with PMSM [37]. *Simsir and Ertan* stated in their study that the axial flux PMSM had only 1/10 of the core mass for the same torque capability over the IM machine [38]. As a high strength magnetic field is created by compact sized rare earth magnets, the motor volume could be kept relatively small, thus, the machine power density is higher. *Huang et al* had a

study on power density comparison between a few axial flux machines based on the sizing equation [39]. They found that when rare earth magnets were used, the power density could be improved up to three times. Furthermore, since permanent magnet is used to create the magnetic field rather than conductor coils, the rotor copper loss is eliminated [40]. Some other benefits of PMSM, like fault-tolerant, field weakening capabilities, etc. are also reviewed in [41-43].

Under the synchronous machine category, two topologies are easy to be obscured, which are the brushless DC (BLDC) machine and the synchronous AC machine. The physical structure for these two machines could be very similar. The differences are the inverter output current waveform and the induced electromotive force (back-EMF) from the windings. The brushless DC motor is fed with square wave current (actually is trapezoidal due to the inductance) and generates trapezoidal back-EMF. The three phase BLDC is controlled through six-step scheme. At every instant, there are only two phase windings connected to the DC bus and one phase in open loop. This is called 120° inverter since every inverter leg has three status, i.e. up, down and off. Thus, for the shaft position feedback, only six positons detection is needed for the controller. Therefore, very cheap hall sensors can meet the requirements. The Synchronous AC motor is running with sinusoidal current wave and the back-EMF is sinusoidal as well. A 180° inverter is usually implemented. This means that all three phases are always conducting current. A high precision shaft encoder is demanded since the sinusoidal voltage input control, mainly through pulse width modulation (PWM), needs to know the exact instantaneous field orientation. This gives the synchronous AC machine superior stability especially at low speed. However, since the motor torque is directly related to the fundamental harmonic of the phase current, the BLDC has slightly advantage over the synchronous AC motor, because the fundamental harmonic RMS of a square wave is higher than the sinusoidal when the peak current limit is the same for both [44]. More details of the inverter control will be discussed later.

2.3.1 Radial flux versus axial flux

Regarding to the PM flux direction, synchronous machines could be classified as radial flux type if the main flux lines are perpendicular to the motor shaft and axial flux type if the main flux lines are in the same orientation as the shaft. Since the axial flux permanent magnet machine (AFPM) utilises more surface area of the rotor, it has advantages over the more conventional radial flux counterpart (RFPM), such as shorter axial length, higher torque density, more efficient, mechanically adjustable air gap and so on [40, 45].

In the study from *Cavagnino et al* [46], they undertook a comparison procedure between a conventional RFPM machine and a double-stator single rotor AFPM machine. The overall volume, losses per wasted surface and air-gap flux density were kept identical for both machines. The analysis was focusing on the electromagnetic torque and torque density variation by varying two geometry ratios (axial length/motor outer diameter and motor inner diameter/outer diameter). The results indicated when the axial length was restricted and high pole number was determined, the axial flux motor performed better than radial flux one.

A comparison between an ironless (coreless) AFPM and a RFPM for solar power race car drivetrain was conducted by *Al Zaher et al* [47]. Both motors were tested in a relatively narrow speed and torque ranges (800-1100rpm and 10-22 Nm) as for this particular application. The AFPM motor was favoured in the low torque region due to the absence of iron loss with the coreless design. When higher torque was needed, more current has to be fed to the coreless coil. This caused increased copper loss which makes the AFPM less efficient. However, considering the overall efficiency, size and weight, the AFPM was still preferred. In this paper, the authors mentioned a special magnet arrangement used on a production motor – the *Halbach array*. It could increase the flux density on one side while weaken or even eliminate flux on the other side.

That means lighter material can be used for the rotor yoke rather than steel. However, no test data was provided for this type of motor.

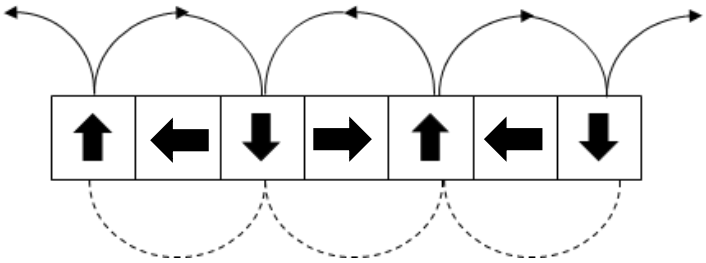

Figure 2-7 Halbach array

Sitapati and Krishnan did a very detailed and comprehensive comparison between RFPM and AFPM [48]. Four different designs of AFPM were tested which were single-stator-single-rotor slotted machine, single-stator-single-rotor coreless machines, dual-stator-single-rotor slotted machine and dual-stator-single-rotor coreless machines. These motors were compared at five power settings. At each power demand, the same external diameter was used for all of them including the radial flux motor. The other parameters, such as the air gap flux density, the phase resistance, the slot fill factor and so on, were kept to be as close as possible except the axial length. The test data demonstrated that as the power demand increased, the motor volume difference between each AFPM machine type was not very significant, and they all much smaller than the RFPM. At 10kW, the RFPM was at least twice the volume as the AFPMs. In addition, the amount of iron required was less in the AFPMs. Therefore, the iron loss was lower in the AFPMS since the air gap flux were kept similar. However, as expected, the two coreless AFPM needs higher current to produce the same torque as the others. Hence, more copper loss was observed while the other three motors types were very close.

In the work from *Pippuri et al* [49], AFPM, RFPM and transverse flux machines were compared in a 200 rpm application. All the design and analysis processes were performed in virtual environment. In order to obtain similar efficiency, the RFPM required fewer pole pairs (8 to 10) than AFPM (10 to 12), but with a bigger physical

volume. In order to compare with the transverse flux machine, a 20 pole-pair design was used for AFPM and RFPM, which is not the optimum quantity for both. The RFPM provides the best torque density under this condition over the other two designs.

2.3.2 Motor windings

As the field in a PM machine is created by the magnetic poles on the rotor, the winding coils only exist in the stator. The arrangement of these copper wires i.e. the way they wind around the iron teeth or cores is a crucial consideration during motor design stage since the layout determines the machine performance characteristics. The study on the various winding types will be reviewed in this section.

In a slotted machine, according to the number of coils inserted in each slot, the winding could be single layer (if there is only one coil side in every slot, i.e. every other teeth is wound) or double layer (two coil sides from two different coils overlapped, i.e. all teeth are wound). If donate the total number of slots with s, then a single-layer winding has $s/2$ coils and for double-layer one, there are s coils. An important winding parameter is the number of slots per pole per phase (SPP). It is calculated as

$$q = \frac{s}{2p \times m} \tag{2-1}$$

Where,
m is the number of phases,
p is the number of pole pairs.

Regarding to the value of SPP, winding categories are classified. When q is an integer, it is called an integral slot winding; for non-integral q, it is called a fractional slot winding. If $q > 1$, the stator has distributed windings, otherwise, if $q \leq 1$, concentrated windings are presented [50]. Figure 2-8 illustrates four winding arrangements presented in a few four-pole machines. In a concentrated winding, every turn on the same stator pole is wound around the common central line while in the

distributed type, not all the turns are aligned. The portion of each coil that contributes to the torque production is the section parallel to stator slots. The remaining section, around the ends of the teeth, are called end winding, which does not contribute to the motor power but losses.

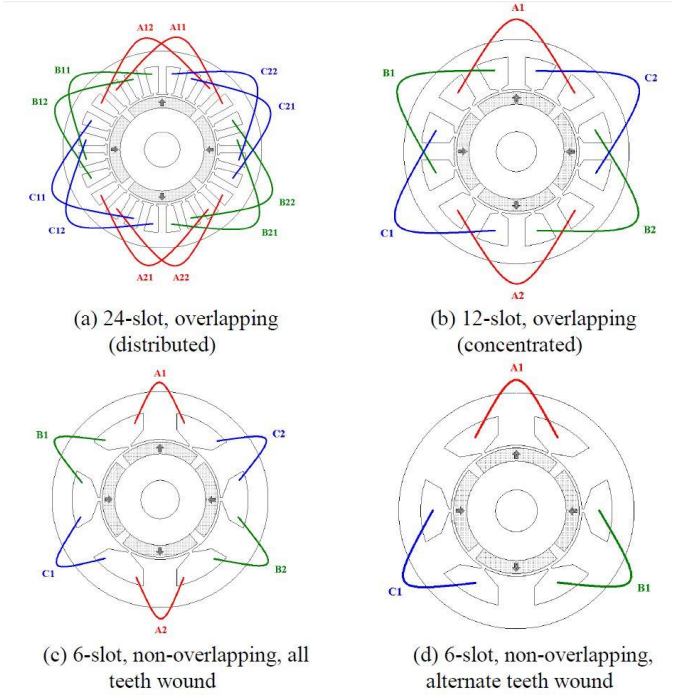

Figure 2-8 Typical winding arrangement (4 poles) [51]

Since the coils in series of one phase are dispersed around the stator circumference, the induced electromotive force (EMF) also called the back-EMF of each coil, consequently, may not be necessarily in phase. That leads the resultant back-EMF (phasor sum) is smaller than their arithmetic sum. The ratio between these two values is defined as the distribution factor, k_d. It reflects how the coil group is distributed in the stator. For the fundamental harmonic,

$$k_d = \frac{\sin(\frac{\pi}{2m})}{q \sin(\frac{\pi}{2qm})} \tag{2-2}$$

Each coil wraps around a certain number of slots. The distance between the two sides of a single coil is called coil span. It could be in the unit of angle, length or

quantity of slots. Pole pitch (in the same unit) may not be equal to coil span as show in Figure 2-9. It results the rotor flux linking the coil is less than the full flux of one pole. This layout helps to reduce the winding turn length and the harmonic contents [52]. The pitch factor (k_p) is used to describe this fact. For the fundamental harmonic,

$$k_p = \sin(\frac{\pi}{2} \times \frac{coil\ span}{pole\ pitch}) \tag{2-3}$$

If the coil is fully pitched i.e. the coil span is equal to pole pitch, $k_p = 1$.

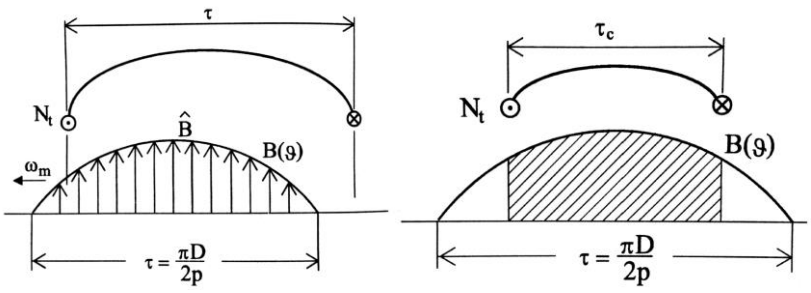

Figure 2-9 Full-pitch coil (left) and non-full-pitch coil (right) [52]

The winding factor is defined as the product of the distribution factor (k_d) and the pitch factor (k_p). The slot skew is not considered here.

$$k_\omega = k_d \cdot k_p \tag{2-4}$$

According to the torque production analysis in [53], the electromagnetic torque of axial flux PM machine is

$$T = \int 2\pi k_\omega A(r) B_{avg} r^2 dr \tag{2-5}$$

Where,

r is the radius,

$A(r)$ is the line current density,

B_{avg} is the average flux density in the air gap.

From the equation, it clearly shows that the winding factor is a crucial parameter in motor design stage since it directly affects the output torque. The motor electromagnet torque could be expressed in various formats or equations, however, all of them agree this correlation [50, 54-56].

There are a large amount of study work has been done on different winding formats and their effects on the motor performance. As this will be a general review on motor winding, the comparison will focus on three most important aspects, concentrated vs distributed, single layer vs double layer and factional slotted vs integral slotted.

In the work from *Chong et al* [55], two same physical sized interior PM radial flux (IPM) machines were compared with 84-slot distributed and 18-slot concentrated non-overlapping windings respectively. The analysis was done with time stepped finite element method (FEM). The distributed winding had longer end winding which resulted higher copper loss. A sketch in the paper showed the end winding length could be reduced half in a single layer concentrated winding and up to one fourth for double layer if the total effective copper volume kept the same. The copper loss was dominant in the low speed range, however, in the high frequency condition (high speed and field weakening scenarios), iron loss were prominent. The iron loss was mainly affected by the leakage harmonics of magnetomotive force (MMF) which, including sub and high order harmonics, were not in synchronous frequency. The eddy current and hysteresis losses were then introduced in the in stator cores and magnets due to the asynchrony. The fundamental flux linkage harmonics distribution in a distributed winding was more sinusoidal in the air gap than a concentrated one, hence less the iron loss. Other papers on the same topic showed the same results [57-59].

In [54], *Magnussen et al* did more detailed research on these two winding types with both FEM and experimental tests. A distributed winding motor and two concentrated winding motors with different SPP were studied. The three motors had

the same rotor and active dimensions. Apart from the losses analysis, the torque capability difference was demonstrated. The distributed winding produces more torque at base speed. This result was also affected by the higher fundamental winding factor. *Jun et* al found the same results in their research [58]. However, concentrated winding motors provide larger constant-power speed range (CPSR) when flux is weakened. This is due the higher stator leakage inductance. In the case of torque ripple, three machines are fed with pure sinusoidal wave in various magnitudes. Lower torque ripple was found in the distributed winding machines. The coincident verdict was presented in [58, 59]. The authors of [54, 55] both mentioned the effective use of a laminated stator core and PM could reduce the loss, however, the manufacturing cost would increase.

In [56], *Donato et al* studied fractional slot concentrated machines with single and double layer windings and also the effect of using soft magnet composite (SMC) wedges to close slots. The single layer winding offered a higher winding factor therefore higher torque than the double layer, but at the same time, higher torque ripple comes with the high harmonic winding factors. Another reason for lower torque output from double layer winding is due to higher saturation at the stator teeth [60]. The double layer winding has less MMF harmonic components which introduce less loss in the magnets and stator cores. A further significant difference between single and double layer windings is the inductance. In [61], *Ishak et al* use both measured results and FEM to show that single layer winding possesses higher self-inductance which is desired for field-weakening operation and lower mutual inductance which is preferred for fault tolerance. The high inductance is due to high slot leakage inductance [51].

Apart from the arrangement used to wind in the stator, the choice of the number of slots that are covered by each pole is also a key feature for motor performance. The fact is reflected by SPP value. The most significant benefit the fractional-slot offers is the considerable reduction in cogging torque which is the torque fluctuation when coils are not excited. *Donato et al* compared two concentrated winding machines with

integral-slot (SPP=1) and fractional-slot (SPP=2/5) windings respectively [50]. These two motors were deliberately designed having the same electrical and magnetic loading and active material volume to give more convincible results. The cogging torque from the factional-slot machine measured is one third of that from the integral-slot machine. In [54, 55], the similar effects were also found with even higher reduction factors. *Magnussen et al* mentioned the cogging torque could be weakened with skewed winding in distribute winding machines, but the fundamental winding factor would decrease as well [54]. Other than skewing the winding, the torque pulsation is also possible minimized with carefully designed magnets skew angle [62]. Other than smoothened torque output, fractional-slot machine also shows a better field weakening capability since its higher winding inductance. The drawbacks are lower average torque performance than integral-slot machines and more loss due to higher sub-harmonics [63].

2.3.3 Machines periodicity and winding feasibility

Since the electric machine is in circular shape, the machine might be divided into a few sections that repeat itself i.e. have the same or exactly inversed winding and magnet layout [53]. It is call machine periodicity. This is important for machine finite element analysis since only a motor section is needed to reduce the computational cost and time. It is the great common diviosr between the number of slots and the number of pole pairs.

$$mp = G.C.D.\{s, p\} \tag{2-6}$$

In order to have a symmetrical winding layout, the following equation must give an integral result [52].

$$\frac{s}{m \cdot mp} \tag{2-7}$$

2.3.4 Phase winding connection

The three phase windings could be connected in star (wye) or delta (Δ) fashions as shown in Figure 2-10. The delta connection is not very popular in motor windings. The reason for this is that there is potential for current circulating in the delta loop. It is caused by not perfectly balanced system or third harmonic of back-EMF [64]. This current has no contribution to the torque production but introduces more copper losses leading to possible motor overheat [65]. However, *Mevey* [64] stated that with delta connection the coils are easier to wind than in the star style, and in some special applications both winding types could be combined together with dynamic switching to allow different supply voltages.

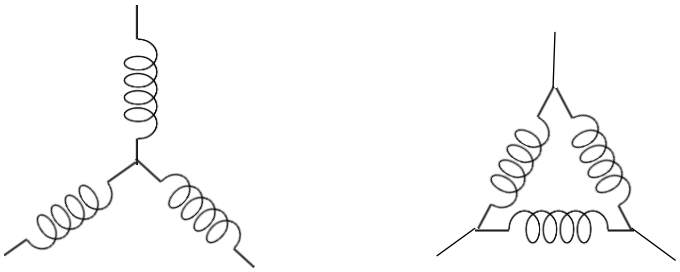

Figure 2-10 Star (left) and delta (right) connections

Since the special case will not be discussed here, the motors are assumed to be in star connection unless otherwise mentioned in the rest of the thesis. In the star winding connection type, all three phases link to a common neutral point which may not always be accessible and is therefore floating electronically when the motor is assembled. The sum of the three-phase current should be zero at neutral in a balanced system ($i_a + i_b + i_c = 0$). For motor current and voltage measurements, the reading between terminal and neutral point is called phase value while the line-to-line value is measured across the terminals. The phase current in the star configuration is the same as line-to-line current, but the phase voltage and line-to-line voltage are different due the existence of neutral point. The relationship between these quantities in a balance three phase (120^o apart) system is shown in Table 2-1.

Table 2-1 Voltage and current relationship in two phase winding connections

	Star (wye) connection	Delta connection
Current	$\boldsymbol{I_{line} = I_{phase}}$	$\boldsymbol{I_{line} = \sqrt{3} I_{phase}}$
Voltage	$\boldsymbol{V_{line} = \sqrt{3} V_{phase}}$	$\boldsymbol{V_{line} = V_{phase}}$

2.3.5 Motor control

It is possible to run an electric machine by connecting the terminals directly to the power source either DC or AC. However, for the applications such as automotive propulsion, adjustable speed and precise control of the torque output are required at both steady state and transient conditions. This leads to the demand of high performance power electronics and control algorithms. For AC machines, the controller inverts a fixed DC supply to a variable AC source hence called inverter. This section gives a brief description of a few popular motor control algorithms.

For induction machines, the most conventional way to vary the speed and torque is by scalar control (also called V/f control). As the name indicates, this method tries to maintain the ratio of two variables' magnitude (the supply voltage and the frequency). The synchronous speed (n) of the motor is expressed in Equation (2-8). It indicates that the motor speed could be varied by simply adjusting the frequency. The air gap flux, which directly influences the motor torque, is inversely proportional to the frequency (the higher frequency the lower current hence less flux linkage) but proportional to the supply voltage (the higher supply voltage the higher current and the more flux are produced). Therefore, for example, when the motor needs to speed up under a certain load, the controller raises the feeding frequency. In order to retain the torque, the voltage has to be increased to cancel out the influence on the air gap flux due to the frequency rise. As a result, the V/f ratio is preserved. In practical, the ratio is kept to give the peak torque output (constant torque region in the torque-speed envelop) until the motor base speed is reached. The supply voltage reaches the limit at this point and is no longer able to increase proportionally with the frequency. Any further speed rise will result in torque reduction. That is where the constant power

region begins. The scalar control theory is very simple and sufficient for steady state control. However, the inadequate implementation in dynamic response prevents its use for high performance motor drive nowadays.

$$n = \frac{60f}{p} \tag{2-8}$$

Where,
f is the supply frequency,
p is the number of pole pairs.

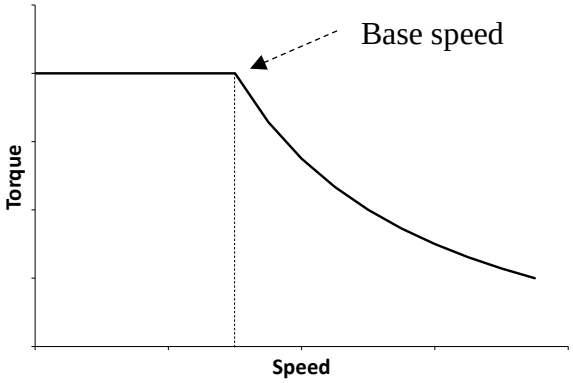

Figure 2-11 Typical electric motor torque curve

The more advanced vector control was first introduced in early 1970s by *K. Hasse* and *F. Blaschke* to achieve more precise control of the induction motor [66]. The control scheme is also called field-oriented control (FOC) since motor variables are transformed into a rotating field coordinate system. It decouples the field current and torque current and controls them separately. There are many studies comparing both control methods applied to then induction motor, such as [67-70], with theoretical analysis and experimental test results. They all agree that the scalar control might be satisfactory for steady state performance when closed loop is used, but the very poor performance for dynamic response. Vector control exhibits much better ability in precise control in both conditions. In mid of 1980s, *M. Depenbrock* and *I. Takahashi* proposed direct torque control (DTC) [71]. It is also a vector based method but comes with simpler structure and control diagram [72]. Since this report is focusing on the

PMSM which is normally driven under vector based control, only FOC and DTC will be detailed in the following section.

2.3.5.1 Field-oriented control (FOC)

The basic principle of the FOC is to control the instantaneous position of the stator magnetic motive force (MMF). It is achieved by decoupling the three-phase AC current to two fictional DC current terms which are responsible for torque production and interacting with rotor field respectively. Since the rotating stator MMF is in synchronisation with the rotor field, it is more convenient to undertake all the analysis on an orthogonal coordinate system that is locked to the rotor. For a balanced 120° apart three-phase system, all the quantities (current, voltage and flux linkage) will be transferred to a static orthogonal coordinate system ($\alpha\beta$ frame) Clarke Transformation and then to a rotating one (dq frame) through the Park Transformation. The quantities relationship are given in Equation (2-9) and (2-10).

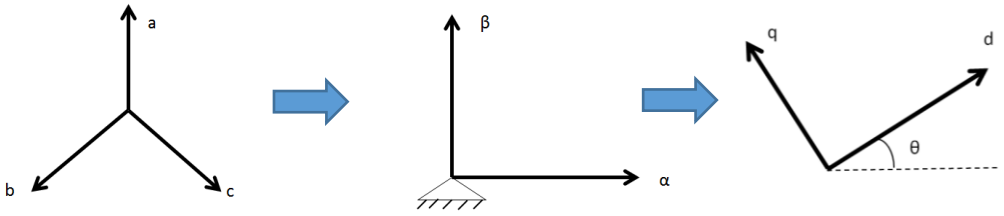

Figure 2-12 Three-phase system to dq frame

$$\begin{bmatrix} X_\alpha \\ X_\beta \end{bmatrix} = \frac{2}{3}\begin{bmatrix} 1 & -1/2 & -1/2 \\ 0 & \sqrt{3}/2 & -\sqrt{3}/2 \end{bmatrix}\begin{bmatrix} X_a \\ X_b \\ X_c \end{bmatrix} \quad (2\text{-}9)$$

$$\begin{bmatrix} X_d \\ X_q \end{bmatrix} = \begin{bmatrix} \cos\theta & -\sin\theta \\ \sin\theta & \cos\theta \end{bmatrix}\begin{bmatrix} X_\alpha \\ X_\beta \end{bmatrix} \quad (2\text{-}10)$$

Where,
X_a, X_b, X_c could be voltage, current or flux linkage and $X_a + X_b + X_c = 0$,
θ is the electrical angular position.

The electrical angle is related to the magnet pole pitch on the rotor. The angle between two adjacent opposite polarity magnets is defined as 180° electrical. Consequently, for example in a two pole rotor (one pair of N-S), the rotor disc is 360° in electrical which is coincidently the same as in mechanical. For a four-pole rotor, it will be 720° electrical. Therefore, if ω_{mech} is the actual rotor speed in mechanical angle, $\omega_{mech} = \omega/P$ where P is the number of pole pairs.

By definition, the d-axis is aligned with rotor flux direction and q-axis is 90° electrical ahead to d-axis in the rotating direction. Consider a surface-mount radial flux machine. From the rotor section view, the d-axis passes through the centre of a magnet while the q-axis lies at the middle of this magnet and the following one. When decoupling the current vector into dq frame, the component on the d-axis creates the field that interacts with rotor field and the q-axis component is responsible for torque production. Torque equation in the dq frame is

$$T = \frac{3}{2}P(\psi_r \cdot i_q + (L_d - L_q)i_d i_q) \tag{2-11}$$

Where,
ψ_r is the rotor PM flux,
i_d, i_q are the dq axes current,
L_d, L_q are the dq axes inductance, in some cases, $L_d = L_q = L_s$.

The space vector diagram for this equation is shown in Figure 2-13. Since the d-axis is aligned to the magnet, the PM flux λ is on the d-axis and the induced voltage (back-EMF) e is 90° electrical in advance on the q-axis. The resistive load voltage is in phase with the current vector and the inductance load voltage is 90° electrical ahead which is perpendicular to the iR term. The input voltage v is the phasor sum of the three vectors.

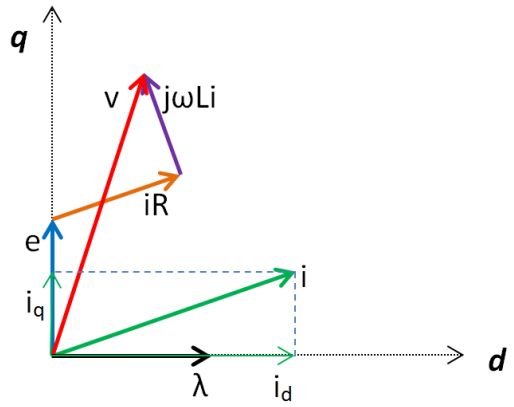

Figure 2-13 General electric motor space vector diagram

With the convenience of separately controlled field current, field weakening is easy to implement. The concept of field weakening was originally developed for DC-excited field motors. As the motor field is regulated by a separated DC current, the air gap flux could be easily varied. However, in a PM machine, applying the same approach is not realistic. With FOC, field weakening could be realised by advancing the voltage vector more to allow the current vector to move into the second quadrant. The i_d component is now on the negative half of d-axis creating an opposite-direction field to weak the air gap flux density. However, the process needs to be carefully controlled, otherwise irreversible demagnetization of the rotor PMs may occur [73].

2.3.5.2 Direct torque control (DTC)

Instead of using a rotating dq frame, DTC refers to the stationary αβ frame which is fixed to the stator. The stator flux magnitude and the motor torque are the two controlled variables by mean of selecting proper stator voltage vector. This method uses the hysteresis control to substitute the decoupling control in FOC, which 'meets very well with on-off operation of the inverter semiconductor power device' [66].

The relationship between torque and the flux from both stator and rotor is expressed as

$$T = \frac{3}{2} p \cdot \psi_r \cdot \frac{\psi_s}{L_s} \sin \phi \tag{2-12}$$

Where,
ψ_s is the flux from the stator winding,
ϕ is the load angle. The angle between the stator flux and rotor flux.

The motor torque is controlled by varying the stator flux position relative to the rotor flux and reaches the maximum when they are 90° apart. This agrees with the maximum torque condition in the FOC. The stator flux is always in phase with the stator current and the rotor flux is on the d-axis. When the stator current lies on the q-axis which is 90° in advance to rotor flux (λ), there is no i_d and i_q is maximised where peak torque occurs.

The stator flux space vector can be estimated by

$$\overrightarrow{\psi_s} = \int (\overrightarrow{V_s} - R_s \overrightarrow{I_s}) dt + \psi_{s0} \tag{2-13}$$

Where
ψ_{s0} is the initial value of the stator flux depending on the rotor position,
$\overrightarrow{V_s}$ is the stator voltage space vector.

The formula for the stator voltage vector is

$$\overrightarrow{V_s} = \frac{2}{3} V_{dc} (S_a + S_b e^{j2\pi/3} + S_c e^{j4\pi/3}) \tag{2-14}$$

S_a, S_b and S_c are the inverter switching state of the three phases. Zero value means the phase is connected to the negative while one means connected to positive.

When the motor is in control, the stator flux vector position angle (referencing to the positive α-axis, $\tan^{-1}(\psi_{s\beta}/\psi_{s\alpha})$ decides which sector the vector is in (Figure 2-14). Then, the torque and flux comparator give signals whether the two variables are in the hysteresis tolerance band. If $d_\psi = 1$, the flux linkage is below the limit while

$d_\psi = 0$ means it is above the limit. When $d_m = 1$, the torque is below the tolerance boundary, and $d_m = -1$ when torque is above the boundary; otherwise, $d_m = 0$. The look-up table (Table 2-2) is used to determine the states of the switching power electronics with above information.

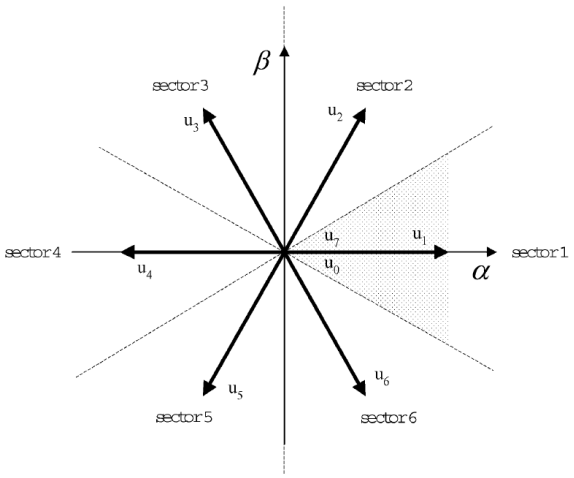

Figure 2-14 Voltage vector sector for DTC [66]

Table 2-2 Switching look-up table for DTC

		1	*2*	*3*	*4*	*5*	*6*
$d_\psi = 1$	$d_m = 1$	$u_2(110)$	$u_3(010)$	$u_4(011)$	$u_5(001)$	$u_6(101)$	$u_1(100)$
	$d_m = 0$	$u_7(111)$	$u_0(000)$	$u_7(111)$	$u_0(000)$	$u_7(111)$	$u_0(000)$
	$d_m = -1$	$u_6(101)$	$u_1(100)$	$u_2(110)$	$u_3(010)$	$u_4(011)$	$u_5(001)$
$d_\psi = 0$	$d_m = 1$	$u_3(010)$	$u_4(011)$	$u_5(001)$	$u_6(101)$	$u_1(100)$	$u_2(110)$
	$d_m = 0$	$u_0(000)$	$u_7(111)$	$u_0(000)$	$u_7(111)$	$u_0(000)$	$u_7(111)$
	$d_m = -1$	$u_5(001)$	$u_6(101)$	$u_1(100)$	$u_2(110)$	$u_3(010)$	$u_4(011)$

Regarding to these information, the corresponding voltage vector is selected. It could be either active (u_1-u_6) or zero (u_0 and u_7). Forward active vector makes the flux vector moving forward to enlarge the load to rotor flux. Zero vector stops the flux moving. Consequently, the load angle is reduced since the rotor flux is moving towards it. By continuously selecting the appropriate voltage vector, the torque is 'directly' controlled within a hysteresis band. Sometimes, backward active vector is also used if

the speed is low. Stator flux moves back towards the rotor flux since a zero vector is too slow to achieve fast torque reduction [66].

Comparing these two control schemes, DTC needs neither to transform the coordinate system nor to know the rotor position which eliminates the requirement for a tachometer or shaft encoder as in FOC (there is sensorless FOC, but it is still need to estimate the rotor position instead of mechanically measuring). *Garcia et al* compared the two control scheme on PMSM [72]. Their simulation results show that both methods are capable of high performance response while FOC is better for steady-state operation and DTC has faster torque dynamics.

2.3.6 Inverter

Voltage Source Inverter (VSI)

There are two fundamental types of voltage-fed inverters commonly used in the industry: Voltage Source Inverter (VSI) which supplies a switched voltage waveform with a capacitor on the DC bus link, and Current Source Inverter (CSI) which supplies a switched current waveform with a inductor between DC bus terminals. CSI is more reliable than VSI due to high tolerance to short circuit fault and electromagnetic noise [74]. However, VSI is dominant in the motor control field [64], because the Pulse Width Modulation (PWM) technique of motor terminal voltage can lead to smooth current waveforms due to the motor winding inductance. This is preferred in motor operation as less torque output fluctuation is achieved. Furthermore, the VSI has a higher frequency range and the cost is less than the same rating CSI [74].

Inverter switching power electronics

In order to achieve inverting DC voltage source to AC through PWM, high frequency switching power transistors are required. The bipolar junction transistor (BJT) was the first to be used as a switching device [75]. Although the BJT owns the advantage of low collector-emitter voltage which gives low conduction loss, the need of a high current to turn on the device and the long current tail time during switching off phase are not desired. In 1970s, the metal oxide semiconductor field effect transistor (MOSFET) [76] was introduced. Instead of being controlled by base current, the MOSFET is governed by the gate voltage, which is usually very low. Thus, a low power logic circuit is required. Later in the 1980s, the insulated gate bipolar transistor (IGBT) came to prominence with combined attractive features of BJT and MOSFET [76]. It has the capability of handling high current, relatively low power loss as the BJT and ease of control as for the MOSFET. Both MOSFET and IGBT are commonly used in the industry nowadays. Their specific characteristics make them suitable for different applications. The MOSFET tends to be used in low voltage and low power output cases (<250V and <500W) while the IGBT handles high voltage and power applications [77]. The IGBT also has better thermal behaviour, therefore prois favoured in high temperature conditions (>100^0C). However, it does not have the high switching frequency capability of the MOSFET, so they usually work under 20 kHz. Another disadvantage of IGBTs is the unavoidable current tail due to their physical design. The current takes a small amount of time to dissipate after the device turned off, which leads to loss during every switching action[76, 77].

2.3.7 Inverter control methods

Following the brief introduction to machine control theory, the techniques to generate the required AC voltage from a DC source through the inverter need to be understood. The mainstream inverter control methods, i.e. the gate control, will be reviewed in the following section. A typical three-phase inverter is depicted in Figure

2-15. Each half-bridge (leg) is connected to one motor phase and each leg contains two semiconductors associated with freewheeling diodes.

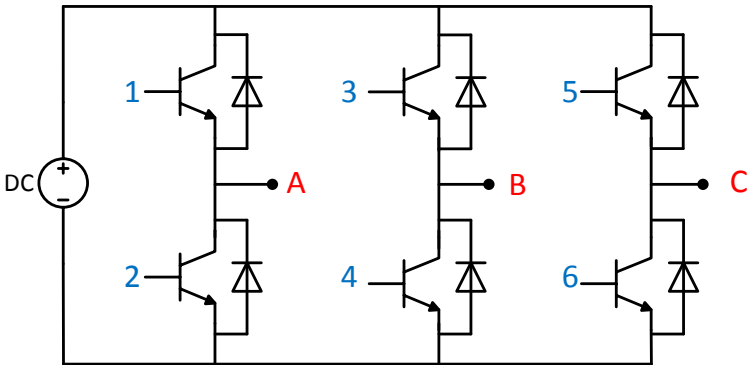

Figure 2-15 A typical inverter schematic

For each inverter leg, the two semiconductors should not be turned on at the same time, otherwise the DC bus is short circuited. Therefore, one leg can only have three status – current flows through the upper half, the lower half or neither (both off). When all three status could occur on every leg, it is called 120° inverter. If every leg is never totally off, it is classified as 180° inverter. The former is seldom seen in motor control applications because of the lower fundamental harmonic amplitude (since the current conduction period is shorter) than the later one [64]. Therefore, only 180^0 class inverter will be discussed here unless otherwise specified.

Six-step square wave

The first control method is the six-step square wave usually used for BLDC. As the name suggests, for each mechanical revolution only six shaft positions are required. During one electrical revolution, each semiconductor only switches once and always performs at 50% duty cycle. The actual voltage delivered to the terminals is a square shape.

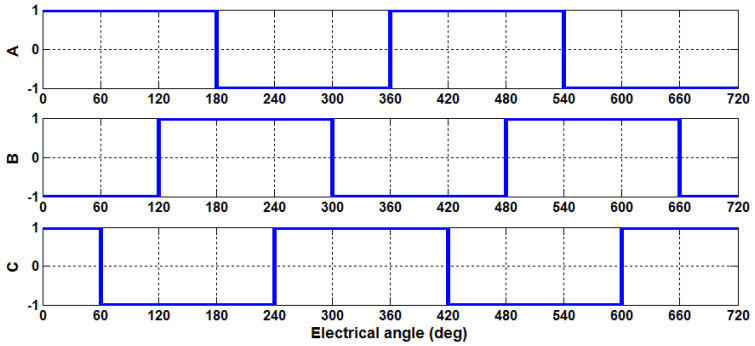

Figure 2-16 180º six-step control gate signal

Six-step control is a very simple control scheme and the square waveform shape offers the highest fundamental harmonic amplitude ($\frac{2}{\pi}V_{dc}$). It only requires a low resolution encoder (hall sensors can accomplish the target) and relatively low switching frequency power electronics. Therefore, its overall cost is another advantage. However, some drawbacks are inevitable, such as the unwanted torque ripples caused by the sharp change of the transistor status [44].

Sinusoidal PWM (SPWM)

When an inverter is implemented with fast switching semiconductors, by varying the switch duty cycle can, in combination with the damping effect of the inductive load e.g. motoring windings, make the current waveforms more sinusoidal. This is favoured by synchronous AC machines since only the fundamental harmonic has an effect on the machine output. The traditional way to define the gate switching timing is to compare the reference voltage signals with a fixed frequency carrier wave which is normally a triangle wave. Figure 2-17 shows a typical SPWM gate signals at steady state. The ratio between the amplitudes of the reference wave and the carrier wave is called modulation index.

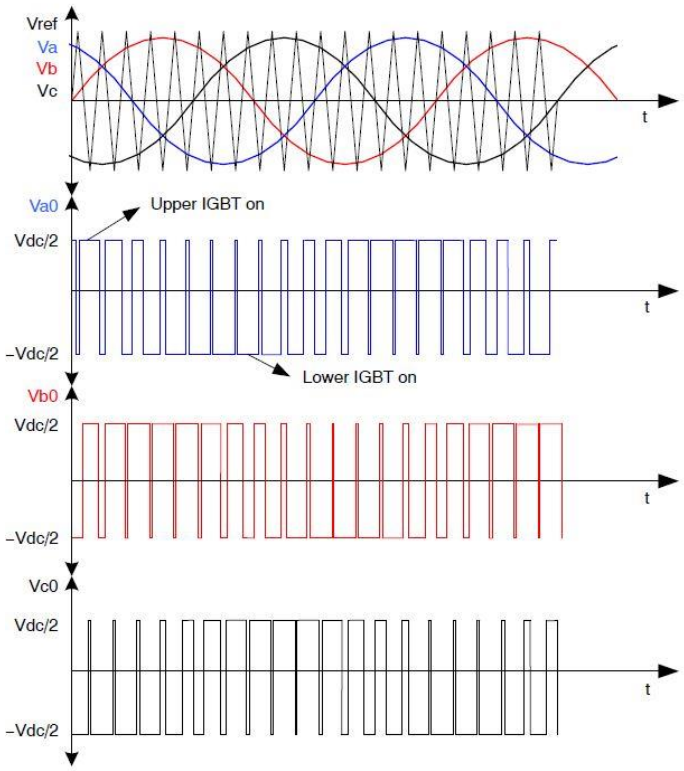

Figure 2-17 SPWM control gate signals [74]

As can be seen in Figure 2-17, once the modulation index is beyond one, there would be a period near the reference wave peak area where the semiconductor duty cycle is 100%. It is called over modulation which is a non-linear modulating region, i.e. the fundamental harmonic amplitude is not linearly increasing with the modulation index. The extreme case is that the SPWM becomes a six-step control which is the hardware physical limit. This is not preferred in some cases since significant harmonics will be introduced to the system. However, there is a compromise method commonly used which is called Third harmonic injection (THI) [64, 78]. By deliberately imposing a third order harmonic onto the fundamental reference wave, the resultant wave acquires flat tips as shown in Figure 2-18. This helps to gain up to 15.47% more fundamental voltage that can be sensed by motor windings compared to SPWM.

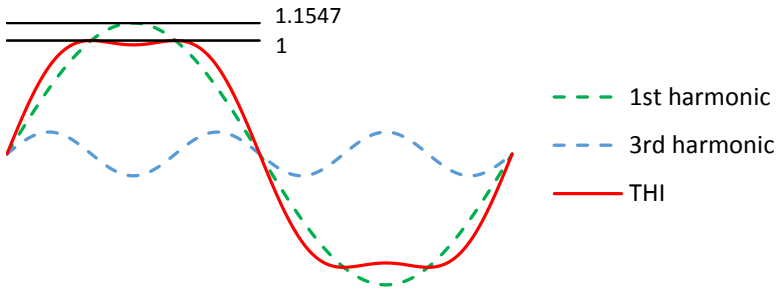

Figure 2-18 THI-SPWM theory

Space vector PWM (SVPWM)

The space vector PWM technique controls the inverter's three legs as a whole instead of separate monitoring as in SPWM. This so-called 'vector' is the voltage vector which is rotating in the $\alpha\beta$ coordinate system. The $\alpha\beta$ plane, as described in earlier, is fixed to the stator as opposite to the dq plane which is spinning with the rotor. As there are six switching devices inside the inverter and each leg can only have one semiconductor turned on at a time, there are $2^3 = 8$ inverter status in total. Among them, two status have all either upper or lower half semiconductors closed. Therefore, all three coil groups have no phase voltage. The voltage vector at this two status are called null vectors. As seen in Figure 2-20, V0 and V7 are the two null vectors with zero magnitude and stack on the origin. The rest six are the active vectors corresponding to six different overall switch positions. For example, at the instant when the upper switch of phase A and the lower switches of phase B and C are closed, the phase voltages are $V_{A,phase} = \frac{2}{3}V_{DC}$ and $V_{B,phase} = V_{C,phase} = -\frac{1}{3}V_{DC}$. Figure 2-19 is the equivalent circuit diagram developed from Figure 2-15. Having the three phase voltage transformed from ABC system to $\alpha\beta$ plane through Clark transformation (Equation (2-9)), the synthesised voltage vector lies on the α axis with magnitude of $\frac{2}{3}V_{DC}$. The space vector (SV) under this inverter status is named as V1. The rest of the SVs can be easily derived in the same way with corresponding inverter status.

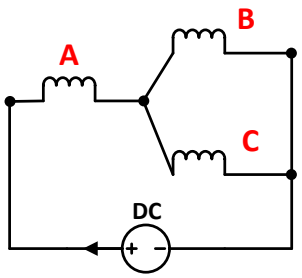

Figure 2-19 Equivalent circuit of space vector V1

After all eight SVs have been defined, any arbitrary voltage phasor in the $\alpha\beta$ plane can be represented by two closest active vectors and two null vector with appropriate time distributions during one switching cycle. Although the null vectors do not contribute to forming the voltage phasor due to their nil magnitude, they are crucial in implementing the inverter switching scheme. One advantage of SVPWM is that though four status need to be altered in one cycle, by arranging the order of the SVs to be used, only one leg's status needs to be switched at a time. The details are explained in the inverter modelling chapter.

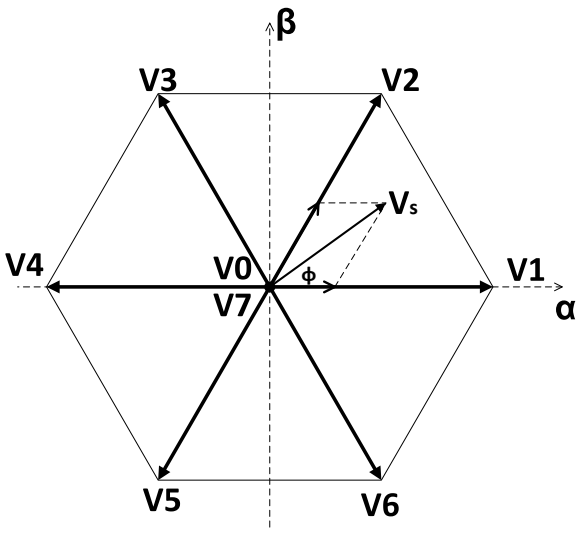

Figure 2-20 SVPWM voltage vectors

As a more sophisticate control technique, SVPWM offers more advantages over SPWM, such as less current harmonic distortion, less torque ripple, more utilisation of the DC bus voltage, etc. [78-83]. The DC bus voltage utilisation, or the fundamental phase voltage amplitude that can be seen by the motor, is plotted in Figure 2-21 with

these four control techniques for comparison. However, since the voltage vector of the SVPWM can only rotate within the hexagon, its maximum value cannot be achieved at any vector position.

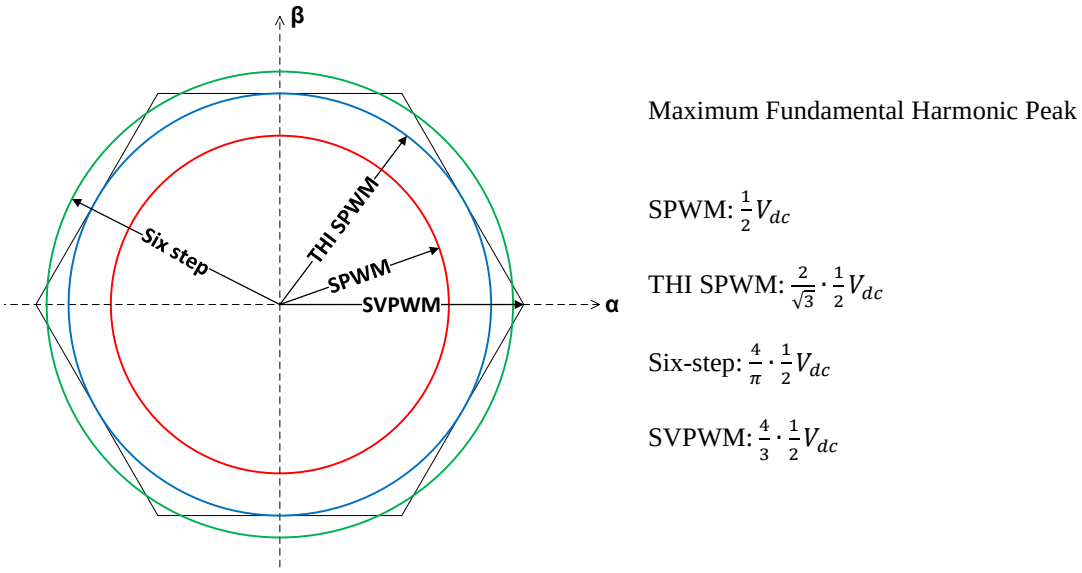

Figure 2-21 Maximum DC voltage utilisation for different control techniques

In fact, SVPWM achieves a similar effect to the THI-SPWM without deliberately referring to a 'distorted' sinusoidal wave. According to the analysis by *Mevey* [64], the reason is the zero sequence component that SVSPWM introduced. The zero sequence component, which is usually used to analysis unbalanced multi-phase system, is the potential difference between the DC bus midpoint and the phase neutral point in this case. In SPWM, the zero sequence component is always zero (not true for instantaneous case). On the contrary, in SVPWM, the zero sequence component is in a triangle waveform with a frequency three times frequency of the fundamental harmonic. Therefore, the actual voltage waveform applied to the windings is similar to THI-SPWM which explains the reason for the comparable final control effect. This phenomenon occurs naturally due to the SVPWM switching scheme.

As SVPWM was used for the inverter control in the prototype APU for this research work, more detailed explanation and modelling work will be given in CHAPTER - 4 .

Hysteresis PWM

Hysteresis PWM uses the devices on-off switching characteristic to control the signal within a tolerance band. The reference signal can be current, torque (as in the direct torque control), etc. However, the switching event does not occur regularly, i.e. not a fixed switching frequency. It will not be discussed in more details since it is out of this research scope.

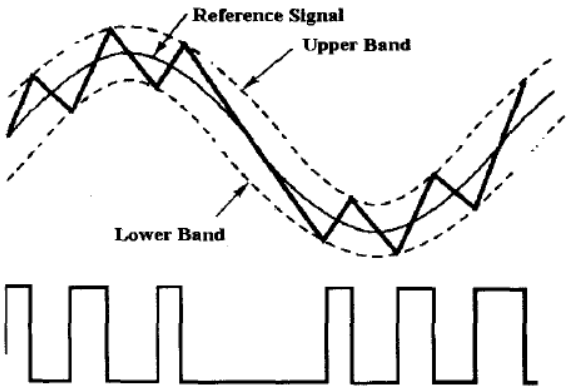

Figure 2-22 Hysteresis PWM [82]

2.3.8 Electric machine parameters determination through measurement

Back-EMF constant

The open circuit test is a key test that can determine one of the most important parameters of an electric machine, the back-EMF constant k_e. It also helps to determine the rotor flux linkage ψ_r.

For a permanent magnet machine, the test setup is very simple. The electric machine is turned at a constant speed by an external mover (dynamometer) and the phase terminals are left open circuit. The induced line voltage across two terminals is measured by a multimeter or a potentiometer. As per the relationship given in Table

2-1, the induced phase voltage can be derived. The back-EMF constant is calculated with the phase voltage RMS value and the rotor mechanical speed.

$$k_e = \frac{V_{phase,rms}}{\omega_{mech}} \tag{2-15}$$

For the rotor flux linkage calculation, it is easier to understand with help of the DQ system voltage equations. They will be introduced in CHAPTER - 4 (Equation (4-6) and (4-7)). Since the motor is not excited, there is no current in the system. The equations are simplified as

$$u_d = 0 \tag{2-16}$$

$$u_q = \omega_{elec} \cdot \psi_r \tag{2-17}$$

According to the coordinate system transformation as described previously, the rotating voltage vector amplitude is equal to the phase voltage peak value. Since in this case no voltage on d-axis, the rotor flux linkage can be derived by the following equations.

$$U = V_{phase,peak} = \sqrt{{u_d}^2 + {u_q}^2} = u_q \tag{2-18}$$

$$\psi_r = \frac{V_{phase,peak}}{\omega_{elec}} \tag{2-19}$$

Winding inductance

The inductances of the d and q axes are not equal ($L_d \neq L_q$) in the cases of the rotor with salient characteristics such as interior magnet rotor. The inductance is inversely proportional to the material permeance. Since the permanent magnets have similar magnetic permeability to the air (vacuum), the buried magnets inside a round rotor are equivalent to introducing extra air gaps on the flux path, i.e. inductance gets lower. Determining the inductance is one of the key procedures in charactering the

electric machine, which contributes to the motor performance analysis, and simulation modelling. Various techniques could be applied to accomplish the measurement as stated in the literature [84-87]. One of the most commonly used measurement methods is explained here.

Since the direct measurement of the winding inductance across the terminals varies depending on the salient rotor position, alignment of rotor dq axes to a reference phase winding is necessary before conducting further actions. If taking the d-axis as an example, the convention is to align the d-axis to the phase-A winding when the stator peak MMF (one peak of the sinusoidal rotating field) falls on it. This occurs when the phase-A current is at the peak and the current in phase B and phase C is in half of the magnitude with opposite polarity, i.e. $I_b = I_c = -\frac{1}{2} I_a$ (balanced three-phase). In the laboratory, this could be done by connecting phase A to a DC positive and grounding phase B&C. The circuit diagram is shown in Figure 2-23. Now the rotor position should be locked to prevent any movement in the later measurement. Once the rotor d-axis is aligned to the peak MMF, this is the condition when no torque is produced since the fields from rotor and stator are aligned. It is equivalent to the instant that, under normal machine operation, all the current is applied on d-axis and no current is applied on q-axis (no torque production, $\varphi = 0°$). Since the circuit is supplied by a DC source, in the d-axis circuit, the dynamic term could be eliminated as shown in Figure 2-24. Now the d-axis circuit is a simple RL circuit and equivalent to the simplified circuit in Figure 2-23.

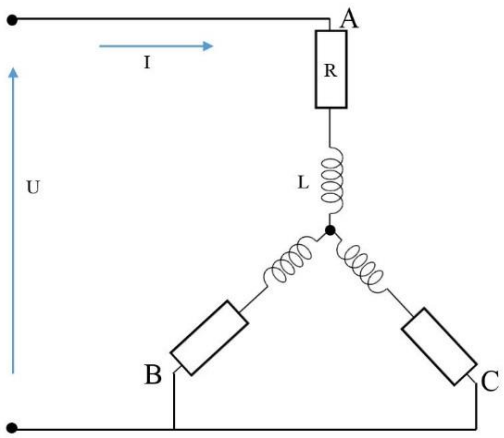

Figure 2-23 dq axes inductance measurement setup diagram

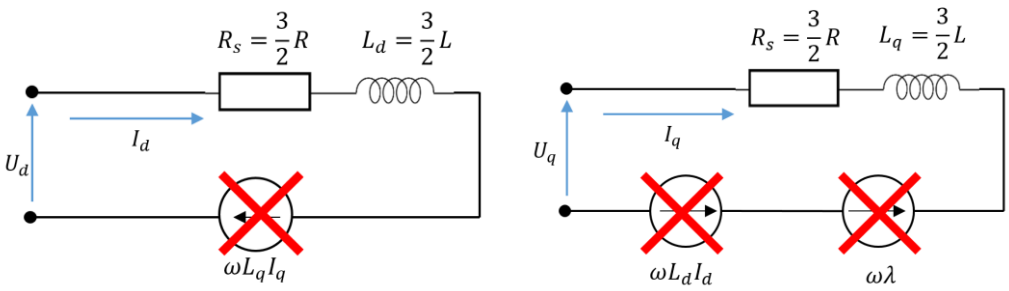

Figure 2-24 d-axis (left) and q-axis (right) circuit during measurement

For a RL circuit, the current equation is

$$I = \frac{V}{R}(1 - e^{-\frac{t}{\tau}}) \tag{2-20}$$

The time constant $\tau = L/R$. If a voltage step input is applied to the circuit and the current time response is measured on an oscilloscope, the d-axis inductance L_d can be easily calculated with above equation.

L_q can be measured in the same setup and procedure, but rotor q-axis need to be aligned and locked first. In order to do so, the phase B terminal and phase C terminal will be connected to a DC supply and ground respectively. The phase A is left floating. This is equivalent to the instant when current angle is set to 90^0, i.e. all phase current

falls on q-axis after transformation. After locking the rotor position, the setup shall change to the one in Figure 2-23 again and the same steps can be followed to derive q-axis inductance.

2.4 Conclusion

This chapter presents a literature review of APU and electric machines. The APU operation strategy and the NVH reduction methods set the fundamentals for the later strategy design for this particular project. Understanding the principles of the permanent electric motor/generator and its control techniques is crucial for the modelling work in the next few chapters.

Since the APU in a REEV is not directly connected to the drive shaft, the IC engine inside does not have to output high torque other than turning a electric generator, especially at low revolution speed. Therefore, a low-cylinder-count engine is commonly used in this type of system for the reduction of cost, weight, package size, etc. Also, the engine operation range is more flexible. The operation strategies of APU in different applications were compared in the previous studies. The curve (or multiple points) operating strategy is more favoured than the single point strategy. This is because the APU could follow the vehicle power demand closely to maintain the battery SOC. If the APU supplied too much energy, the excess power must be stored in the battery, which will cause more charge/discharge cycles on battery and less efficient system in terms of energy conversion.

The low-cylinder-count engine inherently exposes more vibration and speed fluctuation due to the less frequent firing event. This leads to the requirements of vibration minimisation either passively or actively. There is good agreement in the literature that using the electric motor to counteract the engine in-cycle torque ripple could smoothen the crankshaft speed fluctuation. The advanced vector control allows the PM synchronous machines response accurately and rapidly, which makes the

concept achievable. Various techniques and torque waveforms on the electric machine have been investigated to validate the effectiveness. They all promoted positive results. In most of the real product, considering the cost, reliability and implementing difficulty, many sensors for pressure, torque, speed/position, etc. could not be installed in the final system. Some controls could not be closed-loop which relies on those feedback signals. Too many PID control might bring the instability and slow down the system response time. The close-loop control, especially the more advanced algorithms, can put heavy load on the processors. Therefore, most of the controllers are map based open-loop control with combination of the simple PID close-loop. There leaves the opportunity to design the specific torque waveform off-line with known engine characteristics, and feedforward it in the control with simpler PIDs.

CHAPTER - 3
Engine Modelling

The chapter describes the modelling of the IC engine for the APU. The main aim of this model is to recreate the in-cycle shaft torque variation and speed fluctuation. The gas pressure, the moving inertia and the friction loss were the three main torque sources modelled. The engine model showed satisfying results compared to the bench test data.

3.1 Introduction

As the research work aims to minimise the engine crankshaft in-cycle speed fluctuation, the origin of this phenomenon needs to be investigated and modelled. This is a vital part of the system analysis as it lays the foundation for the later Dynamic Torque Control (DTC) design. The engine torque exerted on the crankshaft mainly comes from three sources, the gas pressure, the inertia torque from reciprocating parts and the contact friction. The model developed in this chapter is to recreate the instantaneous engine torque waveforms resolved in crank angle and the corresponding resultant in-cycle speed waveforms for the whole operating range.

The base engine used in the APU prototype is a naturally aspirated twin-cylinder petrol engine. The main specifications are given in Table 3-1. This engine is in mass production and fitted in a small passenger car. In order to meet package and performance criterion for an APU application, it was specifically calibrated and optimised. Since the process is not in the scope of this research work, all the test data used were from the engine with final settings.

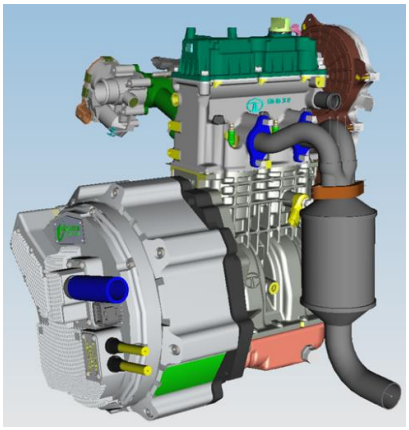

Figure 3-1 Rendered final APU

Table 3-1 Base engine specifications

No. of cylinders	2 in-line
Capacity	624cc
Firing order	1-2 (360°)
Max. power	35 PS @ 5250 rpm
Max torque	48Nm @ 3000 rpm
Fuel system	Port fuel injection

3.2 Engine modelling

The crankshaft speed fluctuation is inherently more severe in a low-cylinder-count engine. This is mainly due to the low firing frequency as the number of cylinders drops. The power stroke generates the torque that accelerates the crankshaft. When the gap between the adjacent two power strokes from different cylinders is large, there is long enough time for the crankshaft to decelerate to a significant level hence creates a large peak-to-peak variation. Since this piece of research work was not focusing on the other engine performance characteristics, such as thermal efficiency, brake specific fuel consumption (BSFC), etc., the output of this engine model is the recreation of the in-cycle torque waveforms and corresponding speed fluctuations. The model was created in the Matlab/Simulink environment. In the following sub-sections, the model development details will be presented. A 1-D engine model using GT Power was also provided by the manufacturer. A small amount of calibration work for this model was done by the author and used as another reference for the Simulink model.

3.2.1 Gas torque

The gas torque or the indicated torque is delivered by the in-cylinder pressure acting on the piston surface. The pressure change is due to the air/fuel mixture status transformations, i.e. pumping, compression and combustion.

On the test bench, the engine was instrumented with in-cylinder pressure sensor in each cylinder for instantaneous measurement. The in-cylinder pressure signals together with all other implemented engine measurements were synchronised with crank angle position and input to the combustion analysis system (CAS) for real time monitoring. The details of the test bench setup are described in the following rig testing section.

In the Simulink model, a three-dimensional table of each cylinder was populated by the instantaneous pressure data gathered from the bench testing. The three inputs to the tables were the mean torque demand, the shaft speed and the crank position.

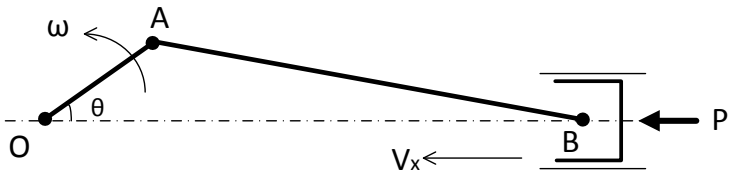

Figure 3-2 Cylinder slider schematic

The instantaneous gas torque in the Simulink model was derived by the energy conservation principle. As shown in the cylinder slider schematic (Figure 3-2), the gas pressure acting on the piston surface generates a force. Since the piston only moves along the cylinder axis, the instantaneous power at this point is

$$P = V_x pA \tag{3-1}$$

Where,
P is the instantaneous power,
p is the instantaneous cylinder pressure,
A is the piston surface area.

If the gas power was totally transmitted to the crankshaft, the shaft torque is

$$T_{gas} = \frac{Power}{\omega_{mech}} = \frac{V_x pA}{\omega_{mech}} \tag{3-2}$$

Where,
ω_{mech} is the instantaneous shaft angular speed in rad/s.

However, when considering the in-cycle engine shaft torque, the sliding parts inertia and friction loss have to be deducted from the gas torque. Especially at high speed, the inertia torque has significant influence on the torque waveform shape, although its mean value is zero. The calculation of these two components are detailed as follow.

3.2.2 Inertia torque

From the power balance perspective, the equation for the entire system is

$$V_x pA = T_{gas}\omega = T\omega + \frac{dKE}{dt} + T_f\omega \tag{3-3}$$

Where,
T is the shaft torque,
KE is the kinetic energy of all moving parts that affect the torque waveform,
T_f is the mean friction torque.

From Equation (3-3), the expression for the inertia torque (T_i) is

$$T_i = \frac{dKE}{dt}\frac{1}{\omega} \tag{3-4}$$

When considering the inertia torque, the commonly used dual equivalent masses method for the connecting rod is not valid anymore. This because its actual moment of inertia at the centre of gravity is smaller than the scenario where two masses are attached at each end [88]. As a result, the kinetic energy of the two moving parts need to be considered individually. The detailed crank-rod schematic is shown in Figure 3-3. The piston assembly has only translational motion. Therefore, it is represented as a single term in the Equation (3-5). For the connecting rod, by referring to its centre of gravity, the more complicated movement was decomposed into two orthogonal translational directions and one rotating motion.

One remark to be noted here is that the rotating inertia on the crank axis (the crankshaft and the electric machine rotor for this case) should not be included in this part of calculation. The intrinsic non-linear movement trajectories of the piston assembly and the connecting rod cause the torque waveform to differ from the in-cylinder pressure profile. However, the crank axis rotating mass does not have this inherent nature. On the contrary, it is the object of the torque variation which leads to

the in-cycle speed fluctuation. Therefore, it was placed in the 'inertia' block rather than in the 'engine model' block as described later on in Figure 3-7.

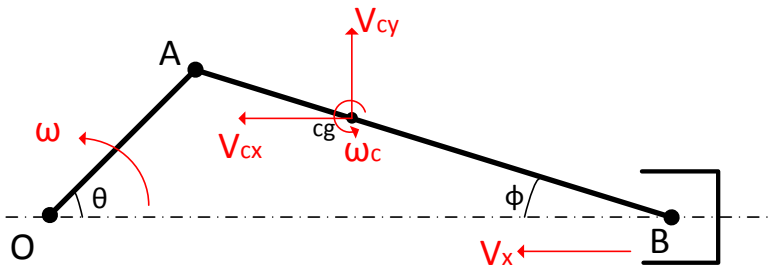

Figure 3-3 Detailed crank-rod schematic

$$KE = \frac{1}{2}(m_p {V_x}^2 + m_c {V_{cx}}^2 + m_c {V_{cy}}^2 + I_c {\omega_c}^2) \tag{3-5}$$

Where,

m_p is the mass of the piston assembly,

m_c is the mass of the connecting rod,

I_c is the moment of inertia of the connecting rod,

V_{cx} and V_{cy} are the orthogonal components of the connecting rod translational speed,

ω_c is the connecting rod rotational speed around its centre of gravity.

By substituting Equation (3-5) into Equation (3-4),

$$T_i = \frac{1}{\omega}\left(m_p V_x \dot{V_x} + m_c V_{cx} \dot{V_{cx}} + m_c V_{cy} \dot{V_{cy}} + I_c \omega_c \dot{\omega_c}\right) \tag{3-6}$$

The next step is to establish the connecting rod and piston assembly individual speed as the functions of the crank speed/position. The geometry notations were given in Figure 3-4. The piston wrist pin offset was not considered in this calculation since the actual value is very small (0.6mm) for this engine.

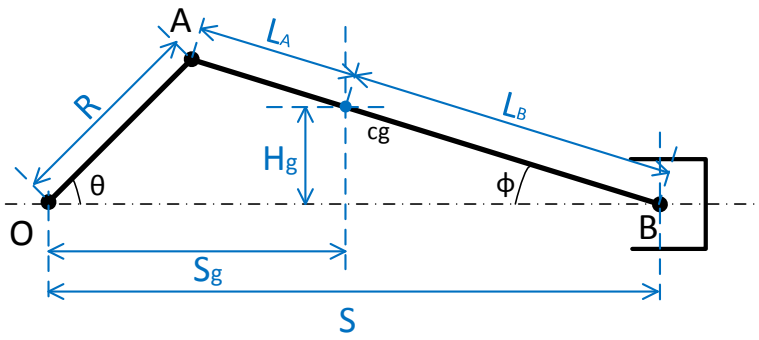

Figure 3-4 Engine crank slider mechanism geometry notations

Some basic relationships between the geometries are given below.

$$\theta = \omega_{mech} t \tag{3-7}$$

$$L = L_A + L_B \tag{3-8}$$

$$R\sin(\theta) = L\sin(\phi) \tag{3-9}$$

$$\phi = \sin^{-1}\left(\frac{R\sin(\omega t)}{L}\right) \tag{3-10}$$

For the translational displacements thus the speeds, they can be easily represented by the above two angles and other physical geometries as follow.

$$S = R\cos(\theta) + L\cos(\phi) \tag{3-11}$$

$$S_g = R\cos(\theta) + L_A\cos(\phi) \tag{3-12}$$

$$H_g = L_B \sin\phi \tag{3-13}$$

$$V_x = \dot{S} = -\omega R[\sin(\omega t) + \cos(\omega t)\tan(\phi)] \tag{3-14}$$

$$V_{cx} = \dot{S_g} = -\omega R[\sin(\omega t) + \frac{L_A}{L}\cos(\omega t)\tan(\phi)] \tag{3-15}$$

$$V_{cy} = \dot{H_g} = \omega R\frac{L_B}{L}\cos(\omega t) \tag{3-16}$$

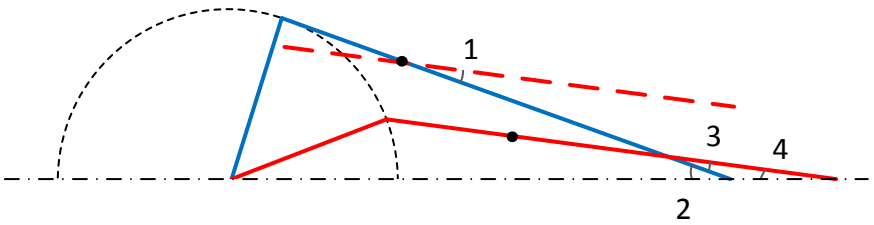

Figure 3-5 Connecting rod sweep angle ∠1

For the connecting rod rotational motion, the sweep angle is equal to the change of angle ϕ. As shown in Figure 3-5, the connecting rod and crank throw at two instances were coloured in red and blue respectively. It can be easily proved that $\angle 1$ is equal to $\angle 2 - \angle 4$. Therefore,

$$\omega_c = \dot{\phi} \tag{3-17}$$

By differentiating both sides of Equation (3-9), the equation for the connecting rod rotating speed is

$$\omega_c = \frac{\omega R \cos(\omega t)}{\cos(\phi)} \tag{3-18}$$

All the property constants of the engine parts were obtained either by actual measurements or through the 3D CAD models provided by the engine manufacturer.

3.2.3 Friction torque

The engine friction comes from three main sources, rubbing friction between relative moving surfaces, pumping loss during intake and exhaust processes and auxiliary friction from ancillary engine components, such as oil pump, water pump and alternator. Among the engine parts, the piston assembly is the largest contribution and followed by valvetrain and crankshaft bearings. The piston assembly could

account more than half of the total friction [89, 90] for engines prior to 1969. With more improved design, it has been reduced by 15~20% in recent years [90, 91].

Before introducing the friction model, the term Mean Effective Pressure (MEP) needs to be explained first. It is commonly used to describe the engine output and for the convenience of comparing engine performance with different displacements. The friction here is regarded as a negative torque that occurs inside the engine. The MEP is calculated as

$$MEP = \frac{T\, n_c}{V_d}\, 2\pi \tag{3-19}$$

Where,
T is the torque,
n_c is the number of revolution per power cycle (i.e. for 4-stroke engine n_c =2),
V_d is the engine displacement.

In order to include friction torque in the simulation, the typical Chen-Flynn model is used here. It delivers the friction mean effective pressure (FMEP), i.e. mean engine friction, with knowledge of the piston mean speed and maximum cylinder pressure.

$$FMEP = MPSSF \cdot \overline{v_p}^2 + MPSF \cdot \overline{v_p} + Const. + PCPF \cdot p_{max} \tag{3-20}$$

Where,
$MPSSF$ is mean piston speed squared factor,
$MPSF$ is mean piston speed factor,
$\overline{v_p}$ is the mean piston speed,
$PCPF$ is peak cylinder pressure factor,
p_{max} is the peak cylinder pressure.

In the Chen-Flynn model, the first three terms in the Equation (3-20) are parabolic curve fitted FMEP with regard to the mean piston speed. They are due to turbulent dissipation, hydrodynamic friction and boundary friction respectively [89].

The last term is a correcting element accounting the effects from engine load, blow-by, heat transfer and rubbing loss caused by cylinder pressure [92].

To calibrate this friction model, the FMEP data collected from engine rig tests at full speed range with WOT. A few methods can be used to measure the engine fiction. However, calculating the FMEP from measured engine IMEP and BMEP is recommended in [89] over the other methods that switch off the sparks during the testing, such as direct motoring test, Morse test, etc. This is because in that cases some operating conditions might be different to a fired engine, for example, the gas load, oil temperature, exhaust blowdown phase and so on. The recommended method also has a drawback. It is the error brought in when calculating from two large measurement values (IMEP and BMEP). Therefore, the average of multiple cycle measurements is required to minimise this error.

Thanks to the combustion analyse system, the in-cycle instantaneous pressure is possible to be logged and thus the calculated IMEP. Figure 3-6 shows one real time logged P-V diagram for one cylinder. The engine was running with wide-open throttle to minimise the pumping loss. Since the IMEP is the integration of the in-cylinder pressure, the pumping loss, which generates negative pressure, was already removed from gross IMEP. The FMEP is derived by calculating the difference between the mean net IMEP and the mean BMEP.

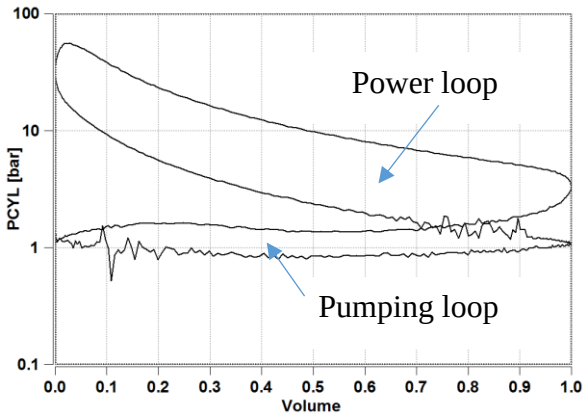

Figure 3-6 Real time logged P-V diagram from CAS

$$FMEP = net\ IMEP - BMEP \tag{3-21}$$

By looking at the equation for the Chen-Flynn model, the first three terms assembles a parabolic function of the mean piston speed. To find the function coefficients, the peak pressure term with $PCPF$ of 0.005 was subtracted from the actual FMEP measurements and a parabolic function was generated to fit those scattered modified FMEP against the mean piston speed. This particular $PCPF$ value was suggested by the engine 1-D simulation software, GT Power, user manual [93]. After these coefficient defined, the peak pressure term was put back to the model equation.

By having the equations for the three torque sources prepared, the model torque output simply follows the equation:

$$T(\theta, \omega) = T_{gas}(\theta, \omega) - T_i(\theta, \omega) - T_f(\omega) \tag{3-22}$$

Since this engine model was empirical based, the inputs/feedback to it were the shaft position and speed and the output was the instantaneous torque to the rotating inertia (crankshaft and electric machine rotor for this case). The system model schematic is shown in Figure 3-7.

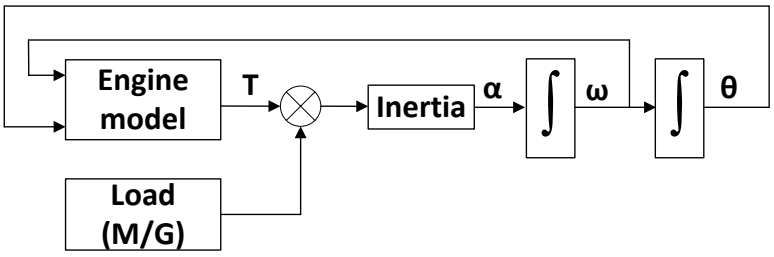

Figure 3-7 Engine model structure

3.3 Engine rig testing

3.3.1 Test rig setup

The twin-cylinder engine was installed on the test bench for standalone baseline testing before having the M/G directly coupled to the crankshaft. The braking load (dynamometer) to the engine was applied using a 50kW AC motor supplied by Sierra CP Engineering, which has a peak speed of 8500rpm and peak torque of 164Nm. On the engine timing belt side, there is a high resolution AVL optical encoder (0.2CA deg/ pulse) installed on the crankshaft. All the engine measurements going into the combustion analysis system (CAS) were synchronised to this signal. The dynamometer has an encoder with 1024 pulses per revolution for drive control purposes. A drive shaft connects the engine flywheel and the dynamometer. The shaft torque measurement was done by a HBM T40B torque flange, which was located at the dynamometer end. The cylinder pressure sensors, which were supplied by Kistler, have a sensitivity of -20pC/bar bandwidth. They were installed on the cylinder head intake side to access the combustion chamber. Figure 3-8 and Figure 3-9 show the test bench set up.

Figure 3-8 Test bench (left) and the drive shaft (right)

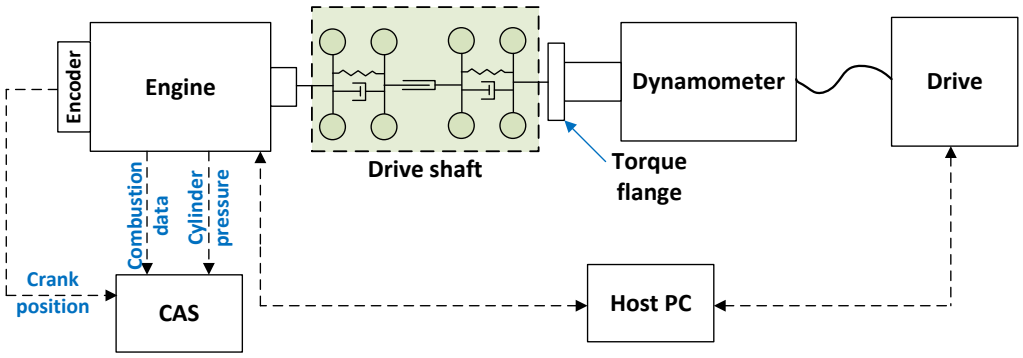

Figure 3-9 Engine standalone testing setup schematic

The drive shaft contains elastic elements (rubber) which are intended to shift the system natural frequency away from the engine speed range to avoid unstable operation. However, this meant that the torque flange was not able to measure the true instantaneous torque ripple. It was very difficult to model the drive shaft accurately since the supplier could not provide the elements damping characteristics and the rubber material was expected to express non-linear behaviour. Therefore, in-cycle torque of the Simulink engine model was validated with the GT Power model.

3.3.2 Cylinder pressure data collection

In order to obtain the cylinder pressure data sets for the complete engine operating range, they were collected during the brake specific fuel consumption (BSFC) mapping test. The steady state condition data at each set point was logged. The engine speed was controlled from 1500rpm to 5000rpm with 500rpm incremental while the torque demand was requested from 10Nm to wide-open-throttle (WOT) in 5Nm steps.

When logging, the CAS recorded data for 300 engine cycles and the average values were used in the model look-up table. An example is shown in Figure 3-10. The zero CA deg is the top dead centre firing (TDCF). Since the engine is even fired, the two pressure peaks should be 360 CA deg apart. In order to compare the cylinder-to-cylinder variation, the two traces were shifted to be co-located. As can be observed, the cylinder 2 developed higher peak pressure than cylinder 1. This difference was a

fact that consistently experienced in all other tests. Later investigations confirmed that this was not due to the sensor defects. Therefore, the pressure data was not averaged between cylinders to allow the model replicating the behaviour.

Since this research is at the early stage of the development of the dynamic torque control strategy, to study its effectiveness preliminarily in a relatively ideal environment is in priority. Therefore, the engine behaviour cycle-to-cycle variation was not included in the model, although this is an important factor need to be considered in a real application.

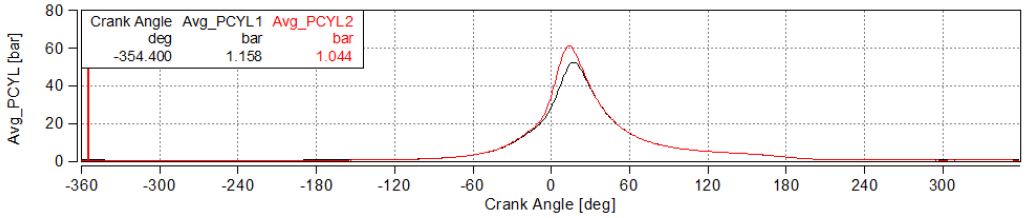

Figure 3-10 Averaged in-cylinder pressure test data

3.3.3 Engine friction loss test

IMEP and BMEP were the key parameters for the friction loss determination. The piston TDC is crucial for the IMEP calculation since one CA deg misalignment could lead to 10% IMEP error [94]. The TDC was detected when engine was motored with the help of the high precision encoder. The BMEP is calculated from the torque measurement by the torque transducer on the drive shaft. The IMEP was a 300-cycle averaged log from the CAS while the BMEP was 30 seconds averaged log from the host PC at the same time.

Three sets of test data were analysed to confirm the consistency of the estimated engine friction. The first two sets were the data collected from the Engine 1 before and after the spark timing optimisation. The raw corrected FMEP and the parabolic curve fitted trend lines are shown in Figure 3-11. With extracted parabolic function coefficients and the peak cylinder pressure term, the Chen-Flynn fiction model results

were plotted in Figure 3-12. The Test 1 was conducted on 19/02/2015 while the Test 2 was on 16/09/2016. During the test, at 2500rpm, the rig experienced resonance. This led to abnormally high friction at that speed. This single point was not included in the further analysis. The two fitted curves showed a similar trend but with slightly magnitude difference. However, when coverting the FMEP value into torque, the average difference between the two was 0.34Nm. By considering the 7 months' time between the two tests, the small offset could be due to condition differences, such as temperature, engine wear, etc.

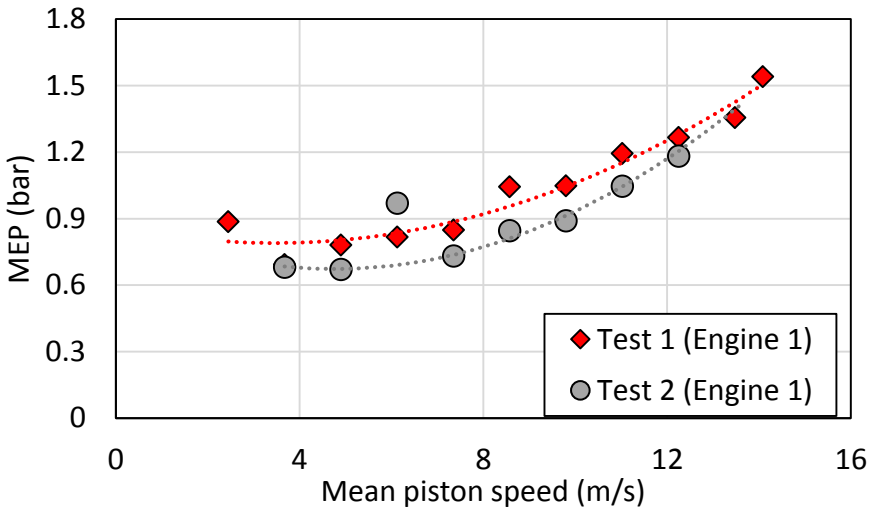

Figure 3-11 Parabolic curve fitted raw FMEP data

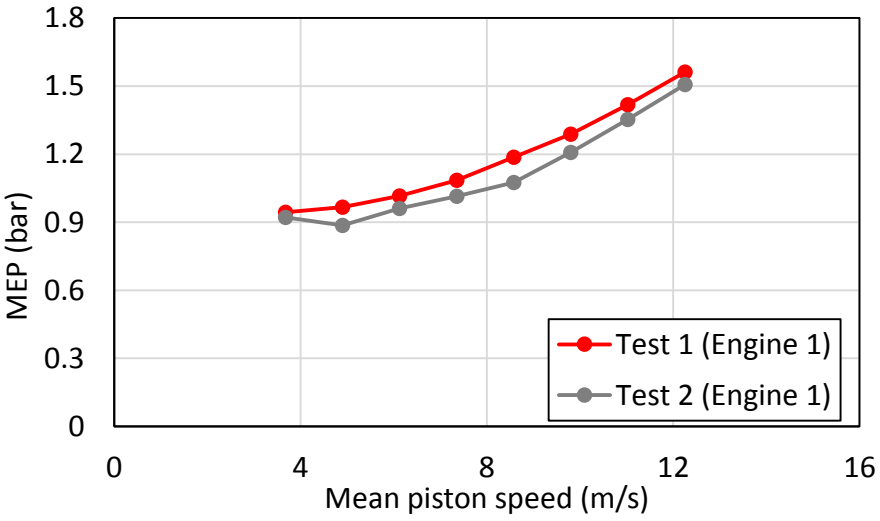

Figure 3-12 FMEP from Chen-Flynn model based on two sets of test data

In the later stage of this project, the Engine 1 was replaced with a notionally identical production engine (Engine 2). It was installed on the test rig with more instrumentation implemented and finally coupled with the motor/generator as the prototype APU. Another set of test data (Test 3 on 02/11/2015) for this engine was collected and analysed to check the overall friction. The result is compared with previous Engine 1 data and shown in Figure 3-13. Both engines have the same friction trend against engine speed, however, Engine 2's FMEP is consistently about 0.22 bar higher which translates to approximately 1Nm more friction. By the time of collecting the first FMEP test data of the Engine 1, the engine already had an accumulated running time of 133.59 hours and 36 hours more by the time of the second set of test data collected. Engine 2 was only run for 23 hours by the date of friction testing. Engine 2 was equipped with an electric water pump which was intended to reduce the ancillary friction loss. However, the test data did not support this idea. There is a high chance that the insufficient run-in time and inherent component manufacturing tolerance variation caused the friction difference. Another possible cause to this issue is that when modifying the original mechanical water pump propeller, the shaft bearings were affected leading to more friction. When the other performance specifications of Engine 2 were confirmed consistent with the Engine 1, it was coupled with the motor/generator soon afterwards. There was no extra data from Engine 2 to have more back-to-back friction behaviour comparison. Since there is no direct torque measurement inside the APU, thus no estimate of BMEP, the proportion of friction change due to run-in time was not be able to be evaluated again in the later stage. To match the engine standalone test data, the Engine 2's Chen-Flynn FMEP result eventually was used in the APU simulation model.

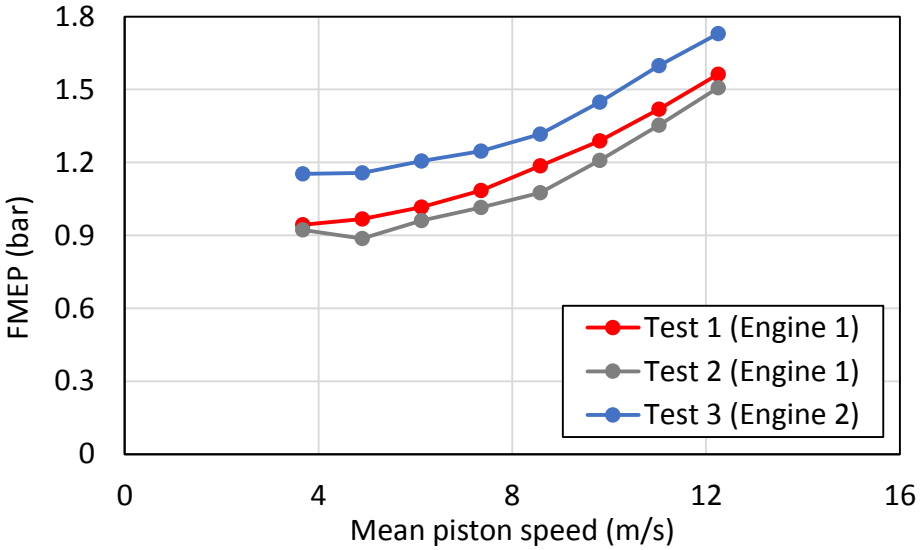

Figure 3-13 FMEP of Engine 2 compares to Engine 1

To determine the impact of the $PCPF$ on the results, the friction model sensitivity was examined. In fact, the nominal range of $PCPF$ is between 0.002 and 0.005 as suggested in the GT Power software manual and the . The FMEP Chen-Flynn model was recalibrated with various $PCPF$ values. The results can be viewed in Figure 3-14. As shown, for this two cylinder naturally aspirated engine with maximum peak cylinder pressure around 50~60 bar, the FMEP curve did not vary obviously when changing the $PCPF$. As a result, it was left as $PCPF = 0.005$ in the final model.

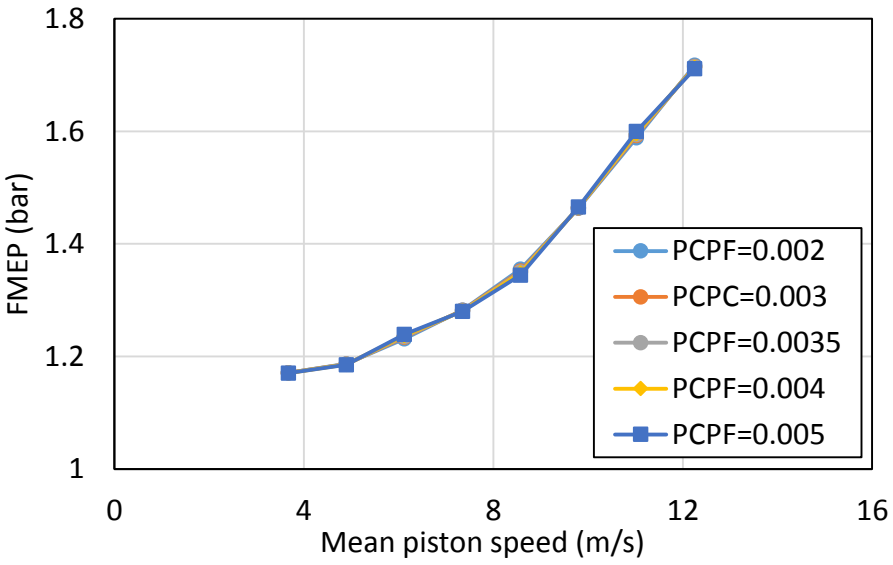

Figure 3-14 Chen-Flynn friction model with various PCPF for Engine 2

3.4 Model simulation results

The Simulink engine model schematic is shown in Figure 3-15.

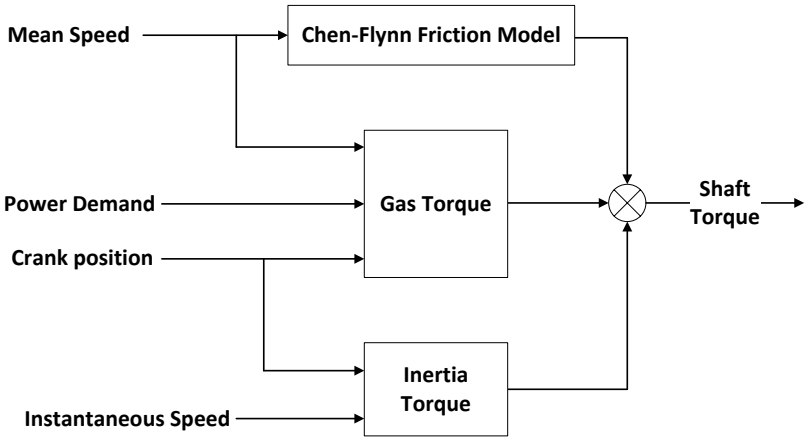

Figure 3-15 Simulink engine model schematic

The mean engine torque results were plotted in Figure 3-16. The GT model showed some torque offsets especially at the medium and low speed. The combustion model was calibrated through the three-pressure-analysis (TPA) method. The difference between the experimental and predicted torque was within 5% which was regarded as acceptable. On the other side, the Simulink model showed a very good match to the test data. This was mainly due to the direct use of the actual cylinder pressure data and no combustion model was implemented. A slight over prediction by the Simulink model occurred at 2500rpm. This was because of the abnormally high friction excluded from the Chen-Flynn model, which due to the rig resonance.

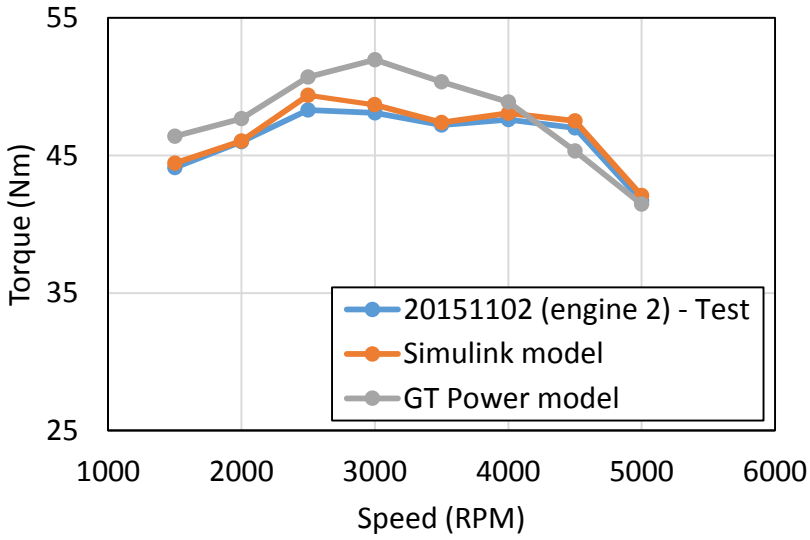

Figure 3-16 Mean torque comparison between models and test data

Since the engine shaft torque was transmitted to the torque flange through a non-rigid drive shaft, the true torque variation could not be captured by the measurement system. It was attempted to model the drive shaft as a flexible shaft and by using the high-resolution speed signals from both engine and dynamometer ends and the torque measurement to recreate the engine torque waveform. However, it was difficult to estimate a single damping constant that can fulfil a series of testing conditions. It might be due to the non-linear behaviour of the rubber material.

The GT Suite is the most widely used engine simulation tool. It should be able to provide a reference when some parameters cannot be confidently measured. Therefore, the GT Power model in-cycle torque variation output was used to verify the Simulink model results. Figure 3-17 presented the torque waveforms at 2000rpm and 4500rpm WOT as examples. The Simulink model showed a very close fit to the GT model. Figure 3-18 illustrated the comparison at 3000rpm WOT where the largest mean torque dissimilarity occurs. Although the major difference was at the instantaneous peak torque area which was a consequence of the combustion model, the rest part still recreated enough detailed curve features.

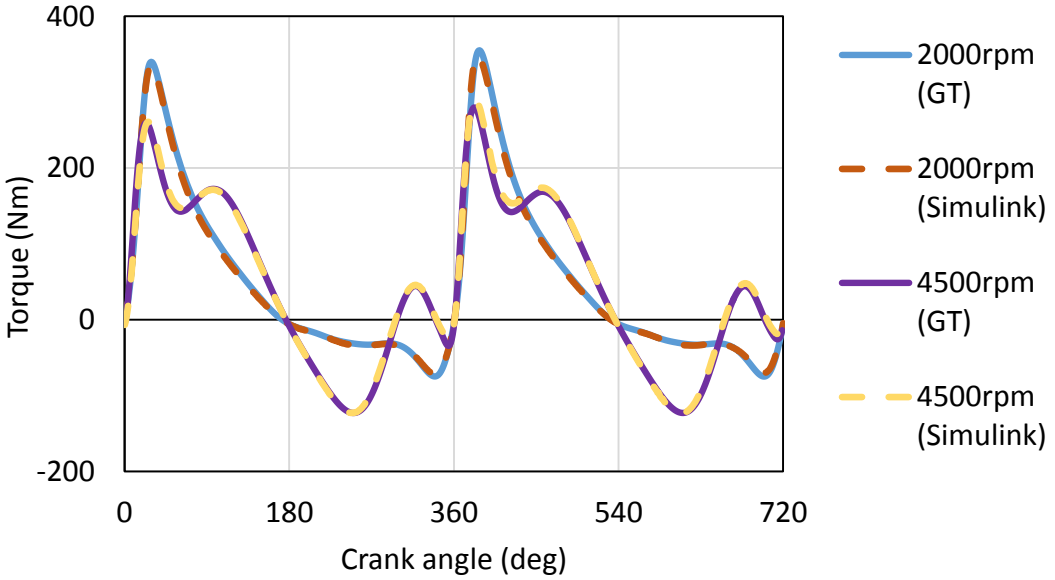

Figure 3-17 In-cycle torque variation of GT and Simulink model at 2000rpm and 4500rpm

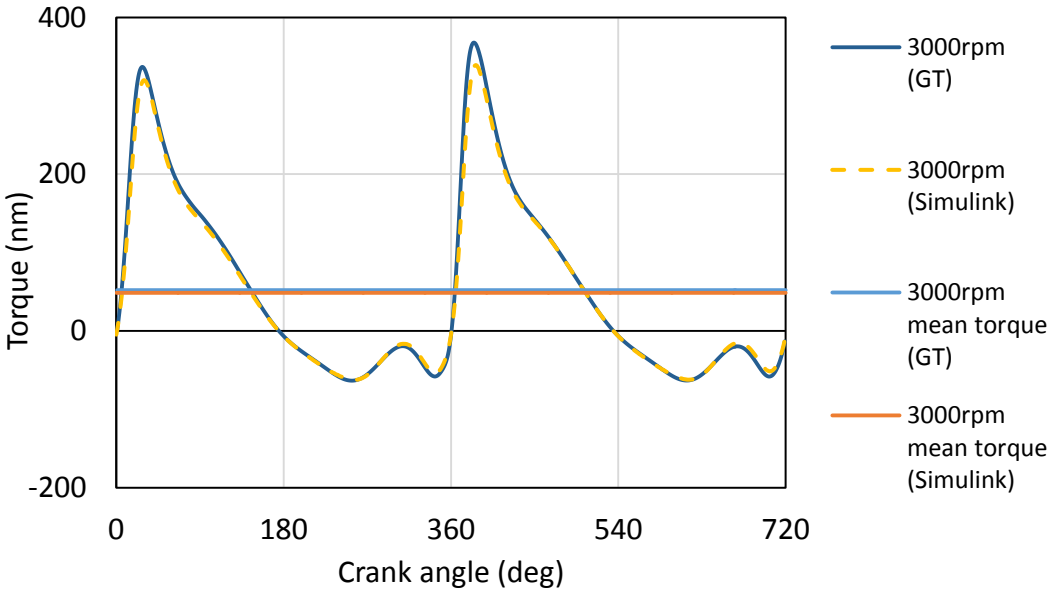

Figure 3-18 In-cycle torque variation of GT and Simulink model at 3000rpm

The model in-cycle speed fluctuation results were also compared to the bench testing data. Since the test bench setup and system physical specifications, such as the stiffness and inertia, for the final APU were different to the engine standalone test condition, this part will be presented and discussed in CHAPTER - 6 .

3.5 Conclusion

This chapter presents the modelling process of the IC engine used in the prototype APU. The base unit is a naturally aspirated twin-cylinder petrol engine. Since the firing frequency is low, the in-cycle speed fluctuation is more noticeable due to the in-cycle torque variation. Therefore, the aim of this model is to reproduce the instantaneous torque waveforms. The test rig was equipped with a high-resolution encoder and a combustion analysis system. The cylinder pressure, thus the IMEP, and the BMEP data were collected across the entire engine operating range and used for the model calibration. The three major torque sources considered in the model were from the gas pressure, the friction and the crank slider inertia. The former two were calibrated from the bench test data while the later one was analytically modelled. The mean engine torque results showed good match to the test data. Due to the damping effect of the drive shaft, the in-cycle shaft torque variations could not be captured on the test bench. Consequently, they were compared to the 1-D engine model and showed satisfying results.

A limitation of this model needs to be noted here. As mentioned in the inertia torque section, the rotating inertia block is the combination of the crankshaft and the electric machine rotor. However, this is not the actual total system inertia, since a number of other components are attached to the crankshaft, such as the connecting rods, valvetrain, oil pump, etc. The effective inertia is higher than that used in the model. Usually the extra effective inertia is cycle averaged for simplicity. The inertia torque from the crank sliders (calculated in the previous section) only have an effect on the instantaneous torque variation as long as the machine is spinning. It should not be confused with this cycle averaged effective rotating inertia, which leads to a speed variation when the torques from both input sides are unbalanced. This total effective rotating inertia of the APU could not be determined specifically during the project. However, the in-cycle speed variation simulation results (presented in the next chapter)

showed a good match to the testing data. This indicates that the actual effective inertia was close to the assumptions made in the simulation model.

CHAPTER - 4
Electric Machine Modelling

This chapter presents the modelling process of the prototype electric machine. The analytical model was established with some details extracted from the FEA model to improve the fidelity. The model performance behaviour matched the test data well after calibration. On the inverter side, both the Space Vector PWM control algorithm and the hardware electrical losses were explained and modelled individually.

4.1 Introduction

The electric machine is another major part of the APU system as the IC engine. It was directly coupled to the engine crankshaft as the braking source to generate the electrical energy and control the engine speed at the same time. Instead of applying a constant braking torque as in a conventional generator set, the motor/generator (M/G) in this APU was designed to impose a counteracting torque waveform dynamically which aims to minimise the crankshaft in-cycle speed fluctuation caused by the engine torque ripples. It was named as Dynamic Torque Control (DTC). In this chapter, the M/G was modelled analytically in the Simulink environment with some machine details of the model that were extracted from the finite element analysis (FEA) model. It helped to obtain a higher model fidelity while reduce the simulation time. The inverter's control logic and electrical losses were also modelled separately as the other two main components in the electrical system.

The electric machine used in the prototype APU was an interior permanent magnets (IPM) synchronous machine. It served as the engine starter motor as well when the APU is requested to be on. Figure 4-1 shows a simplified 2D section view of the actual machine. Its main specifications are given in Table 4-1.

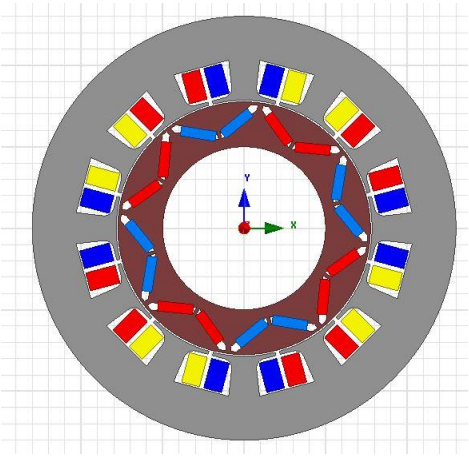

Figure 4-1 Simplified IPM 2D section

Table 4-1 Main IPM specifications

Operating voltage	350-450V
Maximum speed	6000rpm
Rated power	20 kW(4000rpm) 25 kW(5000rpm)
Cranking torque (<5s)	52Nm (-7^{0}C) 80Nm (-25^{0}C)

4.2 Electric machine modelling

4.2.1 The analytical model

The DQ control theory for the electric machine has been explained in the literature review chapter (CHAPTER - 2). It was meant to control the three overlapped AC phase terms with two individual DC terms – one is responsible for the torque production while the other is to create field as in a DC machine. It much simplified the control complexity.

Consider an equivalent circuit of a simplified single-phase motor as seen in Figure 4-2. According to the Kirchhoff's law, the general relationship in a PM synchronous machine is

$$v = iR + e + L\frac{di}{dt} \tag{4-1}$$

Where,
v is terminal voltage,
L is the stator inductance,
e is the back-EMF due to PM.

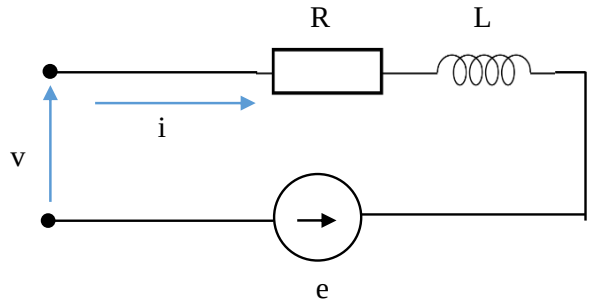

Figure 4-2 Equivalent circuit for a single phase motor

Based on Equation (4-1), the fundamental DQ equations after converting from abc-phase system are:

$$u_d = r \cdot i_d + L_d \frac{di_d}{dt} - \omega\psi_q \tag{4-2}$$

$$u_q = r \cdot i_q + L_q \frac{di_q}{dt} + \omega\psi_d \tag{4-3}$$

Where,
ψ is the flux linkage.

In the above equations, the very last term in each one are the induced voltage caused by the flux linkage. Since flux is always 90 degrees advance to induced voltage, these two terms reflect the cross coupling effect between the two axes. De-couple them from the equations can make the system model stabilise faster. This will be explained later in this chapter. The flux linkage can be expressed by following equations.

$$\psi_d = L_d i_d + \psi_r \tag{4-4}$$

$$\psi_q = L_q i_q \tag{4-5}$$

Where,
ψ_r is the flux introduced by the permanent magnets.

By substituting Equation (4-4) and (4-5) into (4-2) and (4-3),

$$u_d = r \cdot i_d + L_d \frac{di_d}{dt} - \omega L_q i_q \tag{4-6}$$

$$u_q = r \cdot i_q + L_q \frac{di_q}{dt} + \omega L_d i_d + \omega\psi_r \tag{4-7}$$

The machine torque equation under the DQ coordinate system is

$$T = \frac{3}{2} P(\psi_r \cdot i_q + (L_d - L_q) i_d i_q) \tag{4-8}$$

Where,
P is the number of pole pairs.

Since the machine rotor has the magnets buried in rather than on the surface, the magnets increase the d-axis reluctance, because magnet is normally considered owning similar magnetic permeance as vacuum. Therefore, the rotor inductance is uneven

along the circumference and called salient rotor. In the case of IPM, L_d is lower than L_q. This rotor saliency provides another type of torque that can be utilised, the reluctant torque caused by the attraction between a magnetic field and ferrite material. As indicated in the Equation (4-8), by appropriately decomposing the current vector on the two axes, the total torque can be larger than having the current vector completely laying on the q-axis. The angle measured between the current vector and the positive half of q-axis is normally represented by γ. Figure 4-3 shows a generic DQ axes vector diagram.

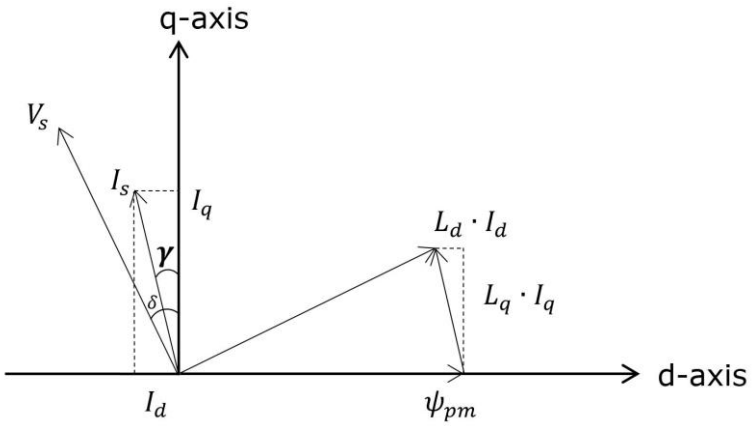

Figure 4-3 Generic DQ coordinate system vector diagram.

The diagram unveils the following relationships,

$$I_s = \sqrt{{I_d}^2 + {I_q}^2} \tag{4-9}$$

$$\tan\gamma = {I_q}/{-I_d} \tag{4-10}$$

By substituting Equation (4-9) and (4-10) into Equation (4-8), the torque could be represented with current vector magnitude and the current angle γ as:

$$T_e = \frac{3}{2} \cdot p \cdot (\psi_r \cdot I_s \cdot \cos\gamma - (L_d - L_q) \cdot {I_s}^2 \cdot \sin\gamma\cos\gamma) \tag{4-11}$$

At a certain current load, the torque becomes a function of the current angle. Figure 4-4 shows the torque variation regarding to the γ angle change at phase rms current of 110A.

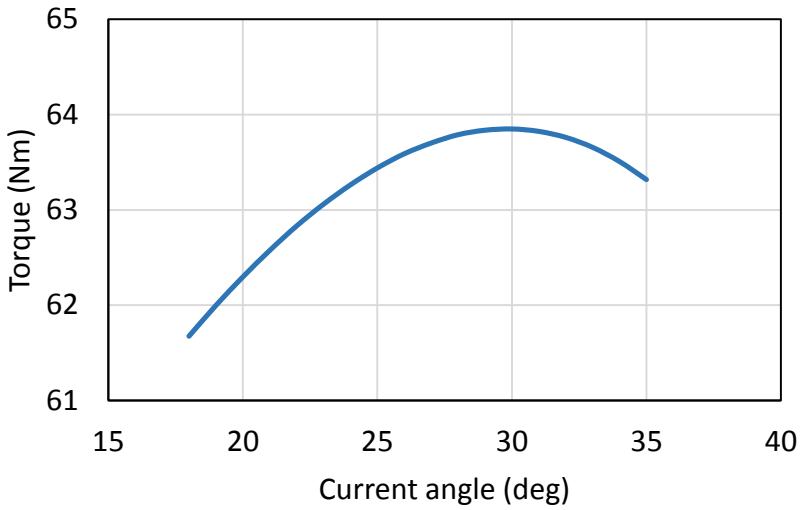

Figure 4-4 Current angle effect on the torque (I_{rms}=110A)

To make the most use of the current, in the control logic the γ will be selected to the angle where the maximum torque delivered. This type of control strategy is called maximum torque per ampere (MTPA). There are also other types of control strategies, such as unity power factor control, constant mutual flux linkages control, etc. are discussed in [41, 83]. As shown in the above plot, in order to calculate the optimum angle, the zero slope position of the torque curve needs to be defined, i.e.

$$\frac{d\,T_e(\gamma, I_s)}{d\,\gamma} = 0 \tag{4-12}$$

By solving this equation, γ can be represented as

$$\gamma = \sin^{-1}\left(\frac{\psi_r + \sqrt{{\psi_r}^2 + 8\left(L_d - L_q\right)^2 {I_s}^2}}{4\left(L_d - L_q\right) I_s}\right) \tag{4-13}$$

Since the winding inductance and the rotor flux linkage can be determine through experimental measurement methods as described in CHAPTER - 2 , it is possible to define the current angle analytically at different load conditions.

However, in reality, the winding inductance varies regarding to the phase current rather than staying as a constant. This is because the stator iron tends to be saturated with flux when the current is high and consequently the magnetic path permeance changes. This effect is difficult to measure physically with the current lab setup. However, neglecting this variation will affect the model accuracy. Therefore, the final Simulink model was implemented with a variable inductance block with help from the FEA model. The procedure will be presented in the next section.

The analytical model for the electric machine itself was rather simple to create since there was no physical dimension or spatial magnetic flux loop considered. It is fully based on the two first order differential equations rearranged from Equation (4-6) and (4-7). This model is preferred when evaluating system level performance since it requires much shorter computing time compared to an FEA model. The electric machine model equations and schematics are shown as below.

$$\frac{di_d}{dt} = \frac{1}{L_d}(u_d - r \cdot i_d + \omega L_q i_q) \tag{4-14}$$

$$\frac{di_q}{dt} = \frac{1}{L_q}(u_q - r \cdot i_q - \omega L_d i_d - \omega \psi_r) \tag{4-15}$$

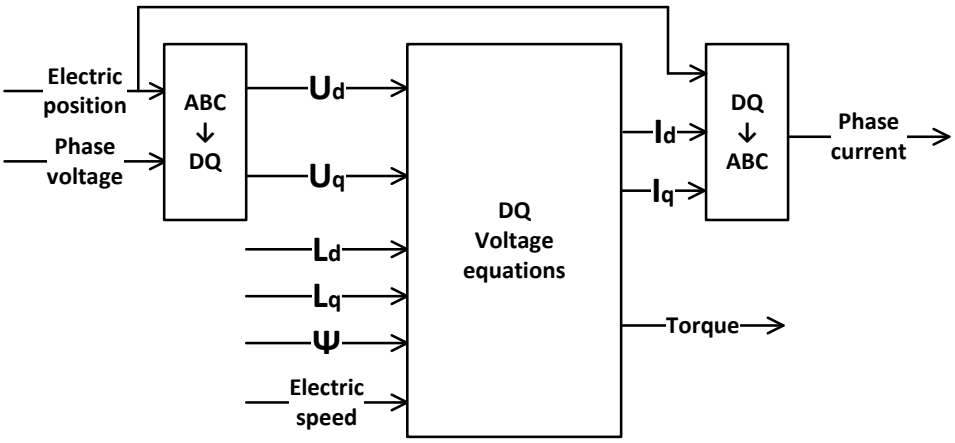

Figure 4-5 Electric machine model schematic

4.2.2 The FEA model

Although the analytical model of the electric machine is simple and fast to solve, the more specific characteristics of the machine still need to be analysed through the FE tool, such as the electric losses, cogging torque etc. However, the FEA model does take a considerable amount of time to solve. For this particular model, it took about three hours to finish two rotor revolutions. It is not suitable for real time co-simulation with other analytical models when the system level performance is of interest. Therefore, the electric machine was first modelled and calibrated in the FEA software individually, and the winding inductance results were extracted and stored as tables in the analytical model to improve its fidelity. This method was seen in [95].

The FEA software used here was the ANSYS Maxwell with the officially released Electric Machines Design Toolkit. When building up the FEA model, the actual machine's geometry and material specifications were required. However, due to the intellectual property protection considerations, the complete geometric details of the prototype M/G were not fully disclosed by the OEM. The protected areas were mostly on the very fine detail designs, such as the rotor magnet locating slots, stator tooth end and so on. These features were deployed mainly to improve the M/G cogging torque behaviour and for certain manufacturing purposes. Since this research mainly

focused on the machine mean performance, these features were abandoned and the model geometry was simplified with only the information provided.

The prototype M/G was a radial flux machine. The sections on the axial direction were identical. To reduce the computational cost and also because of the lack of geometrical details, the electric machine was modelled in 2D instead of 3D. The stator's outer diameter was 260mm while the rotor outer diameter was 155mm. The air gap was 1mm. The machine had the bar would concentrated winding with 56 turns on each tooth. The copper bar wire section was 1*3mm rectangular. Although each winding section was represented as one solid square in the 2D view, it was set as stranded wire with actual number of turns. Due to the 12 tooth and 8 poles configuration, the 2D section had a periodicity of four according to Equation (2-6). Therefore, the complete 2D section could be reduced to a quarter as shown in Figure 4-6. For analysis purpose, the rotor edge next to the air gap was divided into three thin layers and one tooth was separated out from the rest stator iron. This process enabled these particular areas having finer mesh and more specific results can be obtained. The mesh plot was shown in Figure 4-7.

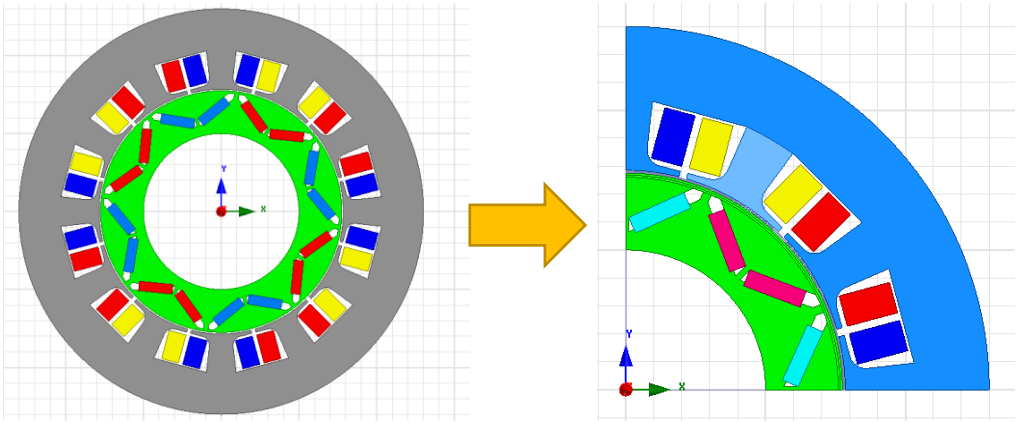

Figure 4-6 FEA model size reduction

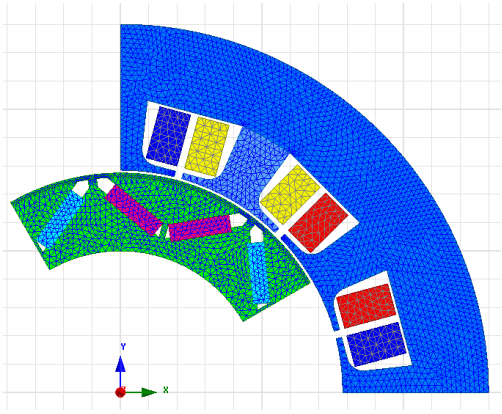

Figure 4-7 FEA model mesh plot

The rotor magnet was neodymium (NdFeB) with grade of 38H. The stator electric steel was in grade of M235-35A. The materials' specifications from the provided data were used to create new material definitions for this particular FEA model. In order to calculate the Eddy current loss in the magnets, they were assigned with current excitation of zero current. The FEA model time step was set to 10ms (1e-5s).

To validate the FEA model, the back-EMF waveforms were compared first. The open circuit test were conducted by the author and his colleague in the OEM's test cell. The terminal line-to-line voltage was measured through a potentiometer and the data was captured by an oscilloscope. The results at 2000rpm and 4500rpm are given in Figure 4-8 and Figure 4-9. The FEA results generally followed the same wave shape and delivered a similar voltage amplitude as the test data. The differences were primarily due to the missed geometry details. This can result in the dissimilarity of torque ripples. However, it is in high frequency which cannot bring significant effect on the system level speed fluctuation due to the inertia. This point will be proved in the next chapter. Therefore, the model geometries was not further modified to match the back-EMF test data better.

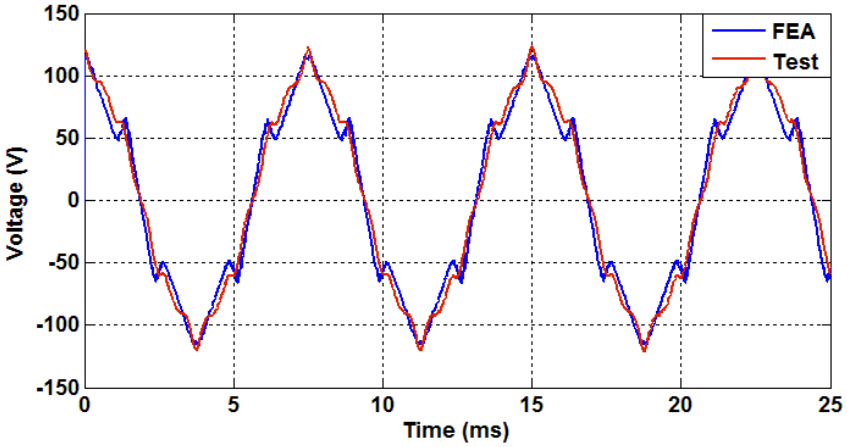

Figure 4-8 Line-to-line back-EMF from FEA model and bench testing at 2000rpm

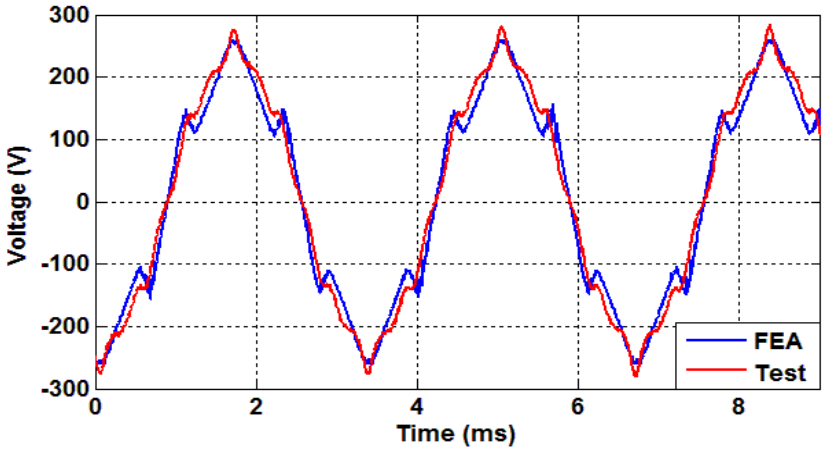

Figure 4-9 Line-to-line back-EMF from FEA model and bench testing at 4500rpm

The second validation test was the torque performance against phase current. Although the optimal current angle γ for the maximum torque can be analytically calculated, due to the saturation effect the actual angle could be very different as explained earlier. To acquire the optimal current angle in the FEA with consideration of the inductance variation, the FEA model was simulated with RMS phase current load from 1A to 140A with 3A incremental step. At each current condition, γ swept from 0° to 40° with 1° step. The maximum torques, corresponding current angles and DQ inductances at each current load were recoded. The current angle results were plotted in Figure 4-10 in comparison with the analytical calculated results with fixed inductance. A significant difference was observed between the two methods. To

compare the corresponding delivered torque, Equation (4-8) was used since this is how the final M/G Simulink model calculated the output torque. The torque curves were plotted in Figure 4-11.

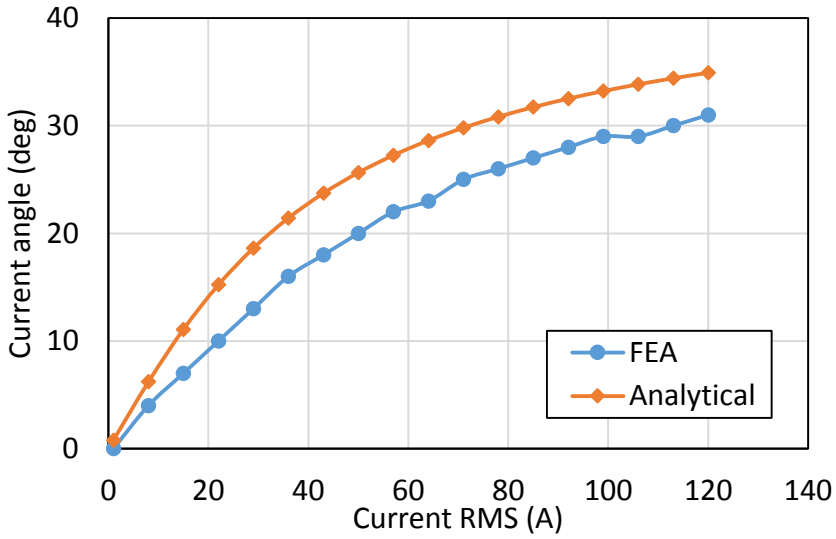

Figure 4-10 Current angle derived from FEA and analytical calculation

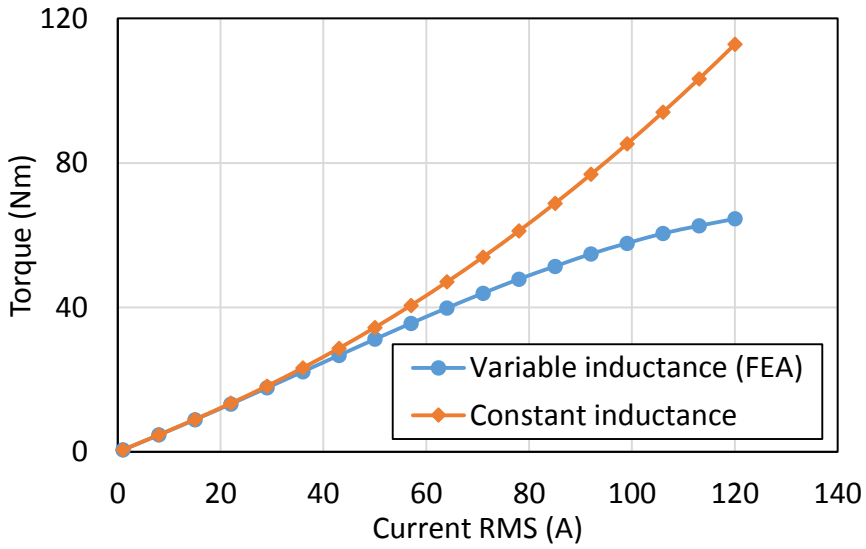

Figure 4-11 Torque curves with variable inductance and constant inductance

In the above plot, the two lines were overlapped at the left end, which indicates that at low current condition, the torque is not sensitive to γ. However, obviously, with fixed inductance, the torque was over estimated when current increases and the higher current is, the more severe the result can be. At 120A RMS (170A peak), the torque

estimated was almost doubled and still did not shown any sign of torque saturation. The results unveiled the necessity of using variable inductance tables in the final model. To capture the inductance variation, in the FEA, the phase flux linkages are derived first and transferred to QD coordinate system by Equation (4-16). The DQ inductance can be calculated with Equation (4-4) and (4-5).

$$C = \frac{2}{3}\begin{bmatrix} \cos\theta & -\sin\theta \\ \cos(\theta - \frac{2}{3}\pi) & -\sin(\theta - \frac{2}{3}\pi) \\ \cos(\theta + \frac{2}{3}\pi) & -\sin(\theta + \frac{2}{3}\pi) \end{bmatrix}$$

$$\begin{bmatrix} \lambda_d \\ \lambda_q \end{bmatrix} = C^T * \begin{bmatrix} \lambda_A \\ \lambda_B \\ \lambda_C \end{bmatrix} \tag{4-16}$$

To confirm the accuracy of the torque calculated from the variable inductance model, it was compared to the bench test data. Due to the unavailability of the prototype machine to be tested in the university laboratory, the only data set could be used was provided by the OEM which was conducted by the company test engineer. The scatter plot and the data trendline was plotted in Figure 4-12. Since this is the only data available, the torque transducer offset data was not known. From the graph, the original torque line apparently would not cross the axes origin, i.e. zero torque at zero current. Due to the lack of actual test condition information, this offset was considered caused by the inaccuracy of the torque transducer calibration. To correct this, the linear part of the raw data was fitted with a straight line. The constant (2Nm) in the fitting curve equation was assumed as the offset and removed from the complete data set. The new curve was also plotted in the same figure.

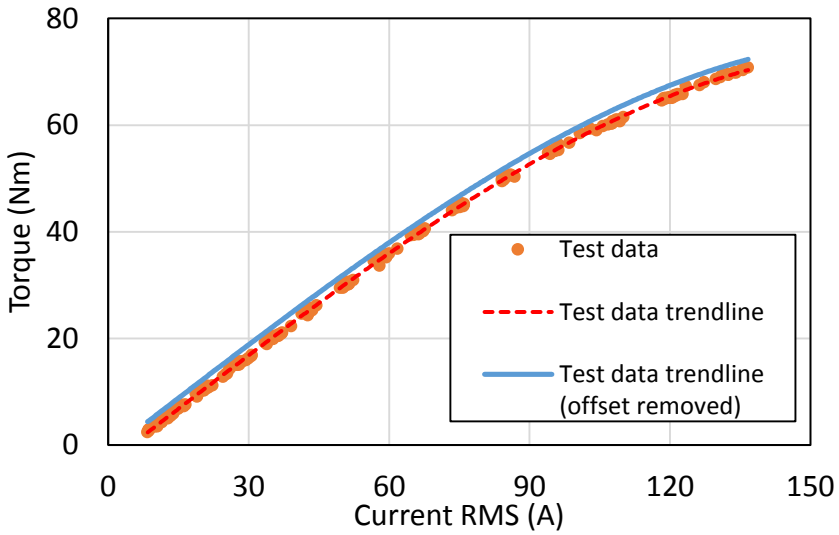

Figure 4-12 M/G torque bench test data

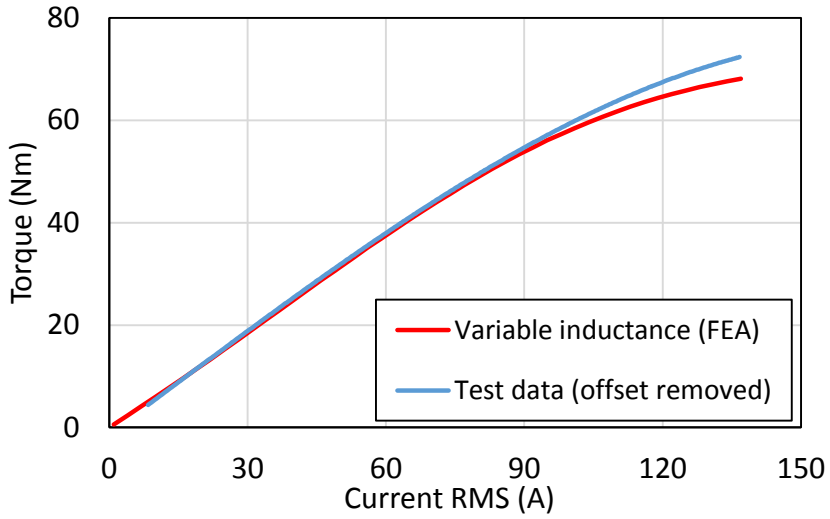

Figure 4-13 M/G torque curve from FEA and bench testing

Comparing to the test data as shown in Figure 4-13, the calculated torque matched well until the RMS current reached about 90A where the two curves started to diverge. At 140A RMS (~200A peak), the torque was underestimated by 5.6%. The high torque area was crucial for this model since the in the dynamic torque control (DTC) strategy the peak torque is the one of the key aspect to minimise the in-cycle speed fluctuation. More details will be explained in the next chapter.

By investigating the FEA model results, it suggested that there were errors on the inductance estimation in the FEA model at these extreme cases. The raw DQ inductance results were plotted against the phase current in Figure 4-14. Clearly, the two inductance lines crossed at the high load condition which was unrealistic. In reality, when the iron were completely saturated, the rotor would have identical magnetic permeance along the circumference and lost the saliency. In this ultimate case, L_d is equal to L_q and one could never be higher or lower than the other one. The unrealistic results were considered mainly due to the incorrect extrapolation of the material B-H curves as manually imported from the provided manufacturer data sheets. To approve this point, a software pre-defined material was assigned to the model and simulated at the same conditions. The inductance result is plotted in Figure 4-15. In this case, even with a higher phase current, the inductance curves still did not cross each other. (Due to the larger data point interval used, the curves were not as smooth as in the other plot.)

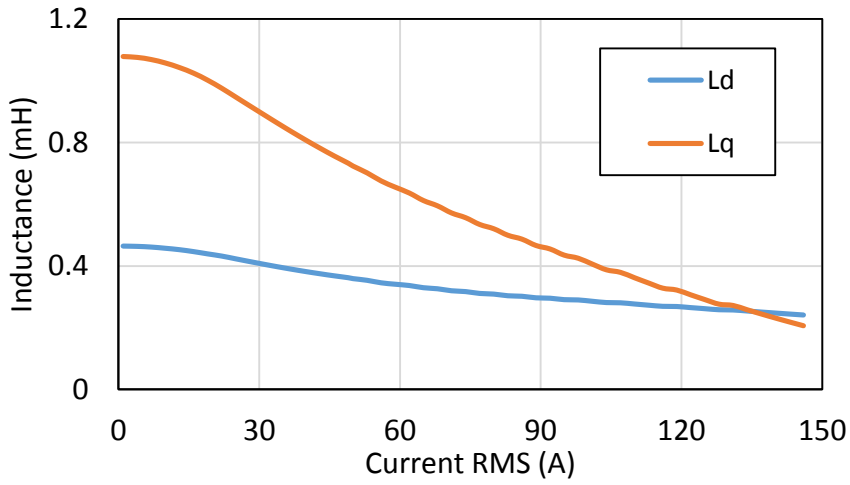

Figure 4-14 Original FEA DQ axes inductance results with user defined material

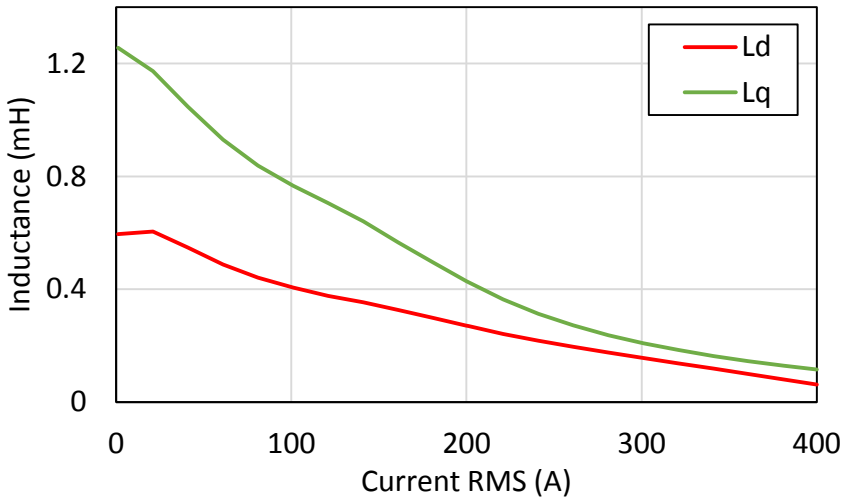

Figure 4-15 FEA DQ axes inductance results with software pre-defined material

To correct the issue, the two axes inductances were assumed equal at a high load and extrapolated from the raw FEA data. This point was chosen at 200A RMS since the curves were tended to coincide after 130A RMS with the user defined material. The d-axis inductance curve was extrapolated to 200A based on the data points after 90A. A third order polynomial function was used. The same inductance value at 200A was used for q-axis. For L_q, the raw FEA data after where the torque curves divergence started (at 90A RMS) was discarded. Instead, five points before 90A and the 200A point were used to interpolate a curve with a third order polynomial function. The modified inductance curves are shown in Figure 4-16. Figure 4-17 shows the torque curve with modified inductance tables. A better fitting was achieved with this method. The torque difference at 140A RMS dropped from 5.6% to 1.2%.

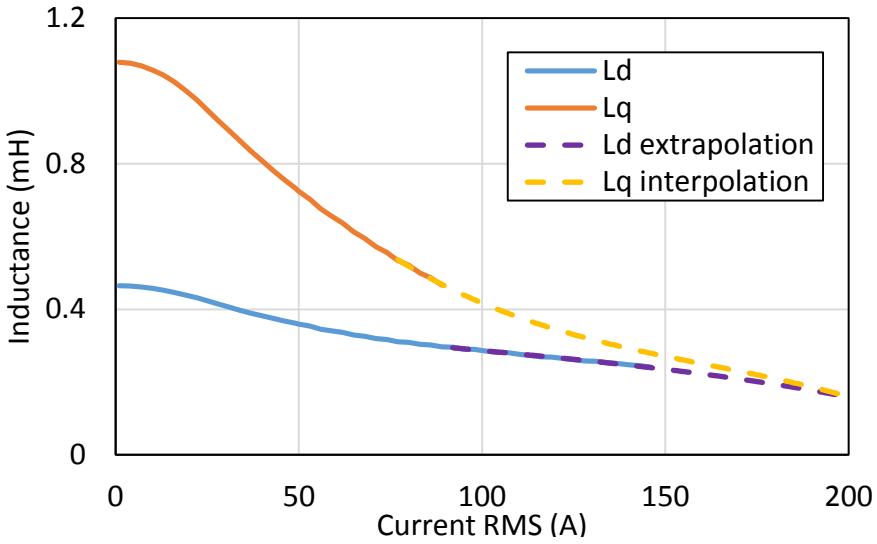

Figure 4-16 Modified FEA DQ inductance

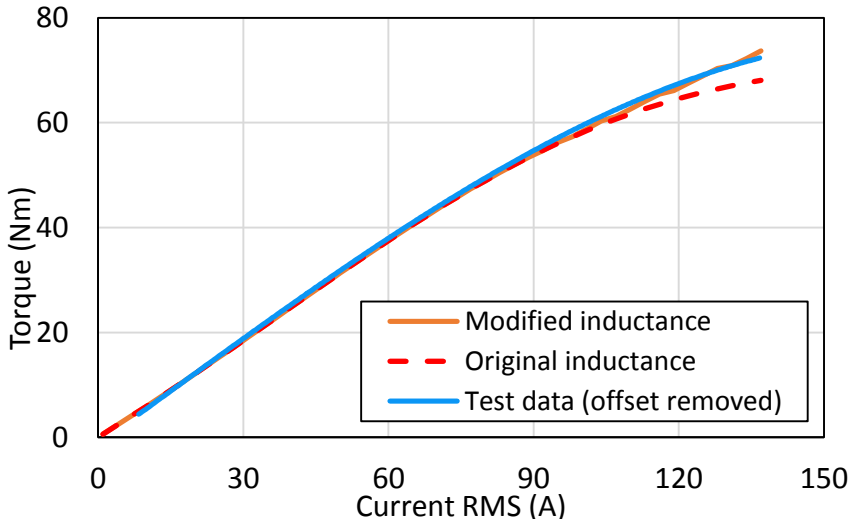

Figure 4-17 Calculated torque curve with modified inductance

In the later stage of the project, the OEM claimed that the current angle demanded in the actual controller programme was constantly set to 30° to simplify the control. The corresponding change was made in the FEA model to meet the actual system specifications. Again, the inductances derived from the FEA model were not realistic at high current load conditions. The same method as used in the MTPA was applied to correct the issue. The torque result of $\gamma = 30°$ strategy is shown in Figure 4-18 together with the MTPA. As seen in the plot, the torque performance from the FEA model was very close to each other with these two strategies. If reviewing the plot in Figure 4-10, the current angle in MTPA was actually around 30° after 80A

RMS, and at lower load, the torque was not sensitive to γ which was realised in Figure 4-11. These two points explained the above performance similarity for this particular electric machine. Both strategies were made available to be chosen in the system model, although there was no significant performance difference between them.

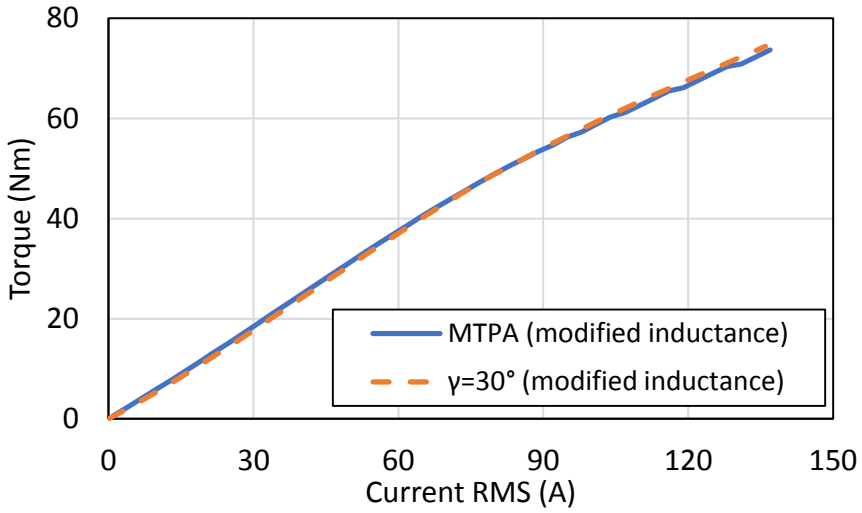

Figure 4-18 Torque curves with MTPA and γ=30° strategies

As analysed above, the necessity of variable inductance is inevitable for model fidelity. Although the FEA model did not directly deliver satisfied inductance results, the post calibration work helped to develop the variable inductance tables which allowed the model to match the test data better. In the final system Simulink model, instead of using constant inductance, these two look-up tables were implemented. The DQ inductances output was regarding to the instantaneous current feedback and sent to corresponding input ports of the electric machine model as seen in Figure 4-5.

4.3 Inverter modelling

As reviewed in the CHAPTER - 2 motor control section, the vector control algorithm expresses superior characteristics over the V/f control. For this project, since the M/G that directly mounted on the engine crankshaft was intended to deliver a dynamic in-cycle variable torque, fast response, precision and stability are crucial

aspects for achieving the final target. The inverter is the control unit (drive) for electric machine. As one of the crucial parts that directly influence the electric machine performance, the model for the inverter control logic, hardware and the power electronic electrical losses will be detail explained in this section.

The inverter will be modelled as two separate components, the control logic, which outputs gate signals for the power electronics, and the power electronics model, which links the battery and the M/G models and calculates the inverter hardware loss. The overall M/G system schematic is shown in Figure 4-19.

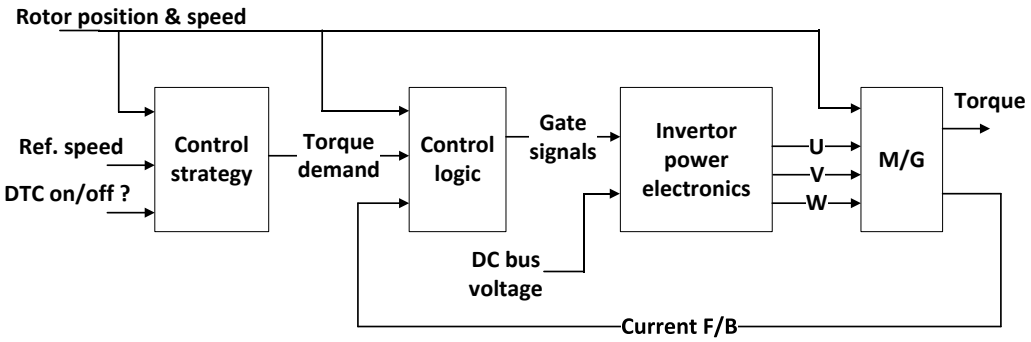

Figure 4-19 M/G system schematic

4.3.1 Current and speed control

The M/G was designed to be in speed control mode. Therefore, there were two feedback control circuits in the control block. The outer one is the speed loop while the inner one is the current loop. The speed loop schematic is shown in Figure 4-20. There were two control strategies that can be chosen. One is the traditional feedback PID control while the other one is the Dynamic Torque Control (DTC). The later one will be explained with more details in CHAPTER - 5 . For the prior one, a feedforward look-up table was used to help the system stabilise faster. Since the speed control loop has a bandwidth of 200Hz, the speed feedback was downsampled before reaching the PID controller.

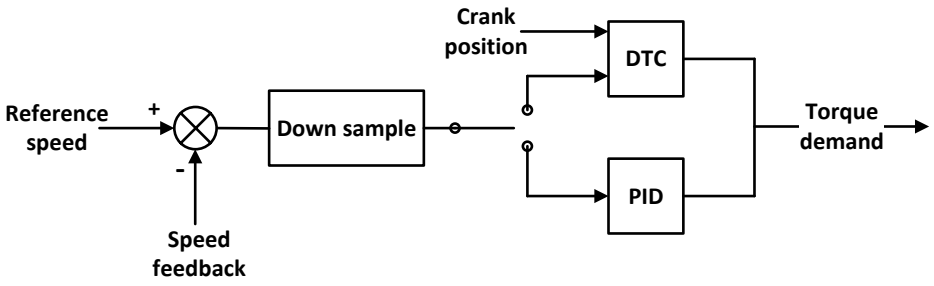

Figure 4-20 M/G speed control loop

Figure 4-21 depicts the current control loop. Together with the torque demand from the speed control loop, the current feedback from the M/G were downsampled to 10 kHz which is the current control frequency. According to the current feedback, the DQ axes inductances were looked up from the tables populated from the FEA results. These tables actually could be either inside the electric machine model or in the control model as long as their outputs were available globally. The torque demand was converted to DQ current demands through the look-up table created from the FEA/test results as well. There were two tables for selection, which were for MTPA and $\gamma = 30°$ strategies respectively, although, as compared earlier, they deliver very similar results. Then, the two PIDs output two voltage values regarding to the current errors. However, the two values were not the final voltages that is to be delivered to the M/G by the inverter. As seen in Equation (4-2) and (4-3), there exist two cross coupling terms. They were added back to the corresponding axis after the PIDs to reduce the influence from each other. The decoupling action is not an essential, but a technique that can make the system converge faster. Once the current loop is closed, the voltage requirements to correct the current error were sent to the inverter control block which is described in the following section.

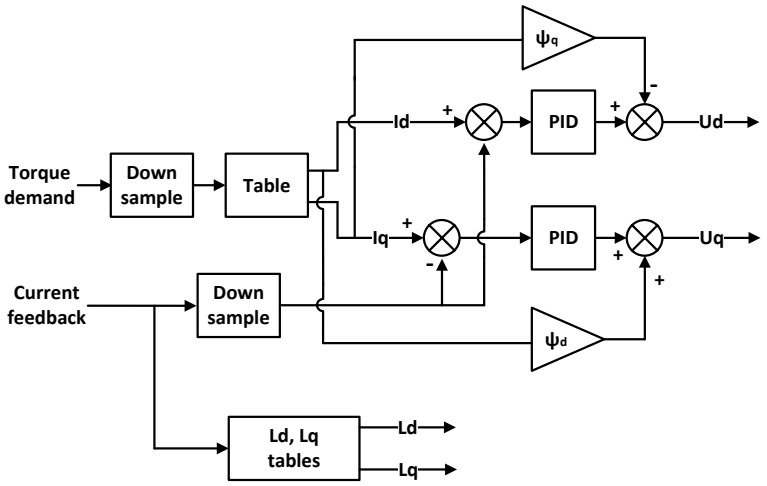

Figure 4-21 Current control loop schematic

4.3.2 Inverter control

A brief introduction of the inverter control methods was given in CHAPTER - 2 . Since the space vector PWM was used in the inverter according to the OEM, this control scheme and its modelling process is to be detailed.

As introduced earlier, each SV represents an overall inverter switches positon as shown in Figure 4-22. For the convenience to denote the switch status, ‘1’ indicates the upper IGBT is closed of the leg while ‘0’ is for the lower one closed. The three digitals from left to right corresponds to A, B and C phase respectively. For SVPWM, to command the switching device gate status, three things need to be determined: which SVs to be used, what order of these vectors to be conducted and what time duration for each SV is.

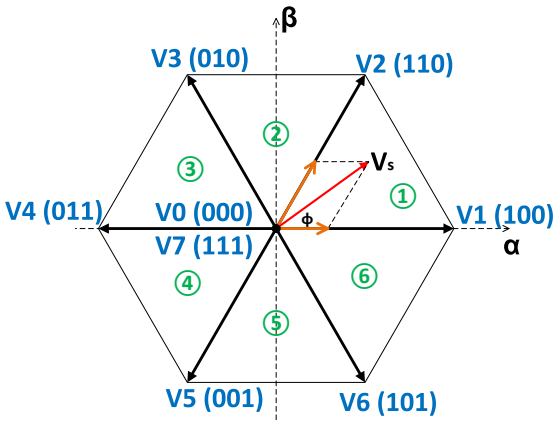

Figure 4-22 SVPWM hexagon

The inputs to the SVPWM block are the voltage demands in DQ plane from the current control loop. u_d and u_q will be transferred to $\alpha\beta$ plane and synthesised to a phasor. The active vectors that will be used are the boundaries vectors of the sector that the voltage phasor fell in. The benefits to use these two SVs is that, as can be seen in the graph above, the inverter status transfer between them only involves one leg to be switched.

As mentioned earlier, SVPWM controls the inverter as a whole and in order to reduce the switching events to the minimum and consequently the loss as well, a special order needs to be followed to conduct SVs in the inverter. Consider the situation that at one instance the voltage phasor is in Sector 1 and needs to jump to Sector 4 at next moment. Whichever V1 or V2 with which the first instance ended, there has to be at least two legs to be switched when changing to either V4 or V5. This does not meet requirements. To solve the problem, the two null vectors are used as a 'buffer' between PWM periods. Now, under the same situation, the procedure can start from a null vector (for example V0), then follows the order of V1, V2 and finishes with V7. For the next instance, V4 should be used before V5 to keep only one leg to be switched. However, if at the second instance the phasor still in Sector 1, switching from V7 to V1 will result in two legs changing states again. Therefore, the common method is to split each active vector time in two and follow the order as

$$V_0 \rightarrow V_a \rightarrow V_b \rightarrow V_7 \rightarrow V_b \rightarrow V_a \rightarrow V_0$$

In each Sector, to make sure only one leg change each time, the order of V_a and V_b need to be changed accordingly. In the odd Sectors, the right boundary side vector is used before left side one and vice versa for the even Sectors.

The time duration of the active vectors are determined through simple trigonometry calculation and the null vectors evenly share the rest of the PWM cycle time. If one total PWM period is $T_t = \frac{1}{f_{pwm}} = T_0 + T_a + T_b$, the time duration of each vector corresponding to the order above is

$$\frac{1}{4}T_0 \rightarrow \frac{1}{2}T_a \rightarrow \frac{1}{2}T_b \rightarrow (\frac{1}{4}+\frac{1}{4})T_0 \rightarrow \frac{1}{2}T_b \rightarrow \frac{1}{2}T_a \rightarrow \frac{1}{4}T_0$$

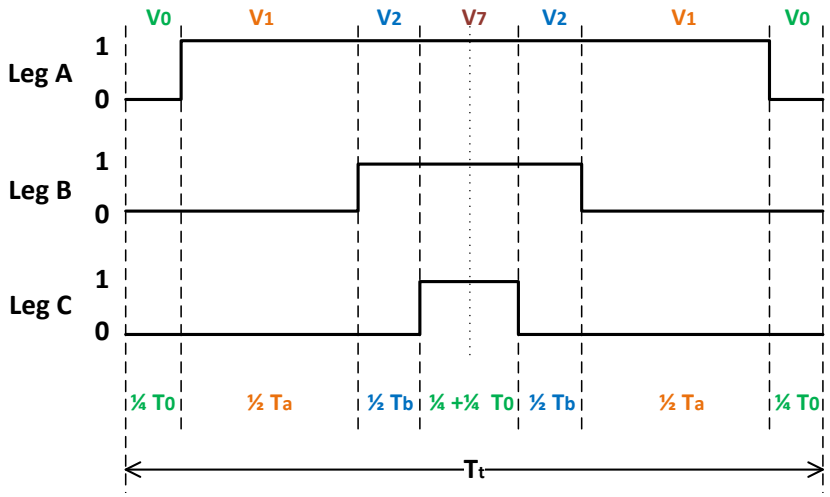

Figure 4-23 Switching states of an arbitrary voltage phasor in Sector 1

To calculate the exact time duration, as depicted in Figure 4-24, the following relationship can be derived by Law of sines.

$$\frac{|V_s|}{\sin(\frac{2\pi}{3})} = \frac{\frac{T_a}{T_t}|V_a|}{\sin(\frac{\pi}{3}-\phi)} = \frac{\frac{T_b}{T_t}|V_b|}{\sin\phi} \qquad (4\text{-}17)$$

Since

$$|V_a| = |V_b| = \frac{2}{3}V_{dc} \tag{4-18}$$

Therefore,

$$T_a = T_t \frac{\sqrt{3}|V_s|}{V_{dc}} \sin(\frac{\pi}{3} - \phi) \tag{4-19}$$

$$T_b = T_t \frac{\sqrt{3}|V_s|}{V_{dc}} \sin(\phi) \tag{4-20}$$

$$T_0 = T_t - T_a - T_b \tag{4-21}$$

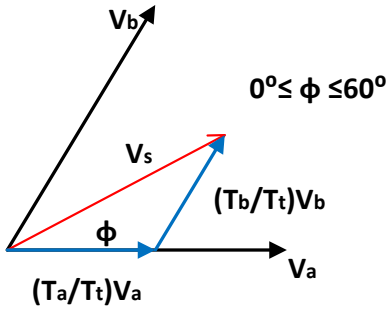

Figure 4-24 Voltage phasor and SVs

As the time duration (T_0, T_a *and* T_b) for each vector is known, the on-time (use S1~S6 to donate) for each semiconductor can be defined regarding to the corresponding schematic as in Figure 4-23, or simply follow the table in Appendix C as given in [80].

Simulink model implementation

As described previously, the procedure to derive the phasor sector and calculate the switching devices on/off time are relatively simple and easy to be modelled. Therefore, only the method to convert these details to actual gate signals is focused here.

Since the switching pattern is symmetrical along the central axis, the first half PWM period is considered first. As the inverter starts from vector V0, all the legs are in zero state. Use IGBT 1 as an example. With an in-cycle counter counting down from $\frac{1}{2}T_t$ to zero, it is the timing to turn on IGBT 1 when the counter's value is lower than half of the IGBT 1 total on-time (i.e. $\frac{1}{2}S_1$). This on state should be held to the end of the PWM first half period. Now, if the counter was made to count from zero up to $\frac{1}{2}T_t$. IGBT 1 should be kept on until $\frac{1}{2}S_1$ is lower than the counter value. To achieve this action, an invert isosceles triangle wave with the same frequency as the PWM is setup as the in-cycle counter. It is to compare with the $\frac{1}{2}S_1$, $\frac{1}{2}S_3$ and $\frac{1}{2}S_5$ while the leg's lower half states are always opposite to the upper one. An example of the phase A leg is shown in Figure 4-25.

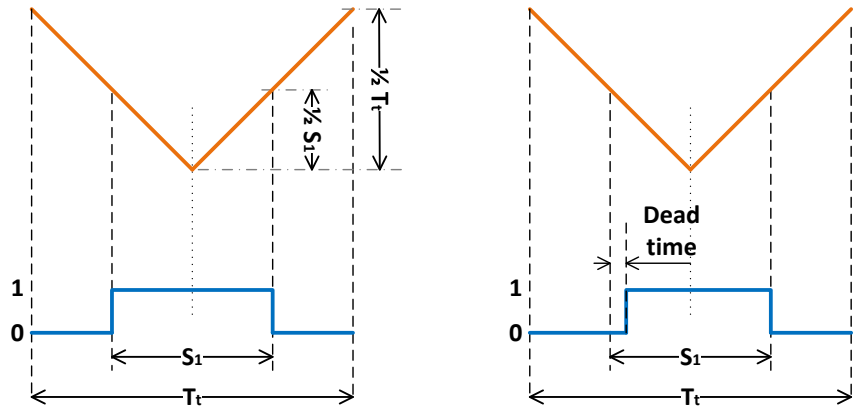

Figure 4-25 Triangle wave to define the switch timing

This method also enable the model to include the dead time when switching on a semiconductor as shown above. In an actual inverter, one switch is turned off on time while the opposite one is turned on with a dead time delay to avoid DC bus short circuit [83]. However, due to the simulation time consideration, the time step used was larger than the dead time as indicated in the hardware specification. This effect was not able to be included in the results eventually.

4.3.3 Inverter power electronics hardware model

For this particular project, as the APU system operating voltage is defined between 350 – 400V and potentially high temperature working environment due to the common cooling circuit of the engine and the motor/generator, the IGBTs were chosen to be used as the power electronics switching devices. The inverter module was developed from the Hybrid Kit for HybridPACK™1 from Infineon Technologies AG [96].

Inverter losses

In a typical H-bridge inverter, a freewheeling diode (or anti-parallel diode) comes with every IGBT in order to prevent potential high voltage damage from the induction load (motor windings) during switching phases. Losses from both devices need to be considered. As current flows through either the transistors or the diodes, the voltage drop across the terminals due to their internal resistance creates heat dissipation i.e. power loss. It is regarded as the conduction loss. This type of loss is duty cycle (ON time) dependent. For the IGBTs, every time its state switches, the voltage and current takes finite time to reach the designated levels. This process generates switching loss which is frequency dominated. Figure 4-26 shows a typical on-off current and voltage transition. For the freewheeling diode, there is also a state change between conducting and blocking current. Before the diode starts to block the reverse current from conducting, there is amount of stored electric charge to be discharged. This period is called reverse recovery time and causes the recovery loss. However, the power loss during the inverse process (blocking to conducting) of the diode are normally neglected [97]. Therefore, the total loss of the IGBT module is:

$$\begin{aligned} P_{loss} &= P_{IGBT} + P_{diode} \\ &= (P_{cond.IGBT} + P_{sw.IGBT}) + (P_{cond.diode} + P_{rec.diode}) \end{aligned} \tag{4-22}$$

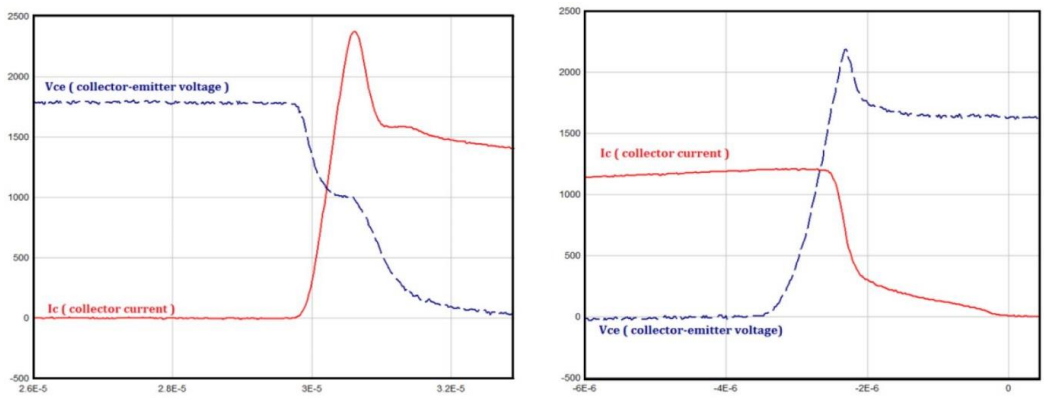

Figure 4-26 Typical switching transistor current and voltage on-off transition [98].

Conduction losses

The power dissipation during the current conduction period is calculated by multiplying the current and the collector-emitter voltage for IGBT or the forward voltage for diode.

$$P_{cond.IGBT} = U_{CE} \cdot I_C = U_{CE0} \cdot I_C + R_C \cdot {I_C}^2 \quad (4\text{-}23)$$

$$P_{cond.diode} = U_D \cdot I_D = U_{D0} \cdot I_D + R_D \cdot {I_D}^2 \quad (4\text{-}24)$$

The R_C and R_D values can be computed from the devices datasheet readings as shown in Figure 4-27 and Figure 4-28. The U_{CE0} and U_{D0} can be conservatively approximated as a result of considering the parameters variation [97]. At 125^0C temperature condition, these four constants are given in the table below. Since the model has access the instantaneous current, the voltage drop can be looked up from the graphs. Alternatively, the average loss could also be calculated through the log of the instantaneous product of the current and voltage drop.

Table 4-2 Inverter IGBT and diode parameters at 125℃

IGBT	$R_C = 2\ m\Omega$
	$U_{CE0} = 0.814\ V$
Diode	$R_D = 1\ m\Omega$
	$U_{D0} = 1.04\ V$

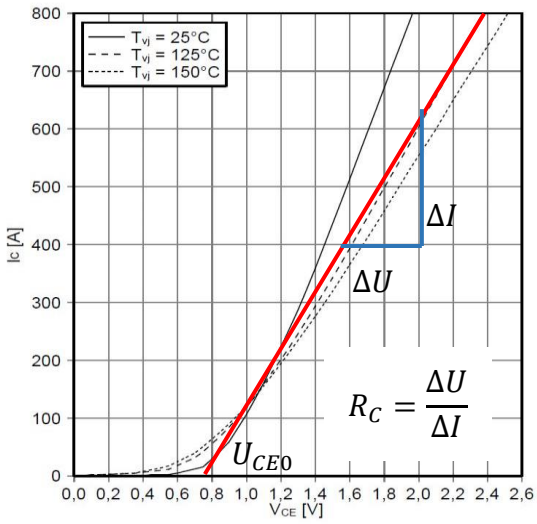

Figure 4-27 IGBT output characteristics [99]

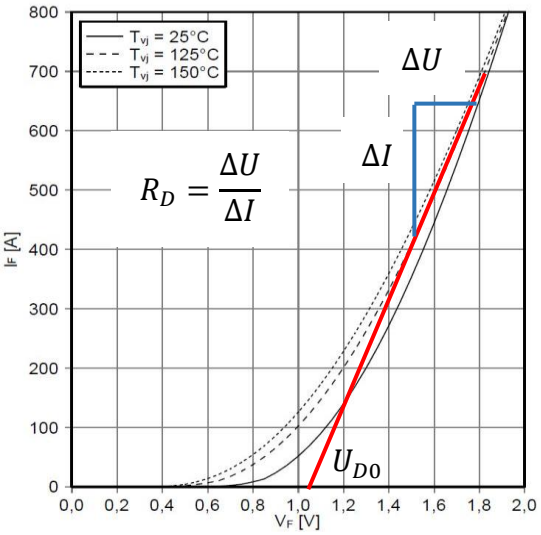

Figure 4-28 Freewheeling diode forward characteristics [99]

Under sinusoidal-PWM scheme, the steady state average power loss is given by [97, 98].

$$P_{cond.IGBT} = U_{CE0} \cdot I_p \cdot \left(\frac{1}{2\pi} + \frac{m_{mod} \cdot PF}{8}\right) + R_C \cdot {I_p}^2 \cdot \left(\frac{1}{8} + \frac{m_{mod} \cdot PF}{3\pi}\right) \quad (4\text{-}25)$$

$$P_{cond.diode} = U_{D0} \cdot I_p \cdot \left(\frac{1}{2\pi} - \frac{m_{mod} \cdot PF}{8}\right) + R_D \cdot {I_p}^2 \cdot \left(\frac{1}{8} - \frac{m_{mod} \cdot PF}{3\pi}\right) \quad (4\text{-}26)$$

Where,

I_p is the peak phase current,

m_{mod} is the PWM modulation index,

PF is the motor power factor.

Switching losses

The switching energy loss E_{on} and E_{off} of IGBT and E_{rec} of diode are normally given in the device specifications as shown in Figure 4-29 and Figure 4-30. For the sinusoidal PWM, during every electric cycle, the current conducting through each IGBT/diode only half of the period time (one half of a full-wave rectifier) though the IGBTs are switching all the time. This can observed in the simulation results as shown in Figure 4-31, which is the upper half of one phase leg in the inverter current pulses. The lower half phase leg has the same pulse magnitude but opposite polarity. To simplify the calculation, [97] suggests that use an equivalent DC current instead of AC to find the switching loss in the device specification data sheet. Since the switching energy loss is the product of voltage and current rather than multiplication of resistance and square of current, the time average value of the 'half sinusoidal impulse' (Equation(4-27)) is used to derive the equivalent DC current rather than the RMS. With the knowledge of inverter switching frequency, the average loss can be calculated by Equation (4-28) and (4-29).

$$I_{dc} = \frac{I_{phase\ pk}}{\pi} \quad (4\text{-}27)$$

$$P_{sw.IGBT} = (E_{on} + E_{off}) \cdot f_{sw} \quad (4\text{-}28)$$

$$P_{sw.diode} = E_{rec} \cdot f_{sw} \quad (4\text{-}29)$$

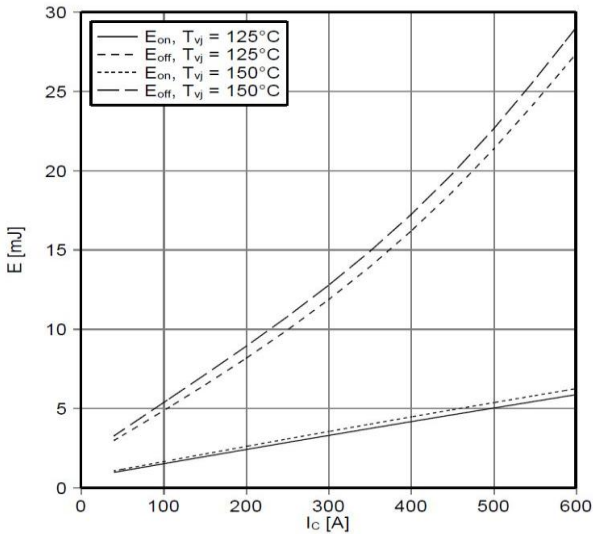

Figure 4-29 Inverter IGBT switching loss characteristic

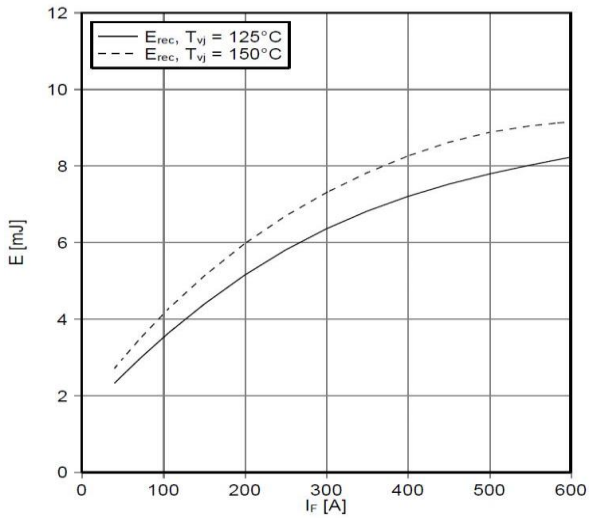

Figure 4-30 Inverter freewheeling diode reverse recovery loss characteristic

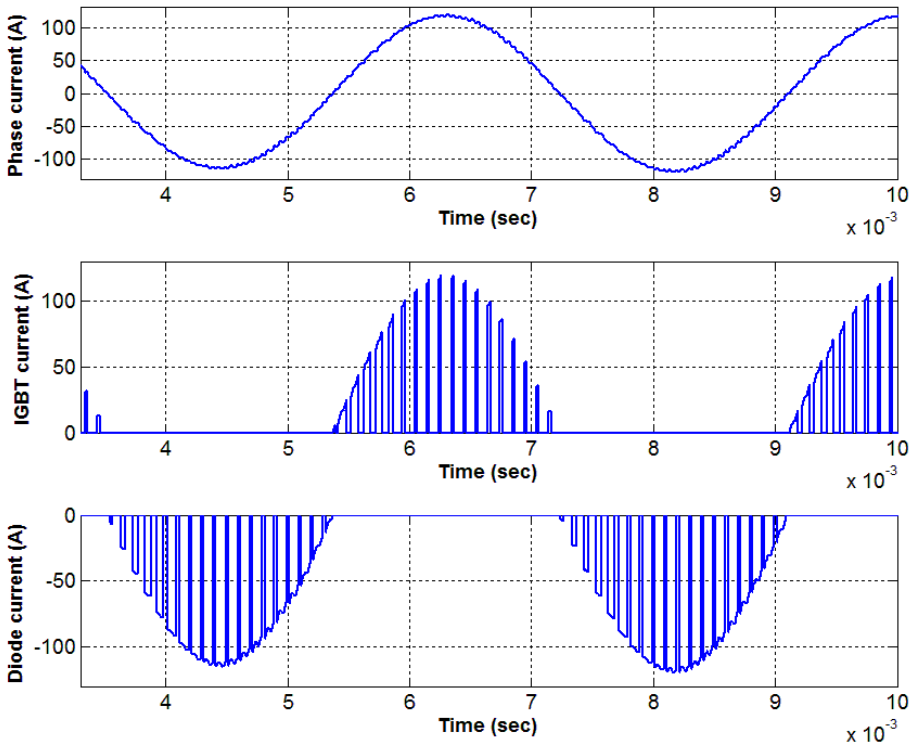

Figure 4-31 Phase current and the upper half IGBT/diode current pulses in the corresponding phase leg

Simulink model implementation

The Simulink model imitates the actual inverter physical structure that contains six power electronics modules as seen in Figure 4-32. The DC terminals were connected to the battery model in parallel with a capacitor. It has a capacity of 300 µF according to the APU hardware specification. The model for the IGBT was the build-in 'IGBT/Diode' Simscape model [100] with the parameter extracted from the hardware manual. The gate control signal was from the inverter control logic model as described previously.

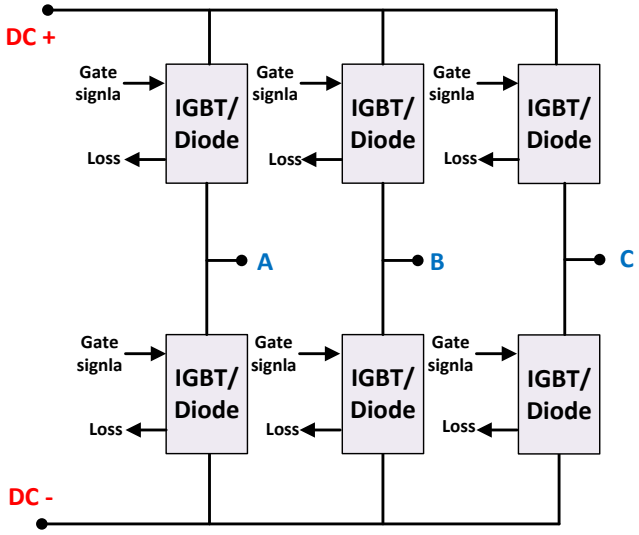

Figure 4-32 Inverter power electronics model schematic

For the loss calculation module, it was based on the analytical calculation as described in the last section. The instantaneous conduction current was from the 'IGBT/Diode' model. Positive value indicates the current flowing through the IGBT while negative values indicates the freewheeling current in the diode. When detecting a current rising or falling edge, the previous step current value will be used to look for the corresponding device switching loss from the tables. All the instantaneous losses were window averaged with a width of two engine revolutions. The temperature reading of the IGBT was found following the coolant temperature well during the bench test due to the direct contact to the liquid. As the coolant temperature setpoint was set to 80°C in the final combined loop for the APU, the power electronics internal temperature for the loss calculation was assumed to be 10 degrees higher which was 90^0C.

Since in the prototype APU the inverter is integrated in the M/G casing, the inverter output leads were directly bolted on the electric machine terminals. Moreover, the integrated cooling circuit is used for the M/G and the inverter, it was rather difficult to separate them and create the space to measure the phase current. Consequently, neither the specific loss type nor the overall loss could be measured to calibrate the

model. However, the loss value simulated still can be used for comparative study in the later control strategies analysis.

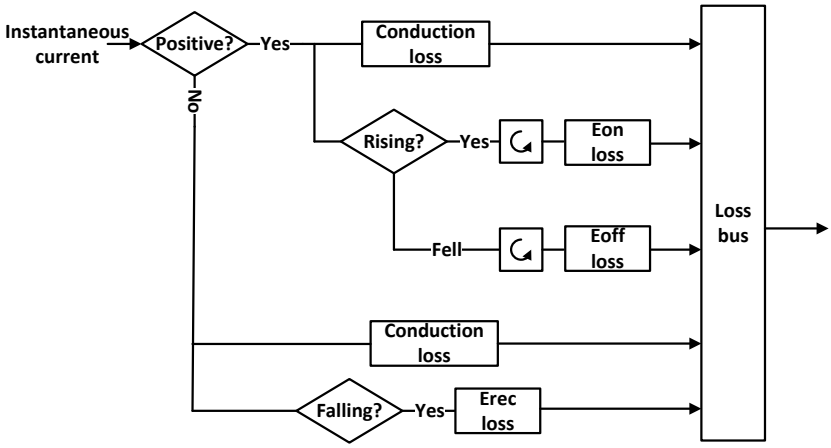

Figure 4-33 IGBT/diode loss model schematic

4.4 Model step response

Since the prototype M/G was targeted to deliver fast in-cycle variable torque, the machine's step response is an important aspect to be checked for model validation and it also laid the foundation for the later Dynamic Torque Control (DTC) pattern design. The first test was the model step response with multiple amplitudes at one speed. The results are plotted in Figure 4-34 with rising demand step change at 0.01s. The rising demand is defined as increasing torque from low to high in motoring mode or decreasing the torque from high to low in generating mode (i.e. negative torque). The falling demand is defined as the opposite torque change direction as the rising torque demand. The initial torque rise slopes of the machine were the same regardless of the target amplitudes at the same speed. This was expected in a real machine.

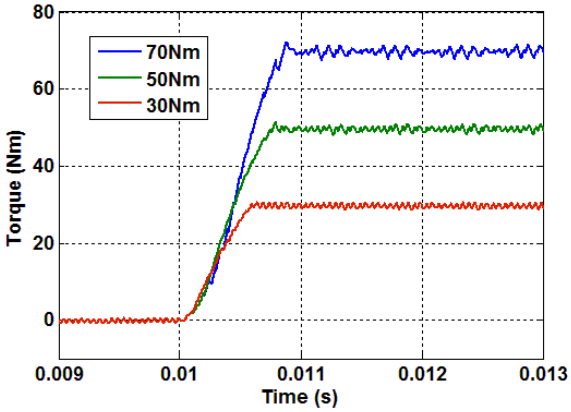

Figure 4-34 Rising step response at 4500rpm

However, the shaft speed does have an effect on the torque response as can be seen in Figure 4-35. With rising torque demand, the higher the speed is, the slower the torque raises. This is due to the DC bus voltage availability. When the speed is high, the controller has to 'reserve' more voltage counteracting with the back-EMF in order to maintain no current in the winding before step change started. Therefore, the DC bus headroom is smaller and less voltage can be used to 'squeeze' out current faster for the transient torque demand. As explained in CHAPTER - 2 inverter control section, for SVPWM, the maximum DC voltage utilisation is $\frac{1}{\sqrt{3}}V_{dc}$. Since the 'excess' voltage is less at 4500rpm, the period of staying at the maximum DC utilisation had to be longer to deliver the same final torque. However, it was found that, with a falling step change torque demand, the result was opposite. The general response was faster when decreasing the torque and the higher the shaft speed the shorter the reaction time as seen in Figure 4-36.

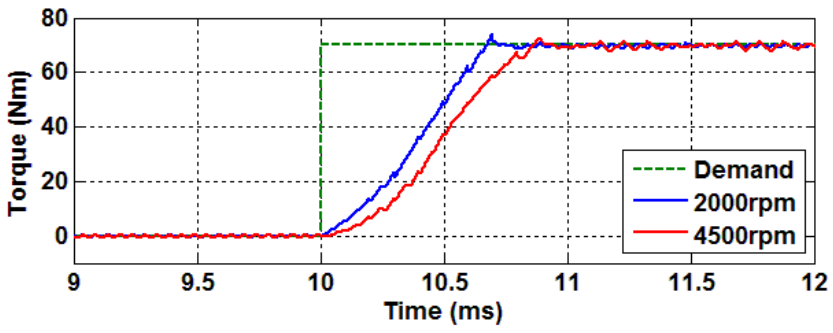

Figure 4-35 Rising step response at 2000rpm and 4500rpm

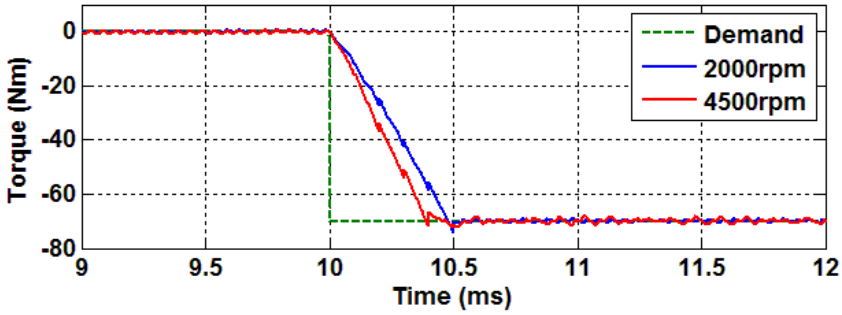

Figure 4-36 Falling step response at 2000rpm and 4500rpm

To explain this point, the single-phase motor equivalent circuit (Figure 4-2) needs to be considered. When increasing the torque, i.e. a current rise, the terminal voltage needs to overcome the back-EMF transiently (ignoring the resistance). However, it is limited by the DC bus voltage as explained earlier. The maximum available voltage exerting on the winding inductance is $|V_{DC\ limit} - e|$. When decreasing torque is requested, the terminal voltage could simply drop below the steady state value to have the current fall. If a very quick response required, such as step falling demand, the terminal voltage could temporarily drop to zero or even change polarity to work together with the back-EMF for 'braking'. In this case the maximum available voltage to drop the current is $|V_{DC\ limit} + e|$. This one-direction only characteristic of the back-EMF leads to the asymmetric step response of a PM machine.

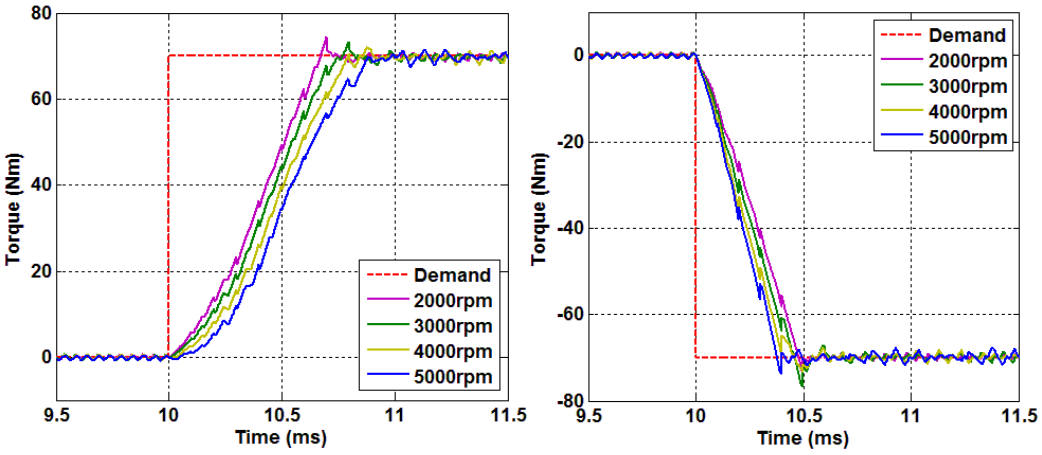

Figure 4-37 Step responses at different speed

Figure 4-37 shows the torque response across the speed range with both rising and falling step changes from zero to motoring and generating peak. The differences between different speeds were actually marginal which may not contribute significant effect on the overall DTC performance. In general, the rising response time is about 0.7ms while falling response is about 0.4ms for a step amplitude of 70Nm. Since the prototype machine was not available to be test individually, these results could not be verified. However, the findings could still be used as references for the later DTC torque pattern design.

4.5 Conclusion

This chapter presented the modelling process of the prototype motor/generator used in the APU. The analytical model of the electric machine was established based on the DQ plane control theory. The 2D FEA model was also created for more detailed machine analysis with consideration of the physical geometries and material characteristics. However, since the system level performance was of interest for this research work, the FEA model, which took much longer time to solve, was not suitable for the real-time co-simulation. The FEA model clearly showed that the winding inductance varied due to the iron saturation at high current load for this particular machine. The current angle selection for MTPA control and the torque performance were significantly affected by this effect. Therefore, it was necessary to use variable inductances rather than constant values in the analytical model.in order to improve its fidelity.

However, caused by the incorrect extrapolation of the user defined material B-H curves by the FEA software, the inductance figures exported were unrealistic leading to underestimation of the machine torque performance at high current load. The L_d and L_q data were calibrated through the extrapolation and interpolation processes to correct the 'crossing' issue. The simulation torque curve showed better match to the test data. At peak current condition (140A RMS), the torque error dropped

from 5.6% to 1.2%. Both MTPA and $\gamma = 30°$ control strategies were applied to the model and displayed similar performance results. This was because at lower load the torque was not sensitive to γ and at high load γ was around 30° when MTPA used. Furthermore, the inverter control logic, which is SV-PWM, and the hardware were also modelled separately. They helped to have a better estimation of the inverter behaviour and its electrical losses.

The final electrical machine and inverter models were simulated with step torque impulse to establish the knowledge of the APU system transient response. The results showed that the reaction time was short when demanding a falling step change than a rising step change. This was mainly due to the one-direction only characteristic of the back-EMF. With a step amplitude of 70Nm, the response time was about 0.7ms for rising action while 0.4ms for falling action. This information is one important foundation for the Dynamic Torque Control pattern design in the next chapter.

CHAPTER - 5
APU System Control Strategy

This chapter presents the development of the dynamic torque control of the M/G in the prototype APU. It starts from a series of simple square torque pulse patterns. The causes for the in-cycle speed fluctuation and electric losses were analysed. These understandings helped to refine the final design of the dynamic torque control. The simulation results of the final torque pattern were presented in last part.

5.1 Introduction

To minimise the APU package size and weight, a low-cylinder-count internal combustion engine is usually used in the APU. As shown in CHAPTER - 3 , this type of engine experiences more severe torque pulsation inherently and consequent speed oscillation due to low firing frequency. This speed and torque fluctuation can lead to noticeable noise and vibration to the passengers which has negative impacts on the driving comfort.

In CHAPTER - 4 , the fast response of the PMSM with vector control algorithm was evaluated. It makes the motor/generator capable of applying counteracting in-cycle torque to reduce the shaft speed fluctuation. To output a comparable level of in-cycle torque as that produced by the engine would require the electric machine to be significantly oversized. From a cost saving perspective, a lower rated machine is preferred. However, to minimise speed fluctuation, the motor/generator needs to be stretched to its performance limit when torque spikes occur. Therefore, the dynamic torque control (DTC) will lead to greater electric losses and thermal behaviour from the M/G. There are crucial aspects that need to be carefully examined when designing the dynamic torque waveform.

5.2 The complete APU system model

The individual simulation models of the IC engine and the M/G have been established as described in the previous two chapters. In this section, the assembly of the complete APU system model is presented.

As explained in the engine modelling section, the mass/inertia that rotating along the crankshaft axis is the exerting target for the torques from both the engine and the M/G. The instantaneous resultant torque variation caused the in-cycle shaft speed fluctuation. The inertia in the case of this APU system was the engine crankshaft and

the electric machine rotor assembly. The data used in the simulation was derived from the CAD model and the measurement values provided by the manufacturers. The transient shaft acceleration can be calculated by Newton's Second Law for rotation ($\tau = I\alpha$). By integrating the acceleration, the shaft instantaneous speed and position can be derived. The information was fed back to both the engine and the M/G to determine the torque outputs for the next time step.

The same as in the actual system, the engine model was in torque/power control while the M/G model was in speed control. The Simulink model schematic is given in Figure 5-1.

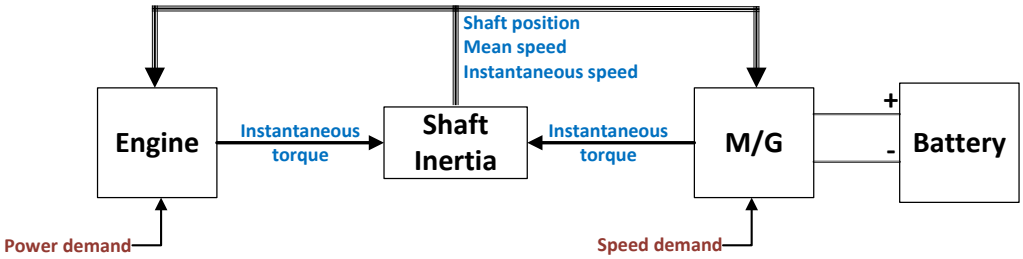

Figure 5-1 APU system model schematic

By compromising the trade-off between simulation time and the result accuracy, the time step was set to one millisecond (1e-6s). The actual inverter drive PWM frequency was 10 kHz. This time step guaranteed 100 sampling points on each carrier wave cycle to determine the power electronics switching points. The switching dead time is normally set for each power electronic device to avoid the short circuit which is caused by the upper and lower transistors on the same half-bridge are closed at same time. However, this fact could not be reproduced by the model with this time step since the dead time is shorter than one millisecond regarding to the hardware specifications [99]. Considering the dead time effect has minor effect on overall torque output and it was not in the major area that concerned in this research, the simulation time step was not reduced further.

Since the mean value of some parameters in the model was more useful than the instantaneous value, such as losses and power, a customised moving average block was added whenever required. Considering the cylinder-to-cylinder variation, the time window width was defined as two engine revolutions.

The battery model used here was the standard lithium-ion battery model provided by the Simulink library [100]. The nominal voltage was set at 350V. The capacity was set to 100Ah while the state of charge was 50%. All the other parameters were left as default.

5.3 Simple square counteracting torque impulse

Since the APU does not connect to the vehicle drive shaft directly, the engine is allowed to operate with wide open throttle (WOT) most of the time to reduce the throttle loss, gaining better efficiency. As discussed in CHAPTER - 3 , the engine indicated torque waveforms (due to the gas pressure) are nearly identical at full load across the speed range. The shaft torque variation is mainly due to the rotating component inertias and their effect have a positive correlation with the speed. Therefore, by studying the cases of speed at both ends of the APU operating range, the inchoate results at extreme circumstances could be established.

With knowledge of the engine in-cycle torque ripples, the dynamic torque pattern design was conducted starting with simple square torque impulses. The impulses' position, amplitude and duration were adjusted to assess their influence on the speed fluctuation. At this stage, the M/G performance limit was not considered i.e. the torque demand amplitude may be higher than its realistic capability in order to explore trend in a wider range. These torque patterns were categorised into six groups and only one feature varied within each group. Two speed conditions were selected: 2000rpm WOT, which is the lowest speed for APU steady state operation, and 4500rpm WOT, which is the mean speed for target rated power. For the convenience

to compare the engine torque and M/G torque, the sign convention from now on for the M/G is defined as *positive for generating/braking torque* and *negative for motoring torque* unless otherwise specified. The following simple square torque patterns were shown in 4500rpm WOT condition only. The designs for 2000rpm WOT were similar consequently only results were presented. All the pattern details were given in Appendix A. The torque pattern naming convention in the following content is that the first number represents the group number while the number after the hyphen is the pattern number in that group.

Torque pattern group No.01

In every shaft revolution, the M/G switches between motoring and generating modes only once. These patterns request the M/G to start generating from the engine top dead centre firing (TDCF) and stops at various crank positions but before 180deg. Then it motors the engine during 180 to 360 deg crank angle with the same mean torque amplitude as the engine during that period. The generating torque amplitude varies depending on the impulse width to give the same overall mean torque as the engine. This group were selected to determine whether a high short generating torque pulse or a low wide pulse during the engine power stroke was more beneficial to the speed fluctuation reduction. The generating torque stop position starts from 180 back to 60 CA deg with 30 deg incremental for torque pattern 01-01 to 01-05. The first three patterns were plotted in Figure 5-2.

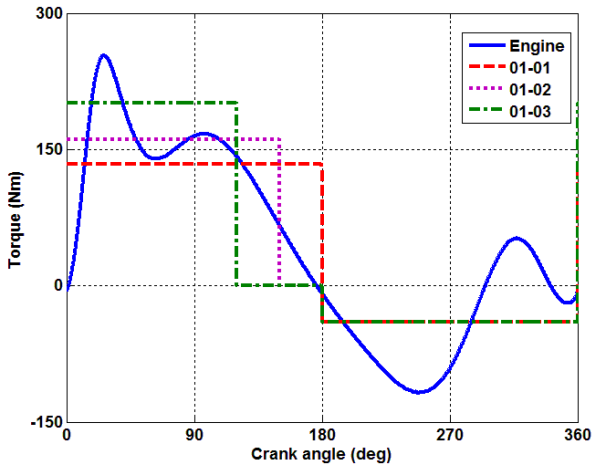

Figure 5-2 Torque pattern group No.01 example plots at 4500rpm WOT

Torque pattern group No.02

Following from series No. 01, the generating/motoring torque switching point was extended beyond 180 deg crank angle while the motoring torque was kept the same amplitude as in group No. 01. This group looks at the influence of a wider period generating torque on the speed variation. The switching position was from 210 to 300 deg with 30 deg incremental for pattern 02-01 to 02-04. The first three were plotted in Figure 5-3.

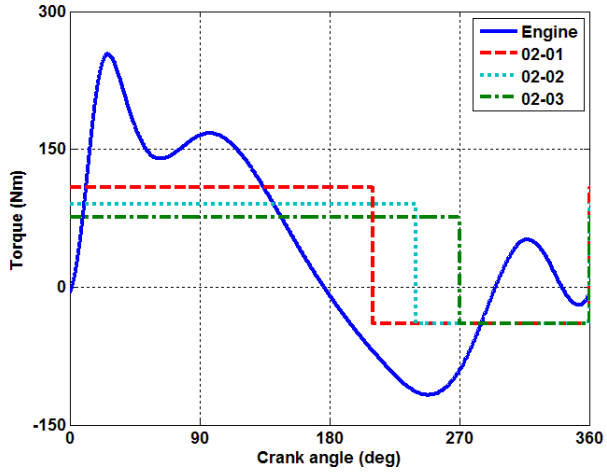

Figure 5-3 Torque pattern group No.02 example plots at 4500rpm WOT

Torque pattern group No.03

The generator and motor modes switch point was moving from 90 to 270 deg with 30 deg incremental for pattern 03-01 to 03-07. Both generating and motoring torque amplitudes were varied and determined by the mean engine torque in the corresponding generating/motoring phases. The first three were plotted in Figure 5-4.

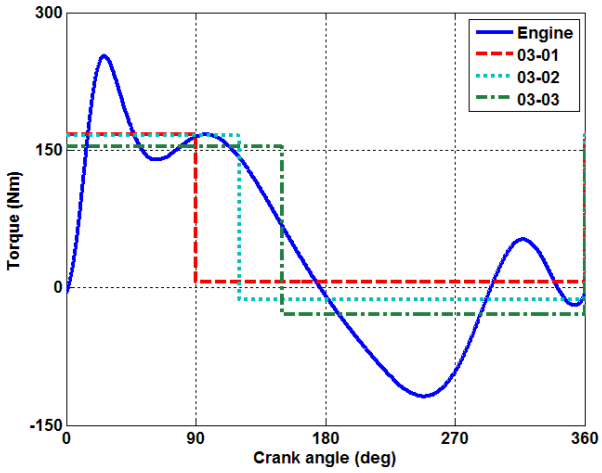

Figure 5-4 Torque pattern group No.03 example plots at 4500rpm WOT

Torque pattern group No.04

Two impulse torques were exerted by the M/G at the two engine torque spikes in one revolution. At 4500rpm, the engine positive torque spike was at 26deg while negative one was at 248deg crank angle. The two M/G torque impulses were centred on these two positions and the pulse width varied from 60 deg to 120 deg with 20 deg incremental for pattern 04-01 to 04-04. Their amplitudes were defined by engine mean torque during 0-180deg and 180-360 CA deg respectively. This group was to check whether injecting the two pulses against the engine torque spikes is beneficial to the speed variation. The first three were plotted in Figure 5-5. At 2000rpm, the two engine torque peak positions were too close to each other which were at crank angle of 27deg and 339deg respectively. This caused the two M/G pulses overlapped. Therefore, this torque pattern group was not applied at 2000rpm condition.

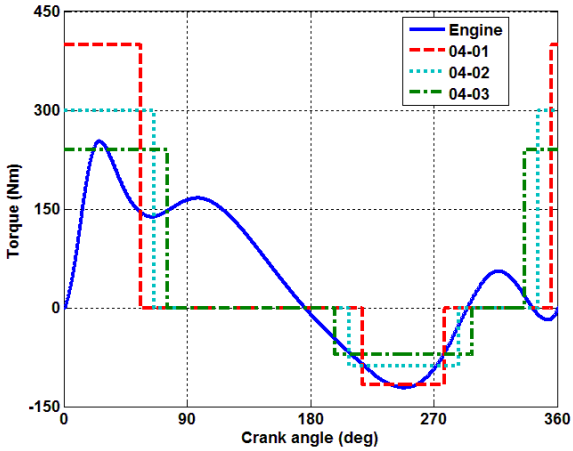

Figure 5-5 Torque pattern group No.04 example plots at 4500rpm WOT

Torque pattern group No.05

This group was a variation of No.04 series. Instead of aligning the generating torque impulse around the engine peak torque position, it was made start from TDCF with the same pulse width as in previous group. The motoring torque pulse stayed at the same position. This change was brought in due to a significant negative speed spike being introduced before the engine reached the peak torque when group No. 04 torque patterns were applied. The impulse width varies from 60 deg to 140 deg with 20 deg incremental for pattern 05-01 to 05-05. The first three were plotted under 4500rpm in Figure 5-6.

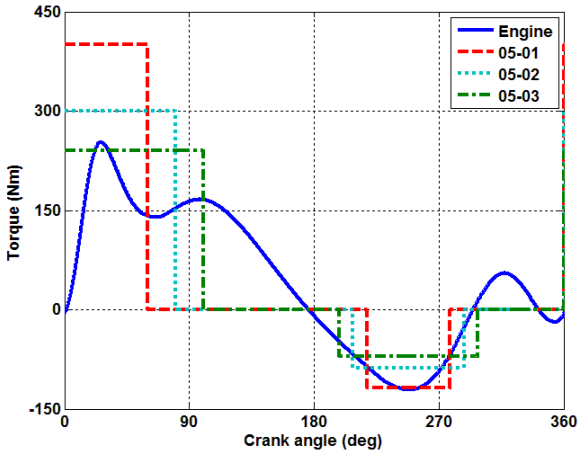

Figure 5-6 Torque pattern group No.05 example plots at 4500rpm WOT

Speed fluctuation results with square impulse torque

The speed fluctuation simulation results of the nine groups simple square torque at 2000 rpm and 4500rpm WOT were plotted in Figure 5-7 and Figure 5-8. Interestingly, either a high amplitude short pulse torque or a wide but low torque pulse was not necessarily helpful to the speed fluctuation reduction. This was indicated by the result knee point of group No.03 and No.05. Therefore, the compromise between torque amplitude and width need to be considered at later detail design stage.

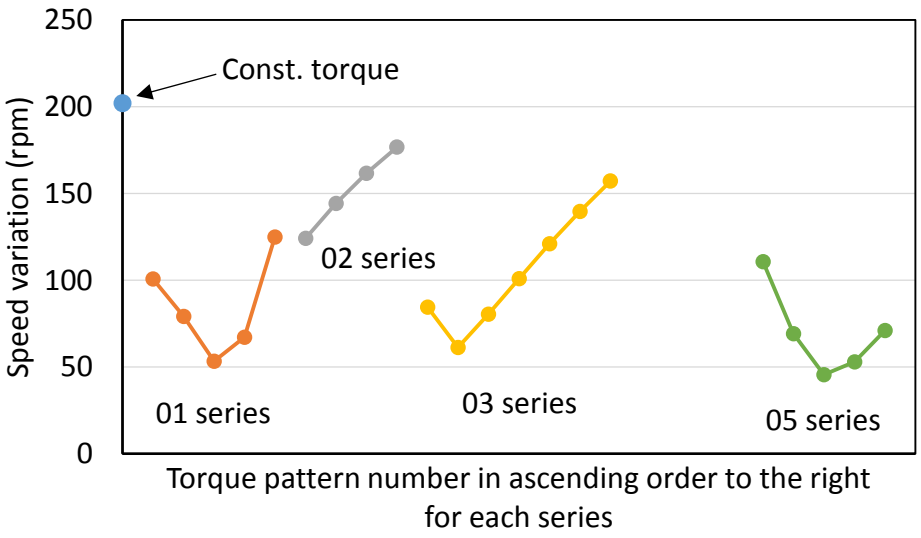

Figure 5-7 Speed fluctuation results at 2000rpm

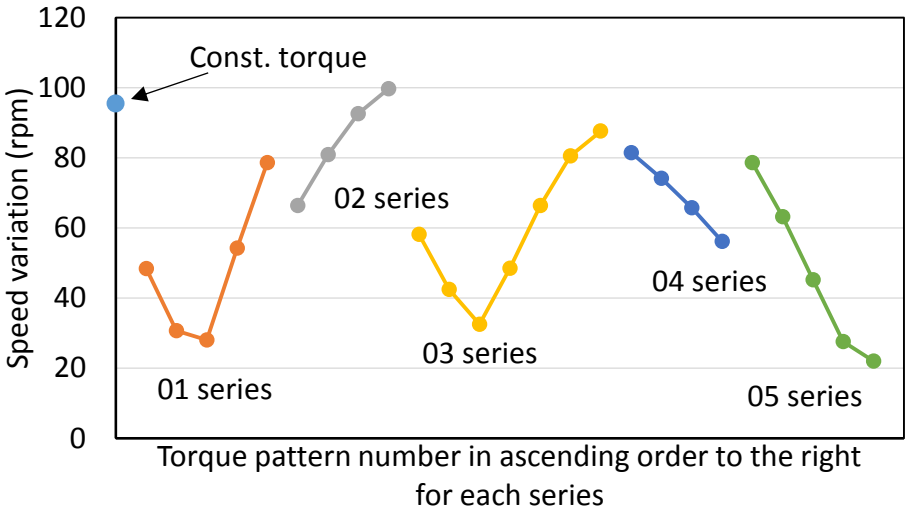

Figure 5-8 Speed fluctuation results at 4500rpm

Another finding observed in the group No.04 and No.05 when comparing the first four patterns that align the counteracting torque pulse to the engine torque peak may not beneficial especially when the pulse width was large. If the counteracting torque started too early before the engine torque raising, a significant negative speed drop could be introduced which even further enlarge the peak-to-peak speed difference. The effect is plotted in Figure 5-9. The 04-04 torque pattern started the torque impulse much earlier than the 05-04 pattern.

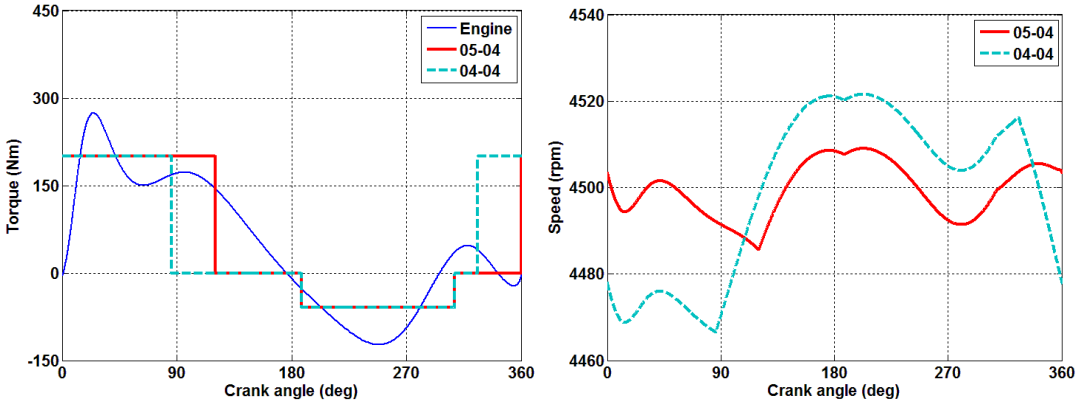

Figure 5-9 Instantaneous torque (left) and speed (right) of 05-04 and 04-04

5.4 Initial torque pattern design with consideration of prototype capability

As per the prototype APU specifications, the M/G peak torque was set to 72Nm (200A peak phase current). Not all the above torque patterns were feasible for the M/G to achieve. A new group of torque patterns (Figure 5-10) was design by taking the consideration of the M/G capability and the findings from previous results. The APU was targeted to operate between 4000rpm and 5000rpm most of the time. Therefore, the 4500rpm WOT condition was primarily simulated here and these patterns were specifically modified and used for later on M/G electric loss analysis.

The first one (06-01) was a simple square pattern. The M/G torque was demanded to follow the engine torque trace until reached its limit and stayed at the peak. When the engine average torque from the TDC fell to 72Nm, the M/G switched to motoring mode until the end of the revolution.

In the second pattern (06-02), the M/G ramped down from peak generating torque to a motoring torque at about 180 CA deg position. The slope followed the engine torque gradient during the engine negative torque pulse period. When the M/G climbing back to the generating, it stays at about 50Nm which is the minor engine torque spike amplitude just before the end of the cycle. The M/G was not design to follow the engine torque trace exactly even though the torque was within the M/G capability. Some adjustments have to be done in order to maintain the mean torques of the M/G and the engine equal, in the case of a APU application.

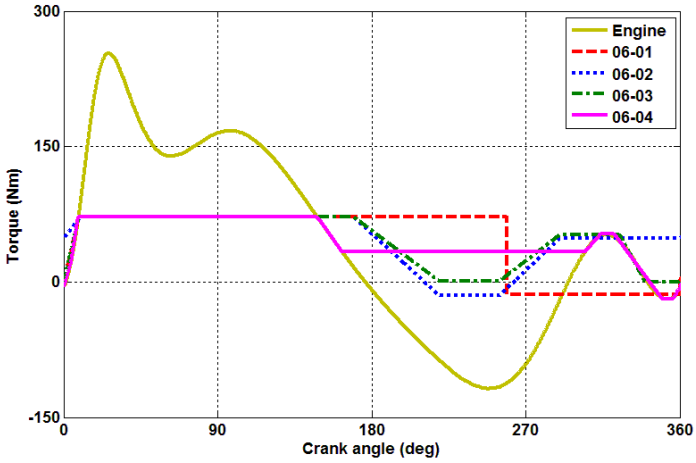

Figure 5-10 Torque pattern 06-01 to 06-04.

The third pattern (06-03) was made to follow the minor torque variation during the last 90 deg of the engine revolution. In addition, the M/G was limited not to motor the engine i.e. saturated at 0Nm. Consequently, the torque demand during 180 to 270 deg was adjusted to make sure the mean torque was equal to the engine.

The last pattern (06-04) was design to follow the engine torque. However, again, in order to meet the mean torque requirement, during the engine negative torque period, the M/G was still braking (generating) but with a low torque amplitude.

Speed fluctuation results with group No.06

The speed fluctuation results of group No.06 is given in Table 5-1. No. 06-01 approved again that the speed fluctuation reduction was not optimised when a high generating torque presented for too long. Another finding was that within the electric machine torque boundary, it appeared that the speed fluctuation was limited to around 83rpm in the case that of 72Nm maximum M/G torque regardless of the torque pattern changes in the engine compression stroke (180 – 360 deg) as long as the peak generating torque terminated in time.

Table 5-1 Group No.06 speed fluctuation results

Pattern No.	06-01	06-02	06-03	06-04
Speed fluctuation (rpm)	97.5	82.3	82.6	83.4

To understand why the wide period of generating torque was not preferred, the in-cycle speed traces of 06-01 and 06-04 were plotted in Figure 5-11. In order to give the same mean speed (4500rpm), the two traces started from different instantaneous speed. As shown, the speed rise to the peak when the engine torque and M/G torque traces intersected which was the same for both cases. The difference, which introduce more speed oscillation, was that the speed was pushed back too much with long high generating torque period. Hence, during the motoring phase the speed has to be pulled back to where it stated to maintain the average speed. This also explained the similar results from the last three patterns although they have different designs in the second half of the engine revolution. As shown in Figure 5-12, in the second half revolution, the M/G is only aiming to pull back the speed however the torque pattern was, as long as the mean torques of the M/G and engine were equal.

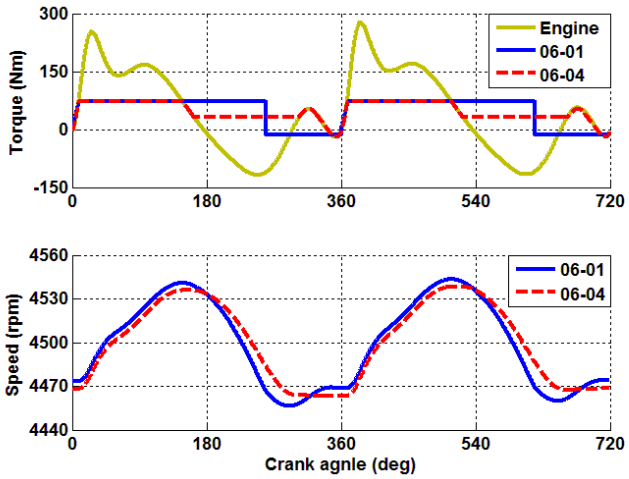

Figure 5-11 Torque and speed comparison between 06-01 and 06-04

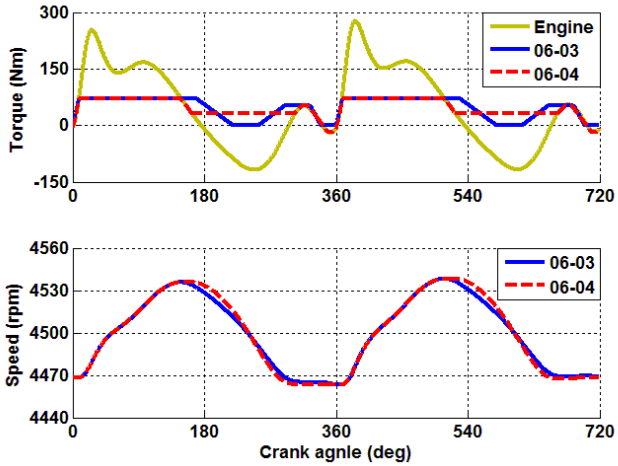

Figure 5-12 Torque and speed comparison between 06-03 and 06-04

The 'saturated' speed fluctuation improvement can be explained by the impulse and momentum principle. Use the 06-04 pattern as an example. If plotting the resultant torque exerted on the rotating inertia, at the beginning and nearly the end of the power stroke, the M/G is able to follow the engine torque. The torque difference in the middle section results in an energy difference (red shaded area in Figure 5-13) which accelerates the crankshaft. Dividing this impulse area by the shaft inertia, the final speed rise could be derived. With a properly designed torque pattern during the second half of a revolution (180 – 360 deg), the best case is to pull back the engine speed to the same level as at the beginning without introducing extra negative speed fluctuations. In other words, in the second half revolution, all the excess energy should be absorbed by the negative shaded area (blue) without having more positive and negative energy fluctuations.

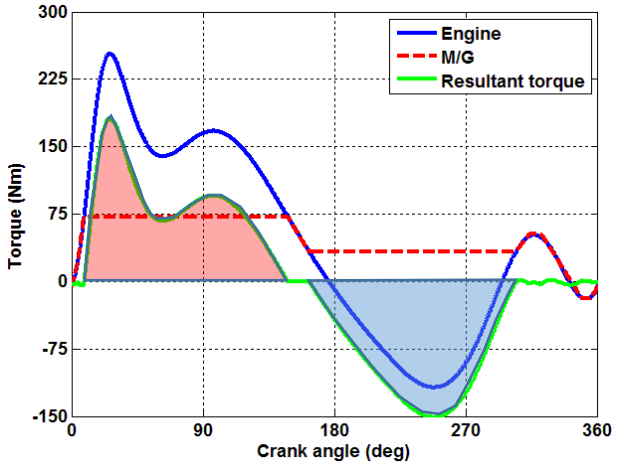

Figure 5-13 Resultant torque exerted on the crankshaft 06-04

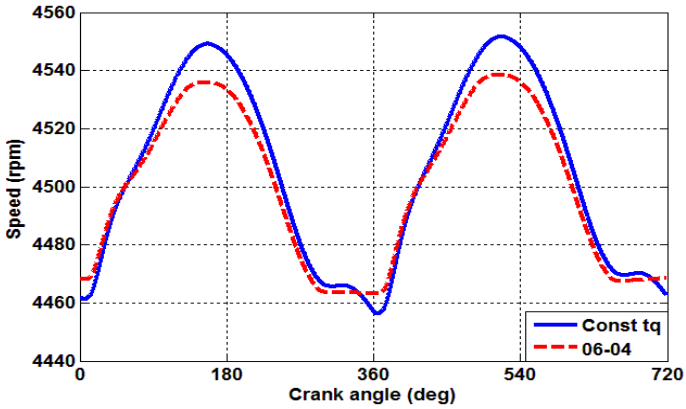

Figure 5-14 In-cycle speed fluctuation of constant torque and 06-04 at 4500rpm WOT

With knowledge of where the speed fluctuation arise, another three torque patterns were defined to verify the above analysis. Their peak torque were deliberately set higher than the M/G actually can achieve by removing the hard limits in the simulation model. Peak torque of 90Nm (06-05), 95Nm (06-06) and 104Nm (06-07) were used. With 104Nm peak torque, it allows the M/G to stay zero torque during part of the engine compression stroke but still maintaining the same mean torque. The speed fluctuation results against the M/G peak torque was plotted in Figure 5-15. When the torque pattern was optimised, as expected they displayed a linear relationship.

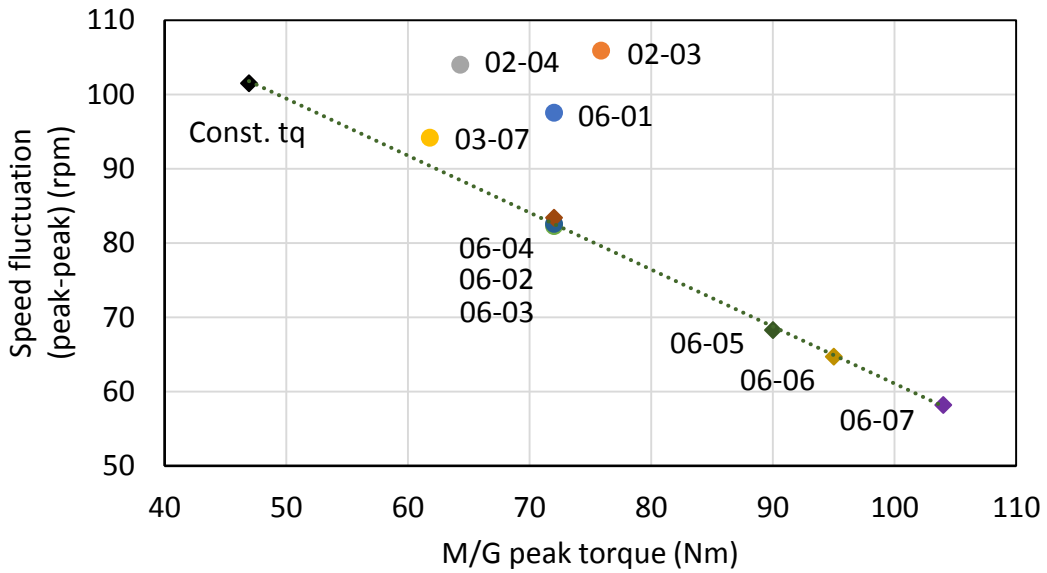

Figure 5-15 Speed fluctuation results against the peak M/G torque

A conclusion could be drawn here is that, when the electric machine is known, the optimal peak-to-peak speed fluctuation could be roughly predicted. However, these results were derived by assuming that the M/G is in ideal condition and no failure would occur when outputting the peak torque for a long period. The fast in-cycle varying torque and current will affect the electric losses and thermal behaviour from the M/G comparing to a constant torque demand. They are the crucial factors to the system efficiency. Another potential factor affecting the DTC performance is that as the motor torque capability increases, the rotor inertia could also increase due to more PM content required. Therefore, the curve slope towards to the right hand side may be steeper as the M/G peak torque rises. However, this factor is beyond the scope of this study, its influence will not considered in this study.

5.5 Motor/generator electric losses analysis

There are three main types of electric losses typically considered in a electric machine which are the copper loss, iron loss and eddy current loss. In [53, 101, 102], the authors introduced the formulae to derive these losses. However, especially the iron loss and eddy current loss, they are rather difficult to be calculated analytically

and the method only provide a simplified way to make an estimation. Therefore, the finite element (FE) tool were used to obtain relatively more accurate results. The analytical methods here were used to analyse the correlation of the influencing factors and the loss results.

5.5.1 Winding loss

The loss occurred in the winding coils are primarily the copper loss i.e. the loss in the form of heat generated due to the resistance of the inductors. It is considered as the dominated part in an electric machine loss, especially at the low frequency condition, i.e. low shaft speed [103]. The loss is governed by Joule's first law as

$$P_{copper} = {I_{rms}}^2 R \tag{5-1}$$

Where,
I_{rms} is the rms value of the current in the conductor;
R is the conductor resistance.

As given in [53], when DC current passes through the windings, the resistance per phase is calculated as

$$R_{dc} = \frac{N l_{avg}}{a_p a_c \sigma s_a} \tag{5-2}$$

Where,
N is number of turns per coil,
l_{avg} is the average length per turn,
a_p is the parallel current paths,
a_c is the number of parallel conductors,
σ is the copper conductivity at certain temperature,
s_a is the conductor cross section area.

Based on the general copper conductivity data given in [104], a third-order polynomial was fitted to determine the copper resistance at arbitrary temperature.

However, some physical parameters used in above equation was difficult to accurately determined, such as the average wire length per turn. Consequently, some idealised assumptions were made based on the actual machine physical dimensions as explained below.

In this IPM, every coil has 56 turns while each phase has four parallel branches. The copper wire is a solid rectangular bar (1*3 mm) rather than stranded. The stator stack length is 45 mm and the tooth end width is 19 mm. By considering the wire thickness and bending radius, the straight wire was assumed 4mm longer than the slot and the end windings were assumed as semicircular with diameter of 30 mm as shown in Figure 5-16. The calculated phase winding DC resistance at 20°C was 17.53mΩ.

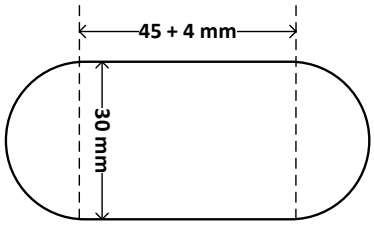

Figure 5-16 Average single coil turn assumption

With current lab facilities, the machine phase resistance can only measure at room temperature (~20°C). An LCR meter was used to read the resistance across two motor terminals. The readings are given in Table 5-2. Since the phases were in star connection, the meter reading was for two sets of phase coils in series. By assuming that all three phase windings were perfectly identical and averaging all the readings (except an obviously wrong one), the phase winding dc resistance measured was 17.63mΩ. These two matching results from calculation and measurement indicated the assumptions made above was plausible.

Table 5-2 Phase resistance measurement

Test current	0.1A		
Measurement No.	Line 1-2	Line 2-3	Line 1-3
	mΩ	mΩ	mΩ
1	37.9	37.6	31.5
2	37.0	31.3	37.9
3	31.6	36.6	36.5
4	37.5	37.6	32.1
5	37.1	31.1	37.6
6	31.9	36.8	36.9
7	~~90.9~~	36.8	31.5
Mean	**35.50**	**35.41**	**34.86**
Mean phase resistance: 17.63 mΩ			

However, the windings in a synchronous machine conduct AC current rather than DC. The skin effect has to be taken into account, especially when thick wire is used, as in this case where the wire was not stranded. The AC current in a conductor tends to cluster to the surface area (skin) rather than distributed evenly across the entire section. The higher the frequency, the more obvious the effect on decreasing the winding conductivity which leads to more copper loss [103]. The conductor skin depth can be derived with formula

$$\delta = \sqrt{\frac{1}{\pi f \mu_0 \sigma}} \tag{5-3}$$

Where,
f is the electrical frequency;
μ_0 is the vacuum permeability;

The AC resistance skin effect factor for the conductor in a stator slot of a double layer winding, as the setup in this prototype M/G, is given in [53].

$$k_R = f(e) + [\frac{{m_{sl}}^2 - 1}{3} - \frac{3\left(1 - \frac{Coil\ span}{Pole\ span}\right)}{16}{m_{sl}}^2]g(e) \quad (5\text{-}4)$$

$$f(e) = e\frac{\sinh(2e) + \sin(2e)}{\cosh(2e) - \cos(2e)} \quad (5\text{-}5)$$

$$g(e) = 2e\frac{\sinh(e) - \sin(e)}{\cosh(e) + \cos(e)} \quad (5\text{-}6)$$

$$e = \frac{h}{\delta}\sqrt{\frac{b}{b_s}} \quad (5\text{-}7)$$

Where,
h is the conductor height in the slot;
$\frac{b}{b_s}$ is the slot width fill factor (0.9 was assumed here);
$m_{sl} = 2$ for the two layer winding.

Once k_R is calculated, the total coil skin effect factor is

$$k_{skin} = \frac{k_R + l_{out}/l_{in}}{1 + l_{out}/l_{in}} \quad (5\text{-}8)$$

$$l_{avg} = 2(l_{out} + l_{in}) \quad (5\text{-}9)$$

Where,
l_{in} is the conductor length in the slot,
l_{out} is the end connection length of a coil.

The copper loss in a three-phase winding can be approximated by

$$P_{copper} = 3 \cdot {I_{rms}}^2 R_{dc} k_{skin} \quad (5\text{-}10)$$

Since the normal operating temperature of the motor winding is in a relative small range, the calculated winding AC resistance for this particular M/G is plotted between 100 and 200 Celsius with quadratic curve fitted (Figure 5-17).

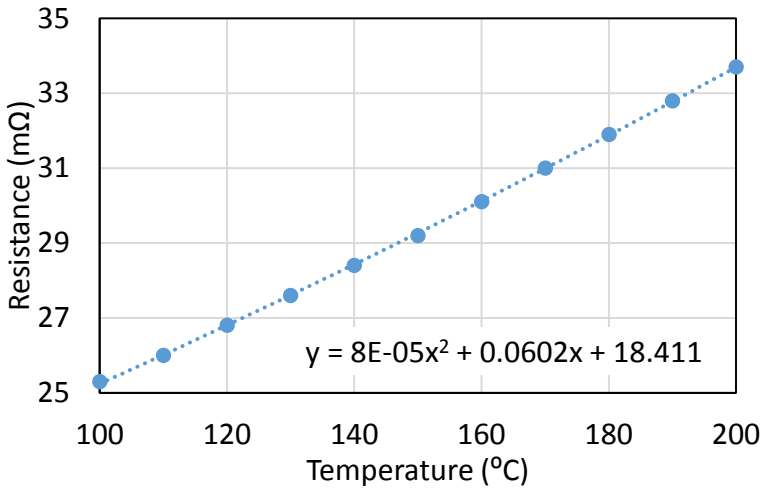

Figure 5-17 Winding AC resistance at different temperature

The prototype M/G has an infrared sensor to measure the stator temperature. The test data showed that during the steady state with constant torque output from the M/G the stator surface temperature was at about 125^0C. Since the entire stator was cured with thermal conducting material, the mean temperature of the copper windings were assumed to be at 130^0C. At this condition, the phase resistance interpolated from the curve fitting equation is 27.6 mΩ.

The copper loss is closely related to square of the effective current (i.e. rms value). Since it contributes significantly to the overall electric loss, when designing the DTC pattern, the high torque demand region should be kept as short as possible in order to minimise this type of loss.

5.5.2 Stator core loss

The loss occurring in the stator yoke is called iron loss which is the second largest loss component after the copper loss [101]. It is caused by the magnetic hysteresis loop of the material and the eddy current generated by the alternating field. The ferromagnetic material normally used in the stator and rotor yoke is called soft magnetic iron as opposite to the 'hard' permanent magnet, because it barely retains the polarity after the external magnetic field is removed. This is a favourable property for

the coil field since it is easier to push flux through rather than against a large amount of remnant field. However, the stator core experiences high frequency alternating polarity field. When the external field changing direction, the flux density in the iron follows a loop path rather than a single line. This is the magnetic hysteresis loop which can be visualised in the material B-H curve (Figure 5-18). The width of this loop is called coercivity. The wider the hysteresis loop is (high coercivity), the 'harder' the magnetic material is (e.g. permanent magnet) and the more energy is needed to reverse the field direction.

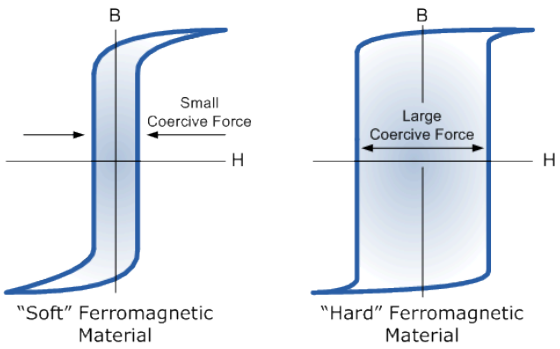

Figure 5-18 Typical B-H curves [105]

There are some methods that can calculate the specific iron loss (watts per kilogram) as reviewed in [106]. Two of them will be introduced here which both are based on the Steinmetz Equation. The first one is the Generalised Steinmetz Equation (5-11) with the knowledge of the instantaneous flux density and the change rate of the flux density.

$$P_{loss} = \frac{1}{T}\int_0^T C_{SE}\left|\frac{dB}{dt}\right|^{\alpha} |B(t)|^{\beta-\alpha} dt \tag{5-11}$$

Where,
C_{SE} is a constant that is defined by the material loss property;
B is the flux density.

Another approach based on the Steinmetz Equation is to have the iron loss divided into eddy current loss and hysteresis loss and additional excess loss [106, 107].

$$P_{loss} = K_h f B^2 + K_c f^2 B^2 + K_e f^{1.5} B^{1.5} \quad (5\text{-}12)$$

Where,

f is the frequency;

K_h, K_c and K_e are the coefficients for the hysteresis loss, eddy current loss and excess loss coefficients respectively.

The coefficients above are all the based on the curve fitting of the actual material loss measurement data at a range of frequencies. The test data is normally provided by the manufacturers. The electric steel used in the prototype machine is in grade of M235-35A. The material data sheet is available in [108]. The coefficients can be extracted from the FEA software when the material loss data is provided. As pointed out in the literatures [101, 106, 107], the above formulae assumes ideal sinusoidal flux presents in the material, however, in the real motor, the flux contains high order harmonics which may make the analytical results lower than the actual loss.

According to the equations above, the loss is highly dependent on the flux density and its rate of change. The Ampere's Law shows that the flux density is proportional to the field intensity (H) which is the product of current (i) and the number of turns (N) (Equation (5-13) (5-14)) for a solenoid. This indicates that the winding current again influences the iron loss.

$$B = \mu H \quad (5\text{-}13)$$

$$H = Ni \quad (5\text{-}14)$$

When a constant torque demand is applied on the M/G at steady state, the field variation and the rate of flux density change are close to a fixed frequency sinusoidal wave. However, when the DTC is activated, some in-cycle rapid field change will be introduced. It can lead to a very high flux density change rate (frequency) and consequently high instantaneous iron loss. Therefore, the DTC pattern is preferred to have mild in-cycle torque alternation to improve the electric machine efficiency.

5.5.3 Losses in the permanent magnets and rotor core

The permanent magnet is not considered as a good electrically conductive material. However, its resistance is not so significant that the eddy current effect can be ignored especially in a slotted machine [53]. The slot opening on the stator changes the flux loop permeance. When the rotor magnets sweeps along the stator tooth, the flux lines always try to find the lowest reluctance path. The alternating flux causing local field change hence generating eddy current in the magnets. The fundamental frequency due to the slot opening experienced by the rotor magnets is

$$f_{sl} = s\frac{rpm}{60} \tag{5-15}$$

Where,
s is the number of slots.

The analytical equation for the eddy current loss in the PMs are given in [53, 102] as follow:

$$P_{PM} = \frac{1}{2} a_{Rv} k_z \frac{|\alpha|^2}{\beta^2} \left(\frac{B_{sl}}{\mu_0 \mu_{PM}}\right)^2 \frac{k_v}{\sigma_{PM}} S_{PM} \tag{5-16}$$

Where,
μ_0 and μ_{PM} are the permeability of vacuum and the magnet,
σ_{PM} is the magnet conductivity,
S_{PM} is the magnet active surface area,
k_z is a constant depends on the slot pitch and rotor length.

The other coefficients in Equation (5-16) can be calculated with the following equations.

$$k_v = \sqrt{\frac{2\pi f_{sl} \mu_{PM} \sigma_{PM}}{2}} \qquad \propto \ {f_{sl}}^{1/2} \tag{5-17}$$

$$\alpha = (1 + j)k_v \qquad \propto \ {f_{sl}}^{1/2} \tag{5-18}$$

$$\beta = \frac{1}{\pi D n f_{sl}} \qquad \propto \ {f_{sl}}^{-1} \qquad (5\text{-}19)$$

$$a_{Rv} = \frac{1}{\sqrt{2}} \sqrt{\sqrt{4 + (\frac{\beta}{k_v})^4} + (\frac{\beta}{k_v})^2} \qquad \propto \ {f_{sl}}^{-3/2} \qquad (5\text{-}20)$$

B_{sl} is the alternating flux that exerts on the magnets. It is calculated as

$$B_{sl} = \beta_{sl} k_c B_{max} \qquad (5\text{-}21)$$

Where,

β_{sl} and k_c are the factors a few machine physical geometries, such as the slot opening, slot pitch, magnet thickness, etc.

B_{max} is the peak air gap flux density.

The above equations unveils that the three parameters are frequency dependent. By substituting Equation (5-18), (5-19) and (5-20) into (5-16) and manipulating the equation, the following correlation can be derived. A similar term was seen in the iron loss Equation (5-12). However, the air gap flux, i.e. the load, influences the loss rather than the intrinsic field change since, for the hard magnet, it varies slightly when moving along the 'flat' part of the BH curve when operating in the designated region. This also explains why the hysteresis loss is normally ignored for PM (the minor hysteresis loop was not considered here).

$$P_{PM} \propto {f_{sl}}^2 {B_{max}}^2 \qquad (5\text{-}22)$$

The loss in the rotor iron is mainly the eddy current loss due to the same cause as in the PMs. However, the effect on the rotor yoke is much less resulting less significance on its loss. As shown in [53], the rotor eddy current loss equation is similar to the one for the magnets. However, with coefficients regarding to the rotor yoke material properties and physical dimensions. The same correlation between its eddy current loss and the frequency together with the flux density is obtained.

$$P_{rotor} = \frac{1}{2} a_{Rr} k_z \frac{|\alpha|^2}{\beta^2} \left(\frac{B_{sl}}{\mu_0 \mu_r}\right)^2 \frac{k_v}{\sigma_r} S_r \tag{5-23}$$

$$P_{rotor} \propto f^2 {B_{max}}^2 \tag{5-24}$$

Clearly, the eddy current loss is closely related to the frequency and stator field strength. This is the same as for the stator iron loss. Therefore, the mild torque amplitude change is crucial to control the eddy current loss.

5.6 FEA electrical loss results with DTC

The analytical calculations introduced in the last section can only give an approximation of the losses and pure sinusoidal flux or current waveforms were assumed for simplification. This is not ideal, especially for the case of DTC where transient in-cycle variation occurs. As *Hendershot and Miller* wrote [101], whenever possible, the calculation should be correlated to precise test data. Since the electric loss is very difficult to measure on the APU test rig due to the physical restrictions of the prototype machine, the FEA package was used to obtain a loss indication of the machine. Although each type of loss in the model could not be validated individually using test data from the APU laboratory setup, and the absolute loss value may not be close to the reality, the FEA still can provide comparable results between different patterns. This provides guidance for the final DTC torque demand waveform design.

The software used for the loss calculation was the ANSYS Maxwell. The core loss model inside is the Steinmetz Equation based model as explained previously. When defining the electric steel material properties, the BP Curves (flux versus power loss) at various frequencies were used to extract the model coefficients. These loss data were from the material supplier. Figure 5-19 shows the settings in the software.

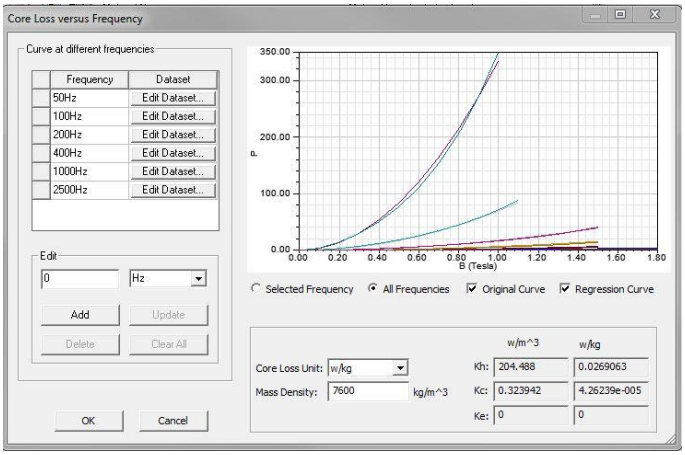

Figure 5-19 BP Curves for the core loss calculation

For the Eddy current loss, an Ohmic loss model in the software was used. In order to have the eddy current effect on the magnets, they were assigned with current excitation but with zero current. The Ohmic loss equation is

$$P_e = \int_{Vol} \frac{J \cdot J^*}{2\sigma} dVol \tag{5-25}$$

Where,
J is the current density,
J^* is the complex conjugate of the current density,
σ is the material conductivity.

For the copper loss, since the FEA model is in 2D, it was underestimated significantly through the software internal calculation. Fortunately, the copper loss is relatively easy to derive when assuming the winding resistance is a constant (since there is no thermal model to capture the dynamic temperature effect on the winding). Therefore, the Simulink model used the instantaneous current to obtain the instantaneous copper loss. The moving window averaged value (over two engine revolutions) was delivered by the model.

The torque patterns designed in previous section were first applied in the Simulink APU model to generate the corresponding instantaneous phase current. The current data was then imported to the FEA model. This approach makes it possible to

include the current ripples and non-perfect sinusoidal current waveforms introduced by the power electronics and the M/G transient behaviour in the FEA model. Since there is no geometric setup in the Simulink analytical model for the electric machine, the cogging torque due to the tooth and rotor PMs could only be reflected in the FEA results. The torque for Pattern 06-04 from the FEA model and the demand are compared in Figure 5-20 as an example. Figure 5-21 shows the in-cycle speed fluctuation at 4500rpm WOT with two different torque sources (FEA and Simulink). Since the cogging torque ripple is in high frequency, it does not have a significant effect on the instantaneous speed. To reduce the computation time, the FEA model was only used for losses analysis while the Simulink model was used for the speed variation determination.

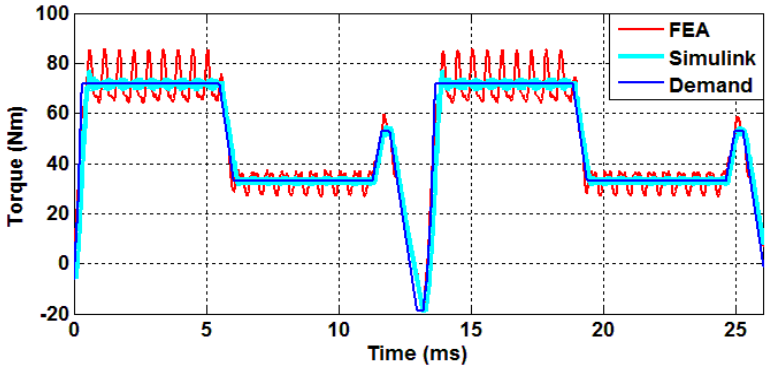

Figure 5-20 Torque results for Pattern 06-04 from the FEA model and the analytical Simulink model

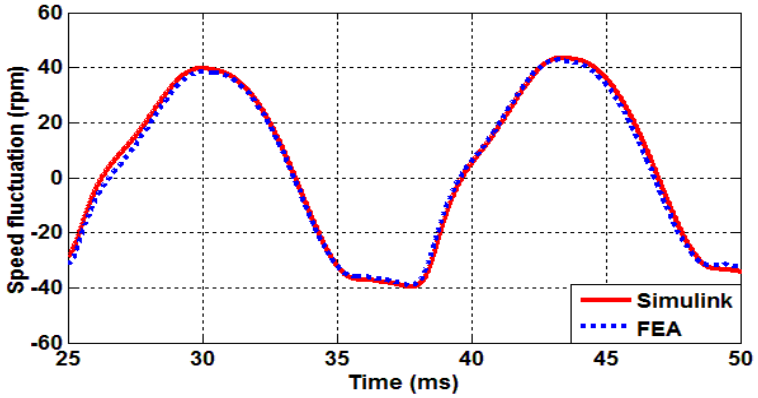

Figure 5-21 Speed fluctuation results for Pattern 06-04 from the FEA model and the analytical Simulink model

All the torque patterns that were within the M/G capability were applied to the FEA model. The loss results are shown in Table 5-3 and Figure 5-22. Clearly, the first three simple square pulse torques are not optimised for either the loss or the speed fluctuation. Consequently. Detailed analysis will be concentrated on Group No. 06.

Table 5-3 Electric loss results for different torque patterns

Patterns No.	Copper loss (W)	Stator loss (W)	Rotor loss (W)	PM loss (W)	Total loss (W)	Speed fluctuation (rpm)
Const. tq	504.4	163.8	32.6	111.7	812.5	101.5
02-03	1230.0	195.4	55.9	212.6	1693.9	105.9
02-04	867.4	185.4	49.2	159.4	1261.4	104.0
03-07	707.1	174.0	38.4	143.3	1062.8	94.2
06-01	992.7	183.2	46.6	175.9	1398.4	97.5
06-02	802.1	166.7	40.3	134.0	1143.1	82.3
06-03	773.6	172.5	38.9	156.1	1141.1	82.6
06-04	703.5	173.1	38.2	156.1	1070.9	83.4

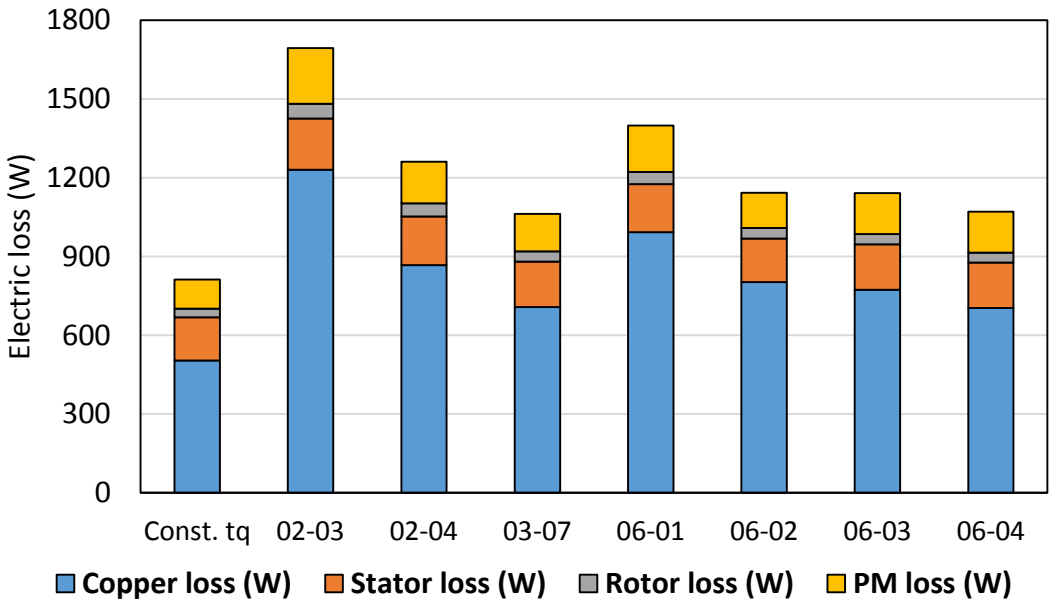

Figure 5-22 Electric losses distribution for different torque patterns at 4500rpm WOT

The machine loss of all the patterns above and the extra three patterns in the Group 06 (06-05 ~ 06-07) are shown in the scatter plot Figure 5-23. The trend line through these optimised torque patterns with different peak torque gives the Pareto

Curve, which indicates that, with current designs, the in-cycle speed fluctuation could not be improved further without introducing more electric loss. When more loss is introduced as the cost for the NVH benefit, the thermal behaviour of the machine is potentially to be different. Consequently, the cooling power increase and the hardware packing issue has to be considered. Unfortunately, the thermal study is not in the scope of this study. This effect was not investigated further.

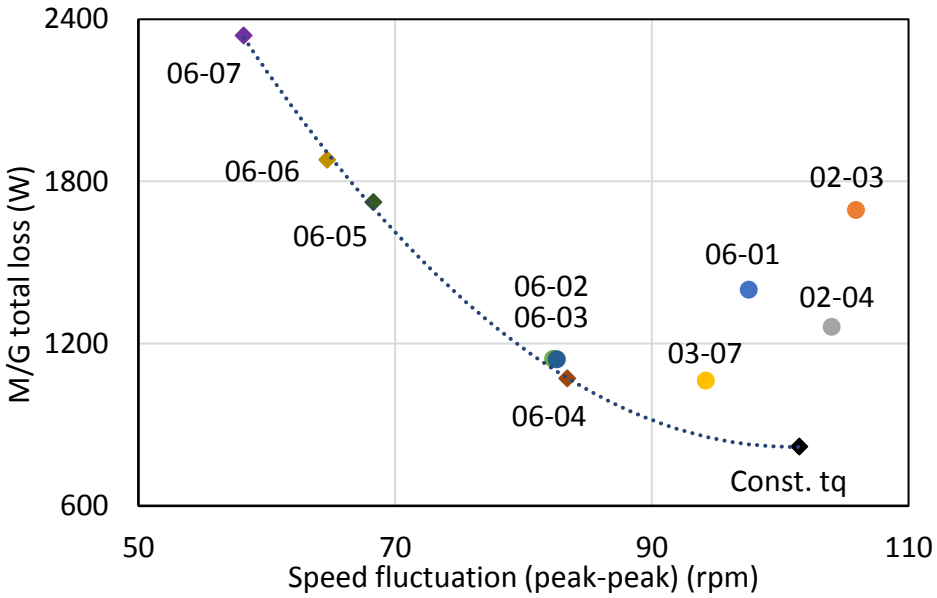

Figure 5-23 Scatter plot of total loss against speed fluctuation

First, 06-02 and 06-03 patterns were compared and analysed (Figure 5-24). They have the same period length of peak torque during the engine power and exhaust strokes (0~180 CA deg). The difference is that in 06-02 the generating torque remains at about 50Nm between 270 and 360 CA deg while 06-03 torque follows the engine torque trace. This means that Pattern 06-02 has to deliver a small amplitude motoring torque during 180-270 CA deg to maintain the same cycle mean torque comparing to zero torque for 06-03. These two differences made the copper loss of 06-02 higher since a higher torque was delivered for a longer time.

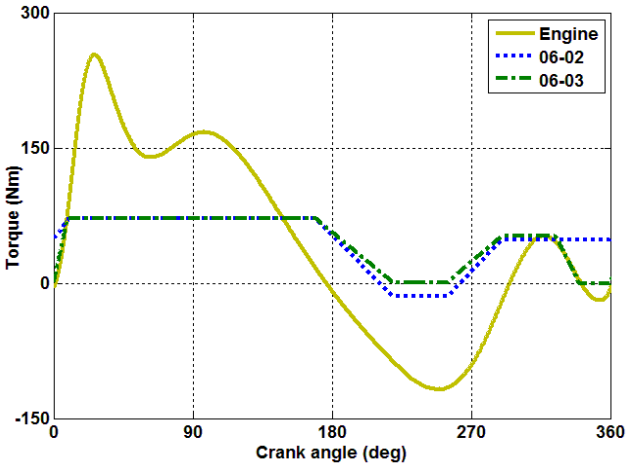

Figure 5-24 Torque pattern 06-02 and 06-03

For the stator loss, the alternating field and flux density mainly occurred at the teeth while the back iron area was less affected. This is can be seen in FEA filed result plot which was developed in CHAPTER - 4 (Figure 5-25). It shows two instants when the same tooth experienced high and low flux density. The results indicated that the iron loss was 0.41W difference between these two patterns for this single tooth while 4.92W for twelve all. It is close to the total stator loss difference as given in Table 5-3. The averaged flux density on this tooth and its loss were plotted in Figure 5-26.

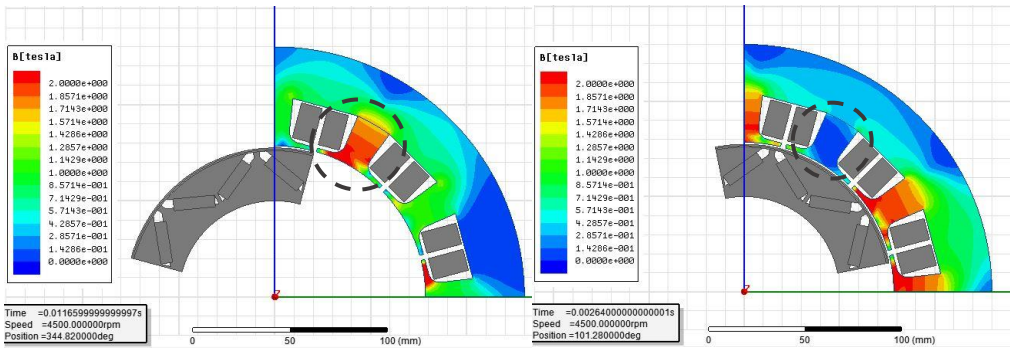

Figure 5-25 Significant flux density variation occurred at stator tooth

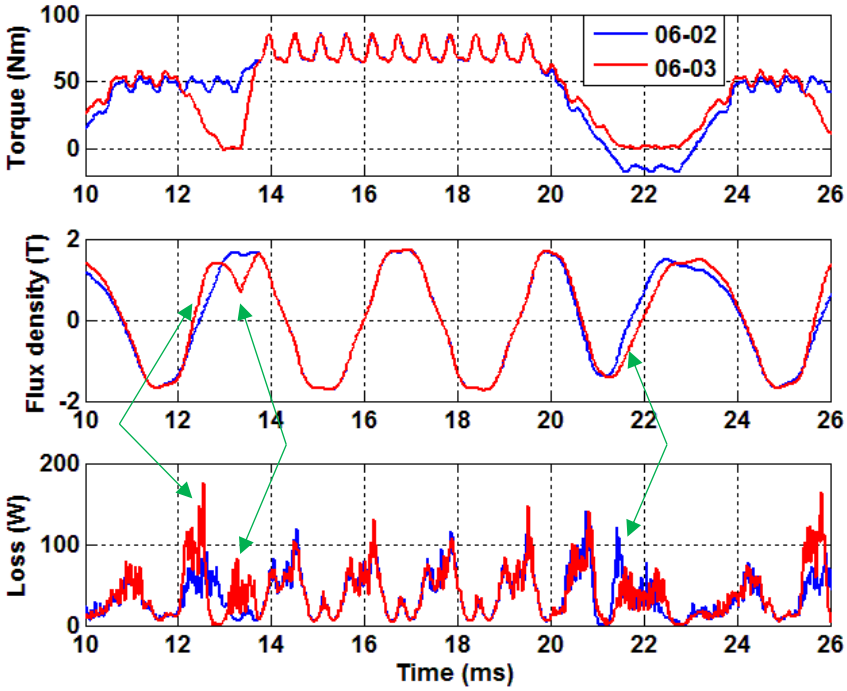

Figure 5-26 Stator tooth loss of 06-02 and 06-03.

Top: torque pattern. Middle: tooth average flux density. Bottom: iron loss on the tooth.

In Figure 5-26, the sudden change on the torque demand leads to a faster flux density variation on the tooth (for example at 12~14ms). As expected from the earlier analysis, higher iron loss was seen. Since 06-02 had a faster torque change requirement, the flux slope was steeper at the beginning thus a loss increase spike. However, the higher torque demand from 06-02 did not translate to an iron loss difference as significant as for the copper loss. This was due to short duration of resulting in only a small increase in iron loss. Furthermore, the actual absolute flux density value varied in a relatively small range (<±2 Tesla). The same effect was also seen at 20~24ms.

The magnet losses presented a similar behaviour as the stator losses. This was expected according to the analysis in the last section. The flux density variation for one piece magnet (of a north pole) and the total magnet loss are plotted in Figure 5-27. The flux density ripple is mainly due to the slot opening, consequently the flux ripple was equal to f_{sl} (Equation (5-15)). Since the loss was caused by all poles (both north and south), therefore loss ripples frequency displayed was twice f_{sl}. The magnet loss

dissimilarity between the two torque patterns occurred at the same places as the iron loss.

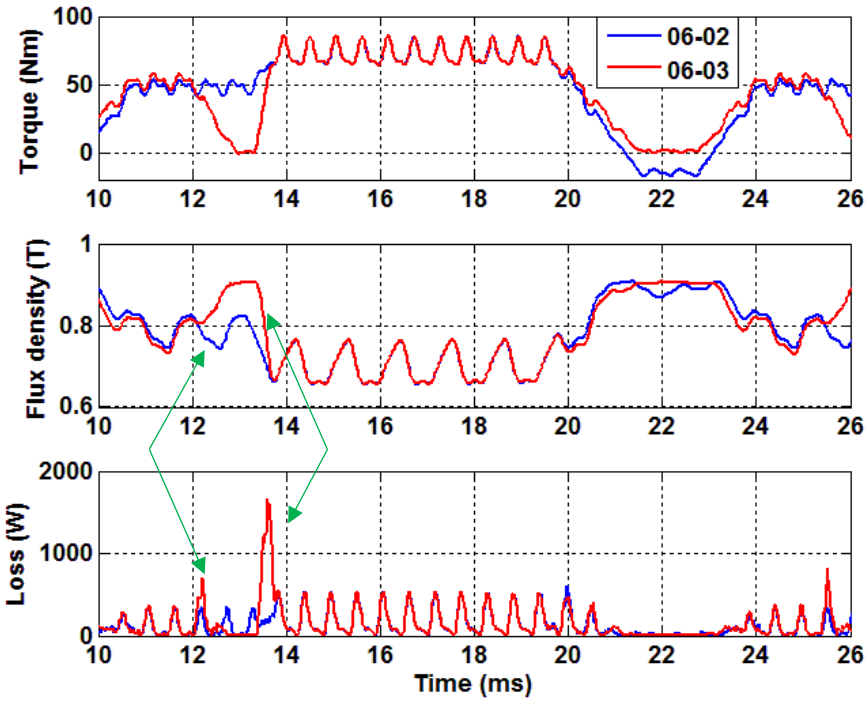

Figure 5-27 Magnet loss of 06-02 and 06-03.

Top: torque pattern. Middle: one north pole average flux density. Bottom: total eddy current loss in all rotor magnets.

The rotor experiences much less magnetic field variation as plotted in Figure 5-28. Therefore, the loss between all of the torque patterns were not that obvious as shown in the Table 5-3 and Figure 5-22.

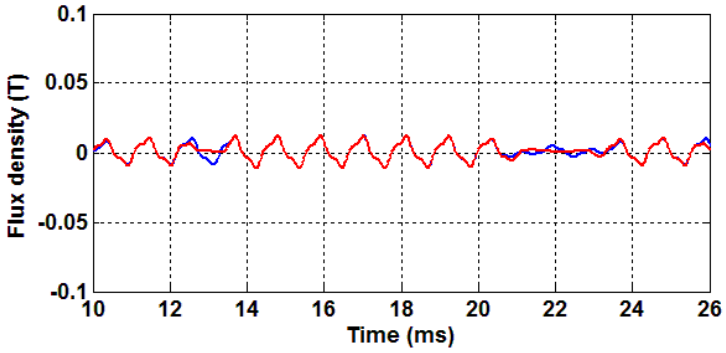

Figure 5-28 Rotor flux density variation of 06-02 and 06-03

When comparing 06-03 and 06-04 (Figure 5-29), they have similar designs with the only divergence highlighted in the circle. If the small torque difference at the very end of one cycle is ignored, the mean torque of the divergence section will be the same. However, for 06-03, the copper loss results in this period showed that the loss generated during the high torque region could not be balanced out by the low torque region. This indicates that when the mean torques are equal, a steady medium torque is superior to a fluctuating torque pattern in terms of copper loss. In fact, this is rather obvious since all DTC torque patterns showed higher copper loss than at the constant torque condition although they delivered the same mean torque.

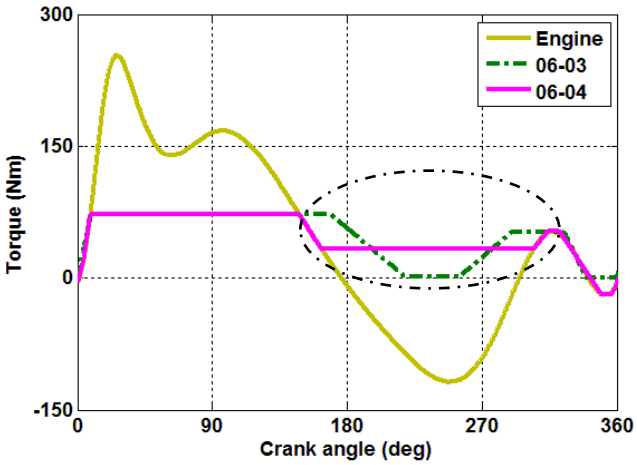

Figure 5-29 Torque pattern 06-03 and 06-04

The stator tooth and the magnets losses were also compared between the constant torque and pattern 06-04. The results were illustrated in Figure 5-30 and Figure 5-31. The same trends for both stator and magnets losses as previously analysed were observed.

Under steady state i.e. constant torque region in 06-04, the magnet loss due to the load magnitude was also observed. During 14~19ms in Figure 5-31, the combined effect of the high torque demand and the slot opening led to high amplitude flux fluctuation in the magnets. Therefore, more eddy current loss was generated than the

DTC off condition. The adverse result was seen at 19~24ms due to the DTC torque request being lower.

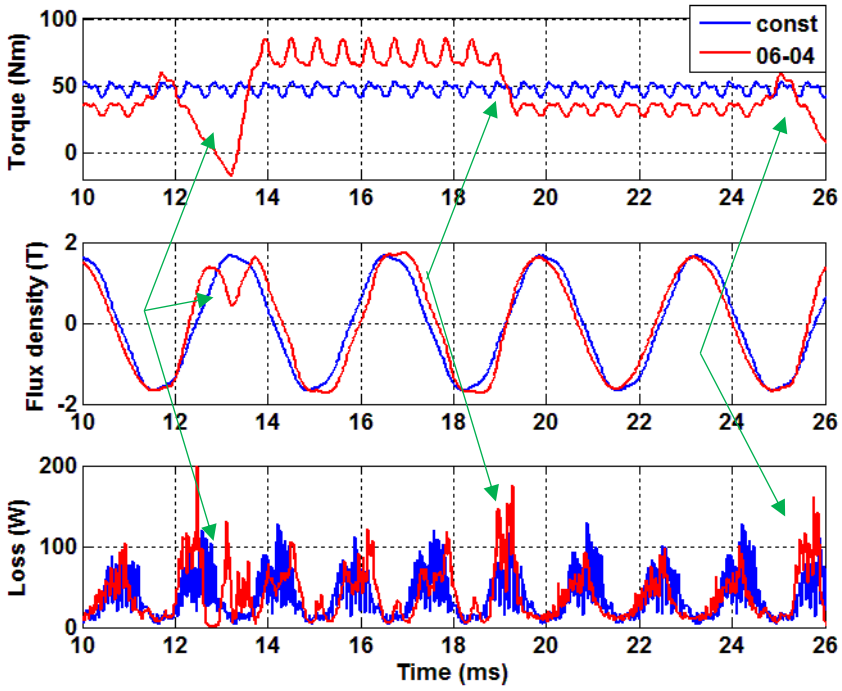

Figure 5-30 Stator tooth loss of constant torque and 06-04.

Top: torque pattern. Middle: tooth average flux density. Bottom: iron loss on the tooth.

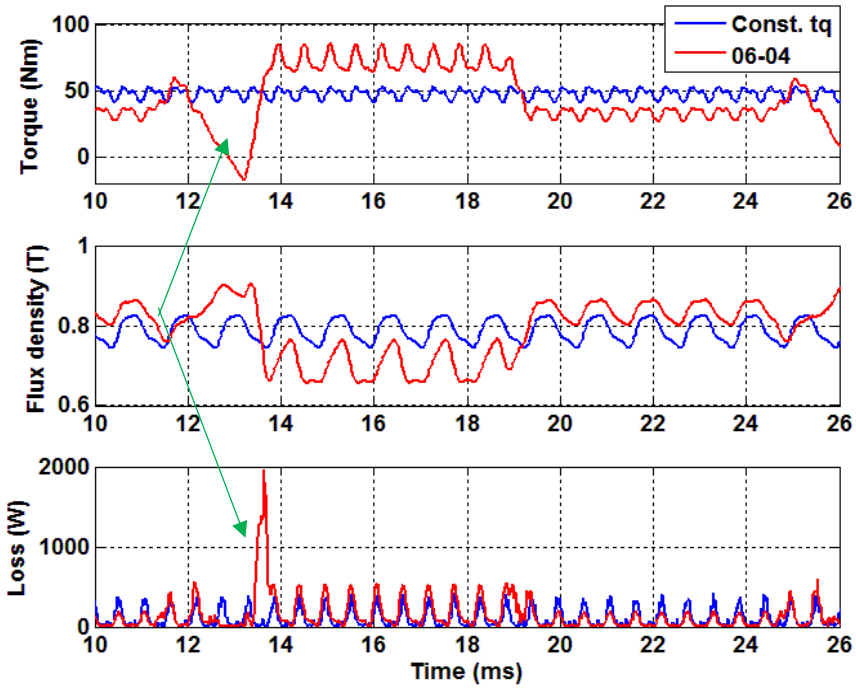

Figure 5-31 Magnet loss of constant torque and 06-04.

Top: torque pattern. Middle: one north pole average flux density. Bottom: total eddy current loss in all rotor magnets.

5.7 Inverter loss

The inverter loss model, as discussed in CHAPTER - 4 , consists of the conduction loss and the switching loss. They both relate to the phase current magnitude, although the latter one is also dependent on the switching frequency. The inverter loss at 4500rpm WOT for the torque patterns that are within the M/G capability is given in Table 5-4. It shows that the loss follows the same trend as the machine losses. However, the loss quantity is much less sensitive to the variation of the torque pattern designs. By following the same design principles as learned in the last section will benefit the inverter loss reduction with the same trend.

Table 5-4 Inverter loss at 4500rpm WOT

Pattern No.	Const. tq	02-03	02-04	03-07	06-01	06-02	06-03	06-04
Loss (W)	696.1	948.2	833.2	747.9	846.5	772.8	759.9	737.8

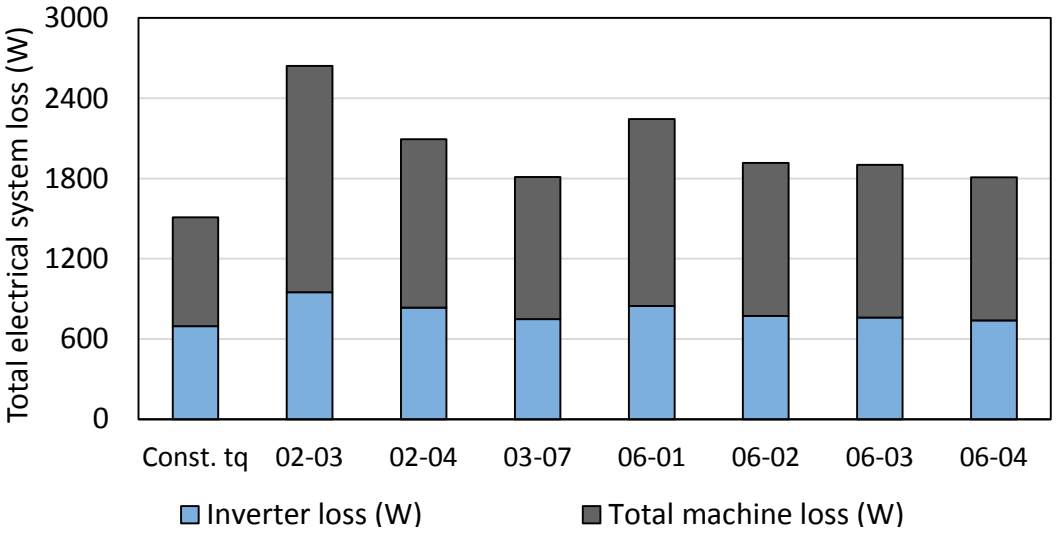

Figure 5-32 Total electrical system loss composed of the inverter loss and total machine loss at 4500rpm WOT

5.8 Final DTC torque pattern design

With understanding of the causes of the speed fluctuation and the electrical losses from the previous sections, the dynamic torque control pattern across the

complete range of APU operating speed could be refined. The instantaneous engine torque in one cycle is plotted in Figure 5-33.

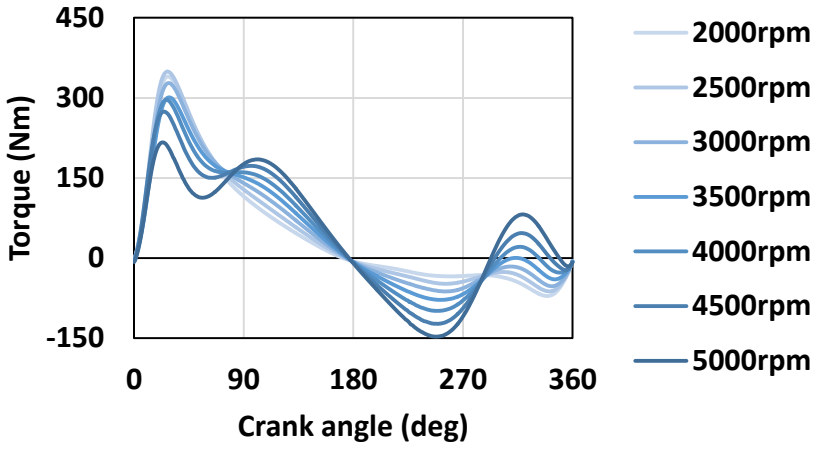

Figure 5-33 Engine in-cycle torque

The peak torque from the prototype M/G was limited to 72Nm, therefore the optimum peak-to-peak speed variation value could be determined according to the linear relationship explained in the previous sections. Since the energy accumulated in first half cycle determines the peak point of the instantaneous speed that the crankshaft can reach to, holding down the acceleration is the priority rather than minimising the electric loss during this period. As per the results of the simple square pulse patterns, keeping the M/G at peak torque further after the engine torque drops below 72Nm did not necessarily help to improve the speed smoothness but did lead to more copper loss. As a result, demanding the M/G to follow the engine torque trace, as the design in 06-04 (Figure 5-13), is a preferred compromise.

During the second half cycle, the best case is to have the crankshaft speed fall back to the starting instantaneous speed without introducing an extra negative speed dip. At the same time, minimising the electric losses is another design task for this phase. Regarding the machine electric losses study, two lessons were drawn. The first one is that a flat medium torque is more beneficial to the copper loss reduction than a demand that switches between high and low torques. The second is that a rapid high

amplitude change of the torque demand will introduce high instantaneous hysteresis loss and eddy current loss. Therefore, the torque pattern in this region should have mild changes or even a flat demand. To avoid introducing an extra speed fluctuation at the end of a cycle, the M/G torque should be always higher than the engine, i.e. the torque patterns between 180 to 360 CA deg are above the engine torque traces across the speed range (Figure 5-33). However, this only needs to be considered when the engine speed is higher than 4500rpm, because at lower speed, the small engine torque ripple near the cycle end (compression stroke) is either negative or very low. A flat torque demand for low engine speed during the second half revolution can easily satisfy this requirement. For comparison purpose, the flat torque demands at 4500rpm and above were also simulated to study the trade-off between electric loss and speed fluctuation reduction (Figure 5-34). When designing the final patterns, the M/G torque response time has to be considered. The fastest response time required occurs at the very beginning of each cycle. According to Figure 5-33, the engine reaches 72Nm (the peak torque of the M/G) at about 9.5 CAD for all speed which is corresponding to 0.3ms at 5000rpm. As explained in previous chapter, the slowest falling torque (rising generating torque) response time is also 0.3ms. This indicates the M/G is able to follow the torque patterns in Figure 5-34 within the target engine speed range.

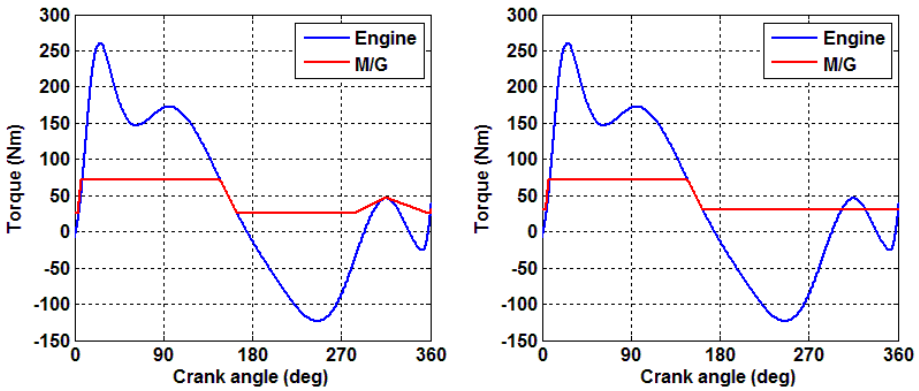

Figure 5-34 Final DTC torque demand at 4500rpm WOT
Left: with compression stroke pulse. Right: without compression stroke pulse.

Since the APU in the REEV does not directly power the driving wheels, its efficiency is prioritised. Therefore, once the engine was warmed up, the APU is

operating with WOT to minimise the throttling loss for the sake of engine efficiency. The DTC was preliminarily designed for the full load condition across the speed range only. The DTC patterns were populated into a map that has the mean engine speed, the rotor mechanical positon and the torque demand as the three axes. Figure 5-35 shows the maps of the two considered final DTC torque maps.

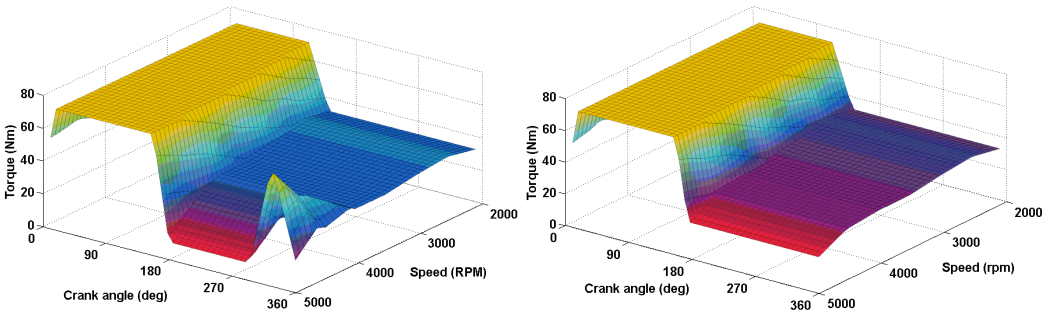

Figure 5-35 Dynamic torque control map for WOT condition.
Left: with compression stroke pulse. Right: without compression stroke pulse.

The M/G was set in speed control mode. Hence, in order to cope with speed disturbance, a PID controller was added to cooperate with the feedforward DTC map. However, simply combining the PID and the DTC map outputs as the torque demand to the M/G may affect the DTC performance. The first reason is that during the first 180 CA deg after the engine TDCF, the M/G ran at its peak load mostly. With a regularly sampling speed controller, whenever the instantaneous PID demand plus the DTC map demand was beyond the M/G physical hard limit, the actual machine output will be capped. Therefore, the PID integrator has the potential to wind up since the speed error keep increasing due to the unachieved torque target. The oscillating nature of the DTC and the response delay of the M/G can make the system unstable. Secondly, according to the previous analysis, the first half revolution, where the peak torque is demanded, is the key to supress the speed rise. If the PID is allowed to operate during this period, it may request a torque that is not at the M/G peak therefore diminish the DTC effectiveness.

To solve this issue, in the speed control loop, the PID output was over written with zero value during the first half revolution thus the system became an open loop control only referencing to the DTC table. During the second half cycle, the PID operated output normally to minimise the mean speed error. In another word, the first half of the M/G torque demand exactly follows the predefined table and the second half DTC torque pattern is floating (with 200 Hz control frequency) to achieve the cycle average torque requirement. The Simulink setup flow chart for this part is shown in Figure 5-36.

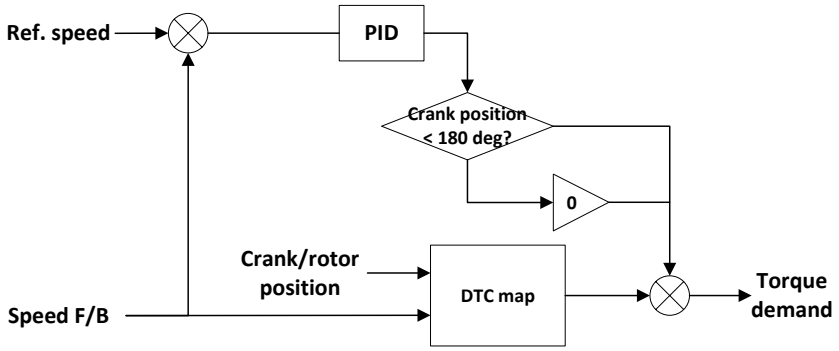

Figure 5-36 Feedforward DTC map and PID for speed control

5.9 Final DTC simulation results

The two final DTC maps were applied to the system model across the entire speed range at full load. All the numerical results are given in Appendix B. The simulation M/G torque responses and corresponding demands at 4500rpm are given in Figure 5-37. The M/G followed the demand closely as expected which indicates the torque patterns designed were achievable.

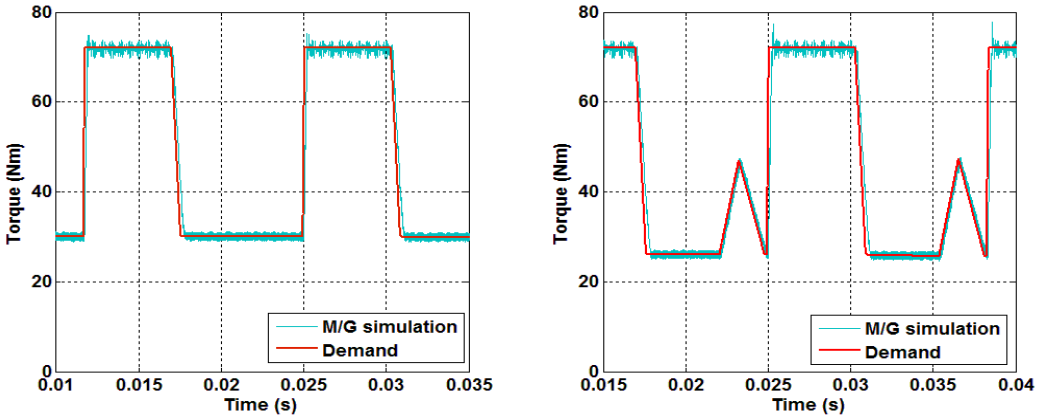

Figure 5-37 M/G torque response in the simulation at 4500rpm

Left: DTC without compression stroke pulse. Right: DTC with compression stroke pulse.

The in-cycle speed oscillation results are depicted in Figure 5-38. The reduced fluctuation can be observed across all speeds compared to the condition with DTC disabled. In percentage terms, the reduction ranged from 16.14% to 25.54%. If referring to Figure 5-33, the higher the speed, the wider the window that the M/G can output the peak torque. Therefore, in percentage terms, the reduction is more effective at high speed. However, since the inherent speed fluctuation is less at high speed due to less time for the rotating inertia to respond to the torque variation, the absolute speed fluctuation reduction in unit of rpm was higher at low speed. The torque pattern with the tip feature only required at 4500rpm and above, the main divergence of the two final DTC maps considered was only apparent at the last two setpoints. The simulation results indicated that the speed fluctuation at 5000rpm had a less than 10rpm growth with the flat end torque demand while at 4500rpm, there was no obvious difference. This level of difference at this two speed may not be noticeable in the real system.

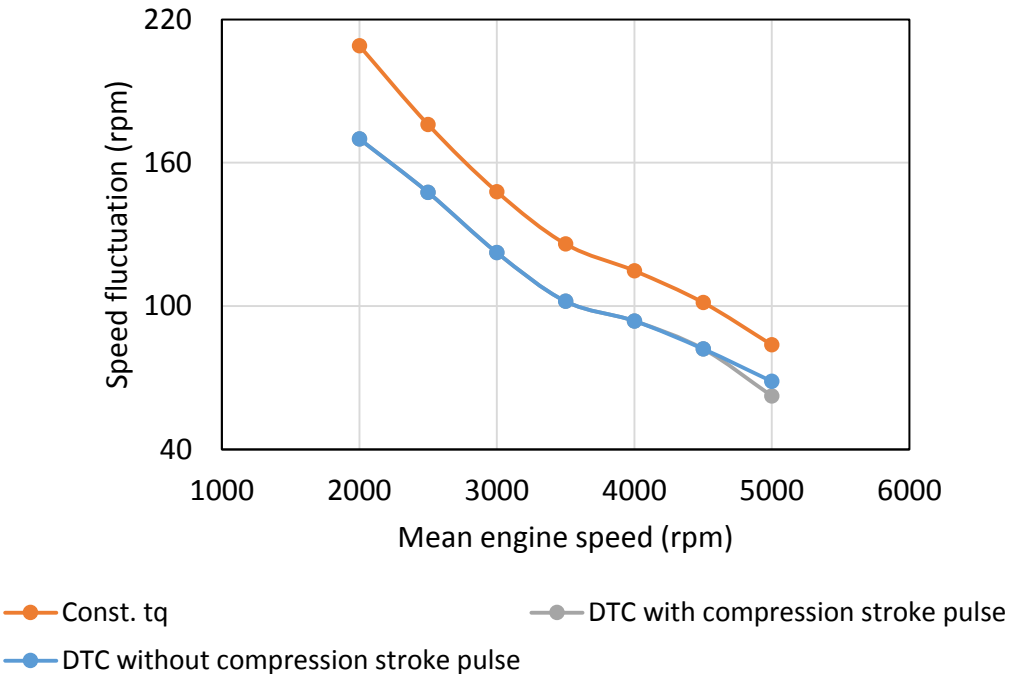

Figure 5-38 Simulation results of the speed fluctuation

The electric losses of the M/G at different speed is given in Figure 5-39 for side-by-side comparison. For each speed, the left bar is for the constant M/G torque condition (DTC off). The middle and right bars are for the DTC with and without compression stroke pulse designs respectively. It is clear that the copper loss was the most significant part of the machine losses, which was primarily load dependent. The losses (iron loss and Eddy current loss) in the stator and rotor increases as the frequency rises. The losses incurred in the magnets were nearly doubled at high speed compared to the constant torque condition. However, these only represent about 1% of the total power at 5000rpm (22kW). The DTC without compression stroke pulse demonstrated the loss benefits over its competitor. The overall loss rise compared to the constant M/G torque condition dropped from 57.38% with compression stroke pulse to 45.24% without compression stroke pulse at 5000rpm WOT.

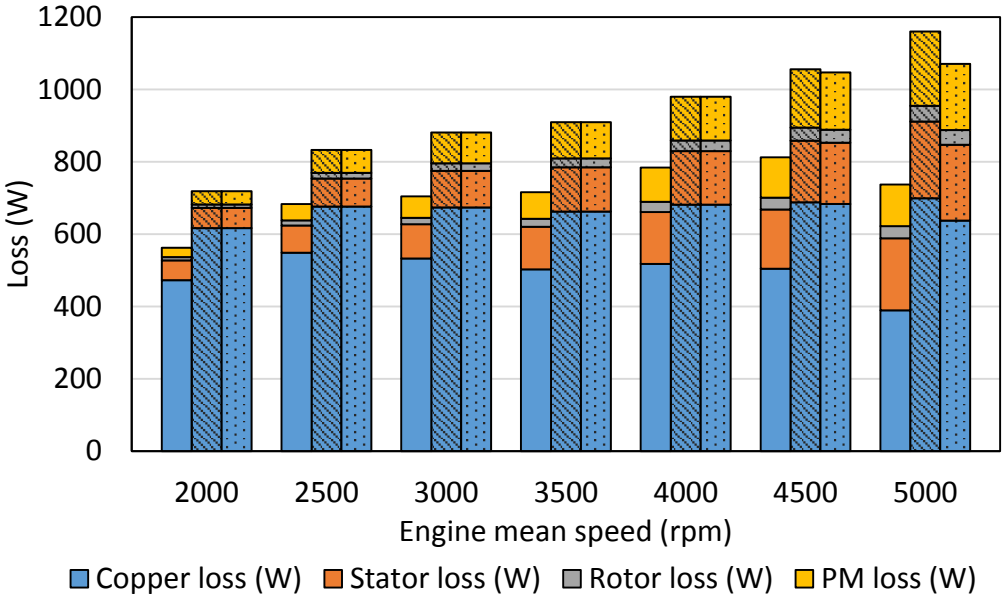

Figure 5-39 Machine loss distribution

Left: constant torque. Middle: DTC with compression stroke pulse. Right: DTC without compression stroke pulse.

The inverter loss (Figure 5-40) as expected follows the same trend as the machine overall loss, but the difference is not as such obvious, which means it is less sensitive to the in-cycle torque variation. The loss increased between 4.42~10.73% for the DTC with compression stroke pulse. When the flat end torque pattern design was applied, the loss rise at 5000rpm drop from 10.73% to 8.62%.

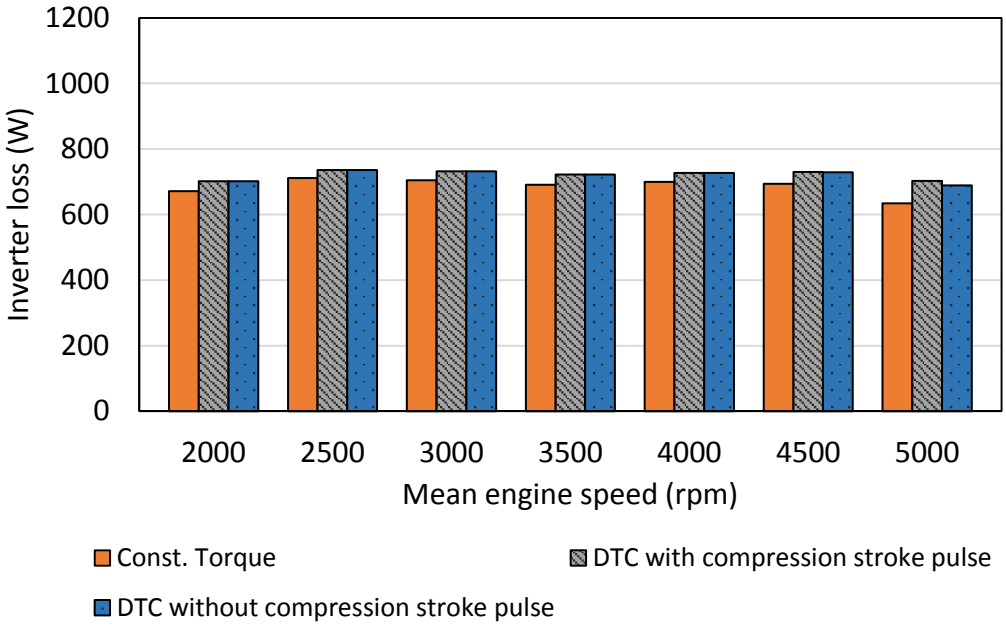

Figure 5-40 Simulation results of the inverter loss

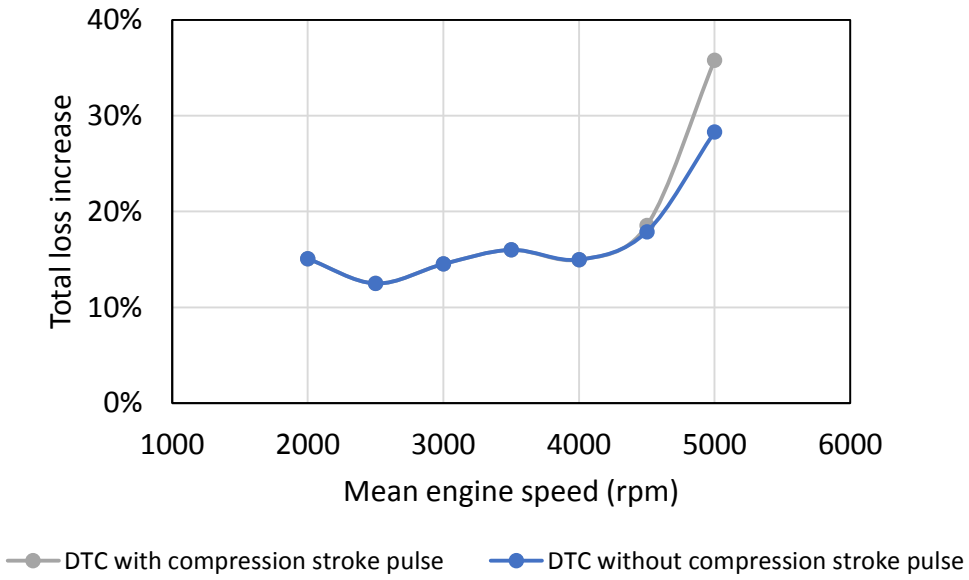

Figure 5-41 Total electrical loss increase over constant torque condition

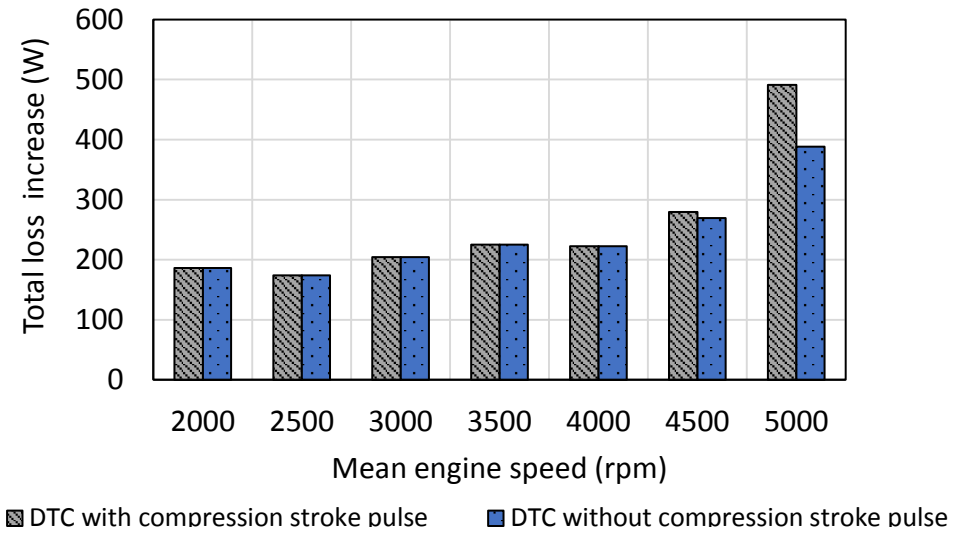

Figure 5-42 Total electrical loss increase due to DTC

The total electrical loss growth (machine and inverter), when the DTC was turned on, was evidently observed in Figure 5-41 and Figure 5-42. From the simulation results, when the DTC map without compression stroke pulse deployed, the total loss could save up to 7.5%, which is 103W less, than the one with compression stroke pulse. This loss reduction is considered more obvious and beneficial to the system than the speed smoothening gain from the compression stroke pulse design, since the speed fluctuation improvement was so marginal that it might not be detected in the actual system.

To assess the APU efficiency, the term Electrical Specific Fuel Consumption (ESFC) was used. It was calculated with Equation (5-26) which is a similar formula as the engine Brake Specific Fuel Consumption (BSFC). The fuel flow rates were measured by a Coriolis flow meter during the same tests as for the cylinder pressure collection.

$$ESFC\ (g/kWh) = \frac{Fuel\ flow\ rate}{Generator\ output\ power} \times 3600 \qquad (5\text{-}26)$$

By assuming the same fuel flow rate was delivered to the engine model when enabled the DTC, the ESFC results are plotted in Figure 5-44. Although the amount of

losses was apparent, the effect on the ESFC was less significant. The increase along the speed range was between 1.2% and 2.43% when applying DTC with compression stroke pulse. When removing the compression stroke pulse, at 5000rpm, the ESFC dropped from 349.87 to 348.10 g/kWh which was hardly noticeable.

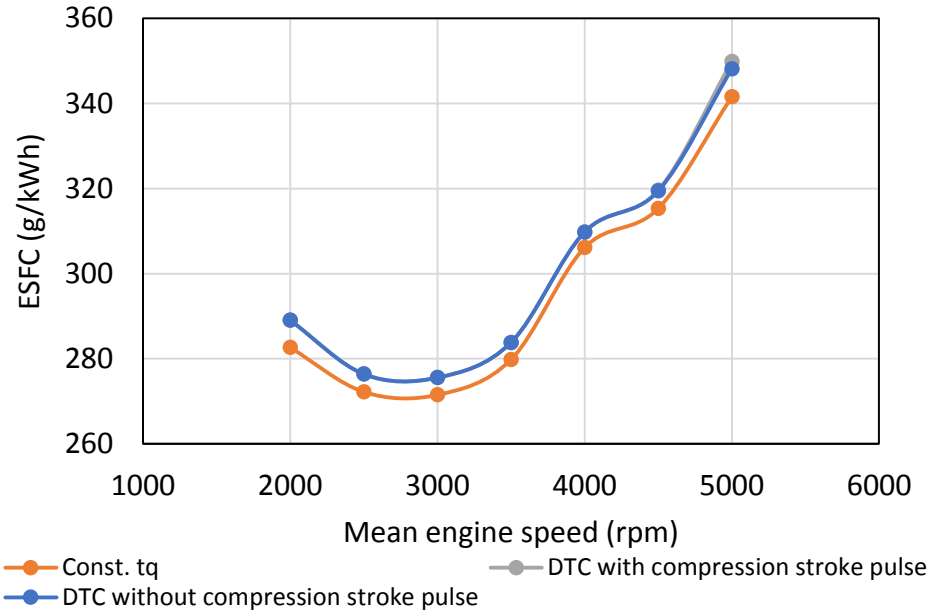

Figure 5-43 APU ESFC change at WOT due to DTC

Figure 5-44 is the scatter plot of the speed fluctuation versus machine loss. The final DTC result at 4500rpm WOT is added in (since the results from the flat end and the tip end map are very close numerically at this operating point, they were not differentiated in this discussion). The data from the final DTC did not show a significant difference to the more complicated pattern design, like 06-04 and it is still on the edge of the Pareto Curve. This fact brought the final DTC map to a more desired position since the patterns were simpler and easier on both control and system stability perspectives.

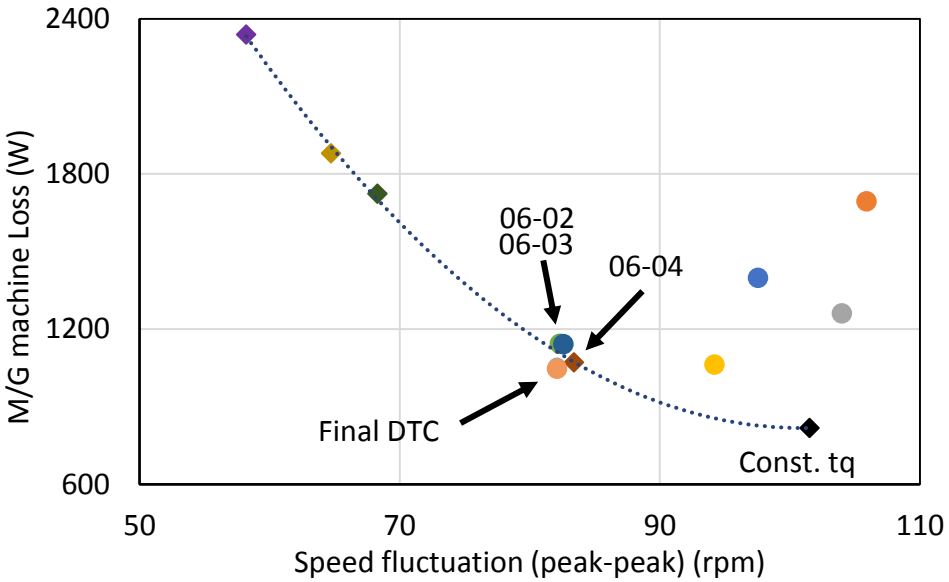

Figure 5-44 Final DTC result at 4500rpm WOT

By assuming that the M/G is able to deliver 95Nm peak torque at 2000rpm (the same assumption as in pattern 06-05 at 4500rpm) by supplying more current without causing a failure, the simulated approximating Prato Curve for 2000rpm is presented in Figure 5-45. Clearly more data points are needed to create the more accurate curves. However, the material properties at higher load than original machine capability need to be verified to obtain reliable results. Unfortunately, this could not be completed with limited access to the motor data during the project. Figure 5-46 presents the ESFC curves for this APU at the same conditions.

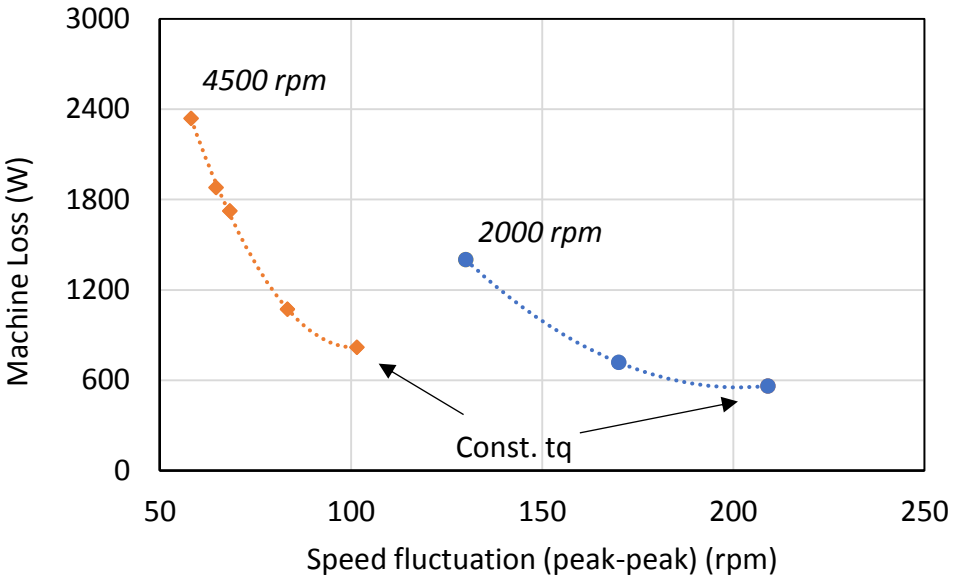

Figure 5-45 Total machine loss versus speed fluctuation at 2000rpm and 4500rpm

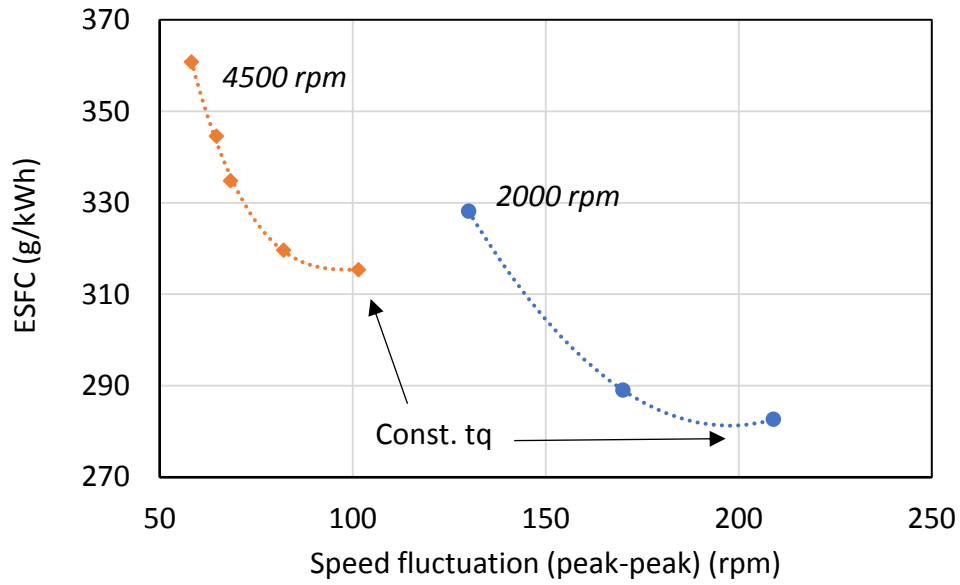

Figure 5-46 ESFC performance versus speed fluctuation at 2000rpm and 4500rpm

5.10 Conclusion

The development process of the APU dynamic torque control is presented in this chapter. At the initial stage, five series of simple square torque patterns were applied to the system at 2000rpm and 4500rpm WOT to explore the potential torque waveform features that could benefit the in-cycle speed fluctuation. It was found that neither a

short high amplitude impulse nor a long low amplitude torque was favourable for the speed fluctuation reduction. A compromise between them is necessary. Then accordingly, a sixth series of torque patterns were tried on the system simulation model. These patterns were design with more complicated shapes to try to maximise the effectiveness of the M/G counteracting torque. However, the minimum in-cycle speed fluctuation was limited by the peak torque capability of the M/G regardless to the torque pattern designs. Based on the energy conservation analysis, a linear correlation between the M/G peak torque and the speed fluctuation was found.

Then, an analysis of the M/G and inverter electrical losses was conducted with help from the analytical and FEA models. It was concluded that an alternating torque would result in more iron loss and eddy current loss than a flat smooth torque. Based on the analysis, two final DTC torque pattern maps for the entire range of the APU operating speed were designed.

The two DTC maps were simulated in the system model. The results showed that both DTC maps caused additional losses when compared with the constant torque strategy. However, the torque pattern without compression stroke pulse design could resulted in less additional loss compared to the one with compression stroke pulse, although a tiny increase on the in-cycle speed fluctuation was observed. Although when translating the additional loss into ESFC the difference was hardly observed, a flat torque demand was easier for the control and beneficial for the system stability. Therefore, the DTC map without compression stroke pulse pattern is more preferred for this system. Both of these two maps were tried on the actual APU on test bench and the results were review in the next chapter.

CHAPTER - 6
APU Rig Testing

This chapter presents the APU bench testing results with Dynamic Torque Control strategy deployed. Two APU operation setpoints were successfully tested with three torque patterns. Expected reduction on in-cycle speed fluctuation was observed. Satisfied results, as compared to the simulation, on the system electrical output power and efficiency decrease were also recorded.

6.1 Introduction

One of the most important targets in this research work is to test the Dynamic Torque Control (DTC) strategy on the prototype APU. The simulation modelling procedure of the major components and the complete system have been presented in details in the previous chapters. The engine and M/G models have been calibrated with the laboratory test data. In CHAPTER - 5 , the development process of the DTC torque patterns were described and those designs were proved that it had considerable effect on the in-cycle shaft speed fluctuation in the simulation.

During the final stage of this research, the DTC final designs were implemented in the actual APU control system and the unit was tested in the laboratory. This chapter describes the test setups, data collecting and processing procedures and the results at both DTC on/off conditions.

6.2 Test bench setup

After the engine finished the standalone benchmark testing and optimisation on the test bench, the dynamometer load motor was decoupled from the engine and the prop shaft was removed. The bespoke prototype motor/generator (M/G) was then installed on the engine crankshaft. The electric machine rotor assembly replaced the original engine flywheel and directly bolted onto the crank palm. Considering the rather short rotor length (~50mm), no bearing was designed to support the rotor inside the M/G unit for cost reduction. The electric machine drive, i.e. the inverter, was integrated in the M/G which was attached on the rear end of the stator. The complete APU on the bench is shown in Figure 6-1. The test bench schematic is given in Figure 6-2.

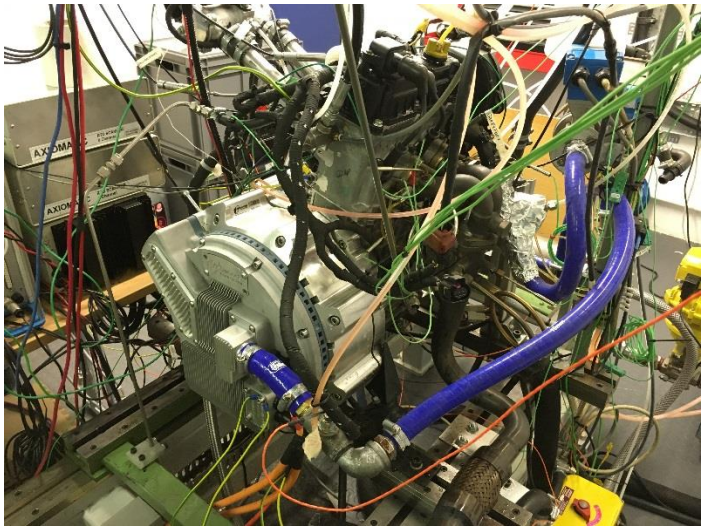

Figure 6-1 Prototype APU on the test bench

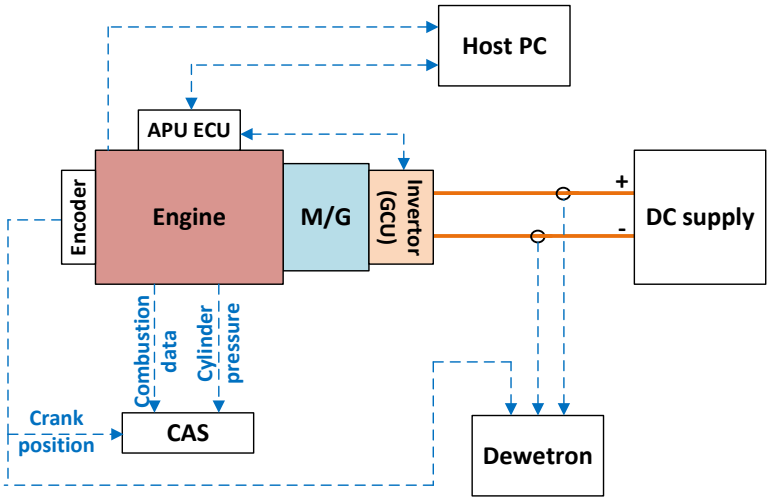

Figure 6-2 Test bench setup schematic

The electric power source that connected to the APU output was a bi-direction DC power supply from Regatron AG. It has a peak power of 40kW with a DC voltage range up to 400V. The supply voltage for this APU was set to 350V as per the target system requirement. The DC voltage and current measurements from this unit were sent to the host PC through CAN bus for real time APU electrical power calculation.

The host PC controlled the APU by communicating with the APU Electronic Control Unit (ECU). The ECU included the APU Supervisory Control (ASC) and the Engine Management System (EMS) which was at a lower control level than ASC. The

ASC also communicated with the Generator Control Unit (GCU) in the inverter though CAN. For the test data logging, on the engine side, the setup was the same as for the engine standalone test. The Combustion Analysis System (CAS) collected all the engine combustion data based on the crank position signal from the high precision (0.2 CA deg/pulse) engine crankshaft optical encoder. For the M/G status (temperatures, voltages, currents, etc.) they were monitored by the GCU. Since there was no open ports available to send data directly from the GCU to any other data acquisition system, the M/G information could only be logged by the host PC through CAN communication which was with a bandwidth of 80Hz.

In order to capture the fast in-cycle speed fluctuation, another high speed data acquisition system supplied by Dewetron GmbH was used. The engine encoder pulsation output was directed into a counter channel. With the acknowledged encoder resolution, the instantaneous signal frequency could be converted into shaft instantaneous speed in real time. This Dewetron kit was also used to log the DC current measurement. Two high performance current transducers from LEM were sleeved on both DC supply cables which helped to remove the common mode noise during the post process. The transducer is rated up to 1000A with a direct current output of 0~1000mA. However, since there was no current channel in the data acquisition device, a conversion box was made by the instrumentation technician to convert the current output to an analogue output up to 10V. The logging frequency was set to 200 kHz which was fast enough to capture the in-cycle speed fluctuation while generating acceptable sized data files. Another Fluke current clamp with range up 300A was clamped on one DC supply cable. This measurement was for the host PC to calculate the DC power generation/consumption.

However, there was one useful measurement that could not be implemented due to the system physical constraints. As the M/G casing was directly fixed on the engine block, there was no exposed shaft between these them. This arrangement made it not possible to install a torque transducer, thus no direct shaft torque measurement can be

implemented. Therefore, the actual M/G torque waveforms when DTC was turned on had to be estimated through other parameters and a few assumptions if needed which will be detailed later.

6.3 In-cycle speed fluctuation with DTC off

The APU in-cycle speed fluctuations were firstly measured with DTC disabled. The M/G simply ran in PID speed control mode with feedback from its own shaft encode. The control loop frequency was 200Hz as per inverter specification document.

In order to create the APU peak-to-peak speed fluctuation map, the data collected at the same setpoints as for the engine BSFC map. The testing speed range was from 2000rpm to 5000rpm with 500rpm step. Since there was no direct torque measurement, the electric power demand was the other setpont, which started from 2kW and then 5kW with 5kW increments until wide-open throttle. At each setpoint, a five-second average data log was recorded. During the test, it was found that the engine speed encoder showed obvious difference to what was read in the inverter graphical user interface (GUI). The engine encoder was believed accurate, as it had been specifically calibrated during the engine standalone test. Since the M/G was in speed control mode, it was considered that the error was from the analogue sinusoidal encoder on the M/G side due to its own calibration. The speed offset was more severe as the mean speed increased as shown in Figure 6-3. However, OEM did not provide a solution to this issue in the meantime.

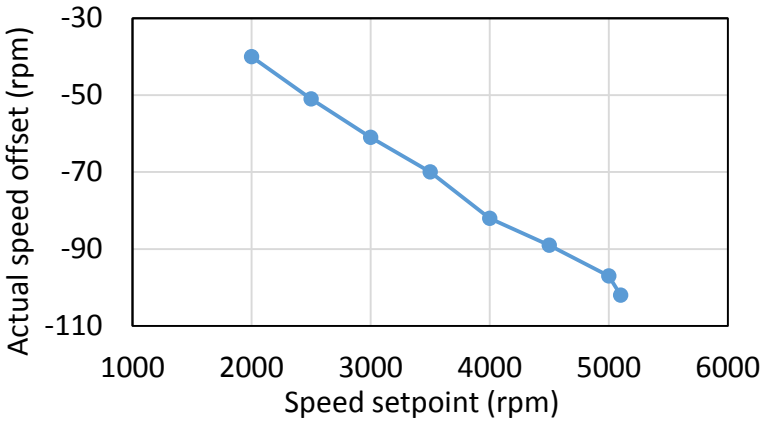

Figure 6-3 M/G encoder speed offset

The Figure 6-4 shows the raw instantaneous speed log from the engine encoder at 2000rpm full load. The plot gives a relatively clear speed profile. However, it could not be used directly for the peak-to-peak speed fluctuation calculation because the signal noise spikes will overstate the results. A fourth order Butterworth low-pass filter with cut-off frequency of 500Hz was designed and applied to the data. The cut-off frequency was chosen to give a relatively smooth speed trace. The result is shown in Figure 6-5. However, a few spikes, which were mainly caused by the discrete high-amplitude random noise (Figure 6-6), could not be removed completely due to their low frequency. This randomly occurring noise existed in all data logs and the cause was not understood.

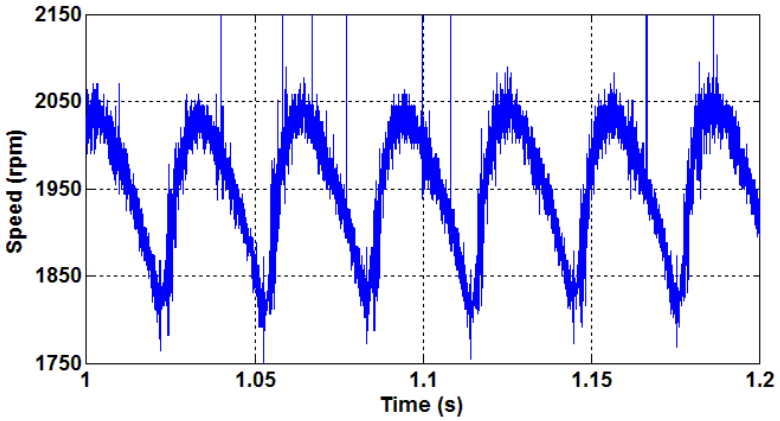

Figure 6-4 Raw engine speed data log at 2000rpm WOT

For the setpoints with high engine speed or at low load, the in-cycle speed fluctuation was inherently low. It was difficult to separate the general signal noise and the useful speed trace information effectively. By applying the same low-pass filter, it resulted in irregular speed waveforms as seen from the two examples in Figure 6-7. However, further reducing the filter cut-off frequency allowed the spikes to be smoothed, but the speed waveform would be distorted and the peak-to-peak fluctuation could be underestimated.

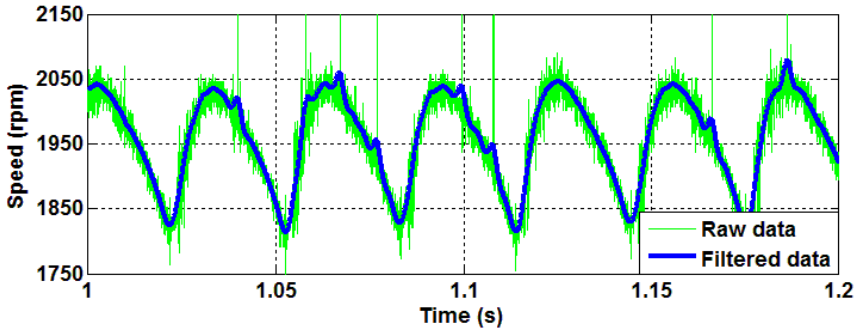

Figure 6-5 Engine speed at 2000rpm WOT with low-pass filter

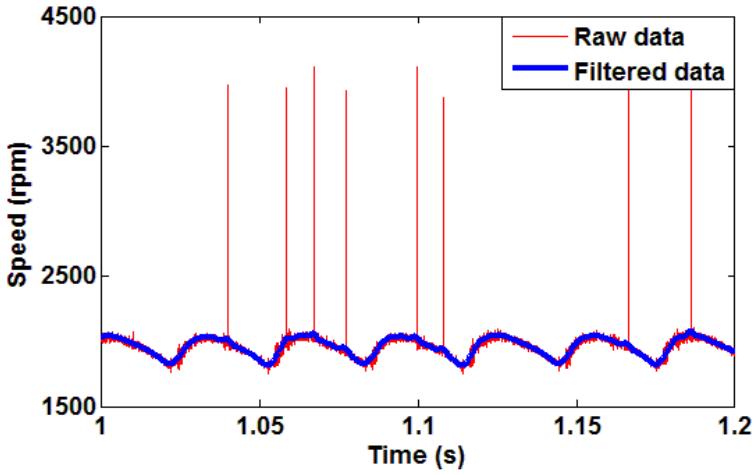

Figure 6-6 Random high amplitude noise spikes in the raw data

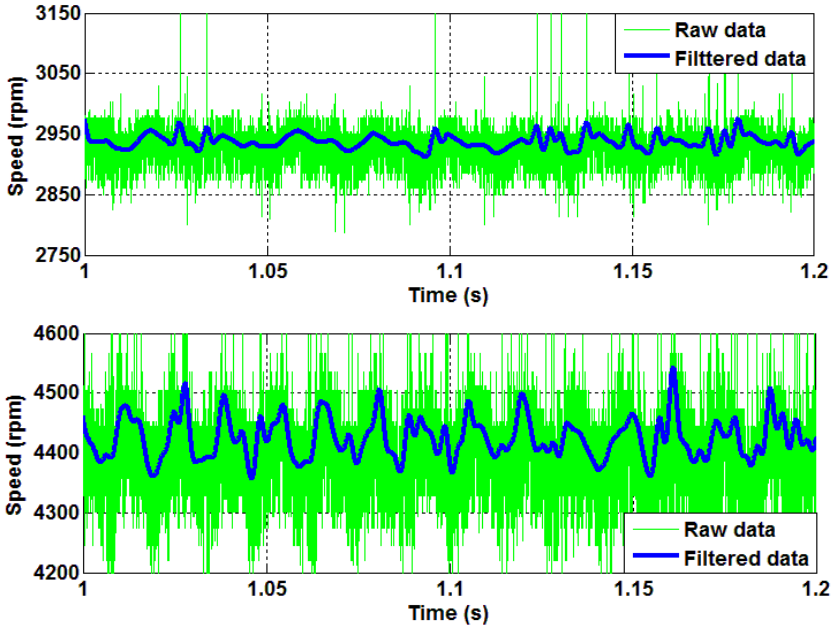

Figure 6-7 Filtered engine speed at 3000 rpm 2kW (above) and 4500 rpm WOT (below)

To solve this issue i.e. generating a relatively regular speed trace from the raw data without distorting the profile, only the 'significant' harmonics were selected to reconstruct the speed waveform. All the speed signals were analysed with FFT. The speed signal at 4500rpm WOT in frequency domain (the 0Hz amplitude was removed) shown in Figure 6-8 as an example. Since the fundamental frequency of the speed fluctuation corresponds to the combustion events, only the integral multiple order of the firing frequency harmonics were picked from the spectrum and used to reconstruct the waveform.

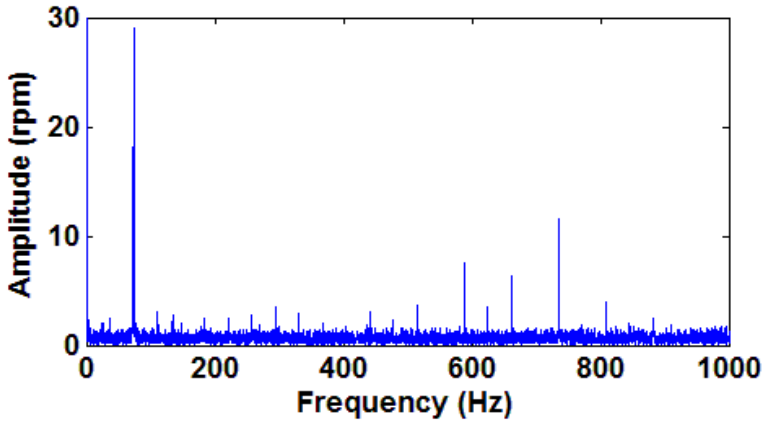

Figure 6-8 FFT of engine speed at 4500rpm WOT

However, when the total number of harmonics used is too high, the rebuilt waveform could become noisy again. In order to define the minimum number of harmonics needed without underestimating the speed information, the number of harmonics was varied from one to thirty-two to visualise the effect on the waveform shape. The peak-to-peak speed oscillation results regarding to the total number of harmonics are shown in Figure 6-9 for 2000rpm and 4500rpm WOT. By assessing both numerical and graphical results, it concluded that using the harmonics up to 10th order could retain the detail recreation and reject the high frequency noise across the entire speed range. The corresponding reconstructed waveforms are plotted in Figure 6-10. The speed fluctuation manner was more clearly displayed. Due to the sampling rate and the total number of data points, the FFT harmonic interval may not allow the engine speed and its harmonics fall in the exact frequency bins. Therefore, all the harmonics within +/- 0.5Hz of the selected frequency were collected. The same technique was also applied to part load condition. The same satisfied results were obtained. One example at 3000rpm and 2kW is presented in Figure 6-11.

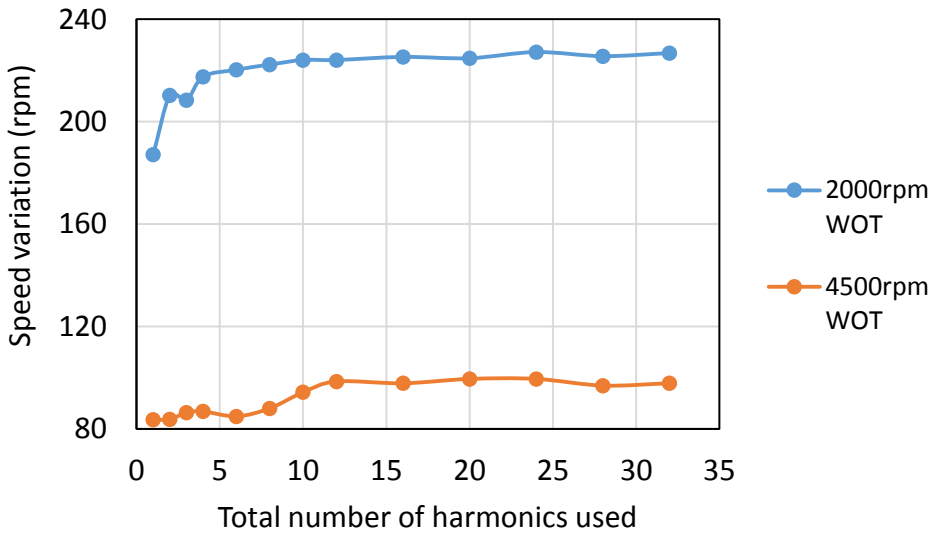

Figure 6-9 The effect of the harmonics number on the speed variation results at 2000rpm (left) and 4500rpm (right) with WOT

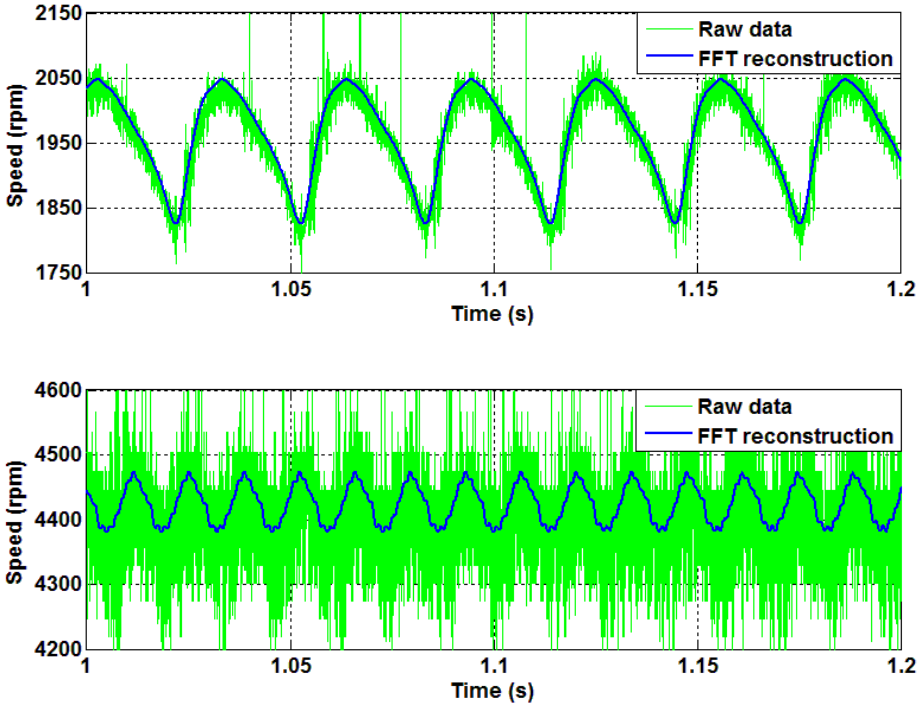

Figure 6-10 Reconstructed speed traces at 2000rpm WOT (up) and 4500rpm WOT (bottom)

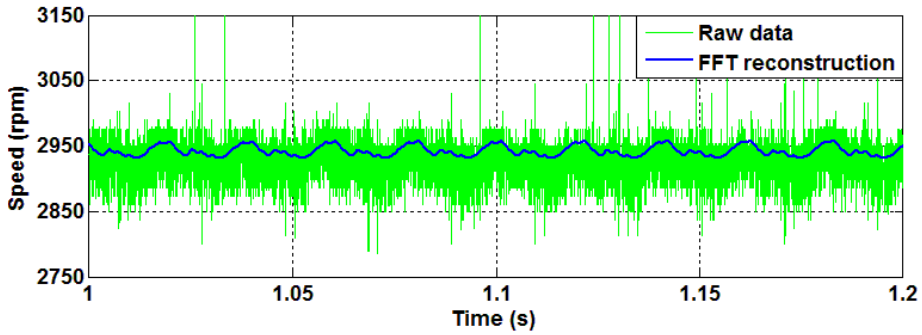

Figure 6-11 Reconstructed speed traces at 3000rpm 2kW

Compared to the reconstructed instantaneous speed trace, the simulation results showed very good match especially at the full throttle conditions. The simulation model was set to run at the same mean speed as the measured mean speed of the data logs. Three examples are plotted in Figure 6-12 with the same y-axis range width (400rpm). Since low load conditions were not the major focus of study (such as the middle plot condition), no further investigation was conducted on these setpoints other than WOT. The coefficient of determination (R^2) between the reconstructed waveforms and the simulation results were calculated for the whole speed range with

WOT (Figure 6-13). The R^2 was significantly high at 2000rpm (0.99), however, gradually fell as the speed getting higher. At high speed, the speed fluctuation was inherently small and at a high frequency. The encoder signal was more likely to be contaminated by the undesired noise. As can be seen in Figure 6-10, with the same number of harmonics used, the 4500rpm waveform is less smooth than the one for 2000rpm. This led to the dropping R^2 results. However, the coherence performance was generally high.

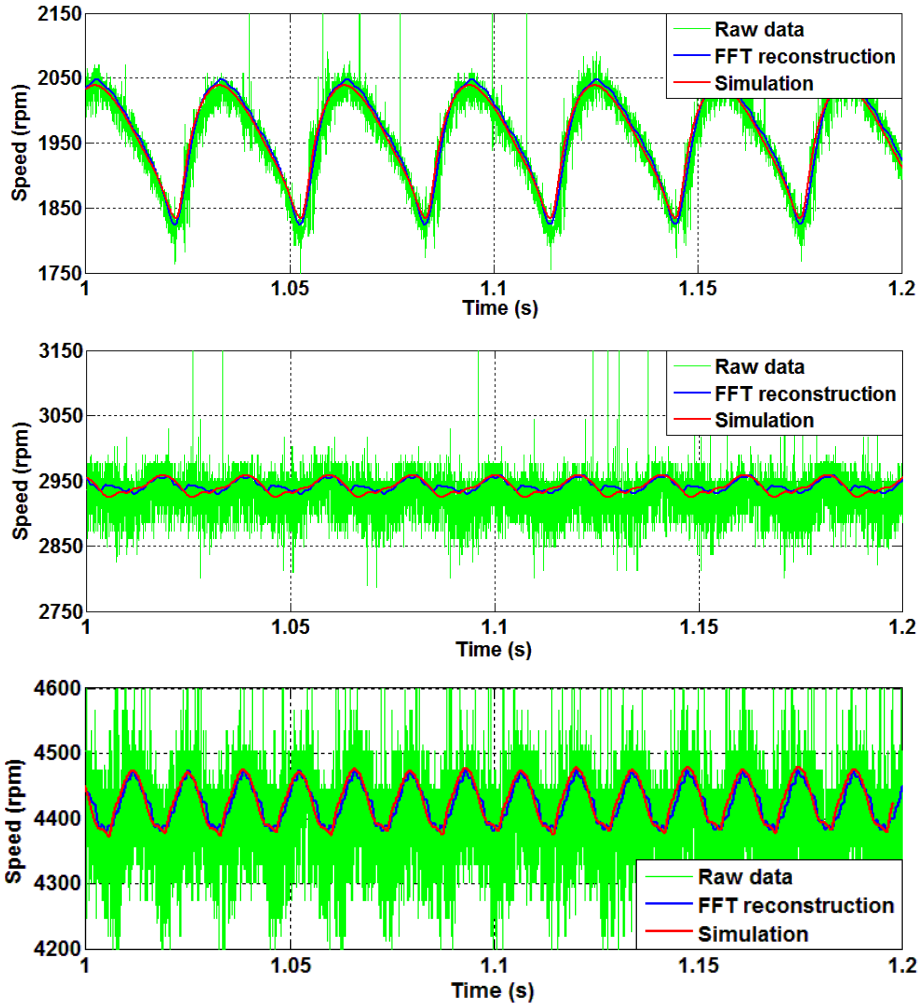

Figure 6-12 Simulation and test data of the speed fluctuation at 2000rpm WOT (top), 3000rpm, 2kW (middle) and 4500rpm WOT (bottom)

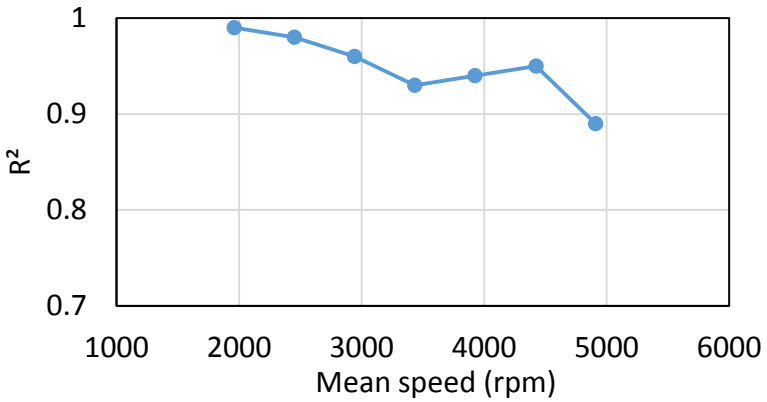

Figure 6-13 R^2 between the test data and simulation results at WOT

With the reconstructed speed profile, more consistent speed fluctuation values across the complete operating range were obtained. The in-cycle speed oscillation map for this prototype APU with DTC disabled is plotted in Figure 6-14. The numbers on the contour line are the speed fluctuation in rpm which were the difference between the maximum and minimum instantaneous speed in the reconstructed traces. As observed in the map, at the same load condition, lower mean speed allowed the rotating inertia having longer time to accelerate/decelerate which resulted in larger speed oscillation. At the same speed, higher load brought high in-cylinder combustion pressure which lead to faster speed acceleration. The general trend showed in the map is that the most severe scenario is at top left corner and spread out to bottom right corner with a dropping manner.

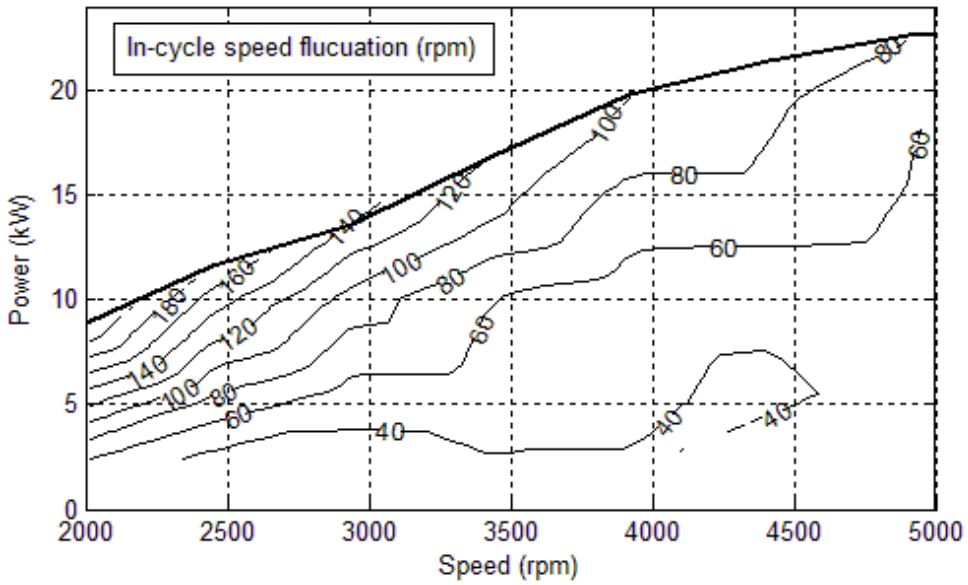

Figure 6-14 In-cycle speed fluctuation map

6.4 In-cycle speed fluctuation with DTC on

After defining the original engine/APU speed fluctuation, the DTC function was turned on to test its effectiveness. Before presenting the test results, the actual control process of the DTC strategy in the generator control unit (GCU) will be introduced first.

The speed control loop was still set at 200Hz. A look-up table was added after the mean torque demand from the speed regulating PID controller. This table was three-dimensional whose axes were the mean APU speed, the mean shaft torque and the crank position. The contents of the table were the predefined torque variations (Δtorque). They will be added on top of the instantaneous mean torque as requested from the speed controller. When the DTC was requested over CAN, the GCU would not instantly enable the function until the rotor mechanical position reached cylinder one TDC (+/- 4 degrees).

Therefore, the DTC maps developed in the CHAPTER - 5 had to be converted to Δtorque instead of the absolute torque regarding to the crank position. Furthermore, since the engine physical TDC was not necessarily the same as the TDC of the inverter encoder, this offset needed to be determined and included in the DTC tables before uploading to the control software. The engine cylinder one spark plug was removed and a dial gauge was inserted to touch the piston crown. The crankshaft was turned manually until the piston reached TDC. The encoder position reading from the GCU software was noted. Due to the rotor magnets cogging effect, the crankshaft was not easy to stop at the exact TDC position. Therefore, the rotor position reading at engine TDC was taken three times and the average was used.

The inverter (Inverter 1) suffered an electrical failure during other testing work before the DTC validation test. It was replaced by an identical back-up inverter (Inverter 2). However, the mean speed offset error had not been solved and the difference became more severe than before. Figure 6-15 shows the offset differences of the two inverters.

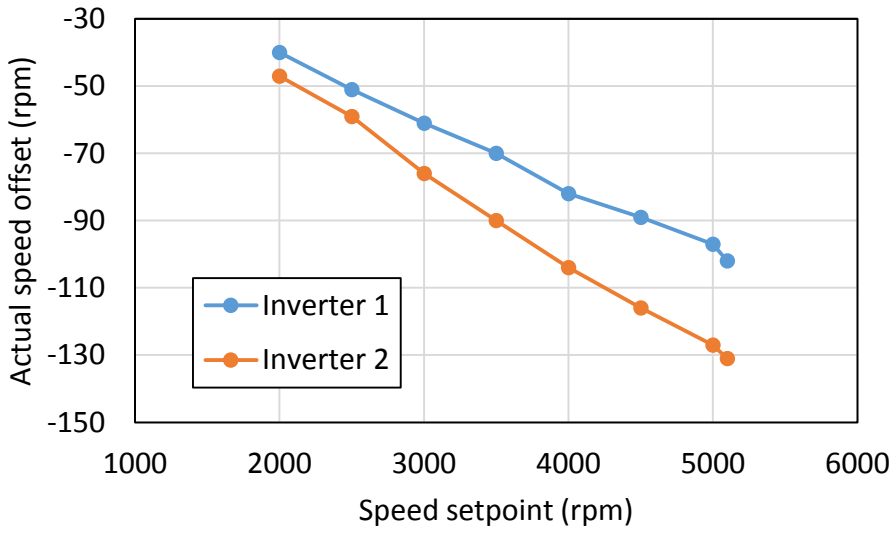

Figure 6-15 Speed offset difference between the two inverters

The APU was set to run at 2000rpm WOT first. The instantaneous speed was logged with both DTC enabled and disabled in the same testing session in order to

have a direct comparison. The speed data was processed by the same reconstruction method, i.e. up to 10th order harmonics were used. The instantaneous speed plot with DTC disabled is shown in Figure 6-16. The simulation results did not match the test data as well as previously with the old inverter (Inverter 1). The previous test data is also plotted in the figure. Since there was difference on the encoder speed offset, the plots were manually aligned to have a clearer comparison.

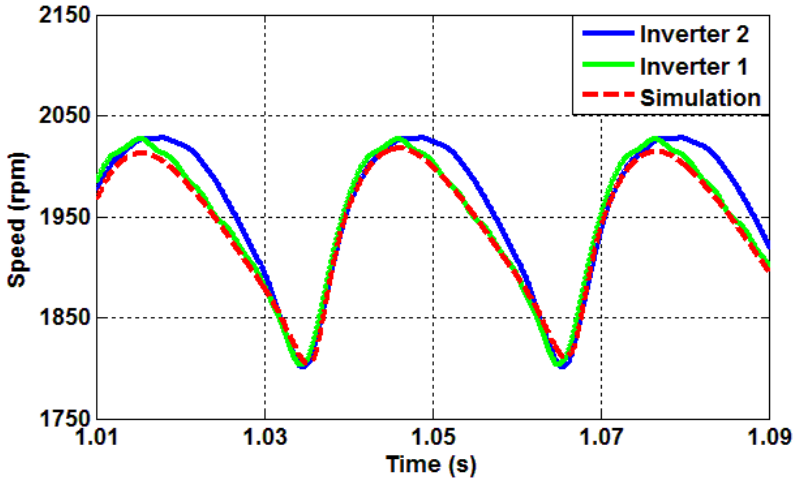

Figure 6-16 Instantaneous speed difference with two inverters at 2000rpm WOT without DTC

The speed trace at 2000rpm WOT with DTC enabled is shown in Figure 6-17 together with the simulation prediction. An obvious mismatch occurred at about the same crank position as the seen in Figure 6-16 with DTC disabled. On the other hand, the results on the peak-to-peak speed compression was closely predicted by the simulation model at this setpoint. The model forecasted that the speed oscillation range could decreased from 213rpm to 174rpm while the actual test data indicated the number dropped from 227rpm to 180rpm. The side-by-side comparison of the simulation and the test data is given in Figure 6-18.

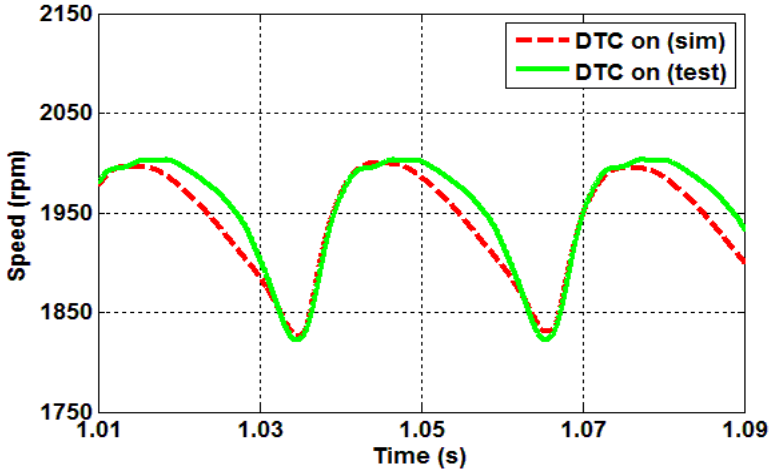

Figure 6-17 Instantaneous speed enabled at 2000rpm WOT with DTC

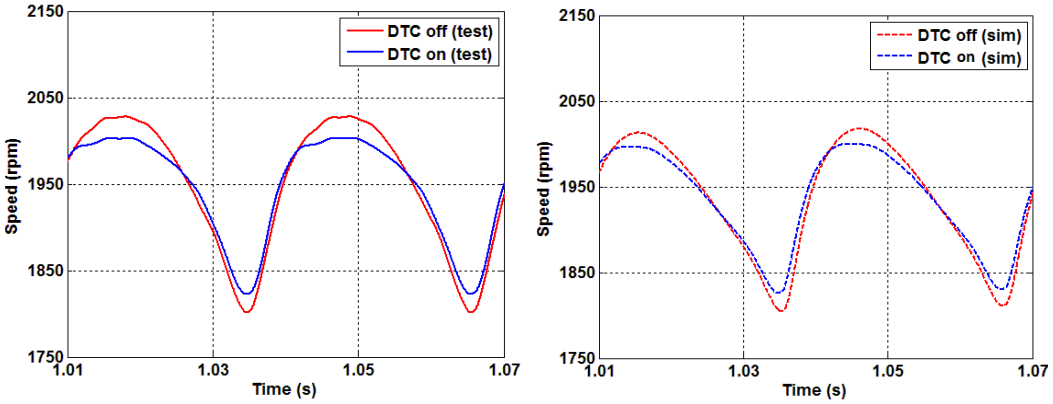

Figure 6-18 DTC effect at 2000rpm WOT from testing (left) and simulation (right)

Since there was no direct torque measurement, what the real M/G output torque was and how well the M/G followed the torque demand were not possible to be captured. Further test and analysis were needed and the results would also be helpful for understanding the speed profile alternation after replacing the inverter. The test conducted first was the torque pattern phase alignment test. the purpose of the test was to check whether the crank positions in the DTC table were wrongly defined with respect to the actual engine TDC, i.e. whether the DTC torque pattern and the engine torque pattern were out of phase. The original DTC definition table was shifted by +/- 15 CA deg with 5 CA deg step and applied to the APU. The speed fluctuations regarding to the table offset at 2000rpm WOT are plotted in Figure 6-19. The results

indicated the original table uploaded in the GCU was correctly aligned. This is not the reason for the mismatched speed profiles.

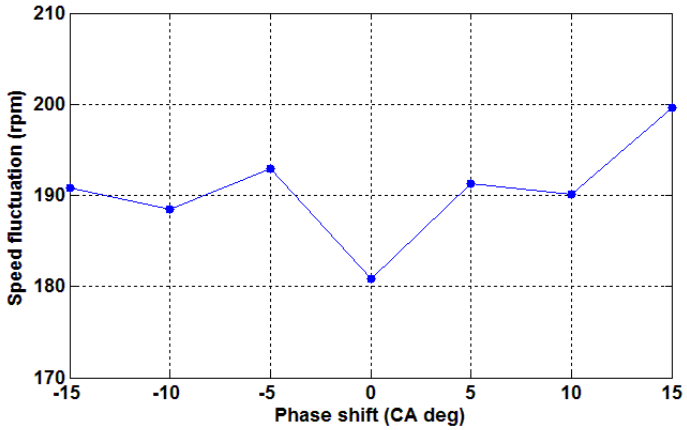

Figure 6-19 DTC phase sensitivity test results at 2000rpm WOT

To restore the real load torque pattern applied by the M/G, the simulation model was used in order to calculate inversely from the only available instantaneous speed test data. Two idealised assumption were made in the model. The first one is that the rotating inertia (crankshaft and the rotor assembly) was assumed as a rigid body, i.e. no twist would occur, while the second one was that the torque delivered by the engine was assumed the same as derived from earlier simulation. The speed data was differentiated to obtain the instantaneous shaft acceleration. The resultant torque from the engine and the M/G was the product of the angular acceleration and the moment of inertia. By removing the hypothetical engine torque, the M/G torque could be crudely restored. The restored M/G torque for Inverter 1 and Inverter 2 at 2000rpm WOT without DTC are presented in Figure 6-20. The less regulated torque control behaviour from the second inverter was obviously shown. It was potentially the major factor which led to the no longer well matched curves from the test data and the simulation. Although this only provided rather rough results, it is still useful for comparison purposes. This method was also used to restore the DTC torque. However, since Inverter 1 was not tested with DTC, there was only result for Inverter 2 as in Figure 6-21. The wider and flatter tip in the speed trace as observed in Figure 6-17 was caused by that the actual M/G torque followed the engine torque trace for longer period

than the demand as seen in the yellow circle. The steeper speed trace slope at the cycle end of the speed trace in Figure 6-17 indicated a higher torque than the demand was exerted as in the purple circle. Both phenomenon suggested a less frequently regulated control presented in Inverter 2.

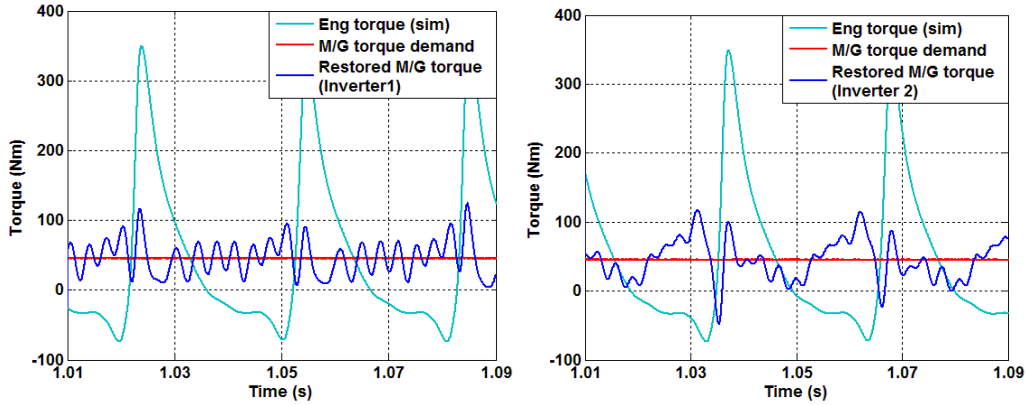

Figure 6-20 Restored M/G torque at 2000rpm WOT with DTC disabled

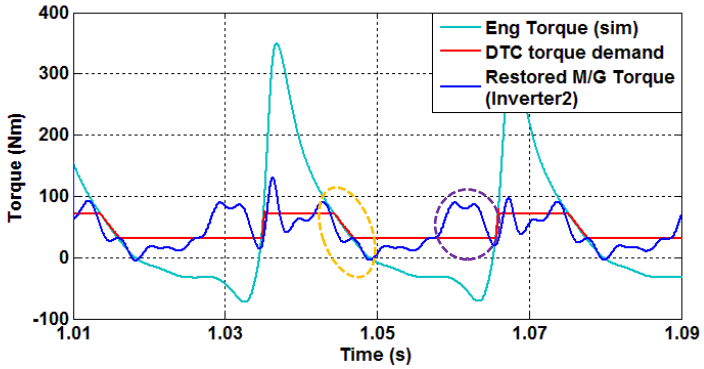

Figure 6-21 Restored torque at 2000rpm WOT with DTC enabled

The second setpoint for the DTC testing was at 4500rpm WOT. The in-cycle speed profile variation between the two inverters was analysed first. The raw data for both inverters were processed with the identical method used previously to remove the unwanted noise. Figure 6-22 shows the comparison after aligned the mean speed offset. Obvious high frequency oscillation still could be observed after the same extent filtering action, although the general trend of the speed profile was close to Inverter 1. This might indicate a lower control frequency, or in other words, a larger control loop interval presented in Inverter 2. Since the shaft speed was higher, larger crank angle swept during the same control interval and resulted more noticeable oscillation than at

2000rpm. Another possible reason for this nosier result could be the less effective electromagnetic interference (EMI) control of the second inverter. The more pronounced noise was picked up by the measurement system and the raw data was contaminated.

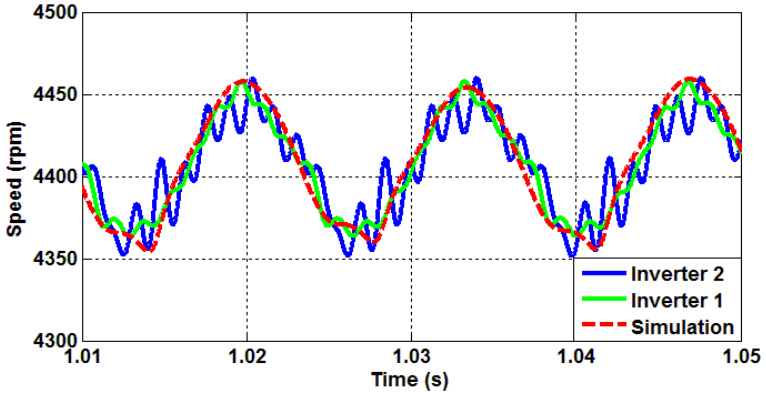

Figure 6-22 Instantaneous speed difference with two inverters at 4500rpm WOT without DTC

However, because of the relatively nosier reconstructed speed profiles from both inverters, the restoration of the M/G torque even at constant torque condition was not ideal. As shown in Figure 6-23, high amplitude spiky results were obtained which could not provide persuasive evidence for any conclusion.

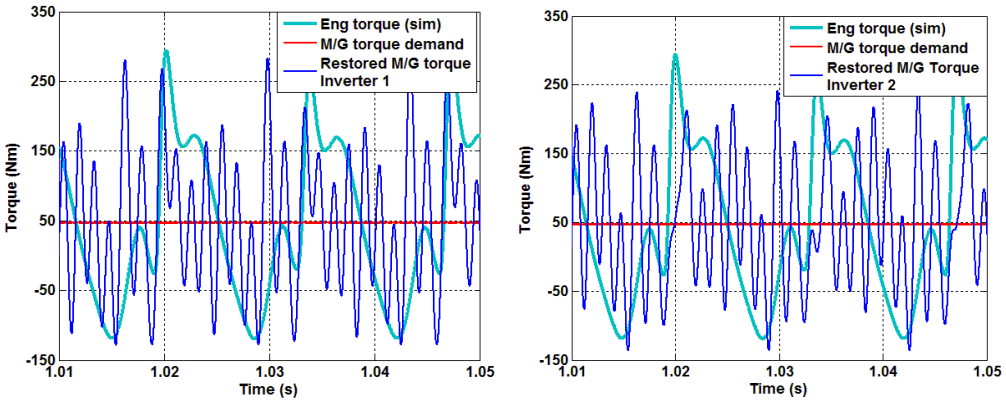

Figure 6-23 Restored M/G torque at 4500rpm WOT with DTC disabled

When the DTC function was enabled, both patterns with and without compression stroke pulse were deployed to examine the difference during the test. The results are plotted in Figure 6-24. The simulation results and the test data showed the

trends that were generally matched. However, the peak-to-peak speed fluctuation numbers were affected by the noise spikes. The DTC with compression stroke pulse gave a peak-to-peak fluctuation of 111.6rpm whist the DTC without compression stroke pulse had a peak-to-peak fluctuation of 97.4rpm. They both are higher than the simulation results which was 82.5 rpm. Nevertheless, if comparing the two reconstructed waveforms, a relatively smoother speed profile was achieved the one without the compression stroke pulse. It suggested that the simpler DTC torque pattern design was beneficial to the controller and made the system easier to stabilise.

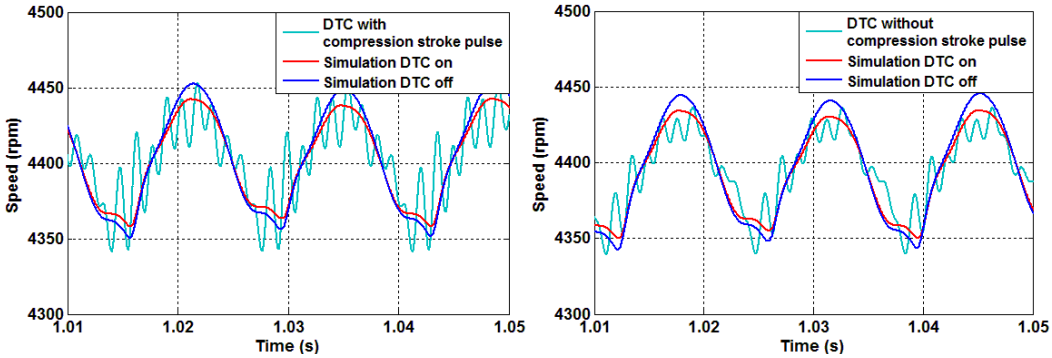

Figure 6-24 DTC effect at 4500rpm WOT

According to the results with both DTC enabled and disabled conditions, the more spiky speed traces after the same filtering process when using Inverter 2 suggested that the second inverter might have lower power electronics switching frequency and less EMI control than the first one. However, this hypothesis could not be verified due to the unavailability of inverter status ports for high-speed data logging. The machine parameters, such as the phase current, would be very helpful for further investigation.

As seen in Figure 6-23, the restored M/G torque from the filtered speed profile was in high frequency and high amplitude, this does not physically exist in real due to the M/G capability. It is potentially because of the difference in the electrical noise control between the two inverter which affected the measurement signals. In order to minimise the effect of the noise spikes on the speed fluctuation results, the raw data

needs to be further filtered. Instead of using the first ten harmonics to reconstruct the speed profile, only the first six were used to obtain relative smoother plots which are shown in Figure 6-25. As seen in Table 6-1, the speed fluctuation peak-to-peak results are closer to the simulation.

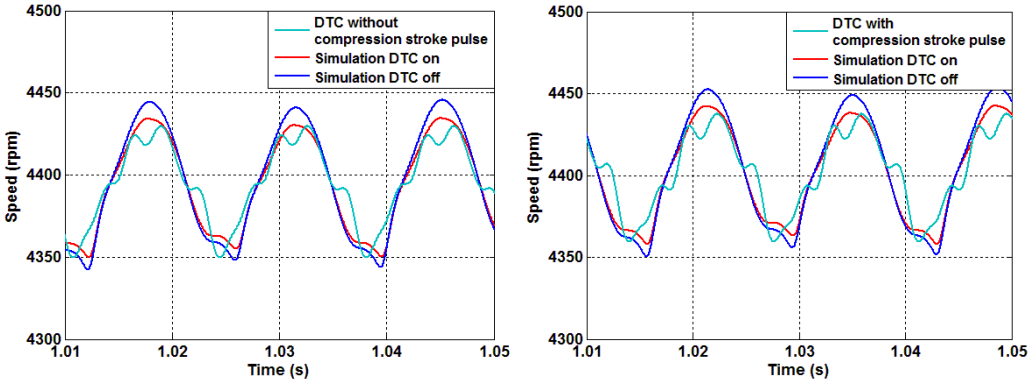

Figure 6-25 Speed fluctuation data at 4500rpm WOT with further filtering

As the prototype APU handled the DTC strategies without issues so far, a more sophisticate torque pattern (06-04, Figure 5-13) was deployed at 4500rpm. This pattern was considered more aggressive since it requested the M/G transfer to motoring mode for a short of period during the engine compression stroke. It was first tried with a partially opened throttle (15%) and the APU expressed audible speed oscillation for about two seconds and stabilised itself afterwards. This consequence and the successful two runs earlier at other setpoints built up the confidence to test this torque pattern at full load condition, for which the torque pattern was designed. However, unfortunately, the APU became unstable and could not regulate itself. The M/G tripped after about five seconds. Then, the engine over sped and triggered the system hardware protection.

When the system restarted, an 'IGBT fault' error displayed in the GCU software which indicated hardware damage. Since all the M/G status monitoring messages were restricted to the CAN channels by the OEM, the GCU can only communicate with the host PC at 80Hz. This bandwidth was too slow to capture useful information during this severe accident for failure analysis. The OEM did not have a conclusive

explanation from this hardware failure by the time this thesis was completed. Considering there were still other tests scheduled after the failure, the DTC strategy was not planned for further testing with the last functioning prototype inverter. Therefore, the DTC experimental data for this study was only available at 2000rpm WOT and 4500rpm WOT. Table 6-1 shows the peak-to-peak speed fluctuation results from simulation and bench test. The numbers in the bracket of the speed column is the actual mean speed due to the encoder offset. The numbers in the bracket for 4500rpm are the results with heavier filtering process to remove the noise spikes.

Table 6-1 APU speed fluctuation results from simulation and bench test

Test No.	Speed (rpm)	DTC	Speed fluctuation (rpm) Simulation	Speed fluctuation (rpm) Test
1 (Inverter 1)	2000 (1960)	Off	208.6	224.1
	4500 (4411)	Off	101.6	94.3
2 (Inverter 2)	2000 (1944)	Off	210.2	226.7
	2000 (1942)	On	171.5	180.8
3 (Inverter 2)	4500 (4391)	Off	102.1	108.0 (*86.6*)
	4500 (4403)	On (with compression stroke pulse)	82.6	111.6 (*78.0*)
	4500 (4395)	On (without compression stroke pulse)	82.5	97.4 (*80.1*)

6.5 The effect on the system efficiency with DTC

Since there was no direct shaft torque measurement in the APU testing setup, the exact mechanical power output from the engine to M/G was not possible to be calculated. Therefore, the direct assessment of the efficiency change of the system energy conversion process due to the DTC strategy was not feasible. The ESFC, as it only considers the source (fuel) and the final product (electrical energy), is an alternative parameter that could be used to calculate the efficiency of the entire APU. However, an assumption still had to be made. The engine performance was assumed not variable regardless whether the DTC was enabled or not. This was plausible since

in the control structure, the ASC did not feed the DTC enable signal to the EMS which controlled the engine operation. Since the engine was in torque control mode, it should not response to the instantaneous speed fluctuation, even if the in-cycle speed was changed by the DTC

Table 6-2 presents the output power and ESFC data collected during the APU bench tests. Test No.0 is the benchmark data which was collected before the M/G installed, i.e. engine standalone test. For all APU tests, 20000rpm WOT condition data is shaded in green while yellow shading for 4500rpm WOT. The numbers in the bracket of the speed column are the actual shaft speed due to the M/G encoder offset.

Table 6-2 APU power and efficiency test data

Test No.	Speed (rpm)	DTC	Electrical power (kW)	Fuel flow rate (g/s)	ESFC (g/kWh)	ESFC growth
0	2000 (2000)	-	9.60 (mech)	0.66	247.58	-
	4500 (4500)	-	22.20 (mech)	1.83	296.79	-
1 (Inverter 1)	2000 (1960)	Off	8.70	0.66	273.10	-
	4500 (4411)	Off	21.21	1.82	308.91	-
2 (Inverter 2)	2000 (1944)	Off	8.63	0.66	275.32	-
	2000 (1942)	On	8.40	0.66	282.86	2.74%
3 (Inverter 2)	4500 (4391)	Off	21.04	1.81	309.70	-
	4500 (4403)	On (with compression stroke pulse)	20.47	1.79	314.80	1.65%
	4500 (4395)	On (without compression stroke pulse)	20.67	1.81	315.24	1.79%

These figures showed that the fuel flow rate was consistent at 2000rpm irrespective to the DTC function while at 4500rpm there was a slightly change. However, the deviation was within 1%. This proved the consistency of the engine behaviour. When the DTC was disabled, the electrical output power reduction was observed between tests. At 2000rpm, the electrical power delivered dropped from 8.70kW (Test 1) to 8.63kW (Test 2) and at 4500rpm, it dropped from 21.21kW (Test

1) to 21.04kW (Test 3). This change was considered caused by the two inverters control behaviour variance rather than the mean speed decrease when Inverter 2 was fitted. This is because that, by assuming the engine torque was not sensitive enough to vary due to such small mean speed difference, the speed differences could not be the reason for the power loss.

When DTC enabled, the electrical power and efficiency drop was recorded as expected due to the in-cycle torque variation. The ESFC increased by 2.74% at 2000rpm WOT while at 4500rpm WOT, it increased by 1.65% and 1.79% with and without compression stroke pulse respectively. The ESFC test data with DTC enabled were compared with the simulation results presented in Table 6-3. A good estimation by the Simulink model was achieved under these three conditions.

Table 6-3 Test data of the ESFC with DTC

ESFC (g/kWh)	Test data	Simulation	Simulation error
2000rpm DTC	282.86	289.05	2.19%
4500rpm DTC (with compression stroke pulse)	314.80	319.59	1.52%
4500rpm DTC (without compression stroke pulse)	315.24	319.44	1.33%

Table 6-4 Test data of the loss increase due to DTC

Electrical loss increase (W)	Test data	Simulation	Simulation error
2000rpm DTC	170	174.2	2.47%
4500rpm DTC (with compression stroke pulse)	570	279.3	-51.00%
4500rpm DTC (without compression stroke pulse)	370	269.5	-27.16%

With DTC was turned on, if the electrical power decease was considered fully due to the additional losses introduced, the results comparison with the simulation are presented in Table 6-4. As the speed increases, the underestimation became more

significant which could be caused by the frequency dependent loss terms, i.e. iron loss and Eddy current loss. However, the difference had very limited effect on the overall system efficiency ESFC estimation as seen in the table above. Nevertheless, since the loss models for the electric machine and the inverter could not be accurately calibrated during the model development process, the well matched ESFC results should be further investigated to determine whether it was a coincidence due to the small absolute value of the loss. However, the project time constraint and the availability of the test unit and facilities made this piece of work could not be conducted any further. No more data sets were available by the time when this thesis was completed.

6.6 Conclusion

This chapter presents the testing work and results for the APU with DTC strategy deployed. After the standalone testing and optimisation, the engine was coupled with the M/G to constitute the prototype APU. A high-speed data acquisition system was used to record the instantaneous shaft speed from the engine side optical encoder in 200kHz. The raw speed data logs contains a significant amount of noise which was undesired for the following analysis especially at low load or high speed operation points. Simply processing the data with a low pass filter was not very effective. Therefore, the speed logs were converted into the frequency domain and reconstructed with first ten harmonics of the engine firing frequency. Satisfiactory results were obtained through this method.

The APU was tested with DTC disabled across the complete operation range. The speed fluctuation profiles were well matched by the simulation results and high coefficient of determination was achieved. The speed fluctuation map of this APU was also created. The APU then was tested with DTC function turned on. The different behaviour of the replacement inverter was noticed and the simulation results could not match the test data as well as before. The inverter inconsistency was evidenced by further data analysis, such as the M/G torque restoration analysis. However, the speed

oscillation reduction effect by the DTC was still captured at 2000rpm WOT and 4500rpm WOT. The system efficiency decreased as the simulation model estimated. The model results on the ESFC raise extent was close to the actual measurements which was within 2.19% error. However, the electrical loss was underestimated at high speed conditions. The reason for this needs further investigation with accurate loss model calibration. However, due to hardware failure and other limitations, this could be completed within the project time timescale.

The DTC strategy did successfully showed the effectiveness on the in-cycle speed fluctuation reduction on a working prototype APU with less than 3% increase on ESFC at 2000rpm WOT and 4500rpm WOT.

CHAPTER - 7
Conclusion and Future Work

This chapter concludes this research work and highlights the key findings and results. The potential improvements and future extension of this research are discussed.

7.1 Conclusion

This research work aims to design and test a Dynamic Torque Control (DTC) strategy for an APU using a novel approach to reduce the system in-cycle speed fluctuation. A low-cylinder-count engine exposes more severe speed fluctuations due to its low firing frequency. Since the engine and the M/G are isolated to the vehicle driving wheels, it is possible to make the electric machine from deliver a counteracting torque to the engine reducing the resultant torque spikes thus the system speed oscillation. The DTC in-cycle torque demand was designed basing on detailed analysis on the contribution factors on the speed fluctuation and the electric machine losses.

The engine used in the APU was modelled to recreate the engine in-cycle torque waveform. Three torque components was considered which are the gas pressure torque, the moving components inertia torque and the friction torque. The gas pressure torque and the friction torque were empirically modelled. They were based on the test bench data while the inertia torque was analytically modelled. The resultant simulation torque was validated against the 1-D engine simulation results. Well matched torque waveforms were seen.

The electric machine was modelled using analytical equations initially. It was found that oversimplified parameters resulted in significant torque overestimation for this machine. Instead of being a constant, in a real machine, the winding inductance tends to saturate as the current increases. The current saturation effect was then assessed using FEA software. In order to include the inductance variation due to current without using the FEA model in the real time simulation, the DQ inductances results at various load were extracted from the FEA model. These data were populated into tables and implemented in the analytical model. However, at high current load, the user defined material properties were wrongly projected which led to unrealistic results in the FEA. This issue was corrected by extrapolating and interpolating the FEA inductance results using a method developed by the author. After the recalibration, at

peak current load, the simulation torque error, as compared to the test data, dropped from 5.6% to 1.2%. Furthermore, the inverter control logic, which is SV-PWM, and the hardware were modelled separately. These measures helped to have a better estimation of the inverter behaviour and its electrical losses. The transient step torque response of the M/G was also studied. The asymmetrical response time on rising and falling demands, which was not previously discussed in the literature, was noticed. It was shown to be due to the one-direction only characteristic of the back-EMF.

With the complete system model created, the DTC strategy was developed. Five series of square wave torque patterns were tried on the system. It was found that a compromise between a short high amplitude impulse and a long low amplitude torque was necessary for optimal speed fluctuation reduction. The sixth pattern series was design with more complicated shapes to maximise the DTC effectiveness. The speed fluctuation was found to be limited by the M/G peak torque capability. A linear correlation between the M/G peak torque and the speed fluctuation was found. Further electric loss analysis was performed on different DTC torque patterns to help understand the DTC effect on the machine and inverter loss. Two final DTC maps for the APU entire speed range were developed. According to the simulation results, the speed fluctuation was reduced along the entire speed range up to 25.54% (2000rpm WOT). As expected, both the machine and the inverter losses increased. When the DTC map without compression stroke pulse was deployed, it can introduced 7.5% less extra loss compared to the one with compression stroke pulse while only hardly noticed higher speed fluctuation was gained at 5000rpm WOT. Furthermore, a flatter torque demand is easier for the control and beneficial for the system stability. Due to the extra losses, the fuel consumption was predicted increased between 1.2% and 2.43%.

The DTC strategy was then implemented in the prototype APU and tested on the rig. The raw speed data, which was collected by a high speed data acquisition system, was reconstructed through FFT analysis to remove the noise. Very well matched

simulation speed profiles and test data were observed with a high coefficient of determination (R^2). Some inconsistent behaviours of a second example of the inverter was noticed and the simulation results could not match the test data as well as before. However, the speed oscillation reduction effects by the DTC was still captured at 2000rpm WOT and 4500rpm WOT. The system efficiency decreased, in line with the simulation model estimates, was within an error of 2.19%. The DTC strategy successfully showed the effectiveness on the in-cycle speed fluctuation reduction on a working prototype APU.

From the simulation and the test results, the speed fluctuation benefits delivered by the DTC strategy is not as obvious as the cost on the fuel economy. The principle, which is to inject torque pulses to the crankshaft, could also be used in other hybrid architectures, such as P1 and P2. By adding additional torque pulses between engine combustion events, the engine vibration could be moved to a higher frequency band which is less noticeable to the passengers and easier to be damped by softer mounts.

7.2 Research limitations

In the course of this study, unforeseen circumstances led to some weakness and limitation of this research work that all readers should be aware.

During the project, the motor/generator was not available to be decoupled from the engine for individual characterisation tests on the rig. Only a few basic test data sets were available from the OEM. This made the electrical machine modelling and model calibration rather difficult. Unnecessary assumptions on some machine parameters, which could be derived by testing, could not be avoided. Furthermore, without individual testing, the machine and inverter loss could not be separated for efficient loss model validation.

In the engine modelling section, a mean friction model was used. However, in a real engine, the rubbing action and load from various parts and auxiliary systems forms the total friction which can never be a constant if resolved in the crank angle domain. However, due to insufficient time allocated to the engine friction tear down test, the detailed friction could not be considered in the model.

The engine in-cycle torque could not be clearly measured during the engine standalone test for model referencing. The torque transducer was located at the dynamometer end resulting in the engine torque being smoothened by the significant damping effect of the propeller shaft. Relocating the torque flange involves a large amount of rig modification work which was not allowed by the project timing frame. This is a lesson learned from the lack of foreseen on these issues.

7.3 Future work

This research work presented the initial development of the DTC strategy for a low cost, high efficiency APU. It laid the foundation for future development and improvement on the both theoretical and practical aspects in this area.

As discussed in the CHAPTER - 5 , the dynamic torque control will bring extra losses on the electrical system which primarily occurred in the electrical machine. The temperature change caused by the loss variation does have influence on the material properties and thus machine performance. Both transient and steady state effect from the fast alternating torque and current should be investigated further. This study leads to the requirement for a system thermal model. The model should be able to interact with the loss results from FEA and feed back the temperature or updated instantaneous material properties for the next time step. This involves more FEA simulation which comes at high computational cost.

Since the IC engine used in this project has only two cylinders with an even firing order, the two pistons always move in the same direction. A large primary rotating force is exerted on the crank bearings and thus the entire engine block. Therefore, a single balancer shaft that rotates at the same speed as the crankshaft but opposite direction is placed inside the engine to balance out the primary force. However, the extra rotating component in the engine will lead to the increase of the cost, weight and friction. In some modern engine design cases, the balance shafts are eliminated. The Ford 1.0L EcoBoost three-cylinder engine gives is a good example. The engineers intentionally make mass distribution of the flywheel and the crank pulley eccentric [109].

As in this project, the electric machine rotor is directly coupled to the crankshaft, there are opportunities to modify the rotor flywheel weight distribution so that the balancer shaft can be removed. Since the flywheel is not the part that contributes to the magnetic flux path of the electric machine, the rotor is still electromagnetically balanced at the circumference but physically eccentric. The possibly resulted additional weight of the flywheel-rotor assembly can also benefit the in-cycle speed variation since the rotating inertia would increase as well. However, this modification will introduce an unbalanced primary moment. The original engine has a single balance counter weight located at the middle point between the two crank pins with the purpose of matching the moments from different locations. Unavoidable unbalanced moment occurs to the crank axis if a counter weight is added at one end only. Therefore, modifying the current rotor mechanical design can be beneficial to the reduction of system friction, overall weight and vibration for this low-cylinder-count engine.

References

1. NADA Used Car Guide, *Plug-in Electric Vehicles: Market Analysis and Used Price Forecast*. 2013, National Automobile Dealers Association, .

2. Hurst, D. and Gartner, J., *Executive Summary: Electric Vehicle Market Forecasts*. 2013, Navigant Research.

3. Ribau, J., Silva, C., Brito, F.P., and Martins, J., "Analysis of four-stroke, Wankel, and microturbine based range extenders for electric vehicles," *Energy Conversion and Management*, 58: 120-133, 2012, doi:10.1016/j.enconman.2012.01.011.

4. Hall, J., Marlok, H., Bassett, M., and Warth, M., "Analysis of Real World Data from a Range Extended Electric Vehicle Demonstrator," *SAE Int. J. Alt. Power.*, 4(1): 20-33, 2014, doi:10.4271/2014-01-2887.

5. Fraidl, G.K., Beste, F., Kapus, P.E., Korman, M., et al., "Challenges and Solutions for Range Extenders - From Concept Considerations to Practical Experiences," SAE Tehcnical Paper 2011-37-0019, 2011, doi: 10.4271/2011-37-0019, (http://dx.doi.org/10.4271/2011-37-0019).

6. Bhiwapurkar, N. and Ganti, V., "Comparison of On-Board Charging Strategies for Range-Extender Hybrid Vehicles with Lead-Acid Batteries," Vehicle Power and Propulsion Conference (VPPC), 2013 IEEE, 15-18 Oct. 2013, 2013, doi: 10.1109/VPPC.2013.6671669

7. Rogge, M., Rothgang, S., and Sauer, D.U., "Operating Strategies for a Range Extender Used in Battery Electric Vehicles," presented at Vehicle Power and Propulsion Conference (VPPC), 2013 IEEE, 15-18 Oct. 2013, 2013, doi: 10.1109/VPPC.2013.6671695

8. Pischinger, M., Tomazic, D., Wittek, K., Esch, H.-J., et al., "A Low NVH Range-Extender Application with a Small V-2 Engine - Based on a New Vibration Compensation System," presented at SAE Tehcnical Paper 2012-32-0081, 2012, doi: 10.4271/2012-32-0081, doi: 10.4271/2012-32-0081, (http://dx.doi.org/10.4271/2012-32-0081).

9. Tulpule, P., Marano, V., and Rizzoni, G., "Effects of different PHEV control strategies on vehicle performance," presented at American Control Conference, 2009. ACC '09., 10-12 June 2009, 2009, doi: 10.1109/ACC.2009.5160595

10. Capaldi, P., "A Compact 10 kW Electric Power Range Extender Suitable for Plug-In and Series Hybrid Vehicles," presented at SAE Technical Paper 2011-

24-0085, 2011, doi: 10.4271/2011-24-0085, (http://dx.doi.org/10.4271/2011-24-0085).

11. Liang, Y.-C., Tsai, H.-C., Peng, Y.-W., and Wu, Y.-Y., "Development of Torque-Based Engine Management System for Range Extender Engine," presented at SAE Technical Paper 2013-32-9062, 2013, doi: 2013-32-9062

12. Bassett, M., Hall, J., Kennedy, G., Cains, T., et al., "The Development of a Range Extender Electric Vehicle Demonstrator," presented at SAE Technical Paper 2013-01-1469, 2013, doi: 10.4271/2013-01-1469, doi: 10.4271/2013-01-1469, (http://dx.doi.org/10.4271/2013-01-1469).

13. Bassett, M., Fraser, N., Brooks, T., Taylor, G., et al., "A Study of Fuel Converter Requirements for an Extended-Range Electric Vehicle," *SAE Int. J. Engines*, 3(1): 631-654, 2010, doi:10.4271/2010-01-0832.

14. Al-Adsani, A.S., Jarushi, A.M., and Schofield, N., "An ICE/HPM generator range extender in a series hybrid electric vehicle," presented at Power Electronics, Machines and Drives (PEMD 2010), 5th IET International Conference on, 19-21 April 2010, 2010, doi: 10.1049/cp.2010.0152

15. Bassett, M., Thatcher, I., Bisordi, A., Hall, J., et al., "Design of a Dedicated Range Extender Engine," SAE Technical Paper 2011-01-0862, 2011, doi: 10.4271/2011-01-0862, (http://dx.doi.org/10.4271/2011-01-0862).

16. Rust, A. and Graf, B.J., "NVH of Electric Vehicles with Range Extender," *SAE Int. J. Passeng. Cars - Mech. Syst.*, 3(1): 860-867, 2010, doi:10.4271/2010-01-1404.

17. Hubmann, C., Beste, F., Friedl, H., and Schoffmann, W., "Single Cylinder 25kW Range Extender as Alternative to a Rotary Engine Maintaining High Compactness and NVH Performance," presented at SAE Tehcnical Paper 2013-32-9132, 2013, doi: 2013-32-9132

18. Govindswamy, K., Tomazic, D., Genender, P., and Schuermann, G., "The NVH Behavior of Internal Combustion Engines used in Range Extended Electric Vehicles," presented at SAE Technical Paper 2013-01-2002, 2013, doi: 10.4271/2013-01-2002, doi: 10.4271/2013-01-2002, (http://dx.doi.org/10.4271/2013-01-2002).

19. Nakajima, Y., Uchida, M., Ogane, H., and Kitajima, Y., "A study on the Reduction of Crankshaft Rotational Vibration velocity by using a Motor-Generator," *JSAE Review*, 21, Issue 3(3): 335-341, 2000, doi:http://dx.doi.org/10.1016/S0389-4304(00)00045-X.

20. Ayana, E., Plahn, P., Wejrzanowski, K., and Mohan, N., "Active Torque Cancellation for Transmitted Vibration Reduction of Low Cylinder Count Engines," presented at Vehicular Technology, IEEE Transactions on, 2011, doi: 10.1109/TVT.2011.2159255

21. Ayana, E., Plahn, P., and Wejrzanowski, K., "Active Torque Cancellation for transmitted vibration reduction of low cylinder count engines," IEEE Vehicle Power and Propulsion Conference, 7-10 Sept., 2009, doi: 10.1109/VPPC.2009.5289833

22. Capaldi, P., Del Pizzo, A., Rizzo, R., and Spina, I., "Torque-oscillations damping in micro-cogeneration units with high brake mean pressure engines and PM-brushless generators," Energy Conference and Exhibition (ENERGYCON), 2012 IEEE International, 9-12 Sept. 2012, 2012, doi: 10.1109/EnergyCon.2012.6347737

23. Teichmann, R., Moik, J., and Hohenberg, G., "Two worlds are merging – Optimization of a hybrid drive," 11th International Symposium on Combustion Diagnostics, 2014

24. Ito, Y., Tomura, S., and Sasaki, S., "Development of Vibration Reduction Motor Control for Hybrid Vehicles," Industrial Electronics Society, 2007. IECON 2007. 33rd Annual Conference of the IEEE, 5-8 Nov. 2007, 2007, doi: 10.1109/IECON.2007.4460237

25. Davis, R.I. and Lorenz, R.D., "Engine torque ripple cancellation with an integrated starter alternator in a hybrid electric vehicle: implementation and control," Industry Applications Conference, 2002. 37th IAS Annual Meeting. Conference Record of the, 13-18 Oct. 2002, 2002, doi: 10.1109/IAS.2002.1043809

26. Morandin, M., Bolognani, S., Pevere, A., Calligaro, S., et al., "Active Torque Ripple Damping in Direct Drive Range Extender Applications: A Comparison and an Original Proposal," Vehicle Power and Propulsion Conference (VPPC), 2015 IEEE, 19-22 Oct. 2015, 2015, doi: 10.1109/VPPC.2015.7352891

27. Park, S., *A Comprehensive Thermal Management System Model for Hybrid Electric Vehicles*, in *Mechanical Engineering*. 2011, University of Michigan.

28. Park, S. and Jung, D., "Numerical Modeling and Simulation of the Vehicle Cooling System for a Heavy Duty Series Hybrid Electric Vehicle," presented at SAE Technical Paper 2008-01-2421, 2008, doi:10.4271/2008-01-2421, doi: 10.4271/2008-01-2421, (http://dx.doi.org/10.4271/2008-01-2421).

29. Kim, K.B., Choi, K.W., Lee, K.H., and Lee, K.S., "Active coolant control strategies in automotive engines," *International Journal of Automotive Technology*, 11(6): 767-772, 2010, doi:10.1007/s12239-010-0091-4.

30. GM-volt.com. *"The Chevrolet Volt Cooling/Heating Systems Explained"*. Available from: http://gm-volt.com/2010/12/09/the-chevrolet-volt-coolingheating-systems-explained/ (last access on 31/08/2014).

31. Klopstein, S., Lauer, S., and Maassen, F., "Interpretation Tools and Concepts for the Heat Management in the Drive Train of the Future," *SAE Technical Paper* 2011, doi:10.4271/2011-01-0650, doi:10.4271/2011-01-0650.

32. Cao, M., Kovent, I., and Ku, J., "Efficient Thermal Modeling and Integrated Control Strategy of Powertrain for a Parallel Hybrid EcoCAR2 Competition Vehicle," *SAE Technical Paper*, 2014, doi:10.4271/2014-01-1927, doi:10.4271/2014-01-1927.

33. Hsu, J.S., Staunton, M.R., and Starke, M.R., *Barriers to the Application of High-Temperature Coolants in Hybrid Electric Vehicles*. 2006, Oak Ridge National Laboratory Technical Report,.

34. Bennion, K. and Thornton, M., "Integrated Vehicle Thermal Management for Advanced Vehicle Propulsion Technologies," presented at SAE Technical Paper 2010-01-0836, 2010, doi: 10.4271/2010-01-0836, doi: 10.4271/2010-01-0836, (http://dx.doi.org/10.4271/2010-01-0836).

35. Ap, N.-S., Guerrero, P., Jouanny, P., Potier, M., et al., "UltimateCooling™ New Cooling System Concept Using the Same Coolant to Cool All Vehicle Fluids," presented at Vehicle Thermal Management Systems Conference (VTMS6), IMechE C599/010/2003, 2003

36. Revereault, P., Rouaud, C., and MarchI, A., "Fuel Economy and Cabin Heating Improvements Thanks to Thermal Management Solutions Installed in a Diesel Hybrid Electric Vehicle," *SAE Technical Paper* 2010, doi:10.4271/2010-01-0800, doi:10.4271/2010-01-0800.

37. Bucherl, D., Nuscheler, R., Meyer, W., and Herzog, H., "Comparison of electrical machine types in hybrid drive trains: Induction machine vs. permanent magnet synchronous machine," Electrical Machines, 2008. ICEM 2008. 18th International Conference on, 6-9 Sept. 2008, 2008, doi: 10.1109/ICELMACH.2008.4800155

38. Balkan Simsir, N. and Bulent Ertan, H., "A comparison of torque capabilities of axial flux and radial flux type of brushless DC (BLDC) drives for wide speed range applications," Power Electronics and Drive Systems, 1999. PEDS '99.

Proceedings of the IEEE 1999 International Conference on, 1999, 1999, doi: 10.1109/PEDS.1999.792793

39. Surong, H., Jian, L., Leonardi, F., and Lipo, T.A., "A comparison of power density for axial flux machines based on general purpose sizing equations," *Energy Conversion, IEEE Transactions on,* 14(2): 185-192, 1999, doi:10.1109/60.766982.

40. Aydin, M., Huang, S., and Lipo, T.A., "Axial Flux Permanent Magnet Disc Machines: A Review," SPEEDAM Capri Italy, 2004, (http://www.skif.biz/files/7d6e86.pdf).

41. Odvarka, E., Mebarki, A., Gerada, D., Brown, N., et al., "Electric motor generator for a hybrid electric vehicle," *Engineering MECHANICS,* 16(2): 131-139, 2006.

42. Barcaro, M., Bianchi, N., and Magnussen, F., "PM motors for hybrid electric vehicles," Universities Power Engineering Conference, 2008. UPEC 2008. 43rd International, 1-4 Sept. 2008, 2008, doi: 10.1109/UPEC.2008.4651682

43. Zhang, C., Tseng, K.J., and Nguyen, T.D., "Analysis and comparison of axial flux PM synchronous motor and induction motor," IPEC, 2010 Conference Proceedings, 27-29 Oct. 2010, 2010, doi: 10.1109/IPECON.2010.5697060

44. Colton, S.W., *Design and Prototyping Methods for Brushless Motors and Motor Control*, in *Department of Mechanical Engineering*. 2010, Massachusetts Institute of Technology.

45. Sung Chul, O. and Emadi, A., "Test and simulation of axial flux-motor characteristics for hybrid electric vehicles," *Vehicular Technology, IEEE Transactions on,* 53(3): 912-919, 2004, doi:10.1109/TVT.2004.827165.

46. Cavagnino, A., Lazzari, M., Profumo, F., and Tenconi, A., "A comparison between the axial flux and the radial flux structures for PM synchronous motors," *Industry Applications, IEEE Transactions on,* 38(6): 1517-1524, 2002, doi:10.1109/TIA.2002.805572.

47. Al Zaher, R., De Groot, S., Polinder, H., and Wieringa, P., "Comparison of an axial flux and a radial flux permanent magnet motor for solar race cars," Electrical Machines (ICEM), 2010 XIX International Conference on, 6-8 Sept. 2010, 2010, doi: 10.1109/ICELMACH.2010.5608195

48. Sitapati, K. and Krishnan, R., "Performance comparisons of radial and axial field, permanent-magnet, brushless machines," *Industry Applications, IEEE Transactions on,* 37(5): 1219-1226, 2001, doi:10.1109/28.952495.

49. Pippuri, J., Manninen, A., Keranen, J., and Tammi, K., "Torque Density of Radial, Axial and Transverse Flux Permanent Magnet Machine Topologies," *Magnetics, IEEE Transactions on*, 49(5): 2339-2342, 2013, doi:10.1109/TMAG.2013.2238520.

50. De Donato, G., Capponi, F.G., Rivellini, G.A., and Caricchi, F., "Integral-Slot Versus Fractional-Slot Concentrated-Winding Axial-Flux Permanent-Magnet Machines: Comparative Design, FEA, and Experimental Tests," *Industry Applications, IEEE Transactions on*, 48(5): 1487-1495, 2012, doi:10.1109/TIA.2012.2210011.

51. El-Refaie, A.M., Zhu, Z.Q., Jahns, T.M., and Howe, D., "Winding Inductances of Fractional Slot Surface-Mounted Permanent Magnet Brushless Machines," Industry Applications Society Annual Meeting, 2008. IAS '08. IEEE, 5-9 Oct. 2008, 2008, doi: 10.1109/08IAS.2008.61

52. Bianchi, N., Prè, M.D., Alberti, L., and Fornasiero, E., *Theory and design of fractional-slot PM machines : IEEE IAS corse (sic) notes*. 2007: CLEUP.

53. Gieras, J.F., Wang, R.-j., and Kamper, M.J., *Axial Flux Permanent Magenet Brushless Machines*. 2nd ed. 2008: Springer.

54. Magnussen, F., Thelin, P., and Sadarangani, C., "Performance evaluation of permanent magnet synchronous machines with concentrated and distributed windings including the effect of field-weakening," Power Electronics, Machines and Drives, 2004. (PEMD 2004). Second International Conference on (Conf. Publ. No. 498), March 31 2004-April 2 2004, 2004, doi: 10.1049/cp:20040370

55. Chong, L., Dutta, R., Dai, N.Q., Rahman, M.F., et al., "Comparison of concentrated and distributed windings in an IPM machine for field weakening applications," Universities Power Engineering Conference (AUPEC), 2010 20th Australasian, 5-8 Dec. 2010, 2010

56. De Donato, G., Giulii Capponi, F., and Caricchi, F., "Fractional-slot concentrated-winding axial-flux permanent magnet machine with core-wound coils," Energy Conversion Congress and Exposition (ECCE), 2010 IEEE, 12-16 Sept. 2010, 2010, doi: 10.1109/ECCE.2010.5617858

57. El-Refaie, A.M., "Fractional-Slot Concentrated-Windings Synchronous Permanent Magnet Machines: Opportunities and Challenges," *Industrial Electronics, IEEE Transactions on*, 57(1): 107-121, 2010, doi:10.1109/TIE.2009.2030211.

58. Jae Jun, L., Won-Ho, K., Jin Seung, Y., Si Yeong, Y., et al., "Comparison between concentrated and distributed winding in IPMSM for traction application," Electrical Machines and Systems (ICEMS), 2010 International Conference on, 10-13 Oct. 2010, 2010

59. Hyung-Woo, L., Chan-Bae, P., and Byung-Song, L., "Performance comparison of the railway traction IPM motors between concentrated winding and distributed winding," Transportation Electrification Conference and Expo (ITEC), 2012 IEEE, 18-20 June 2012, 2012, doi: 10.1109/ITEC.2012.6243417

60. El-Refaie, A.M. and Jahns, T.M., "Impact of Winding Layer Number and Magnet Type on Synchronous Surface PM Machines Designed for Wide Constant-Power Speed Range Operation," Industry Applications Conference, 2006. 41st IAS Annual Meeting. Conference Record of the 2006 IEEE, 8-12 Oct. 2006, 2006, doi: 10.1109/IAS.2006.256726

61. Ishak, D., Zhu, Z.Q., and Howe, D., "Comparison of PM brushless motors, having either all teeth or alternate teeth wound," *Energy Conversion, IEEE Transactions on,* 21(1): 95-103, 2006, doi:10.1109/TEC.2005.853765.

62. Aydin, M., Surong, H., and Lipo, T.A., "Torque quality and comparison of internal and external rotor axial flux surface-magnet disc machines," *Industrial Electronics, IEEE Transactions on,* 53(3): 822-830, 2006, doi:10.1109/TIE.2006.874268.

63. De Donato, G., Giulii Capponi, F., Rivellini, A., and Caricchi, F., "Integer-slot vs fractional-slot concentrated-winding axial-flux permanent magnet machines: Comparative design, FEA and experimental tests," Energy Conversion Congress and Exposition (ECCE), 2011 IEEE, 17-22 Sept. 2011, 2011, doi: 10.1109/ECCE.2011.6064189

64. Mevey, J.R., *Sensorless field oriented control of brushledd permanent magnet synchronous motors*. 2009, Kansas State University: Department of Electrical and Computer Engineering.

65. Moreton, P., *Industrial Brushless Servomotors*. 1st ed. 2000: Burlington Newnes.

66. Buja, G.S. and Kazmierkowski, M.P., "Direct torque control of PWM inverter-fed AC motors - a survey," *Industrial Electronics, IEEE Transactions on,* 51(4): 744-757, 2004, doi:10.1109/TIE.2004.831717.

67. Krein, P.T., Disilvestro, F., Kanellakopoulos, I., and Locker, J., "Comparative analysis of scalar and vector control methods for induction motors," Power

Electronics Specialists Conference, 1993. PESC '93 Record., 24th Annual IEEE, 20-24 Jun 1993, 1993, doi: 10.1109/PESC.1993.472061

68. Finch, J.W., Atkinson, D.J., and Acarnley, P.P., "Scalar to vector: general principles of modern induction motor control," Power Electronics and Variable-Speed Drives, 1991., Fourth International Conference on, 17-19 Jul 1990, 1990

69. Finch, J.W., "Scalar and vector: a simplified treatment of induction motor control performance," Vector Control Revisited (Digest No. 1998/199), IEE Colloquium on, 23 Feb 1998, 1998, doi: 10.1049/ic:19980057

70. chouhan, H., Kumawat, R., and Verma, H.K., "Comparative analysis of scalar and vector control induction machine drive through modeling and simulation," *International of electrical engineering & technology (IJEET)*, 3(2): 39-50, 2012.

71. Merzoug, M.S. and Naceri, F., "Comparison of field-oriented control and direct torque control for permanent magnet synchronous motor (pmsm)," *World academy of science, engineering and technology*, 45: 299-304, 2008.

72. Garcia, X.d.T., Zigmund, B., Terlizzi, A.A., Pavlanin, R., et al., "Comparison between FOC and DTC Strategies for Permanent Magnet Synchronous Motors," *Advances in Electrical and Electronic Engineering*, 5(1-2): 76-81, 2011.

73. Sarikhani, A. and Mohammed, O.A., "Demagnetization Control for Reliable Flux Weakening Control in PM Synchronous Machine," *Energy Conversion, IEEE Transactions on*, 27(4): 1046-1055, 2012, doi:10.1109/TEC.2012.2217968.

74. ON Semiconductor, *ON Semiconductor's Motor Control IGBTs and FreeWheeling Diodes*. 2012, ON Semiconductor Application Note.

75. Hughes, A., *Electric Motors and Drives: Fundamental, Types and Applications*. 3rd ed. 2006: Elsevier Ltd.

76. Blake, C. and Bull, C. *IGBT or MOSFET: Choose Wisely*. Available from: http://www.irf.com/technical-info/whitepaper/choosewisely.pdf.

77. Crowley, I.F. and Leung, H.F. *PWM Techniques: A Pure Sine Wave Inverter*. 2011; Available from: https://www.wpi.edu/Pubs/E-project/Available/E-project-042711-190851/unrestricted/PWM_Techniques_final.pdf.

78. Zhou, G.Y., Kojori, H., and Wu, B., "Comparison of Pulse Width Modulation (PWM) Techniques for Advanced Aerospace Load Power Management Applications," presented at, 2002, doi: 10.4271/2002-01-3183, (http://dx.doi.org/10.4271/2002-01-3183).

79. van der Broeck, H.W., Skudelny, H.C., and Stanke, G.V., "Analysis and realization of a pulsewidth modulator based on voltage space vectors," *Industry Applications, IEEE Transactions on,* 24(1): 142-150, 1988, doi:10.1109/28.87265.

80. P.Ramana, Kuma, B.S., Mary, D.K.A., and Kalavath, D.M.S., "COMPARISON OF VARIOUS PWM TECHNIQUES FOR FIELD ORIENTED CONTROL VSI FED PMSM DRIVE," *International Journal of advanced research in electrical, electronics and instrumentation engineering,* 2(7): 2928-2936, 2013.

81. Kumar, K.V., Michael, P.A., John, J.P., and Kumar, D.S.S., "SIMULATION AND COMPARISON OF SPWM AND SVPWM CONTROL FOR THREE PHASE INVERTER " *Asian Research Publishing Network Journal of Engineering and Applied Sciences*, 5(7): 61-74, 2010.

82. Zhenyu, Y., Mohammed, A., and Panahi, I., "A review of three PWM techniques," American Control Conference, 1997. Proceedings of the 1997, 4-6 Jun 1997, 1997, doi: 10.1109/ACC.1997.611797

83. Krishnan, R., *Permanent magnet synchronous and brushless DC motor drives*. 2010: CRC Press Taylor & Francis Group.

84. Bobek, V., "PMSM Electrical Parameters Measurement," *Freescale Semiconductor Application Note* 2013.

85. Ohm, D.Y. *DYNAMIC MODEL OF PM SYNCHRONOUS MOTORS*. 2000; Available from: http://www.drivetechinc.com/articles/IM97PM_Rev1forPDF.pdf.

86. Chong, L. and Rahman, M.F., "Saliency ratio derivation and optimisation for an interior permanent magnet machine with concentrated windings using finite-element analysis," *Electric Power Applications, IET*, 4(4): 249-258, 2010, doi:10.1049/iet-epa.2009.0119.

87. Liu, Y., Pei, Y., Yu, Y., Shi, Y., et al., "Increasing the saliency ratio of fractional slot concentrated winding interior permanent magnet synchronous motors," *Electric Power Applications, IET,* 9(7): 439-448, 2015, doi:10.1049/iet-epa.2014.0336.

88. Taylor, C.F., *The Internal_combustion Engine in Theory and Practice, Volume 2: Combustion, Fuels, Materials, Design*. 1985: The M.I.T Press.

89. B.Heywood, J., *Internal Combustion Engine Fundamentals*. International ed. 1988: McGraw-Hill Book Co.

90. Sethu, C., Leustek, M.E., Bohac, S.V., Filipi, Z., et al., "An Investigation in Measuring Crank Angle Resolved In-Cylinder Engine Friction Using Instantaneous IMEP Method," 2007-01-3989, 2007, doi: 10.4271/2007-01-3989, (http://dx.doi.org/10.4271/2007-01-3989).

91. Nagar, P. and Miers, S., "Friction between Piston and Cylinder of an IC Engine: a Review," presented at, 2011, doi: 10.4271/2011-01-1405, (http://dx.doi.org/10.4271/2011-01-1405).

92. Chen, S.K. and Flynn, P.F., "Development of a Single Cylinder Compression Ignition Research Engine," presented at, 1965, doi: 10.4271/650733, (http://dx.doi.org/10.4271/650733).

93. Gamma Technologies, "GT-SUITE Engine Performance Application Manual," 2013.

94. Pipitone, E., "A New Simple Friction Model for S. I. Engine," *SAE Technical Paper*, 2009, doi:10.4271/2009-01-1984.

95. Zhou, P., Lin, D., Wimmer, G., Lambert, N., et al., "Determination of d-q Axis Parameters of Interior Permanent Magnet Machine," *IEEE Transactions on Magnetics*, 46(8): 3125-3128, 2010, doi:10.1109/TMAG.2010.2043507.

96. Infineon Technologies AG. *Automotive IGBT Modules*. Available from: http://www.infineon.com/cms/en/product/power/igbt/automotive-igbts/automotive-igbt-module/channel.html?channel=db3a30432ba3fa6f012be33e87b75915#ispnTab2.

97. Graovac, D. and Pürschel, M., "IGBT Power Losses Calculation Using the Data-Sheet Parameters," *Infineon Technologies AG*, 2009.

98. Rao, N. and Chamund, D., "Calculating power losses in an IGBT module," *Dynex Semiconductor Ltd. Application Note*, 2014.

99. Infineon Technologies AG, *HybridPACK™1 module FS400R07A1E3_H5 Data Sheet*.

100. MathWorks, "Simscape User's Guide (MATLAB 2012b)," 2012

101. Hendershot, J.R. and Miller, T.J.E., *Design of Brushless Permanent-Magnet Motors*. 1994: Magna Physics and Oxford University Press.

102. Pyrhonen, J., Jokinen, T., and Hrabovcova, V., *Design of rotating electrical machines*. 2008: John Wiley & Sons, Ltd.

103. Młot, A., Korkosz, M., Grodzki, P., and Łukaniszyn, M., "Analysis of the proximity and skin effects on copper loss in a stator core," *Archives of Electrical Engineering*, Vol. 63(issue 2): 211-225, June 2014.

104. Haynes, W.M., *CRC handbook of chemistry and physics : a ready-reference book of chemical and physical data*. 92nd ed. ed. Handbook of chemistry and physics, ed. W.M. Haynes. 2011, Boca Raton, Fla.: Boca Raton, Fla. : CRC.

105. Electronics Tutorials. *Magnetic Hysteresis*. 2014; Available from: http://www.electronics-tutorials.ws/electromagnetism/magnetic-hysteresis.html.

106. Andreas Krings, Shafigh Nategh, Alexander Stening, Henrik Grop, et al., "Measurement and Modeling of Iron Losses in Electrical Machines," presented at 5th International Conference Magnetism and Metallurgy WMM'12, Gent, Belgium, 2012

107. Ozturk, N. and Celik, E., "APPLICATION OF GENETIC ALGORITHMS TO CORE LOSS COEFFICIENT EXTRACTION," *Progress In Electromagnetics Research*, Vol. 19: 133-146, 2011.

108. Cogent Power. *Typical data for SURA M330-35A*. 2009; Available from: http://cogent-power.com/cms-data/downloads/m330-35a.pdf.

109. Winter, D. *2015 Winner: Ford 1.0L EcoBoost DOHC DI I-3*. 2014; Available from: http://wardsauto.com/2015/2015-winner-ford-10l-ecoboost-dohc-di-i-3.

Appendix A

Simple square wave details at 2000rpm WOT

Group No. 01			
Pattern number	**Impulse torque stop position (CA deg)**	**Generating amplitude (Nm)**	**Motoring amplitude (Nm)**
01-01	180	126.43	-34.43
01-02	150	151.72	-34.43
01-03	120	189.65	-34.43
01-04	90	252.86	-34.43
01-05	60	379.29	-34.43

Group No. 02			
Pattern number	**Impulse torque stop position (CA deg)**	**Generating amplitude (Nm)**	**Motoring amplitude (Nm)**
02-01	210	103.45	-34.43
02-02	240	86.22	-34.43
02-03	270	72.81	-34.43
02-04	300	62.09	-34.43

Group No. 03			
Pattern number	**Impulse torque stop position (CA deg)**	**Generating amplitude (Nm)**	**Motoring amplitude (Nm)**
03-01	90	205.50	-7.17
03-02	120	176.60	-19.30
03-03	150	150.00	-28.29
03-04	180	126.20	-34.20
03-05	210	106.30	-38.42
03-06	240	89.92	-41.84
03-07	270	76.22	-44.66

Group No. 04			
Pattern number	**Impulse torque width (CA deg)**	**Generating amplitude (Nm)**	**Motoring amplitude (Nm)**
04-01	60	/	/
04-02	80	/	/
04-03	100	/	/
04-04	120	/	/

Group No. 05			
Pattern number	**Impulse torque stop position (CA deg)**	**Generating amplitude (Nm)**	**Motoring amplitude (Nm)**
05-01	60	378.60	-103.29
05-02	80	283.95	-77.47
05-03	100	227.16	-61.97
05-04	120	189.30	-51.65
05-05	140	162.26	-44.27

Simple square wave details at 4500rpm WOT

Group No. 01			
Pattern number	**Impulse torque stop position (CA deg)**	**Generating amplitude (Nm)**	**Motoring amplitude (Nm)**
01-01	180	133.8	-40
01-02	150	160.56	-40
01-03	120	200.7	-40
01-04	90	267.6	-40
01-05	60	401.4	-40

Group No. 02			
Pattern number	**Impulse torque stop position (CA deg)**	**Generating amplitude (Nm)**	**Motoring amplitude (Nm)**
02-01	210	108.97	-40
02-02	240	90.35	-40
02-03	270	75.87	-40
02-04	300	64.28	-40

Group No. 03			
Pattern number	**Impulse torque stop position (CA deg)**	**Generating amplitude (Nm)**	**Motoring amplitude (Nm)**
03-01	90	167.24	6.74
03-02	120	165.89	-12.58
03-03	150	154.17	-29.55
03-04	180	133.33	-39.16
03-05	210	108.72	-39.1
03-06	240	83.43	-25.56
03-07	270	61.8	2.7

Group No. 04			
Pattern number	**Impulse torque width (CA deg)**	**Generating amplitude (Nm)**	**Motoring amplitude (Nm)**
04-01	60	400	-117.48
04-02	80	300	-88.11
04-03	100	240	-70.49
04-04	120	200	-58.74

Group No. 05			
Pattern number	**Impulse torque stop position (CA deg)**	**Generating amplitude (Nm)**	**Motoring amplitude (Nm)**
05-01	60	400	-117.48
05-02	80	300	-88.11
05-03	100	240	-70.49
05-04	120	200	-58.74
05-05	140	171.42	50.32

Appendix B

Final DTC simulation results

	RPM	Copper loss (W)	Stator loss (W)	Rotor loss (W)	PM loss (W)	Total machine loss (W)	Inverter loss (W)	Total loss (W)	Speed variation (rpm)
DTC off	**2000**	472.6	54.79	9.1	25.76	562.25	671.7	1233.95	209
	2500	549	75.16	13.9	45	683.06	711.1	1394.16	176
	3000	532.4	94.9	18	58.89	704.19	704.2	1408.39	147.9
	3500	502.6	117.36	22.2	74.08	716.24	690.6	1406.84	126
	4000	517.9	143.2	27.82	95.48	784.4	699.6	1484	114.8
	4500	504.4	163.8	32.6	111.7	812.5	694.1	1506.6	101.5
	5000	389.5	198.73	34.21	114.69	737.13	634.5	1371.63	83.8
DTC with compression stroke pulse	**2000**	616.6	55.98	9.4	36.59	718.57	701.4	1419.97	170
	2500	676.2	77.38	15.71	63.34	832.63	735.7	1568.33	147.6
	3000	673.7	101.06	21.01	85.14	880.91	732	1612.91	122.4
	3500	662.4	122.3	24.69	100.05	909.44	722.5	1631.94	102
	4000	681.5	147.98	29.35	120.91	979.74	726.6	1706.34	93.8
	4500	688	170.3	36.2	161.2	1055.7	730.2	1785.9	82.1
	5000	699.1	212.1	43.44	205.45	1160.09	702.6	1862.69	62.4
DTC without compression stroke pulse	**2000**	616.6	55.98	9.4	36.59	718.57	701.4	1419.97	170
	2500	676.2	77.38	15.71	63.34	832.63	735.7	1568.33	147.6
	3000	673.7	101.06	21.01	85.14	880.91	732	1612.91	122.4
	3500	662.4	122.3	24.69	100.05	909.44	722.5	1631.94	102
	4000	681.5	147.98	29.35	120.91	979.74	726.6	1706.34	93.8
	4500	683.3	169.35	35.95	158.4	1047	729.1	1776.1	82.1
	5000	637.4	209.62	40.7	182.88	1070.6	689.2	1759.8	68.5

Appendix C

SVPWM switching duration table

Sector	Upper switch	Lower switch
1	$S_1 = T_a + T_b + \frac{1}{2}T_0$ $S_3 = T_b + \frac{1}{2}T_0$ $S_5 = \frac{1}{2}T_0$	$S_2 = \frac{1}{2}T_0$ $S_4 = T_a + \frac{1}{2}T_0$ $S_6 = T_a + T_b + \frac{1}{2}T_0$
2	$S_1 = T_a + \frac{1}{2}T_0$ $S_3 = T_a + T_b + \frac{1}{2}T_0$ $S_5 = \frac{1}{2}T_0$	$S_2 = T_b + \frac{1}{2}T_0$ $S_4 = \frac{1}{2}T_0$ $S_6 = T_a + T_b + \frac{1}{2}T_0$
3	$S_1 = \frac{1}{2}T_0$ $S_3 = T_a + T_b + \frac{1}{2}T_0$ $S_5 = T_b + \frac{1}{2}T_0$	$S_2 = T_a + T_b + \frac{1}{2}T_0$ $S_4 = \frac{1}{2}T_0$ $S_6 = T_a + \frac{1}{2}T_0$
4	$S_1 = \frac{1}{2}T_0$ $S_3 = T_a + \frac{1}{2}T_0$ $S_5 = T_a + T_b + \frac{1}{2}T_0$	$S_2 = T_a + T_b + \frac{1}{2}T_0$ $S_4 = T_b + \frac{1}{2}T_0$ $S_6 = \frac{1}{2}T_0$
5	$S_1 = T_b + \frac{1}{2}T_0$ $S_3 = \frac{1}{2}T_0$ $S_5 = T_a + T_b + \frac{1}{2}T_0$	$S_2 = T_a + \frac{1}{2}T_0$ $S_4 = T_a + T_b + \frac{1}{2}T_0$ $S_6 = \frac{1}{2}T_0$
6	$S_1 = T_a + T_b + \frac{1}{2}T_0$ $S_3 = \frac{1}{2}T_0$ $S_5 = T_a + \frac{1}{2}T_0$	$S_2 = \frac{1}{2}T_0$ $S_4 = T_a + T_b + \frac{1}{2}T_0$ $S_6 = T_b + \frac{1}{2}T_0$

Publications

1. 'Test and Simulation of Variable Air Gap Concept on Axial Flux Electric Motor'

Dian Liu, Deepak Hari, Christopher Vagg, Sam Akehurst, Christian Brace, Lloyd Ash

2013 IEEE Vehicle Power and Propulsion Conference (VPPC)

Abstract

One of the most promising methods to reduce vehicle fuel consumption and CO2 emissions is by using an electric motor in the vehicle powertrain system to assist the internal combustion engine, or propel vehicle by itself. This paper discusses a new potential method to improve axial flux motor performance and efficiency, by dynamically changing the air gap between the rotor and the stator. A series of experiments have provided insight into how certain key characteristics of the variable air gap (VAG) across a wide range of air gap settings. The results show that, on increasing the air gap from the normal 1.2mm to as much as 18mm, the peak torque reduces from 72Nm to 16Nm while the maximum speed of the motor increases from 5500rev/min to over 7000rev/min. It was seen that the high efficiency region moves towards the higher speed region as the air gap increases. Also, on increasing the air gap, the motor had a higher torque output at high speed. This behaviour is of limited benefit in a fixed geometry design, but the implementation of a software controlled air gap design allows the motor characteristics to be varied to suit the prevailing operating conditions. To demonstrate this benefit, the experimental data were used to build a model of the motor with a dynamically variable air gap concept incorporated into it. This model was then used with a fixed ratio powertrain, combined with a simple vehicle model and exercised over the NEDC drive cycle to predict the savings it would achieve when compared to a standard electric motor of similar technical specifications. The model predicts the overall battery energy usage reduced by 0.72% when using a VAG design. In addition, the VAG concept has the potential to reduce gearbox complexity and provide better drivability at higher speeds over the standard motor.

2. *'Wireless Sensor for Temperature and Flux Measurements in an Axial Flux Machine'*

Andreas Bock, Dian Liu, Jürgen Funck, Artur Giedymin, Richard Burke, Clemens Gühmann

AMA conferences with SENSOR+TEST 2015

Abstract

In recent years, there has been an increasing interest into electric and hybrid electric vehicles. Axial flux permanent magnet (AFPM) machines appear to be very promising for these applications. To fully exploit the potential of the electric machine to provide short burst of mechanical power higher than the rated continuous power, highly accurate dynamic models of its thermal behaviour are needed. To parameterize and validate these models the temperatures and magnetic flux densities on the rotor need to be measured during operation. This contribution presents the design and implementation of a smart wireless sensor for this purpose. An inductive power supply enables a dependable, continuous operation of the sensor without the need for batteries. Signal processing on the wireless sensor ensures an efficient use of the available wireless bandwidth. The mechanical integration of the sensor into the motor as well as its connection to an existing motor test bench are discussed. The operation of the sensor is verified during experiments in a climate chamber as well as on a motor test bench. The presented wireless sensor enables unprecedented measurements at an AFPM machine and can be easily extended with additional sensor in future experiments.

3. 'Simulation of dynamic torque ripple in an auxiliary power unit for a range extended electric vehicle'

Dian Liu, Sam Akehurst, Christian J Brace, Lloyd Ash, Gary Kirkpatrick, Makarand Khare

IMechE Sustainable Vehicle Technologies (SVT) 2015

Abstract

A low-cylinder-count engine is usually used in the auxiliary power unit of a range extended electric vehicle to save the packaging space. However, this type of engine inherently experiences more severe torque pulsation. By utilizing the vector control of an electric machine, the generator used in the system is able to apply opposite in-cycle torque to reduce the speed fluctuation. In this paper, an improved motor/generator analytical model was developed with the help of FEA and implemented in the active torque control strategy. The results showed that this approach was able to reduce the speed fluctuation by 22.9% compared to an unmodified control strategy.

4. 'A Study on Dynamic Torque Cancellation in a Range Extender Unit'

Dian Liu, Leon Rodrigues, Christian J Brace, Sam Akehurst, Gary Kirkpatrick, Lloyd Ash

SAE World Congress 2016

Abstract

A range extended electric vehicle (REEV) has the benefit of zero pipeline emission for most of the daily commute driving using the full electric mode while maintaining the capability for a long-range trip without the requirement of stop-and-charge. This capability is provided by the on-board auxiliary power unit (APU) which is used to maintain the battery state of charge at a minimum limit. Due to the limited APU package size, a small capacity engine with low-cylinder-count is normally used which inherently exposes more severe torque pulsation, that arises from a low firing frequency.

By using vector control, it is feasible to vary the generator in-cycle torque to counteract the engine torque oscillation dynamically. This allows for a smoother operation of the APU with the possibility of reducing the size of the engine flywheel. In this paper, a series of motor/generator control torque patterns were applied with the aim of cancelling the engine in-cycle torque pulses. The correlation between the electric machine torque profile and the engine in-cycle speed variation was investigated. As more aggressive use of the electric machine was made to achieve better system operation characteristic, the electric losses become more significant compared to constant torque strategy, as does the thermal impact. The results showed that within the target APU specification, the optimum speed fluctuation reduction of 21.9% could be achieved, while the M/G's electric loss percentage rose from 3.5 to 4.7% at 4500rpm. An upgrade for cooling circuit specification was not considered necessary since the electric loss only increased by 2.5%. The Pareto frontier was also plotted for total electric loss against peak-to-peak engine speed variation.

5. 'Thermal Management of a Low Cost Range Extender for Electric Vehicles'

Ashwini Agarwal, Leon Rodrigues, Dian Liu, Andrew GJ Lewis, Sam Akehurst, Christopher J Brace, Gary Kirkpatrick , Lloyd Ash

The 6th Hybrid and Electric Vehicle Conference (HEVC) 2016

Abstract

Range extenders are a solution to partly overcome the limitations of current battery technology and are gaining popularity despite their complexity, due to the potential for reduced tailpipe emissions and fuel consumption. The range extender or Auxiliary Power Unit (APU) consists of an on board fuel convertor that converts fuel such as gasoline into electrical power while the vehicle is in operation. This enables the traction battery storage capacity to be reduced whilst still maintaining an acceptable driving range.

One of the key requirements of an APU is to provide maximum electrical power. In order to do so it is important that the engine as well as the generator are operated at their maximum efficiency in addition to optimising the complete system to reduce any parasitic losses in auxiliary systems.

The conflicting requirements of running the engine at a high temperature (~90°C) and the generator to run as cold as possible (~50°C) has consequences on vehicle system integration such as the need to use separate coolant loops, radiators, pumps etc. Employing a common cooling loop can reduce parasitic loads and simplify vehicle integration, but requires operating the engine and/or the generator under sub-optimum thermal conditions.

The paper discusses the development of a thermal management system using a single coolant loop for the APU. The APU was tested on a bespoke rig first using two independent cooling loops to characterise the APU performance. The benefits of employing a single coolant loop are then weighed against the compromise in performance observed as a result of operating the engine and/or generator under sub-optimum thermal conditions in a single loop. In the single coolant loop, there is a drop in APU power of around 4% and an ESFC penalty of 2.34% at full load across the operating regime. However there is a substantial saving in parasitic losses, simplified package installation with reduction in overall package cost.

6. *'In-cycle speed oscillation reduction of an auxiliary power unit using dynamic torque control'*

Dian Liu, Leon Rodrigues, Christian J Brace, Sam Akehurst, Gary Kirkpatrick, Lloyd Ash

SAE International Journal of Alternative Powertrains (in preparation)

Abstract

A range extended electric vehicle (REEV) powertrain comprises of an electric traction motor typically supplied from a battery that can be used for most daily commutes and an auxiliary power unit (APU) to provide the long range capability. The APU typically consists of a small capacity engine with a low cylinder count combined with an electrical generator that can maintain battery state of charge at a desired minimum, mitigating issues such as range anxiety while keeping low tailpipe emissions.

Low cylinder count engines tend to exhibit large in-cycle torque pulsations thus speed fluctuation, due to its lower firing frequency. This leads to higher engine noise and vibration which degrades vehicle drivability. In conventional powertrains these variations are absorbed using relatively larger flywheels and the powertrain shaft inertia. In an auxiliary power unit, as the generator is mounted directly on to the engine shaft, the torque variations must be cancelled out by alternative means.

This paper describes a method of cancelling the in-cycle torque variations by applying a dynamic counteracting torque in the generator. The APU was modelled in Simulink to calculate optimum in-cycle torque demands. Subsequently, electromagnetic and thermal finite element electric machine models were used to evaluate the effect of dynamic torque control (DTC) on generator losses and thermal performance. The APU was tested using the DTC strategy and the modelled effect of torque cancellation on in-cycle speed fluctuation was validated.